TECHNISCHE
UNIVERSITÄT
WIEN

Vienna University of Technology

DISSERTATION

Two-photon Modification of materials with ultrashort laser radiation:

Z-scan measurements and 3D-modification of selected materials

Realized to obtain the title of Ph. D in technical science under the supervision of

Prof. Dr. Wolfgang Husinsky

Submitted to Institute of Applied Physics

Vienna University of Technology

Faculty of Physics

By

MSc. Aliasghar Ajami

Matr.No: 0727116

Wiedner Hauptstr. 8-10, 1040 Wien

Vienna, 27. June 2012

Acknowledgement

بسم اللہ الرّحمن الرّحیم

Without the support of God, supervisor, family, friends, and coworkers, it was never possible to finish the cumbersome job of my dissertation. As I am going to complete my doctorate soon, I would like to express my gratitude to all those personalities who really helped and supported me during the long way of my Ph.D.

First of all I would like to be highly grateful to my dearest and nearest God (Allah), the most beneficent and merciful, who always listens whenever I call Him heartfeltly. Then I would be highly grateful to my Holy Prophet Muhammad (peace be Upon Him) who is source of knowledge, guidance and good moral values.

I have no words to pay my thanks to my Dear supervisor Professor Wolfgang Husinsky. He was a continuous source of inspiration during five years of my stay at TU Wien. He was always helpful and supportive for me and I found him accommodating and knowledgeable. He always pushed me to work and gave me the full independence to work. He motivated me to pursue my research on this topic and I learnt a lot from him on my research topic. He provided me good, comfortable and supportive research environment. His nice and encouraging attitude was blessing for me. He is a compassionate and kindhearted person.

I am also grateful to Prof. F. Aumayr, Prof. Robert Liska and Prof. Jurgen Stampfl (project leaders in 2PIP innovative project) who were always encouraging for me. Special thanks go to Dr. Shzia Bashir and Prof. Mohammad Shahid who helped me a lot.

I would like to thank all my colleagues in the lab Dr. Niklas Pucher and Mr. Zhiquan Li for preparing 2PIs compounds, Dr. Svecova Blanka for preparing metal glass composite samples, Dr. aleksander Ovsianikov, Mr. Claus cicha and Mr. Claus Stadlmann for their helpful cooperation in 2PIP project. I am really grateful to Mr. Paul Berlinger for technical and electronics help in my institute. I am thankful to technical staff of work shop for their help. I am also thankful to Ms. M. Marik, Ms. C. Toupal-printer for their cooperation.

I would also like to say my heartiest thanks to my dearest wife Elham. I am so lucky and blessed to have such a nice wife who really provided me moral support. It was not easy for her to be far away from her parents and live in a foreign country. She sacrificed the enjoyment of being close to parents and accompanied me in this long and arduous journey. Her loving, kind and caring attitude always made my morals high. During these five years she was mother as well as father for our son Mostafa and our daughter Mahbobeh. I should also grateful to both my kids Mostafa and Mahbobeh for their understanding and kindness. I had not enough time to spend with them as a responsible father should do.

I wish God bless my loving mother who passed away ten years ago. I owe her all my progress in my life. I would thank my selfless father who has endured many troubles to make me who I am

today. All my successes can be attributed to my parents sent me to school and support me for going to university. Without their great devotion I surely was not in this position.

At the last I would be highly thankful to my father and mother in law and also all my sisters, brother, brothers in law, sister in law and all my friends for their moral support.

Abstract

This dissertation consists of three parts; analytical calculations, numerical calculation and experimental measurements. In the section Analytical Calculations, the properties of Gaussian laser beams are outlined. Then, the propagation of a Gaussian beam through free space in the limit of the Fresnel- and Fraunhofer diffraction theory is presented. The Z-scan technique, as a sensitive method for measuring nonlinearities, is explained. For the case of the closed aperture Z-scan geometry, in which the phase distortion results in the amplitude modulation, the transmittance through a small aperture located in the far field has been derived. The normalized transmittance has been calculated assuming different types and orders of nonlinear processes such as third order nonlinearity at the absence of 2PA, third order nonlinearity at the presence of 2PA, fifth order nonlinearity at the absence of 3PA, fifth order nonlinearity at the presence of 3PA, concurrent third and fifth order nonlinearity at the absence of 2PA and 3PA, concurrent third and fifth order nonlinearity at the presence of 2PA and third order nonlinearity at the absence of 2PA assuming an elliptical Gaussian laser beam.

In the case of open aperture Z-scan geometry, the entire energy transmitted through the nonlinear medium is collected. The normalized transmittance assuming the following different order of nonlinearity has been calculated: 2PA as a third order nonlinear absorption using a circular Gaussian beam, 2PA as a third order nonlinear absorption using an elliptical Gaussian beam and 3PA as a fifth order nonlinear absorption using a circular Gaussian beam.

In the numerical calculation part some integrals, whose analytically evaluation is not possible, have been determined numerically. Then the numerical calculation results have been compared with analytical calculation results obtained in an approximation domain in which analytical calculation is allowed to be carried out.

In the main, experimental section of the thesis, results of open aperture Z-scan measurements to determine the 2PA and 3PA coefficients of different types of samples are presented. Three different type of samples for different purposes have been investigated: Two-photon initiators synthesized in the chemistry institute in order to be used in two-photon induced polymerization applications, Metal glass composites prepared at the Nuclear Physics Institute in Prague, Czech Republic, employing ion implantation method and a grafting compound with the commercial name of BAC-M for photo-grafting applications for immobilizing some molecules inside the volume of a polymer matrix.

Ultimately, some 3D microstructures were successfully created via both two-photon polymerization and three-photon grafting.

Kurzfassung

Diese Arbeit besteht aus drei Teilen: Analytische Berechnungen, Numerische Auswertungen und Experimentelle Ergebnisse. Im Rahmen der analytischen Berechnungen werden zuerst die Eigenschaften eines Gauß´schen Strahls im Detail besprochen. Im weiteren wird die Näherung der Fresnel und Frauenhofer Beugung zur Ausbreitung eines Gauß´schen Strahls verwendet. Im Folgenden wird die Z-scan Technik zur Messung von nichtlinearen Größen ausführlich behandelt.

Für den Fall der „closed aperture Z-scan" – Methode (die Phasenänderung bewirkt hier eine Amplitudenänderung) wird die Transmission durch eine kleine Öffnung im Fernfeld detailliert berechnet. Genaue Ableitungen wurden für die normalisierte Transmission für folgende Fälle durchgeführt: Existenz einer Nichtlinearität der dritten Ordnung ohne Zweiphotonenabsorbtion, Existenz einer Nichtlinearität der dritten Ordnung mit gleichzeitiger Zweiphotonenabsorbtion, Existenz einer Nichtlinearität der fünften Ordnung ohne Dreiphotonenabsorbtion, Existenz einer Nichtlinearität der fünften Ordnung bei gleichzeitiger Dreiphotonenabsorbtion, Existenz einer Nichtlinearität der dritten und fünften Ordnung ohne Zwei- und Dreiphotonenabsorbtion, Existenz einer Nichtlinearität der dritten und fünften Ordnung mit Zwei- und Dreiphotonenabsorbtion für einen elliptischen Gaußstrahl.

Im Fall der „open-Aperture" Anordnung wird die gesamte Energie, die durch das nichtlineare Medium transmittiert wird registriert. Berechnungen wurden für folgende Fälle durchgeführt: Zweiphotonenansorption (Nichtlinearität dritter Ordnung) unter der Annahme eines kreisrunden Gaußstrahles, Zweiphotonenansorption (Nichtlinearität dritter Ordnung) unter der Annahme eines elliptischen Gaußstrahles und Dreiphotonenansorption (Nichtlinearität fünfter Ordnung) unter der Annahme eines kreisrunden Gaußstrahles.

Im zweiten Abschnitt wurden einigem analytisch nicht berechenbare Integrale numerisch ausgewertet. Die Ergebnisse wurden dann mit analytischen Ergebnissen, für die im Grenzfall Lösungen existieren überprüft.

Im experimentellen Teil werden die Ergebnisse für drei verschiedene Probentypen präsentiert. Dabei wurden die Zwei- und Dreiphotonenabsorbtionsquerschnitte ermittelt und die Ergebnisse präsentiert und dikuttiert. Diese verschiedenen Probentypen stellen jeweils andere, spezielle experimentelle Anforderungen an die Z-scan Methode. Die Gruppen sind: Zweiphotonen-Initiatoren (entwickelt am Chemieinstitut der TU Wien) für den Einsatz in Zweiphotonenpolimerisationanwendungen; Metall-Glas-Composites hergestellt mit Ionenimplantation am Institut für Kernphysik in Prag; ein Material für Photo-grafting (BAC-M) für 3D Photo-grafting Anwendungen.

Schließlich wurden einige 3D-Mikrostrukturen mittels Zweiphotonenpolymerisation sowie Dreiphotonen-Grafting erzeugt.

Table of contents

Table of Figures

Chapter 1

1. Introduction

1.1. Motivation and goals

Material modification exploiting nonlinear absorption became practicable after the advent of pulsed lasers and its realzation is a consequence of the realization of high peak power ultrashort pulses emitted by femtolasers. This field of research has attracted much interest and has found many practical applications such as two-photon induced polymerization (2PIP), 3D optical data storage and many more. Due to the intensity-dependent nature of nonlinear absorption, any physical or chemical property change via nonlinear absorption can be created within the bulk of transparent materials with a structural resolution beyond the diffraction limit.

2PA in molecular systems using near infrared ultrashort pulsed laser radiation has attracted much attention of researchers so that they have put much emphasis on designing and synthesizing organic molecules with significantly higher 2PA cross sections than in common materials. Several different experimental techniques can be employed to measure 2PA cross sections among them the Z-scan technique is a particularly sensitive technique and also very easy to perform. This technique relies on the transformation of phase distortion to amplitude distortion during beam propagation through a nonlinear medium.

In this dissertation, in the first part the subject is the analytical calculation of the normalized transmittance through a nonlinear medium in at the presence a 2PA, 3PA or concurrence of both order of nonlinearity. The second part deals with Z-scan results for a series of newly synthesized two-photon initiators (2PIs) are presented and ultimately the numerical calculations for prediction of Z-scan results are compared with the experimental results.

1.2. Nonlinear Optics

When a physical oscillating system such as a dipole momentum is overdriven it will exhibit a nonlinear response. an optical nonlinear response can occur when materials are illuminated by high enough intense radiation such those emitted by pulsed lasers [1, 2]. The nonlinearity can be expressed by the polarization of the material which is often written as a power series expansion of the total applied optical field.

$$p = \varepsilon_0(\chi^{(1)} E + \chi^{(2)} E \cdot E + \chi^{(3)} E \cdot E \cdot E + \chi^{(4)} E \cdot E \cdot E \cdot E + \chi^{(5)} E \cdot E \cdot E \cdot E \cdot E + \chi^{(6)} E \cdot E \cdot E \cdot E \cdot E.E + ...) \quad (1.1)$$

In the low intensity regime, when the second and higher order terms in the above equation are negligible, the polarization depends linearly on the applied electric field strength. An area of classical optics dealing with low intensity regime is named linear optics due to the linearity dependence of polarization on the driving electric field strength. The concept of nonlinear optics is derived from the fact that for the high intensity regime the polarization no longer changes linearly with the applied electric field but changes nonlinearly because the second or higher order terms in Eq. (1.1) become comparable with the first term.

In the above power series expansion, the first order or linear susceptibility $\chi^{(1)}$ is responsible for the refractive index and linear (one photon) absorption. The second order susceptibility $\chi^{(2)}$ (which is non-zero only for thoses crystals which have no inversion symmetry) is responsible for nonlinearities such as second harmonic generation, sum frequency and difference frequency generation. In general, the optical susceptibility is a tensor resulting in the linear susceptibility $\chi^{(1)}$ as a second-rank tensor, the second order susceptibility $\chi^{(2)}$ as a third-rank tensor and so on.

1.3. Third order optical nonlinearity

Third-order optical nonlinearities involve the nonlinear susceptibility four-rank tensor $\chi^{(3)}$ in (1.1) which is non-zero in all material. The typical values for $\chi^{(3)}$ are orders of magnitude smaller than $\chi^{(2)}$ coefficients. Third-order susceptibility governs many phenomena such as third harmonic generation, Coherent Stokes and anti-Stokes Raman scattering, frequency mixing, optical Kerr effect and two-photon absorption. The term involving E^3 in Eq. (1.1) implies that three optical fields interact to produce a fourth field. The $\chi^{(3)}$ interaction is thus a four-photon process [3].

In general, the applied electric field can be written as a summation of electric fields of three beams where each beam has a different frequency ω.

$$E = \frac{1}{2}\left(E_1 e^{-i\omega_1 t} + E_2 e^{-i\omega_2 t} + E_3 e^{-i\omega_3 t} + c.c \right) \tag{1.2}$$

For the sake of simplicity, a special case is considered when a linear polarized electric field is traveling through an isotropic medium. In this case, the polarization inside the subjected medium is induced only in the direction of the applied electric field.

The nonlinear polarization resulting from the $\chi^{(3)}$ interaction leads to a total of 108 terms involving all possible permutations of the fields with three frequencies [2].

Ignoring the $\chi^{(1)}$ and $\chi^{(2)}$ components in Eq. (1.1), the nonlinear polarization as a source of radiation emmites light at new generated frequency as $3\omega_1$, $3\omega_2$, $3\omega_3$, $2\omega_1+\omega_2$, $2\omega_1+\omega_3$, $2\omega_2+\omega_1$, $2\omega_2+\omega_3$, $2\omega_3+\omega_1$, $2\omega_3+\omega_2$, $2\omega_1-\omega_2$, $2\omega_1-\omega_3$, $2\omega_2-\omega_1$, $2\omega_2-\omega_3$, $2\omega_3-\omega_1$, $2\omega_3-\omega_2$, $\omega_1+\omega_2+\omega_3$, $\omega_1+\omega_2-\omega_3$, $\omega_1-\omega_2+\omega_3$, $-\omega_1+\omega_2+\omega_3$, $\omega_1-\omega_2-\omega_3$, $-\omega_1+\omega_2-\omega_3$, $-\omega_1-\omega_2+\omega_3$, ω_1, ω_2, ω_3.

$$
\begin{aligned}
P^{(3)}(\omega_4) = \varepsilon_0 \chi^{(3)} E^3 = \varepsilon_0 \chi^{(3)} \left[\frac{1}{2}\left(E_1 e^{-i\omega_1 t} + E_2 e^{-i\omega_2 t} + E_3 e^{-i\omega_3 t} + c.c \right) \right]^3 = \\
\frac{\varepsilon_0}{8} (\chi(\omega_1) E(\omega_1)^3 e^{-i(3\omega_1)t} + \chi(\omega_1,\omega_2) E(\omega_1)^2 E(\omega_2) e^{-i(2\omega_1+\omega_2)t} + \\
\chi(\omega_1,\omega_3) E(\omega_1)^2 E(\omega_3) e^{-i(2\omega_1+\omega_3)t} + \chi(\omega_1) E(\omega_1)^2 E^*(\omega_1) e^{-i(\omega_1)t} + \\
\chi(\omega_1,\omega_2) E(\omega_1)^2 E^*(\omega_2) e^{-i(2\omega_1-\omega_2)t} + \chi(\omega_1,\omega_3) E(\omega_1)^2 E^*(\omega_3) e^{-i(2\omega_1-\omega_3)t} + \\
\chi(\omega_1,\omega_2) E(\omega_1)^2 E(\omega_2) e^{-i(2\omega_1+\omega_2)t} + \chi(\omega_1,\omega_2) E(\omega_1) E(\omega_2)^2 e^{-i(\omega_1+2\omega_2)t} + \\
\chi(\omega_1,\omega_2,\omega_3) E(\omega_1) E(\omega_2) E(\omega_2) e^{-i(\omega_1+\omega_2+\omega_2)t} + \chi(\omega_1,\omega_2) E(\omega_1) E(\omega_2) E^*(\omega_1) e^{-i(\omega_2)t} + \\
\chi(\omega_1,\omega_2) E(\omega_1) E(\omega_2) E^*(\omega_2) e^{-i(\omega_1)t} + \chi(\omega_1,\omega_2,\omega_3) E(\omega_1) E(\omega_2) E^*(\omega_3) e^{-i(\omega_1+\omega_2-\omega_3)t} + \\
\ldots\ldots + c.c.)
\end{aligned}
\tag{1.3}
$$

The existence of 108 terms does not mean there are as many distinct mechanisms involved. For instance, three terms give $\omega_4 = 3\omega_i$, for i = 1, 2, 3, describing exactly the same process of third-harmonic generation (THG). Furthermore, THG is a special case of sum frequency generation (SFG) involving one, two, or three different frequencies giving $\omega_4 = \omega_i+\omega_j+\omega_k$, i, j, k= 1, 2, 3 accounting for 27 terms. If only two distinguishable laser beams are available, the number of permutations decreases to 48.

Table 1. Frequencies and amplitudes for different nonlinear response arising from third-order nonlinear polarization

Type of Nonlinear Process	Amplitude of each process	New generated frequencies
Third harmonic generation (THG)	$E_j^{\,3} \quad j=1,2,3$	$3\omega_1,\ 3\omega_2,\ 3\omega_3$
Sum frequency generation (SFG)	$3E_iE_j^{\,2} \quad i,j=1,2,3 \quad i\neq j$ $6\,E_1\,E_2\,E_3$	$2\omega_1+\omega_2,\ 2\omega_1+\omega_3$ $2\omega_2+\omega_1,\ 2\omega_2+\omega_3$ $2\omega_3+\omega_1,\ 2\omega_3+\omega_2$ $\omega_1+\omega_2+\omega_3$
Frequency mixing Parametric amplification	$3E_i^{*}E_j^{\,2} \quad i,j=1,2,3 \quad i\neq j$	$2\omega_1-\omega_2,\ 2\omega_1-\omega_3$ $2\omega_2-\omega_1,\ 2\omega_2-\omega_3$ $2\omega_3-\omega_1,\ 2\omega_3-\omega_2$
Coherent Stokes Raman scattering	$6E_i^{*}E_jE_k \ \ i,j,k=1,2,3 \ i\neq j\neq k$	$\omega_1+\omega_2-\omega_3$ $\omega_1-\omega_2+\omega_3$ $-\omega_1+\omega_2+\omega_3$
Coherent anti-Stokes Raman scattering	$6E_i^{*}E_j^{\,*}E_k \ \ i,j,k=1,2,3 \ i\neq j\neq k$	$\omega_1-\omega_2-\omega_3$ $-\omega_1-\omega_2+\omega_3$ $-\omega_1+\omega_2-\omega_3$
Bound electronic optical Kerr effect Raman induced Kerr effect (RIKE)	$3E_i^{\,2}E_i^{*} \quad i=1,2,3$	$\omega_1,\ \omega_2,\ \omega_3$
Molecular orientation Kerr effect Two-photon absorption (2PA)	$6E_iE_jE_j^{*} \quad i,j=1,2,3 \quad i\neq j$	$\omega_1,\ \omega_2,\ \omega_3$

When the system is driven by a single monochromatic light beam, the third-order nonlinear response involves only four terms corresponding to three involved mechanisms.

$$P^{(3)} = \varepsilon_0 \chi^{(3)} \left(\frac{1}{2}(E e^{-i\omega t} + c.c.) \right)^3 = \frac{1}{8} \varepsilon_0 \chi^{(3)} \left(E^3 e^{-i(3\omega)t} + 3|E|^2 E e^{-i\omega t} + c.c. \right) \tag{1.4}$$

The first term in Eq. (1.4) indicates the third harmonic generation and the second term describes the Kerr effect and two-photon absorption (2PA) which are explained briefly below.

1.3.1. Third harmonic generation

Third harmonic generation is a nonlinear optical response in which three photons of frequency ω are annihilated and one photon of frequency 3ω is created. This is a parametric process in which the photon energies are conserved. The efficiency of this process depends on the strength of the real part of the third order susceptibility.

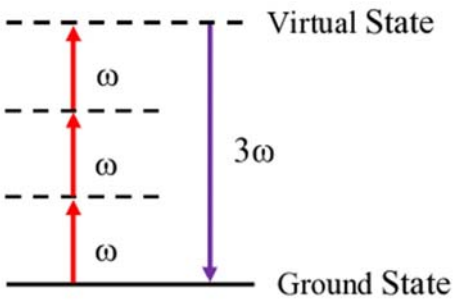

Fig. 1.1 Energy-level description for third-harmonic generation

1.3.2. Kerr effect

The second term in Eq. (1.4) describes the contribution of the third order nonlinearity to the induced polarization oscillating at the frequency of the incident field. Therefore, the total induced polarization oscillating at the frequency of the driven electric field can be written as

$$P(\omega) = \varepsilon_0 (\chi^{(1)} E\cos(\omega) + \frac{3}{4}\chi^{(3)}|E|^2 E\cos(\omega)) = \varepsilon_0 (\chi^{(1)} + \frac{3}{4}\chi^{(3)}|E|^2) E\cos(\omega) \tag{1.5}$$

The effective susceptibility now, compared to the linear regime, contains an additional term proportional to the light intensity square given by

$$\chi^{(1)}{}_{eff} = \chi^{(1)} + \frac{3}{4}\chi^{(3)}\left|E\right|^2 \tag{1.6}$$

Since the real and imaginary components of the linear susceptibility $\chi^{(1)}$ are associated with refraction and absorption, the refraction index and absorption coefficient are no longer constant but they depend linearly on the light intensity, which will be described in greater details in section 2.3. The $\chi^{(3)}$ process resulting in an intensity-dependent refractive index is known as the Optical Kerr Effect (OKE).

$$n(I) = n_0 + n_2 I \tag{1.7}$$

where n_0 is the linear refractive index and n_2 is the third order refractive index. Any variation in the intensity distribution, whether spatially or temporally, will cause a corresponding change in the refractive index. For instance, a Gaussian-like spatially-varying intensity distribution gives rise to self-lensing (Kerr lens), which results in self-focusing (for positive n_2) or self-defocusing (for negative n_2). Also a Gaussian-like temporally-varying intensity distribution will result in a time-dependent refractive index leading to self-phase modulation, which introduces chirp to a non-chirped pulse. In such a chirped pulse, the frequency is no longer constant over the pulse duration but it increases or decreases corresponding to the positive or negative sign of n_2. This means that the longer wavelengths arrive earlier and shorter wavelengths arrive later assuming a positive sign for n_2 and vice versa. The time-dependent frequency of a chirped pulse can be written as

$$\omega(t) = \frac{\partial\varphi(t)}{\partial t} = \omega_0 - n_2\frac{2\pi}{\lambda}z\frac{\partial I(t)}{\partial t} \tag{1.8}$$

It is worth mentioning that in regions of anomalous dispersion the longer wavelengths experiences higher refive index thus, the redder portions of the pulse have a lower velocity than the blue portions. Therefore, the front of the self-phase modulated pulse moves slower than the back. This effect can be exploited to some degree to compensate the effect of self-phase modulation in order to produce ultrashort pulse.

1.3.3. Two-photon absorption

Two-photon absorption is a third order optical nonlinear process in which two photons (not necessarily at the same frequency) are simultaneously absorbed to excite a molecule from ground state to a real excited state through a virtual state as shown in Fig. 1.2. The first photon makes a virtual transition to a nonexistent state between the upper and lower levels. If the second photon arrives within the lifetime of that virtual state, the absorption sequence to the upper state can be completed. If not, the virtual state collapses back to the ground state, and no absorption takes place [2]. Therefore, the 2PA probability depends on both the lifetime of the virtual state and photon fluxes. The lifetime of the virtual state is proportional to $1/\Delta E$, where ΔE is the difference

energy between the virtual state and the nearest real state. Therefore, the 2PA probability increases dramatically when the frequency of applied field approaches the resonant frequency of a molecular system. In addition, the dependence of the 2PA probability on the photon flux suggests using a tightly focused laser beam to increase the probability of 2PA [4]. 2PA is observed in a spectral range where the material is normally transparent.

The refractive index and the absorption coefficient are related to the real and imaginary parts of the susceptibility. Hence, a linear dependence on the intensity of the absorption coefficient can be introduced analogous to the intensity dependence of the refractive index in Eq. (1.7).

$$\alpha(I) = \alpha_0 + \alpha_2 I \tag{1.9}$$

where α_0 is the linear absorption coefficient and α_2 is the 2PA coefficient. The relation between the refractive index and the real part of the susceptibility as well as between the absorption coefficient and the imaginary part of susceptibility will be calculated in section 2.3 in more detail.

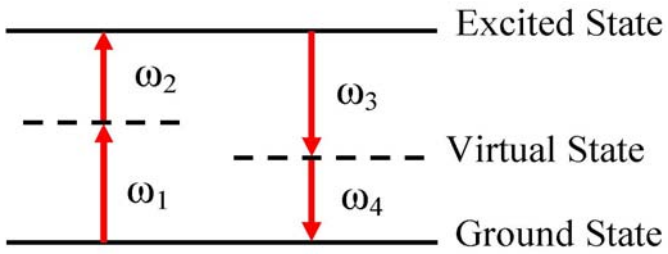

Fig. 1.2 Two-photon absorption

One should notice the difference between the two-photon absorption and second harmonic generation, while in both cases two photons simultaneously "disappear". Two-photon absorption described above may result in emitting a photon at a frequency greater than ω and lower than 2ω, which is referred to as up-converted emission. As seen in Fig. 1.3 (A), absorption of two photons makes the transition from state "a" to state "b". The upper energy level "b" then relaxes to the real state "c" without emitting any photon and ultimately relaxes back to the ground state, emitting a photon at higher frequency than that of exciting field. Second harmonic generation is a second order optical nonlinear process in which two photons at frequency ω are annihilated and one photon at frequency 2ω is created. As shown in Fig. 1.3 (B), two photons make the transition to a virtual state. The virtual state immediately collapses back to the ground state, emitting a photon at a frequency twice of that of the exciting field. In summary, two-photon absorption is a resonant process, whereas second harmonic generation is a non-resonance process. In a resonant process, the lifetime of the excited state is much longer than the lifetime of the virtual state in a non-resonant process. Therefore, the emitted photon after two-photon absorption is no longer coherent with the incident optical field, whereas the second harmonic generated photon is coherent with the incident optical field [5].

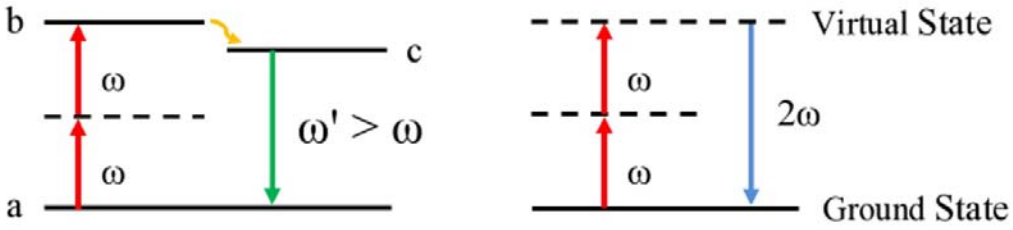

Fig. 1.3 (a) indicates two-photon absorption and the following up-converted emissionand (b) shows second harmonic generation

1.4. Fifth order nonlinearity

Fifth order nonlinearity is described with $\chi^{(5)}$ in the power series expansion in Eq. (1.1). An example for $\chi^{(5)}$ interactions is 3PA, which is an optical nonlinear process, by which the energy gap between two real states is bridged through the simultaneous absorption of three photons, not necessarily at the same frequency. Not only one photon but even two photons together have sufficient energy to complete the transition alone; 3PA is thus observed in the spectral range where the material is completely transparent. Fig. 1.4 shows energy level description of three-photon absorption containing two virtual states through which the ground state is bridged to the first real excited state. The probability for a three-photon absorption process is much less than the probability for a two-photon absorption process. A much higher intensity is required for a three-photon absorption process to take place, since three photons must be absorbed within a very short time interval, requiring a higher rate of photon flux. In both three-photon absorption and third harmonic generation, three photons "disappear". It should be noted that a three-photon absorption process is a resonant process that may results in emission of one photon of higher energy. This photon is not coherent with the incident optical field, whereas third harmonic generation is a non-resonant process resulting in emission of one photon, which is coherent with the incident optical field with an energy three times the energy of either of the incident photons.

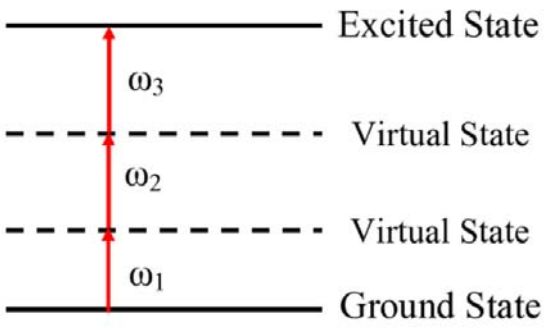

Fig. 1.4 Energy level description of three-photon absorption

1.5. Nonlinear absorption measurements

Nonlinear absorption coefficients such as 2PA coefficients (cross section), 3PA coefficients, etc. can be measured applying a number of different methods, which are described below.

1.5.1. Nonlinear transmission

In this technique, the sample is mounted at the focal point of a focused laser beam and the energy transmitted through the sample is measured as a function of input energy [6]. Fig. 1.5 shows the outline of the experimental setup used in this technique.

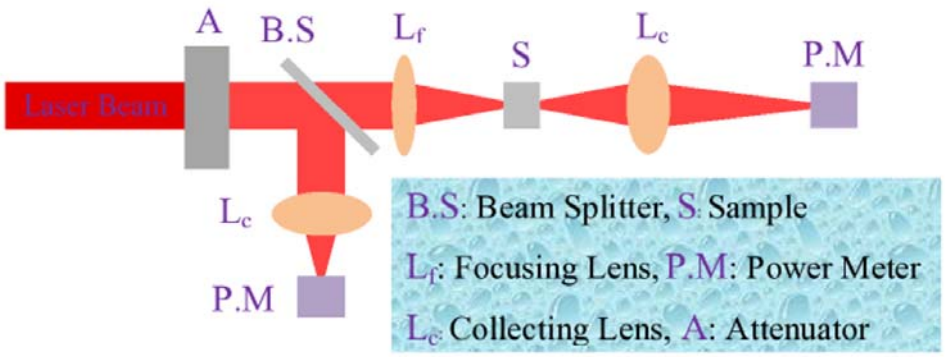

Fig. 1.5. Experimental setup for nonlinear transmission technique

According to basic theoretical considerations, if a CW laser beam has a spatially Gaussian intensity distribution in the medium, the normalized transmittance caused by 2PA (regardless of 1PA) can be expressed as

$$T(I_0) = \frac{\ln(1+\alpha_2 L I_0)}{\alpha_2 L I_0} \tag{1.10}$$

In Eq. (1.10) I_0 is the incident intensity, L the thickness of a given sample, and α_2 the 2PA coefficient of a given 2PA medium (from (1.9)). Fig. 1.5 shows the normalized transmittance as a function of incident intensity given by Eq. (1.10).

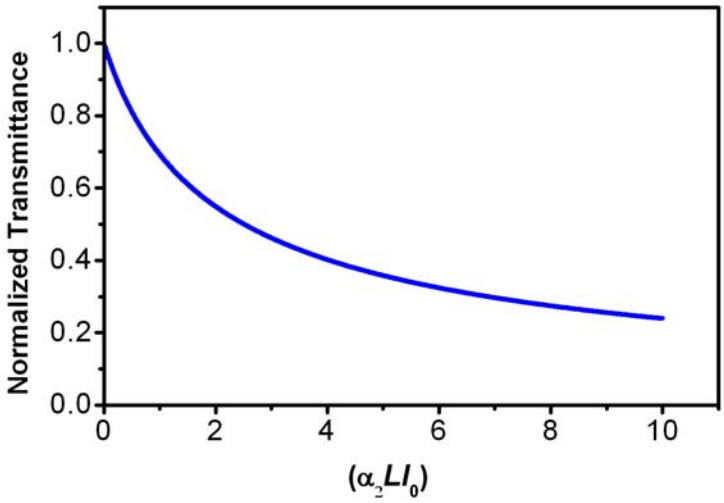

Fig. 1.6 Normalized transmittance given by Eq. (1.10)

1.5.2. Up-converted fluorescence emission

Many organic molecules exhibit up-converted emission as a major mechanism for returning to the ground state. This process derives its name from the molecule in the excited state returning to the ground state via the emission of one photon of shorter wavelength (higher energy) than either of the two initially absorbed photons. This apparent conversion of light at a longer wavelength to light at a shorter wavelength is called up-conversion [5].

To determine the nonlinear absorption cross section, the intensity of up-converted fluorescence emission can be measured as a function of incident intensity. The dependence of fluorescence intensity on the excitation intensity determines the order or nonlinearity. A quadratic dependence as shown in Fig. 1.8 (a) is an indication of two-photon absorption process [7] whereas a cubic dependence as shown in Fig. 1.8 (b) corresponds to three-photon absorption [8].

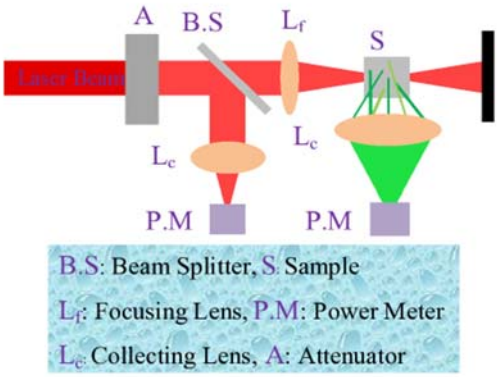

Fig. 1.7 A schematic of up-converted fluorescence emission technique

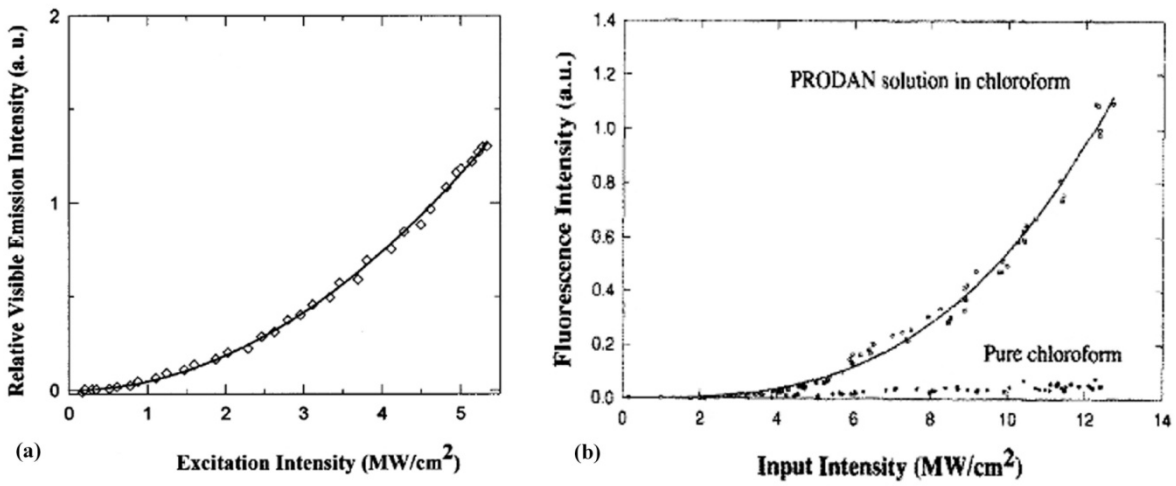

Fig. 1.8 Quadratic dependence of up-converted fluorescence intensity (a) and Cubic dependence of the up-converted fluorescence intensity (b) on the input intensity

1.5.3. Transient absorption (pump-probe experiment)

In this technique the absorption of a lower intensity beam (probe beam) is measured at the presence of a stronger intensity beam (pump beam) as a function of time delay between pump and probe pulses [9].

Fig. 1.9 shows a schematic setup for this experiment. A laser beam consisting of ultrashort laser pulses is divided into two parts (95% as pump beam and 5% as probe beam) using a beam splitter. The time delay between pump and probe pulse is controlled by a retro reflector mounted on a translation stage. Both beams are then focused at the same position into the sample. An aperture in placed after the sample in front of the detectore. The probe beam is transmitted through the aperture while the pump beam is blocked. As the pump and probe beams spatially and temporally overlap within the sample two-photon absorption occurs and a sharp decrease in transmittance (increase in absorbance) of the probe beam can be observed as shown in Fig. 1.10 [10].

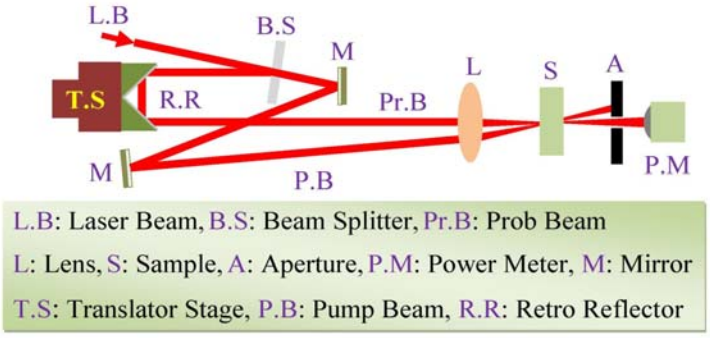

Fig. 1.9 Schematic of transient absorption method

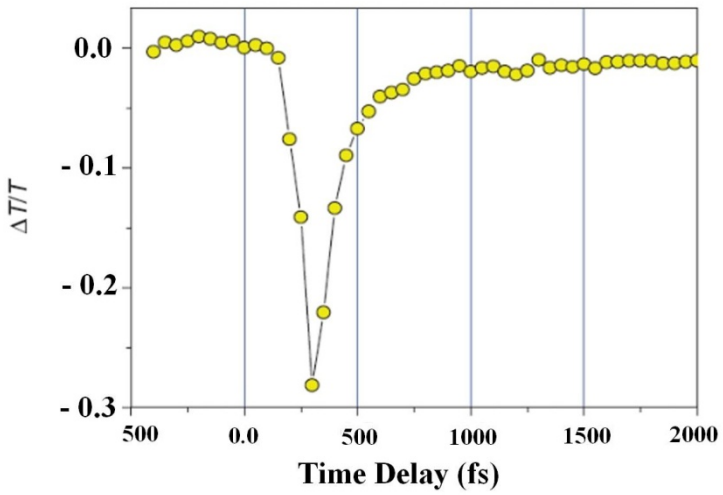

Fig. 1.10 A typical transient absorption signal

1.5.4. Four-wave mixing (FWM)

In FWM three beams specially and temporally overlap to produce the forth beam referred to as FWM signal. Two intense pump beams cross the medium at an angle to form an interference pattern leading to a refractive index modulation. The third beam is used as a probe which "reads" this modulation and the forth beam is the diffracted probe beam whose intensity can be measured as a function of pump beam intensity [11] or time delay of probe beam relative to the pump beams [12] as shown in Fig. 1.12 (a) and (b) respectively. Fig. 1.11 shows a set up for degenerate four-wave mixing (DFWM) [13] in which all three input beams are derived by splitting one input parent beam. In this case, for a material without two-photon absorption, the signal is proportional to the cubic power of the input intensities given as

$$I(\omega) = \left(\frac{\omega}{2\varepsilon_0 c n^2} \right)^2 \left| \chi^{(3)} \right|^2 L^2 I_0^3(\omega) \tag{1.11}$$

where $I(\omega)$ is the DFWM signal intensity, $I_0(\omega)$ is the pump intensity, L is the interaction length, and n is the refractive index of the medium [11].

For a material with two-photon absorption, however, the detected DFWM signal involves two contributions, i.e., the coherent DFWM process such as parametric frequency mixing process and the population grating (population of the excited states created via two-photon absorption) process. For zero delay of the probe beam, the three incident beam pulses arrive together in the sample cell and the DFWM signal is derived from both the coherent four-wave mixing process and the population grating process. The DFWM signal has a power dependence between a third order and a fifth order, depending on the relative contributions from the coherent four-wave

mixing and the population grating. On the other hand, when the probe beam is delayed beyond the pulse width of the grating forming pulses, the instantaneous coherent four-wave mixing process does not occur, but the population grating contribution is still present if the excited state produced by two-photon absorption has a long enough lifetime. In this case, the DFWM signal should obey a fifth-order power dependence on the input intensity [14].

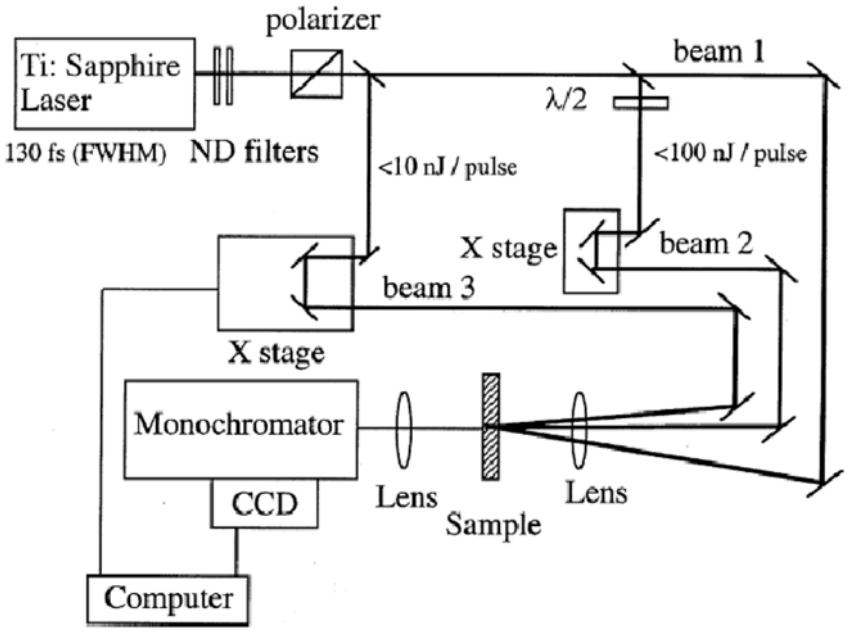

Fig. 1.11 Degenerate four-wave mixing setup

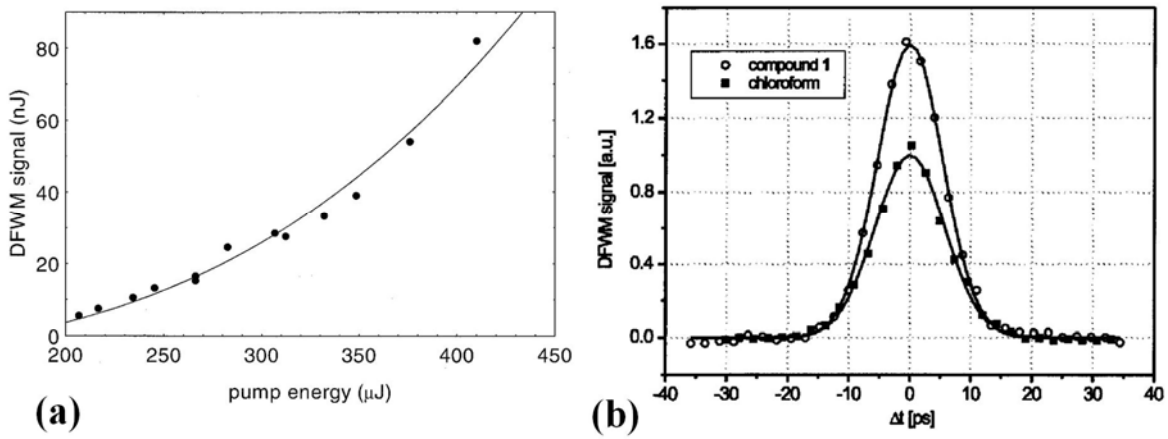

Fig. 1.12 DFWM signal plotted versus (a) pump pulse energy and (b) time delay of probe beam relative to the pump beams.

1.5.5. Z-scan technique

In the Z-scan technique [15-18] the sample is scanned along the propagation direction of a tightly focused laser beam while the transmittance is measured as a function of sample position measured with respect to the focal point. By applying the Z-scan, both nonlinear refractive index and nonlinear absorption coefficient separately and even concurrently can be determined. The Z-scan method is basically performed in two different schemes referred to as closed aperture Z-scan and open aperture Z-scan that are described below in greater details.

1.5.5.1. Closed aperture Z-scan technique

Fig. 1.13 shows a schematic setup of the closed aperture Z-scan technique. A pulsed laser beam is first divided into two parts using a beam splitter (B.S). The less intense beam is directed to a reference diode (D_r) recording the laser intensity (mainly its fluctuations). The more intense beam is focused into the sample using a plano-convex lens (L_f). The sample, which can be a transparent solid (such as a semiconductor, dielectric or polymer) or a cuvette containing a liquid, is mounted on a translation stage, which is moved along the beam propagation direction through the focal point. The beam waist is adjusted to be located at the center of the scanning range. The transmittance of the nonlinear medium through a finite aperture (A) placed in the far field after the sample is recorded for each sample position using a photo-diode (D_c). The measured signal represents the transmittance as a function of sample position. Ultimately, the measured signal is divided by the signal measured with reference diode to get rid of laser pulse energy fluctuations.

At the absence of nonlinear absorption the closed aperture Z-scan signal is a symmetric curve with a minimum followed by a peak that is an indication of positive self-lensing or inversely with a peak followed by a valley that is an indication of negative self-lensing.

The following qualitative description elucidates how the Z-scan trace can be related to the nonlinear refraction and its sign. According to Eq. (1.7) the refractive index of a nonlinear medium changes with intensity when the laser intensity is high enough. Assuming a positive sign for n_2 leads to increasing the refractive index with intensity. The refractive index mimics the intensity profile changing transversely. Thus, if a medium is irradiated with a spatially-varying beam like a Gaussian beam the medium exhibits higher refraction in the center of the beam and lower refraction on the edges of the beam. Therefore, a nonlinear medium irradiated with a Gaussian beam is similar to a gradient convex lens and hence causes focusing the beam. This phenomenon is referred to as self-focusing because the intense laser beam causes focusing itself as illustrated schematically in Fig. 1.14.

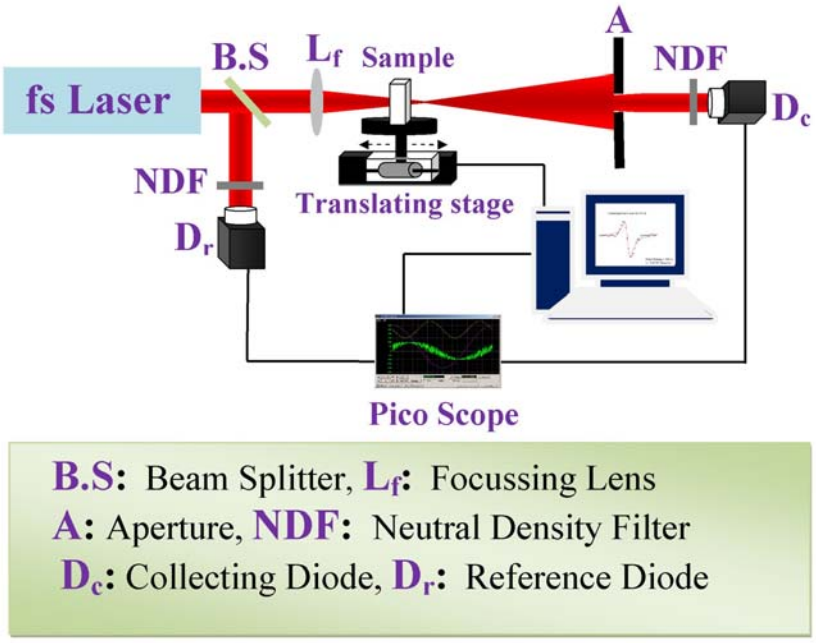

Fig. 1.13 A schematic setup of closed aperture Z-scan technique

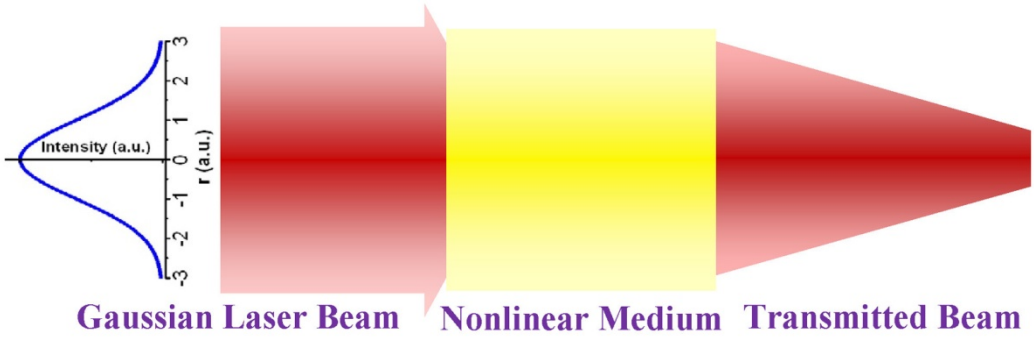

Fig. 1.14 A schematic view of a self-focused Gaussian beam propagating through a nonlinear medium

So far it was illustrated how positive nonlinearity results in self-focusing. The laser intensity of the focused laser beam also changes within the medium as it is moved through the focal plane. Therefore, a nonlinear medium, which is moved along the propagation direction of a focused Gaussian beam, operates as a variable focal length lens. When the medium is at a distance far away from the focal point the laser beam diameter is large and the intensity of laser beam is low and the nonlinear refraction is negligible; hence, the transmittance remains relatively constant. As the sample moves toward the focus, the laser intensity increases leading to self-focusing (positive self-lensing) in the medium that causes focusing the laser beam prior to the previous focal point that results in beam broadening on the aperture plane and thus a decrease in transmittance as shown in Fig. 1.15 (a). As the sample is moved away from the focal plane the same self-focusing tends to collimate the laser beam, leading to beam narrowing on the aperture

plane and thus an increase in transmittance as shown in Fig. 1.15 (b). Again when the sample is far enough from the focus, the intensity is low so that the transmittance remains constant.

An inverse process occurs for a medium possessing negative nonlinear refraction such that the obtained Z-scan signal has a pre-focal peak followed by a post-focal valley. It is an extremely useful feature of the Z-scan method that the sign of the nonlinear refractive index is immediately obvious from the shape of the Z-scan trace.

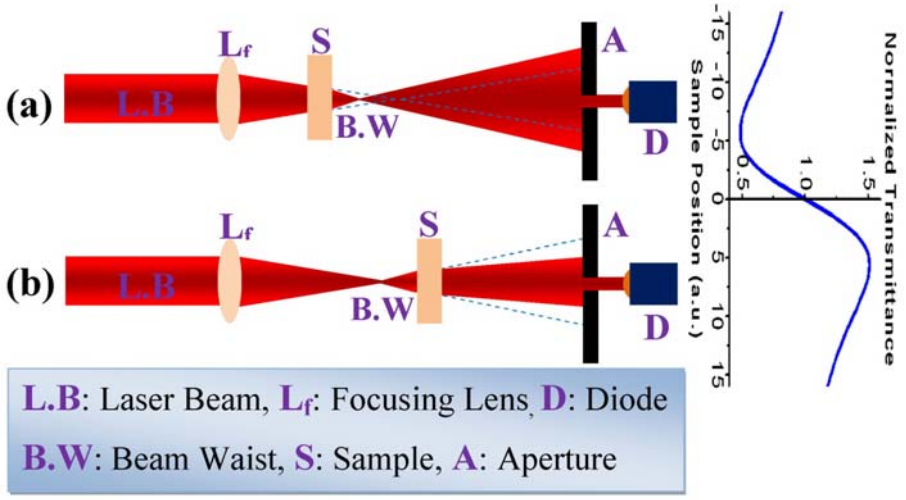

Fig. 1.15 self-focusing causing a pre-focus minimum transmittance (a) and a post-focus maximum transmittance (b)

1.5.5.2. Open aperture Z-scan technique

Fig. 1.16 shows a schematic setup of an open aperture Z-scan experiment in which the finite aperture has been removed and the entire energy transmitted through the nonlinear medium (regardless of its focal conditions) is collected using a lens (L_c) and then detected by a photo-diode (D_c). Due to detecting the entire transmitted energy, this method is no longer sensitive to beam broadening or narrowing and thus not sensitive to nonlinear refraction effects. This method is only sensitive to nonlinear absorption so the nonlinear absorption coefficient can be determined using this method. According to Eq. (1.9), the absorption coefficient of a nonlinear medium increases with intensity if it is irradiated with a pulsed laser beam with a high enough intensity.

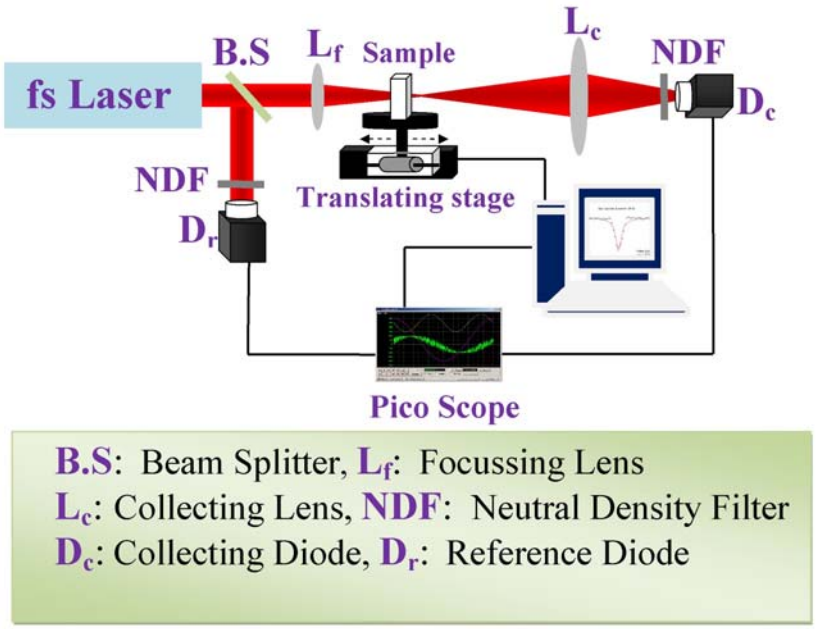

Fig. 1.16 A schematic setup of open aperture Z-scan technique.

The following qualitative description clarifies how an open aperture Z-scan spectrum can be related to the nonlinear absorption of the sample. Starting the scan along the beam propagation direction from a distance far away from the focus, the beam irradiance is low and the nonlinear absorption is negligible. Hence, the transmittance remains relatively constant during the sample translation. As the sample is approaching the focus the beam irradiance increases and thus the absorption increases leading to a decrease in transmittance. As the scan continues and the sample passes through the focus, the beam irradiance decreases leading to a decrease in absorption and thus an increase in transmittance. The Z-scan is completed when the sample is far away from the focus and the transmittance remains constant since the beam irradiance is low again. Therefore, the open aperture Z-scan trace is a V-shape curve whose depth is proportional to the laser intensity at the focal point, the thickness of the sample and the nonlinear absorption coefficient of the sample.

A different effect can occur which results in a modified shape of the Z-scan curve in the open aperture geometry which is a consequence of saturation of absorption. This is a nonlinear response of some materials in which the linear absorption coefficient or even the nonlinear absorption coefficient saturates and hence decreases with intensity. As typical for saturation, the absorption coefficient will behave like

$$\alpha(I) = \frac{\alpha_0}{1 + I/I_s} + \frac{\alpha_2^0}{1 + I^2/I_s^2} I + \frac{\alpha_3^0}{1 + I^3/I_s^3} I^2 \qquad (1.12)$$

where α_0 is the linear absorption coefficient, α^0_2 is the 2PA coefficient at the low intensity approximation [19, 20], α^0_3 is the 3PA coefficient at the low intensity approximation [21, 22], I

is the laser beam intensity and I_s is the saturation intensity at which the linear and nonlinear absorption coefficients and then the absorption coefficient as a whole are reduced by a factor of 2.

1.5.5.3. Closed aperture Z-scan technique at the presence of nonlinear absorption or saturation of absorption.

In section 1.4.5.1, a purely refractive nonlinearity was discussed, assuming that no absorptive nonlinearities are present. In this case, a symmetric Z-scan trace is obtained exhibiting the same magnitude of peak height and valley depth. Presence of multi-photon absorption or saturation of absorption affects the CA Z-scan signal in two aspects as can be seen in Fig. 1.18. First, the null point (where the normalized transmittance passes unity which occurs at focal position z=0) shifts to right or left depending on the sign of nonlinear refractive index and type of nonlinear absorption so that it will be no longer coincides with the focal point. Secondly, the Z-scan trace is no longer symmetric. Influence of multi-photon absorption leads to suppress the peak and enhance the valley whereas, the presence of saturation absorption produces the opposite effect; it causes a peak enhancement and valley reduction. To determine the nonlinear refractive index of a material possessing absorptive nonlinearities a combination of closed and open aperture Z-scan setup, as shown in Fig. 1.17, can be used. In this experiment the signal obtained from diode D_{c1} is divided by the signal obtained from diode D_{c2} to subtract the nonlinear absorption contribution and deducing a pure nonlinear refractive index.

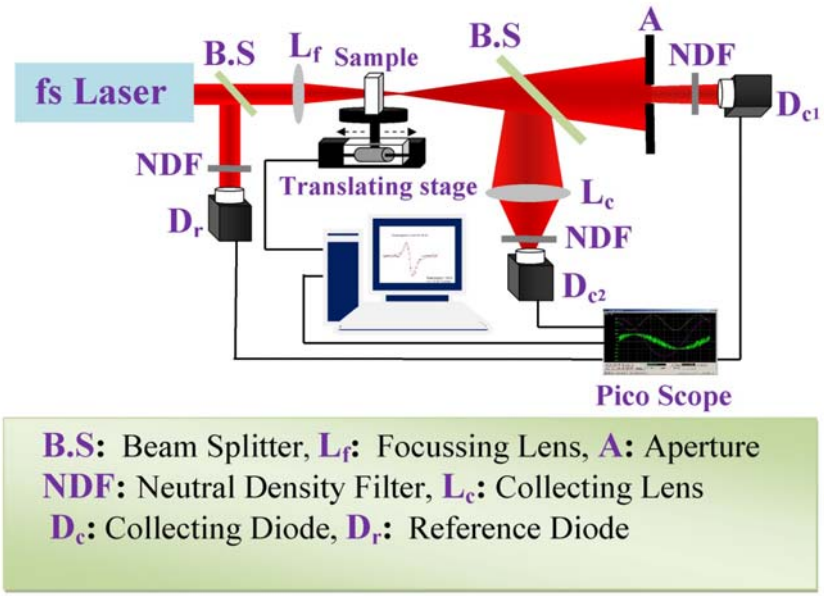

Fig. 1.17 A schematic setup of closed aperture Z-scan method applying for some materials possessing a significant nonlinear absorption

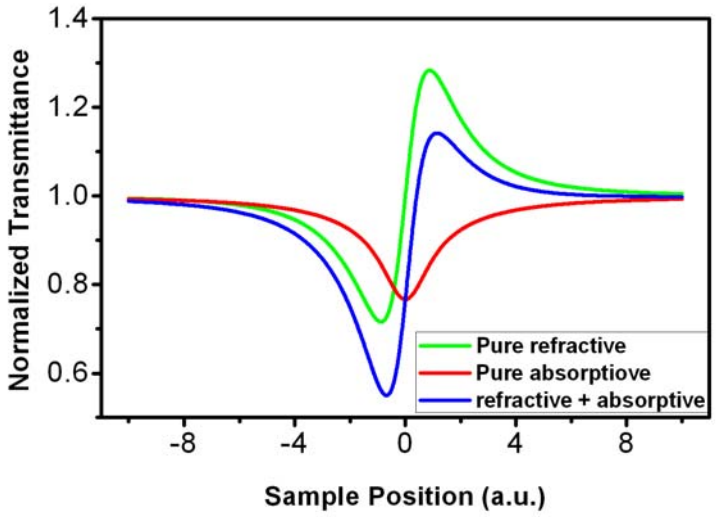

Fig. 1.18 Z-scan signals for a sample having refractive as well as absorptive nonlinearity

In Fig. 1.18 blue curve is the signal obtained from Diode D_{c1} having contributions of absorptive and refractive nonlinearity. Red trace shows the signal measured with Diode D_{c2} having only a contribution of nonlinear absorption. Green trace demonstrates the division of the blue curve by the red one that shows a symmetric trace having only a contribution of nonlinear refraction.

1.6. Application of 2PA

2PA has found numerous fascinating applications due to its unique properties: firstly, the 2PA is intrinsically proportional to intensity squared thus it occurs within a small volume around the focal point of a focused pulsed laser beam. Thus, the size of the affected area can be smaller than the diffraction limited area which is obtained in linear optics. Secondly, due to the quadratic dependence of the 2PA on laser intensity, 3D modification and structuring is feasible by scanning of the focal point of a focused laser beam within the bulk of a transparent material; and thirdly, 2PA implies using laser radiation with wavelength longer than the absorption band thus, the loss of laser beam energy via Rayleigh scattering is greatly reduced compared to what occurs in the linear absorption case. Several applications of 2PA are discussed in the following.

1.6.1. Two-photon induced polymerization

Micro-fabrication based on one-photon induced polymerization (1PIP) has been realized for quite a long time. However, 1PIP cannot satisfy the requirements of modern applications such as micro-optical-electromechanical systems and photonic crystals due to its low-spatial resolution (because of its diffraction limit) and two-dimensional limitations (due to the absorption of radiation on the surface) [23]. Owing to the quadratic dependence of the 2PA on the laser pulse energy and also the threshold behavior of polymerization, two-photon induced polymerization (2PIP) has been shown to provide the means for 3D micro-fabrication with a resolution beyond the diffraction limit [24]. By tightly focusing the laser beam into the sample, the peak intensity in

the focus is sufficient to trigger 2PA and thus polymerization in the very small volume around the focal point. Then the 3D microstructures can be fabricated by translating the focus into the transparent medium three dimensionally. Finally, by developing the structure in a solvent the unpolymerized resins are washed away and the 3D solid structure stands out. In particular, by fabricating periodic 3D micro or sub-micron dielectric structures, photonic band-gap materials can be made.

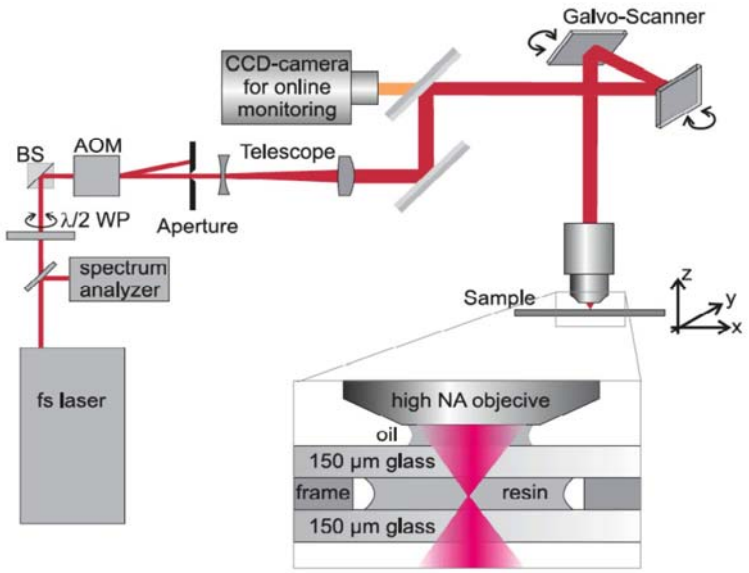

Fig. 1.19 a schematic setup for 3D micro-structuring based on 2PIP. An Acousto-optic modulator (AOM) is used as fast switch (the first order of diffracted beam is taken). A telescope is employed to extend the beam diameter on the objective leading to reduce the beam waist radius on the focus. A camera is also used to monitor the polymerization process

1.6.2. Two-photon induced photo-grafting

Molecular grafting is a versatile tool providing means for tailoring physio-chemical properties of surfaces. Its current applications are ranging from electronic, such as solar cells and sensors [25], to biomedical engineering [26]. Photo-induced grafting provides additional advantages of spatial and temporal control of the process. Apart from producing micro-patterns, the surface density of the covalently immobilized molecules can be adjusted by tuning the exposure doses [27]. Furthermore, using molecules responding to different wavelength it is possible to pattern multiple species onto the same substrate sequentially [28]. Due to technical limitations, until recently, most studies using photo-grafting were conducted on flat surfaces. Possibility of producing volumetric patterns decorated with bio-molecules is very appealing for tissue engineering. True 3D grafting has been recently achieved by multi-photon excited polymerization process [29].

1.6.3. 3D optical data storage

Surface-storage technologies are approaching fundamental limits that may be difficult to overcome, as ever-smaller bits become less thermally stable and harder to access. A possibly fascinating approach for next generation data-storage is to use light to store information within the (three- dimensional) volume of a material. The surface storage density manageable with focused light beams is roughly $1/\lambda^2$ exploiting 1PA. This results in a capacity of 4 Gigabytes (GB) on each side of a 120mm diameter, 1mm thick disk. But by storing data throughout the volume at a density of $1/\lambda^3$ exploiting 2PA, the capacity of the same disk could be increased to 8 Terabytes (TB).

3D optical data storage using 2PA was first introduced by Rentzepis in 1989 [30]. The advantages of two-photon based memory systems are [31]:

1. Immense information storage capacity, $\sim 10^{13}$ bits/cm^3.
2. Random and parallel access.
3. Fast writing and reading rates (nanosecond range).
4. Small size and low cost.
5. Minimal cross talk between adjacent bits.
6. High reading sensitivity.

The basic components of a two-photon process based memory are (would be), a medium which exhibits a change in its optical properties (absorbance, fluorescence, refractive index, etc.) after 2PA, appropriate read and write beams, and a mechanism to precisely access any volume element in the medium [32].

Fig. 1.20 shows a single-beam two-photon recording and one-photon readout system [31]. In this setup, the recording laser beam (532 nm) passes through a beam expander then onto the objective-lens assembly, which focuses it inside the volume of the spinning disk where the data is recorded. The absorption band of molecules used as storage medium in this setup is below 400 nm whereas the absorption band of excited molecules after absorbing two photons of 532 nm shifted to above 600 nm. After recording, a 635-nm laser diode is used to induce one-photon fluorescence from the recorded bits. The fluorescence is picked up by the same objective lens and focused onto a detector, such as a photomultiplier tube or photodiode array.

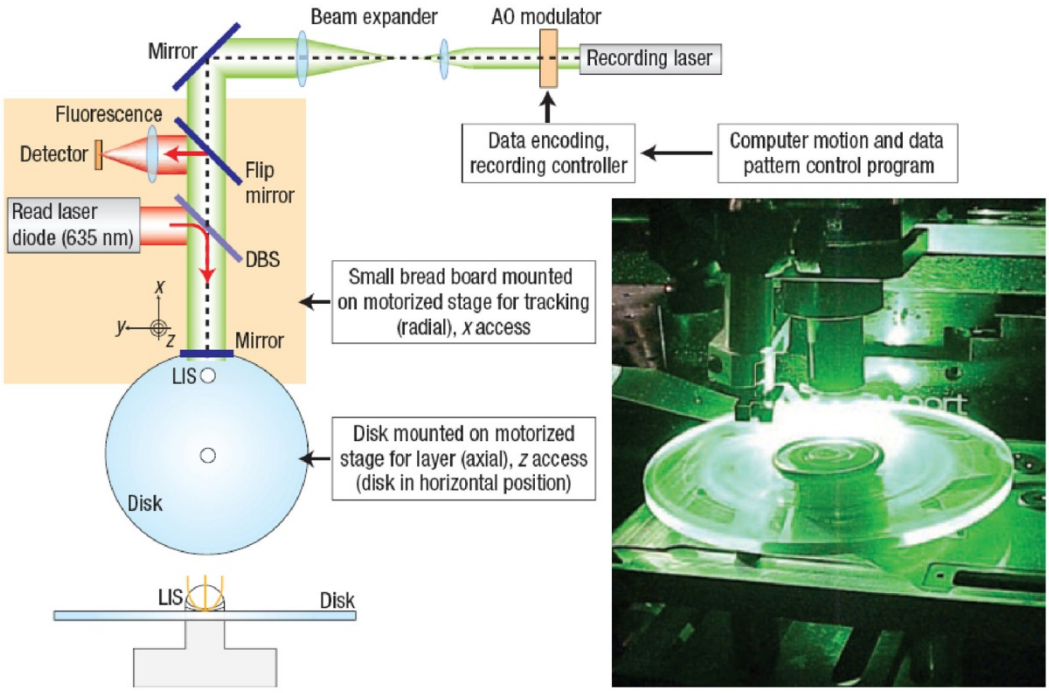

Fig. 1.20 A schematic setup for two-photon write, one-photon read out (inset shows a photo of recording head and storage medium)

Fig. 1.21 shows an Optical image of bits written inside fused silica (a) and read out of data through a phase-contrast microscope (b) [33]. Bit separation in a layer is 1 μm and layer separation is 7 μm. Thus each bit occupies a volume of 1×1×7 μm, corresponding to a memory density of 143 Gb/cm^3.

Readout signal shows less intense radiation and more intense radiation that can be considered as zero "0" and one "1" in computer language. Therefore, any data can be translated in zero and one and then recorded within a transparent storage medium as laser irradiated and non-irradiated volume ppoint.

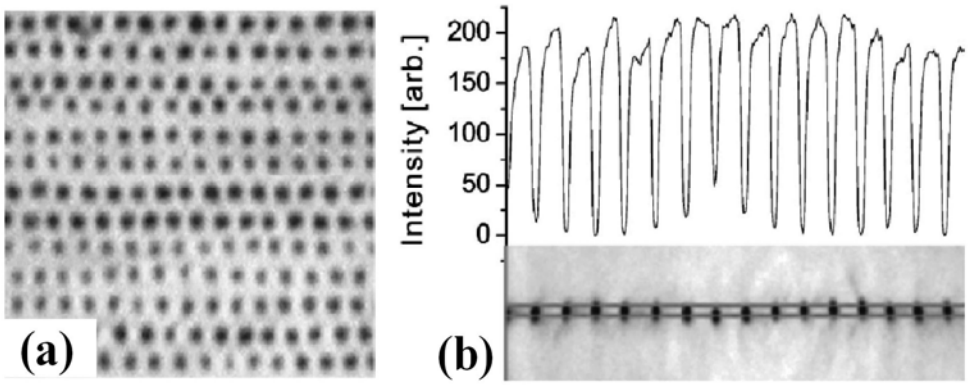

Fig. 1.21. Optical image of bits written inside fused silica using 400 nJ 200 fs excitation pulses. Light is focused by a NA=0.85 objective. In-plane bit separation is 1 μm (a). Read out of data through a phase-contrast microscope. The upper part of the figure is the signal recorded by a single row of the CCD camera. The pits being imaged are shown in the bottom portion, with the two lines denoting the edges of the row (b)

1.6.4. Two-photon fluorescence microscopy

Two-photon excitation microscopy is a fluorescence imaging technique that allows imaging of living tissue up to a very high depth of about one millimeter. By simultaneous absorption of two photons of long wavelength, a molecule is excited to an upper energy level and then relaxes to the ground state by emitting fluorescence that can be detected as a characteristic of emitting molecules.

Two-photon imaging shows particular advantages over the widely used one-photon optical counterpart, confocal fluorescence microscopy [34]. Infrared light used for two-photon excitation fluorescence (2PEF) is subject to less absorption and scattering than UV or visible light. Therefore, the excitation penetrates more deeply into the sample. Quadratic dependence of the 2PA on the laser irradiance leads to confining the fluorescence excitation to a small volume at the focus of the objective. The Photon flux is kept insufficient in the out-of-focus planes to excite fluorescence, except for extremely high laser powers. Photo-bleaching and photo-damage are limited to the zone of 2PEF and do not occur above or beyond the focus.

1.6.5. Frequency up-converted lasing

2PA induced lasing has been considered as a promising approach for frequency up-conversion of coherent light. Frequency up-converted lasing is a process via which a shorter wavelength is produce when the gain medium is pumped with longer wavelength. Exploiting this process enables one to obtain a broad range of visible lasing by pumping with an infrared laser source [35]. Frequency up-converted lasing was reported as early as 1971, when lasing was obtained from a solution of Rhodamine 6G pumped with the output of a ruby laser [36]. This method of producing coherent light has many advantages; for instance, it does not require phase matching (as second harmonic generation requires) and can provide a broad tuning range with considerable ease [37].

Fig. 1.22 shows the two-photon pumped (2PP) frequency up-converted laser output energy versus the input energy of the pump laser. The output energy manifests a quadratic dependence on the input energy which is an intrinsic characteristic of 2PA process [35]. As can be seen in this figure, the efficiency of TPP frequency up-conversion increases by increasing input energy (it has increased from 0.5 % to 1.2 % as input pulse energy has increased from 2 mJ to 4 mJ).

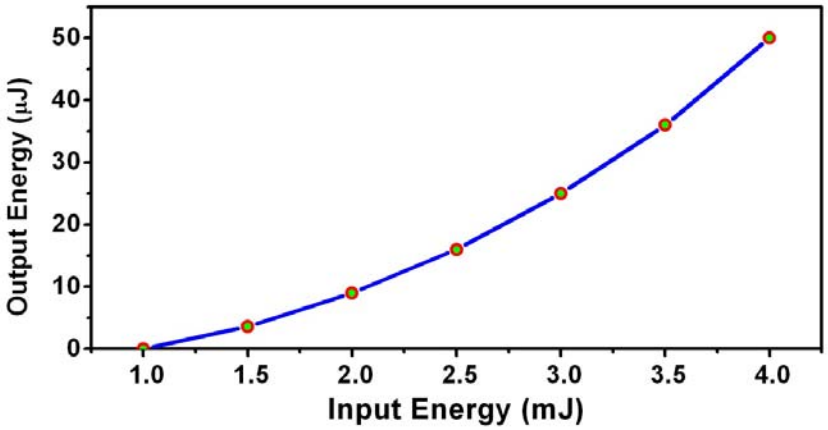

Fig. 1.22 The output energy of a two-photon pumped frequency up-converted laser versus the input energy of the pump laser

1.6.6. Two-photon photodynamic therapy

Over the past two decades photodynamic therapy (PDT), a cell-killing technique where a photosensitizing drug is activated by carefully targeted visible light, has been used to treat diseases caused by neoplasia (abnormal proliferation of cells) such as various cancers [38]. Serious challenges arise, however, with the traditional single-photon PDT for glioma (a type of tumor that starts in the brain) tissues. For example, currently approved single-photon PDT drugs have the drawback of requiring excitation by visible light, which has limited penetration depth due to the restrictive tissue transparency window for target cells that are located deep inside living tissues; photons in this spectral region do not penetrate deep enough, thus making single-photon PDT less effective for glioma tissue treatment [39].

One potential approach for PDT that has been discussed for many years is two-photon excitation of photo-sensitizers, where two photons of infrared light rather than a single visible photon are used for drug activation. This approach has several benefits. It provides better spatial selectivity as drug activation only occurs in regions of high optical intensity (that is, confined to the focal spot of a focused laser beam). It also leads to deeper tissue penetration as infrared light is subject to less scattering than visible light owing to its longer wavelength and also less linear absorption since 2PA spectra window of tissues is between 700 and 1100 nm. The main idea in photodynamic therapy is the following. A photosensitizing drug absorbs two photons of light to create an excited singlet state, which then undergoes intersystem crossing to a triplet state. The lifetime of the triplet state is long enough to interact with molecular oxygen to yield activated

singlet oxygen, which is highly toxic and kills cells. A key aspect of PDT is that the photosensitizing drug is regenerated and therefore is not consumed by the process; indeed it undergoes no chemical change.

1.6.7. Optical power limiting

Optical power limiting is an effect in which the transmission decreases as the incident light intensity increases [40]. This is due to nonlinear absorption, in which the absorption probability of high intensity pulses is larger as compared to the absorption of low intensity pulses. This intensity-dependent transmission feature will limit the output intensity so that, as a consequence, it will remain below a certain maximum value as can be seen in Fig. 1.23 (a). Therefore, the optical-limiters can protect human eyes and sensors exposed to high power light sources. It has been pointed out that materials exhibiting large multi-photon absorption properties could be used as effective optical power limiter for ultrafast pulsed laser system environments. Fig. 1.23 (b) shows optical stabilization [41] as an optical-limiting related application. The optical intensity transmitted through an optical limiter exhibits much lower fluctuation (signal shown in the lower part of the figure (b)) compared to the original intensity signal measured before the optical limiter (signal shown in the higher part of the figure (b)).

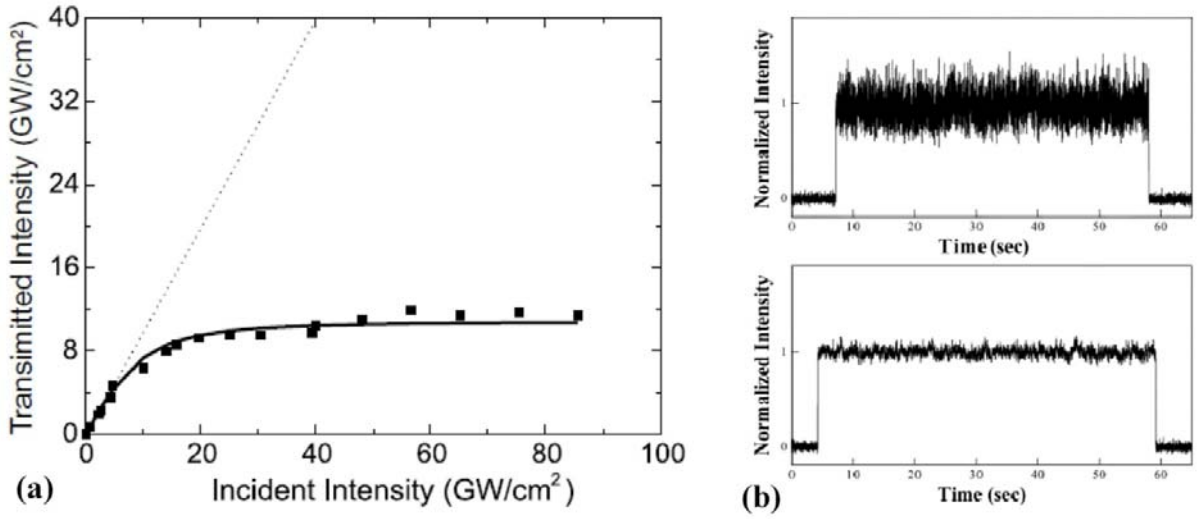

Fig. 1.23. Transmitted intensity versus incident intensity showing an output saturation due to 2PA (a). Optical stabilization based on 2PA (b) (laser fluctuation has been greatly reduced)

Chapter 2

2. Analytical calculation

In this chapter the required calculation to obtain the normalized Z-scan transmittance using a single Gaussian laser beam will be presented. Some of the presented equations are well known and can be found in the literature. Because of their relevance they are discussed in detail in sections 2.2.1, 2.3.2, 2.5.1 and 2.5.2. However, these available equations consider only a limited number of nonlinear effects and are generally restricted to special experimental parameters. In order to include many other nonlinear processes and extend the experimental parameters beyond these limits, the expected curves had to be calculated. These extensions of the existing theory, which are needed for the measurements in following chapters, constitute the major part of this chapter. In detail, the following issues are treated:

- Closed aperture Z-scan for fifth order nonlinearity in section 2.2.2
- Closed aperture Z-scan for simultaneous third and fifth order nonlinearity in section 2.2.3
- Open aperture Z-scan at the presence of three-photon absorption in section 2.3.3
- Closed aperture Z-scan for third order nonlinearity at the presence of two-photon absorption in section 2.4.1
- Closed aperture Z-scan for fifth order nonlinearity at the presence of 3PA in section 2.4.2
- Closed aperture Z-scan for concurrent third and fifth order nonlinearity at the presence of two-photon absorption in section 2.4.3

In order to pursue the calculation of the Z-scan transmittance some text materials about the Gaussian laser beam and its propagation throuth the free space is usefull to be reviewed.

2.1. Gaussian beam

2.1.1. Realizing a Gaussian beam under paraxial approximation

A real laser beam has a unique direction and finite width. A plane wave or a spherical wave both can not be a real laser beam because a plane wave although has a unique direction but does not have finite width and it spreads all over the space. A spherical wave has a finite width but has

not a unique direction and it propagates in all directions. Thus, the wave equation has to be solved with paraxial approximation to derive the Gaussian wave representing a finite width light beam propagating in a certain direction. The electric field E in an electrically neutral, nonmagnetic and homogeneous media obtained by using Maxwell's equations is governed by

$$\nabla^2 E - \frac{1}{c^2}\frac{\partial^2 E}{\partial t^2} = \frac{1}{\varepsilon_0 c^2}\frac{\partial^2 P}{\partial t^2} \tag{2.1}$$

To obtain electric field from Eq. (2.1) the electric dipole moment density P must be specified.

When the radiation propagates through the free space (where the polarization is zero) the Eq. (2.1) turns into a very simple equation given as

$$\nabla^2 E - \frac{1}{c^2}\frac{\partial^2 E}{\partial t^2} = 0 \tag{2.2}$$

The following is textbook knowledge, but it is still worthwhile to repeat here the most relevant formulas, as they will be used extensively for the interpretation of the Z-scan signals in the following.

An spherical monochromatic wave can be the solution of Eq. (2.2) as follows

$$E(r,t) = \frac{A}{r} e^{-ikr}\, e^{-i\omega t} \tag{2.3}$$

where r is the radial coordinate as the distance between the origin and the observation point.

Using paraxial approximation in which a small patch of observation plane around z-axis is considered the radial coordinate r can be approximated as follows

$$r = z\left(1 + \frac{x^2 + y^2}{z^2}\right)^{\frac{1}{2}} \cong z\left(1 + \frac{x^2 + y^2}{2z^2}\right) \tag{2.4}$$

Now the spatial part of Eq. (2.3) is modified as

$$E(r) = \frac{A}{z}\exp\left(-ikz - \frac{ik}{2z}(x^2 + y^2)\right) \tag{2.5}$$

where $E(r)$ is a parabolic wave. It can be easily shown that if the real parameter z in Eq. (2.5) is replaced by the complex parameter $z+iz_0$, $E(r)$ is still a solution for Helmholtz equation but it attains additional remarkable properties. Thus

$$E(r) = \frac{A\, e^{k\, z_0}}{z + i\, z_0} \exp\left(- \frac{i\, k\, (x^2 + y^2)}{z + i\, z_0} \right) e^{-i\, k\, z} \tag{2.6}$$

$$E(r) = \frac{Ae^{k\, z_0}}{iz_0(1 - i\,\dfrac{z}{z_0})} \exp\left(-ik(x^2 + y^2)\, \frac{z - iz_0}{z^2 + z_0^2} \right) e^{-i\, k\, z} \tag{2.7}$$

$$E(r) = \left(\frac{Ae^{k\, z_0}}{iz_0} \right) \frac{e^{i\,\phi}}{\sqrt{1 + \dfrac{z^2}{z_0^2}}} \exp\left(\frac{-ik(x^2 + y^2)}{2R(z)} \right) \exp\left(- \frac{x^2 + y^2}{w(z)^2} \right) e^{-i\, k\, z} \tag{2.8}$$

where

$$\phi\,(z) = tag^{\,-1} \left(\frac{z}{z_0} \right) \tag{2.9}$$

is the propagation phase variation,

$$R(z) = z + \frac{z_0^2}{z} \tag{2.10}$$

is the wave front curvature,

$$w(z) = w_0 \sqrt{\left(1 + \frac{z^{\,2}}{z_0^{\,2}} \right)} \tag{2.11}$$

is the beam radius,

$$w_0 = \sqrt{\frac{2z_0}{k}} \tag{2.12}$$

is beam waist radius and

$$z_0 = \frac{k w_0^2}{2} \tag{2.13}$$

is the Rayleigh range that refers to a distance from the beam waist where the beam spot area increases by a factor of 2 compared to the beam spot at the beam waist.

$E(r)$ in Eq. (2.8) can be representative for a light beam because it has a finite extent that depends on coordinate x, y and z and also it has a unidirectional propagation in the positive z direction.

Since the radial distribution of the electric field in Eq. (2.8) and subsequently the intensity pattern obeys a Gaussian function, this traveling electric field represents the electric field of a Gaussian light beam. By substituting the introduced parameters in equations (2.9)-(2-13) into Eq. (2.8) it can be rewritten as

$$E(r,z,t) = E_0(t)\frac{W_0}{W(z)} e^{i\phi(z)} e^{-ikz} e^{-ik\frac{r^2}{2R(z)}} e^{-\frac{r^2}{W(z)^2}} \tag{2.14}$$

The light intensity is always proportional to the square of the modulus of the electric field thus the spatial intensity distribution of a Gaussian beam is characterized by the Gaussian function as follow:

$$I(r,z,t) = I_0(t)\frac{{w_0}^2}{w(z)^2} e^{-2\frac{r^2}{w(z)^2}} \tag{2.15}$$

The light power is obtained by integration the intensity over r in the plane normal to the propagation direction of the incident beam. So

$$P(t) = \int_0^\infty 2\pi r\, dr\, I(r,z,t) = \frac{\pi w_0^2}{2} I_0(t) \tag{2.16}$$

The power transferred through an aperture of radius a can also be calculated by integration of the intensity over r from the origin up to a distance a.

$$P(t) = \int_0^a 2\pi r\, dr\, I(r,z,t) \tag{2.17}$$

After substituting Eq. (2.15) in Eq. (2.17), the power is obtained:

$$P(t) = \frac{\pi w_0^2}{2} I_0(t) \left(1 - e^{-\frac{2a^2}{w(z)^2}} \right) \tag{2.18}$$

The aperture transmittance defined as the quotient of the power transmitted through the aperture and the entire incident power can be written as:

$$T = \frac{P(r=a)}{P(r \to \infty)} = \left(1 - e^{-\frac{2a^2}{w(z)^2}} \right) \tag{2.19}$$

where a is the aperture radius, $w(z)$ is the beam radius in the aperture plane and z is the aperture position.

At the origin (z=0) the wavefront curvature radius of the light beam $R(z)$ is infinite representing a plane wave. The radius of the wavefront curvature reaches its minimum value of $2z_0$ at the position z = z_0. $2z_0$ is known as the confocal range in analogy with the distance between two mirrors in a laser resonator with confocal configuration. In the confocal configuration the focal points of two identical mirrors are coincident allowing each mirror located at the central point of another mirror that corresponds to a distance of $2f$ (f is the focal length of mirrors) between two mirrors which is equal to the curvature radius of the mirrors.

The Rayleigh range is defined as the distance from the beam waist where the beam radius increases by a factor of √2 or correspondingly the intensity decreases by a factor of 2.

$$w(z_0) = \sqrt{2}\, w_0 \tag{2.20}$$

$$I(z_0) = \frac{I_0}{2} \tag{2.21}$$

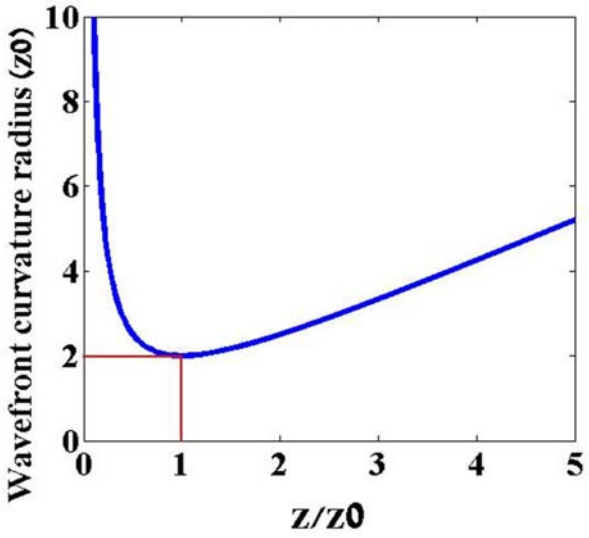

Fig. 2.1. The curvature radius of wave front plotted against the distance from the focal plane as the scale of Rayleigh range

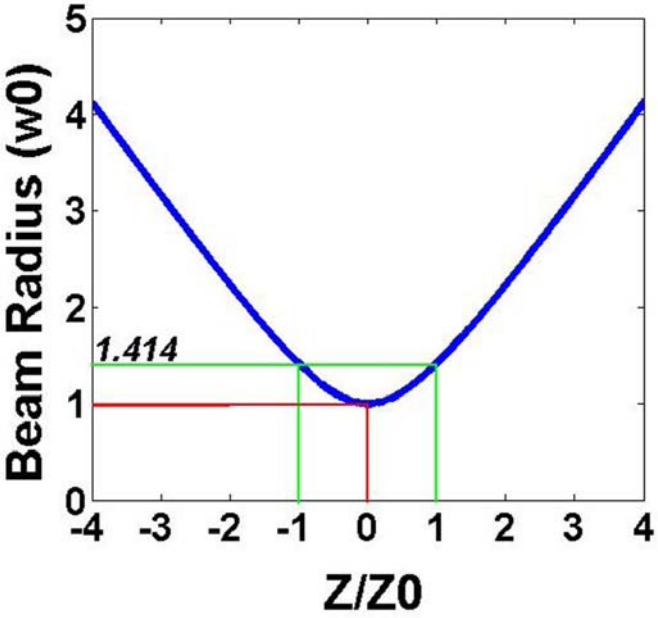

Fig. 2.2. The beam radius plotted versus the distance from the focal plane as the scale of Rayleigh range

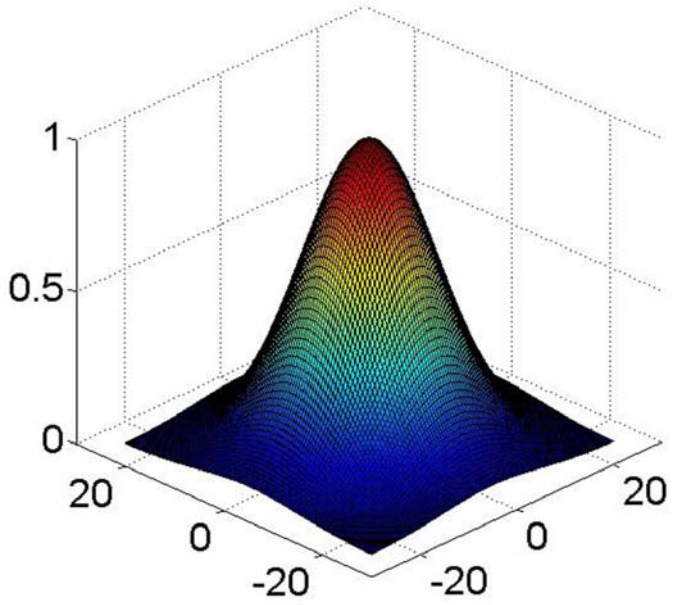

Fig. 2.3. The 2D intensity distribution of a Gaussian beam plotted versus the distance from the optical axis

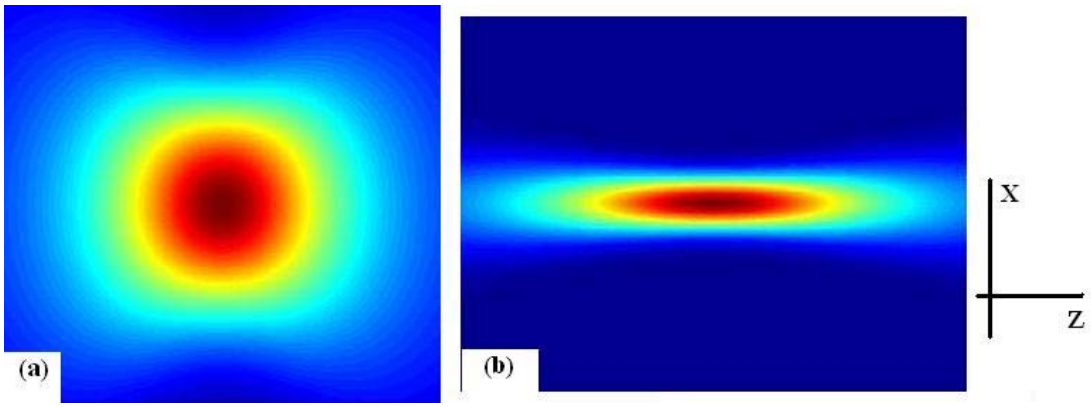

Fig. 2.4. Intensity distribution of a Gaussian beam in the xz plane. Figure (a) represents a spherical Voxel for a beam waist diameter of 330 nm. Figure (b) demonstrates an elliptical Voxel when the beam diameter at the beam waist diameter is 2 Micron (scale is not the same for these two figures).

2.1.2. Propagation of a Gaussian beam through free space

In the Z-scan method a focused laser beam passes through a nonlinear medium. Due to the change in the refractive index of the medium the phase of the laser beam is distorted resulting in the amplitude modulation in the far field observation plane. The intensity distribution at the far field aperture plane is required to be calculated in order to obtain the transmittance through the

aperture. Therefore, one should know how a Gaussian light beam diffracts and propagates through free space to approach the far field plane. For this purpose, it is supposed that some textbook knowledge is useful to be repeated here.

If $f(x',y',z_0)$ is an arbitrary function in the plane located at the position z_0, its Fourier transform will be given as:

$$F(\vartheta_x,\vartheta_y)=\int_{-\infty}^{+\infty}\int_{-\infty}^{+\infty}f(x',y',z_0)e^{2\pi i(\vartheta_x x'+\vartheta_y y')}dx'dy' \tag{2.22}$$

Therefore, $f(x',y',z_0)$ can be written as a summation of harmonic functions (as plane waves) as inverse Fourier transform allows

$$f(x',y',z_0)=\int_{-\infty}^{+\infty}\int_{-\infty}^{+\infty}F(\vartheta_x,\vartheta_y)e^{-2\pi i(\vartheta_x x'+\vartheta_y y')}d\vartheta_x d\vartheta_y \tag{2.23}$$

The phase of a plane wave changes as it propagts in the z direction. Thus the arriving wave on the plane located at position z is multiplied by a factor of $e^{-ik_z(z-z_0)}$ where k_z is the z-component of wave-vector k and $(z-z_0)$ is the traveling length.

k_z can be calculated in term of k, k_y and k_x.

$$k=\sqrt{k_x^2+k_y^2+k_z^2} \tag{2.24}$$

$$\frac{2\pi}{\lambda}=\sqrt{(2\pi\vartheta_x)^2+(2\pi\vartheta_y)^2+k_z^2} \tag{2.25}$$

$$k_z=2\pi\sqrt{\frac{1}{\lambda^2}-\vartheta_x^2-\vartheta_y^2} \tag{2.26}$$

where $1/\lambda$ is called cut-off frequency and $\vartheta_x=k_x/2\pi$ and $\vartheta_y=k_y/2\pi$ are spatial frequencies. If the electric field distribution on a plane located at a given position z_0 is known, one can find the electric field distribution on any output plane placed at a z position. That is

$$f(x,y,z)=\int_{-\infty}^{+\infty}\int_{-\infty}^{+\infty}F(\vartheta_x,\vartheta_y)e^{-2\pi i(\vartheta_x x+\vartheta_y y)}e^{-2\pi i\sqrt{\frac{1}{\lambda^2}-\vartheta_x^2-\vartheta_y^2}\,(z-z_0)}d\vartheta_x d\vartheta_y \tag{2.27}$$

Employing paraxial approximation makes Eq. (2.27) more convenient for calculating. In this approximation the input function $f(x',y',z_0)$ contains only spatial frequencies that are much smaller that the cut-off frequency. That means

$$\vartheta_x^2+\vartheta_y^2 << \frac{1}{\lambda^2} \tag{2.28}$$

Or on the other word

$$\sin\theta^2 << 1 \tag{2.29}$$

where θ is the angle between the propagation direction of a plane wave and the optical axis. Under these conditions

$$\sqrt{\frac{1}{\lambda^2}-\vartheta_x^2-\vartheta_y^2}=\frac{1}{\lambda}\left(1-\lambda^2(\vartheta_x^2+\vartheta_y^2)\right)^{1/2}\cong\frac{1}{\lambda}-\frac{\lambda\left(\vartheta_x^2+\vartheta_y^2\right)}{2} \tag{2.30}$$

where the third and higher order terms in the above expansion have been neglected.

Now, using Fresnel approximation, Eq. (2.27) can be written as:

$$f(x,y,z)=\int_{-\infty}^{+\infty}\int_{-\infty}^{+\infty}F(\vartheta_x,\vartheta_y)e^{-2\pi i(\vartheta_x x+\vartheta_y y)}e^{-i\frac{2\pi}{\lambda}(z-z_0)}e^{i\pi\lambda\left(\vartheta_x^2+\vartheta_y^2\right)(z-z_0)}d\vartheta_x d\vartheta_y \tag{2.31}$$

where $F(\vartheta_x,\vartheta_y)$ is the Fourier transform of $f(x',y',z_0)$. x' and y' are the radial coordinates in the input plane and z_0 is the position of the input plane.

After substituting $F(\vartheta_x,\vartheta_y)$ from Eq. (2.22) into Eq. (2.31), the output function on the observation plane is obtained in terms of the input function.

$$f(x,y,z)=\int_{-\infty}^{+\infty}\int_{-\infty}^{+\infty}\left\{\int_{-\infty}^{+\infty}\int_{-\infty}^{+\infty}f(x',y',z_0)e^{2\pi i(\vartheta_x x'+\vartheta_y y')}\,dx'dy'\right\}\times e^{-2\pi i(\vartheta_x x+\vartheta_y y)}e^{-ik(z-z_0)}e^{i\pi\lambda(\vartheta_x^2+\vartheta_y^2)(z-z_0)}\,d\vartheta_x\,d\vartheta_y \tag{2.32}$$

$$f(x,y,z)=e^{-ik(z-z_0)}\int_{-\infty}^{+\infty}\int_{-\infty}^{+\infty}f(x',y',z_0)\,dx'dy'\left\{\int_{-\infty}^{+\infty}\int_{-\infty}^{+\infty}e^{i\pi\lambda(\vartheta_x^2+\vartheta_y^2)(z-z_0)}\times e^{-2\pi i(\vartheta_x(x-x')+\vartheta_y(y-y'))(z-z_0)}\,d\vartheta_x\,d\vartheta_y\right\} \tag{2.33}$$

In Eq. (2.33), the term inside the bracket is the inverse Fourier transform of the Gaussian function $e^{i\pi\lambda(\vartheta_x^2+\vartheta_y^2)(z-z_0)}$.

Fourier and inverse Fourier transform of a Gaussian function are given by:

$$\textit{Fourier transform of}\left[e^{-\frac{(x^2+y^2)}{a^2}}\right]=\sqrt{\pi}\,a\,e^{-\pi^2a^2(\vartheta_x^2+\vartheta_y^2)} \tag{2.34}$$

$$\textit{Inverse Fourier of}\quad\left[e^{-\pi^2a^2(\vartheta_x^2+\vartheta_y^2)}\right]=\frac{1}{\pi a^2}e^{-\frac{(x^2+y^2)}{a^2}} \tag{2.35}$$

Thus, the term inside the bracket in Eq. (2.33) is obtained as a Gaussian function. That is as follows

$$\int_{-\infty}^{+\infty}\int_{-\infty}^{+\infty}e^{i\pi\lambda(\vartheta_x^2+\vartheta_y^2)(z-z_0)}e^{-2\pi i(\vartheta_x(x-x')+\vartheta_y(y-y'))(z-z_0)}\,d\vartheta_x\,d\vartheta_y=\frac{i}{\lambda(z-z_0)}e^{-i\frac{k}{2(z-z_0)}((x-x')^2+(y-y')^2)} \tag{2.36}$$

After substitution Eq. (2.36) into Eq. (2.33) the relation between an input function in a plane located at z_0 and an output function in a plane located at z is given by the following equation.

$$f(x,y,z)=\frac{i}{\lambda(z-z_0)}e^{-ik(z-z_0)}\int_{-\infty}^{+\infty}\int_{-\infty}^{+\infty}f(x',y',z_0)e^{-i\frac{k}{2(z-z_0)}\left((x-x')^2+(y-y')^2\right)}dx'dy' \qquad (2.37)$$

Eq. (2.37) is the Fresnel diffraction integral which is an approximation of the Huygens integral. Using Eq. (2.37) enables one to calculate the electric field distribution of a laser beam propagating through free space on any observation plane located at the position z if this distribution on another plane located at a different position (z_0) is known. Using some mathematical properties, integrals such as in Eq. (2.37) can be expressed in terms of the convolution of $f(x,y,z_0)$ and $\frac{i}{\lambda(z-z_0)}e^{-ik(z-z_0)}e^{-i\frac{k}{2(z-z_0)}\left(x^2+y^2\right)}$.

2.2. Closed aperture Z-scan at the absence of nonlinear absorption

2.2.1. Closed aperture Z-scan for third order nonlinearity

The polarization induced in a medium by an applied electric field can be expanded as an exponential series of the electric field E as given in Eq.(1.1). As the intensity of applied electric field increases the induced polarization violates from the linear dependence on applied field since the higher order terms in Eq. (1.1) becomes comparable to the first linear term and subsequently the induced polarization changes nonlinearly with the applied electric field. As a consequence, the dielectric constant and thus the complex refractive index depend on the applied electric field strength.

$$\frac{\varepsilon}{\varepsilon_0}=\left(1+\chi^{(1)}+\chi^{(2)}E+\chi^{(3)}E\cdot E+\chi^{(4)}E\cdot E\cdot E+.....\right) \qquad (2.38)$$

$$n(I)=n_0+\xi E+n_2 I+..... \qquad (2.39)$$

In Eq. (2.39), the first term n_0 is the complex linear refractive index describing refraction and linear absorption. The second term, ξE , is the linear electric field dependent change in the refractive index. This refractive behavior is refered to as Pockels effect which can be exploited in designing devices such as Pockels cell. The third term, $n_2 I$, displays the change in the refractive index that is proportional to the light intensity; this term manifests itself in a phenomenon known as the Kerr effect.

The Kerr effect is a third order or cubic nonlinear response when a linear variation in the refractive index as a function of light intensity is observed while a medium is irradiated with more intense radiation such as a pulsed laser beam.

$$n(I) = n_0 + n_2 I \tag{2.40}$$

$$\Delta n = n_2 I \tag{2.41}$$

Eq. (2.41) indicates that the refractive index varies linearly with light intensity whether the light intensity varies temporally at any point within a medium or changes spatially in a medium at any time.

The spatial intensity distribution of a Gaussian beam on the normal plane to the beam propagation direction is governed by the Gaussian function. That means the light intensity is stronger in the center of the beam spot and decreases laterally as a function of distance from the center.

When a spatially Gaussian beam travels through a nonlinear medium the induced changes in the refractive index mimic the light intensity profile leading to create a convergent lens if n_2 possesses a positive sign and inversely a divergent lens if n_2 possesses a negative sign. These effects are known as self-focusing and self-defocusing respectively.

If the medium length, through which the Gaussian beam is propagating, is small enough so that changes in the beam diameter within the medium due to either diffraction or nonlinear refraction can be neglected, the medium is regarded as a thin sample. In the thin sample approximation the electric field amplitude changes only due to absorption and the phase of electric field only changes due to nonlinear refraction.

$$\frac{d(\Delta\Phi)}{dz'} = k\Delta n(I) \tag{2.42}$$

$$\frac{dI}{dz'} = -\alpha(I) I \tag{2.43}$$

In the case of cubic nonlinearity and negligible nonlinear absorption $\Delta n(I)$ is a linear function of intensity and $\alpha(I)$ is a constant as the linear absorption coefficient.

Under these assumptions Eq. (2.42) and (2.43) can be easily solved to find the nonlinear phase shift at the exit surface of the sample.

$$\frac{dI}{dz'} = -\alpha_0 I \tag{2.44}$$

$$I(z') = I(z)e^{-\alpha_0 z'} \tag{2.45}$$

where z is the sample position.

Substituting Eq. (2.41) and (2.45) into Eq. (2.42) yields:

$$\frac{d(\Delta\Phi)}{dz'} = k\, n_2\, I(z') = k\, n_2\, I(z) e^{-\alpha_0 z'} \tag{2.46}$$

After integration over z' for the whole length of the sample, the entire phase change is obtained as:

$$\Delta\Phi(x,y,z,t) = k\, n_2\, I_0(t) \left(\frac{1-e^{-\alpha_0 L}}{\alpha_0} \right) \left(\frac{1}{1+\frac{z^2}{z_0^2}} \right) e^{-2\frac{x^2+y^2}{w(z)^2}} \tag{2.47}$$

The effective length for the sample can be defined as:

$$L_{eff} = \left(\frac{1-e^{-\alpha_0 L}}{\alpha_0} \right) \tag{2.48}$$

where α_0 is the linear absorption coefficient and L is the physical length of the sample. The on-axis phase shift at the focus is defined as:

$$\Delta\Phi(0,0,0,t) = \Delta\Phi_0(t) = k\, n_2\, I_0(t)\, L_{eff} \tag{2.49}$$

Therefore, the on-axis phase shift at the position z is obtained as:

$$\Delta\Phi_0(z,t) = \frac{\Delta\Phi_0(t)}{1+\frac{z^2}{z_0^2}} \tag{2.50}$$

And thus, the phase shift at any point on the wavefront can be written as:

$$\Delta\Phi(x,y,z,t) = \Delta\Phi_0(z,t)e^{-2\frac{(x^2+y^2)}{w(z)^2}} \tag{2.51}$$

where I_0(t) is the on-axis intensity at the focus.

The complex electric field exiting the sample experiences an amplitude reduction by a factor of $e^{-\alpha L/2}$ due to linear absorption and a phase distortion by a factor of $e^{-i\Delta\Phi(x,y,z,t)}$ due to refractive index change. So, the complex electric field on the exit surface of the sample is now containing an amplitude depletion factor as well as nonlinear phase shift. That is

$$E_e(x,y,z,t) = E(x,y,z,t)e^{-\frac{1}{2}\alpha_0 L}e^{-i\Delta\Phi(x,y,z,t)} \tag{2.52}$$

The quantity desired to be calculated is the electric field distribution on an observation screen at a distance *d* from the sample. For this purpose, the integral in Eq. (2.37), in which the electric field in Eq. (2.52) is inserted, must be calculated. Such an integral cannot be calculated diectly. A possible solution proposed by Weaier *et al.* [42] is to decompose the complex electric field at the exit plane of the sample into a summation of Gaussian beams by expansion of the nonlinear phase term, $e^{-i\Delta\Phi(x,y,z,t)}$, using the Taylor series expansion. That is

$$e^{-i\Delta\Phi(x,y,z,t)} = \sum_{m=0}^{\infty}\frac{\left[-i\Delta\Phi(x,y,z,t)\right]^m}{m!} \tag{2.53}$$

$$e^{-i\Delta\Phi(x,y,z,t)} = \sum_{m=0}^{\infty}\frac{\left[-i\Delta\Phi_0(z,t)\right]^m}{m!}e^{-2m\frac{(x^2+y^2)}{w(z)^2}} \tag{2.54}$$

After substituting $E(x,y,z,t)$ and $e^{-i\Delta\Phi(x,y,z,t)}$ from Eq. (2.14) and (2.54) in Eq. (2.52), the electric field exiting the sample is given by:

$$E_e(x,y,z,t)=\sum_{m=0}^{\infty}E_0(t)\frac{w_0}{w(z)}e^{-ikz}e^{-i\omega t}e^{i\phi}e^{-\frac{1}{2}\alpha L}e^{-ik\frac{(x^2+y^2)}{2R(z)}}\frac{\left[-i\Delta\Phi_0(z,t)\right]^m}{m!}e^{-\frac{(x^2+y^2)}{\left(w(z)^2/2m+1\right)}} \tag{2.55}$$

Eq. (2.55) shows a summation of infinite number of Gaussian beams with different radii. In this summation, the beam radius of m^{th} Gaussian beam is given by $w(z)/\sqrt{2m+1}$ showing a decrease with m (m is an integer number). The propagation of each individual Gaussian beam through free space between the sample and the aperture plane obeys Fresnel diffraction where the input plane is the exit surface of the sample and the output plane is the aperture plane located at the distance d away from the sample. On the aperture plane all those Gaussian beam components contained in Eq. (2.55) will add together to reconstruct the intensity distribution of the main Gaussian beam.

Recalling Eq. (2.37) gives a suitable tool to calculate the electric field distribution on the aperture plane located at a distance d far away from the sample while the input plane is the exit surface of the sample.

$$E(x,y,z_a,t)=\frac{i}{\lambda d}e^{-ikd}\int_{-\infty}^{+\infty}\int_{-\infty}^{+\infty}E_e(x',y',z,t)e^{-i\frac{k}{2d}\left((x-x')^2+(y-y')^2\right)}dx'dy' \tag{2.56}$$

where, $d=z_a-z$ and z_a is the position of aperture plane and z is the sample position.

By substituting $E_e(x',y',z,t)$ from Eq. (2.55) into Eq. (2.56), the electric field distribution on the aperture plane can be calculated from the equation below.

$$E(x,y,z_a,t)=\sum_{m=0}^{\infty}\frac{i}{\lambda d}e^{-ikd}E_0(t)\frac{w_0}{w(z)}e^{-ikz}e^{-i\omega t}e^{i\phi}e^{-\frac{1}{2}\alpha L}\frac{\left(-i\Delta\Phi_0(z,t)\right)^m}{m!}\times$$
$$\int_{-\infty}^{+\infty}\int_{-\infty}^{+\infty}e^{-ik\frac{\left(x'^2+y'^2\right)}{2R(z)}}e^{-\frac{\left(x'^2+y'^2\right)}{\left(w(z)^2/2m+1\right)}}e^{-i\frac{k}{2d}\left((x-x')^2+(y-y')^2\right)}dx'dy' \tag{2.57}$$

The double integral in Eq. (2.57) is composed of two independent integrals which have the same integrand. Thus, they can be separately calculated.

$$\int_{-\infty}^{+\infty} e^{-ik\frac{x'^2}{2R(z)}} e^{-\frac{x'^2}{w_{m0}^2}} e^{-ik\frac{(x-x')^2}{2d}} dx' = e^{-ik\frac{x^2}{2d}} \int_{-\infty}^{+\infty} e^{-\left(i\frac{k}{2R(z)}+i\frac{k}{2d}+\frac{1}{w_{m0}^2}\right)x'^2} e^{ik\frac{xx'}{d}} dx' \tag{2.58}$$

where

$$w_{m0}^2 = \frac{w(z)^2}{2m+1} \tag{2.59}$$

The exponent in the right hand side of Eq. (2.58) can be represented as a perfect square. That is:

$$\int_{-\infty}^{+\infty} e^{-ik\frac{x'^2}{2R(z)}} e^{-\frac{x'^2}{w_{m0}^2}} e^{-ik\frac{(x-x')^2}{2d}} dx' = e^{-ik\frac{x^2}{2d}} \exp\left[-\frac{k^2x^2}{4d^2\left(\frac{1}{w_{m0}^2}+i\frac{k}{2R(z)}+i\frac{k}{2d}\right)}\right]\times$$
$$\int_{-\infty}^{+\infty} \exp\left[-\left(\frac{1}{w_{m0}^2}+i\frac{k}{2R(z)}+i\frac{k}{2d}\right)\left(x'-ik\frac{x}{2d\left(\frac{1}{w_{m0}^2}+i\frac{k}{2R(z)}+i\frac{k}{2d}\right)}\right)^2\right] dx' \tag{2.60}$$

According to the following equation, the integral of the Gaussian function on the right hand side of Eq. (2.60) is given in Eq. (2.62).

$$\int_{-\infty}^{+\infty} e^{-\frac{x^2}{a^2}} dx = \sqrt{\pi}\, a \tag{2.61}$$

$$\int_{-\infty}^{+\infty} \exp\left[-\left(\frac{1}{w_{m0}^2}+i\frac{k}{2R(z)}+i\frac{k}{2d}\right)\left(x'-ik\frac{x}{2d\left(\frac{1}{w_{m0}^2}+i\frac{k}{2R(z)}+i\frac{k}{2d}\right)}\right)^2\right]dx' = \frac{\sqrt{\pi}}{\left(\frac{1}{w_{m0}^2}+i\frac{k}{2R(z)}+i\frac{k}{2d}\right)^{1/2}} \tag{2.62}$$

So the total result for the double integral in Eq. (2.57) will be:

$$\int_{-\infty}^{+\infty}\int_{-\infty}^{+\infty} e^{-ik\frac{\left(x'^2+y'^2\right)}{2R(z)}} e^{-\frac{\left(x'^2+y'^2\right)}{w_{m0}^2}} e^{-i\frac{k}{2d}\left((x-x')^2+(y-y')^2\right)} dx'dy' = \exp\left[\left(-i\frac{k}{2d}-\frac{k^2}{4d^2\left(\frac{1}{w_{m0}^2}+i\frac{k}{2R(z)}+i\frac{k}{2d}\right)}\right)\left(x^2+y^2\right)\right]\times\frac{\pi}{\left(\frac{1}{w_{m0}^2}+i\frac{k}{2R(z)}+i\frac{k}{2d}\right)} \tag{2.63}$$

After substitution the double integral from Eq. (2.63) into Eq. (2.57), the electric field distribution on the aperture plane is obtained as:

$$E(x,y,z_a,t) = E(x=0,y=0,z,t)e^{-\frac{1}{2}\alpha L}e^{-ikd}\sum_{m=0}^{\infty}\frac{i\frac{\pi}{\lambda d}}{\left(\frac{1}{w_{m0}^2}+i\frac{k}{2d}\left(1+\frac{d}{R(z)}\right)\right)}\times \frac{\left(-i\Delta\Phi_0(z,t)\right)^m}{m!}\exp\left[\left(-i\frac{k}{2d}-\frac{k^2}{4d^2\left(\frac{1}{w_{m0}^2}+i\frac{k}{2d}\left(1+\frac{d}{R(z)}\right)\right)}\right)\left(x^2+y^2\right)\right] \tag{2.64}$$

In order to simplify and summarize the terms in Eq. (2.64), several parameters are introduced as follows:

$$g = 1 + \frac{d}{R(z)} \tag{2.65}$$

The coefficient of the exponent in the above summation is obtained in term of g.

$$\frac{i\frac{\pi}{\lambda d}}{\left(\frac{1}{w_{m0}^2} + i\frac{k}{2d}\left(1 + \frac{d}{R(z)}\right)\right)} = \frac{\pi}{\lambda d \frac{k}{2d}\left(g - i\frac{2d}{k w_{m0}^2}\right)} = \frac{1}{\left(g - i\frac{d}{d_m}\right)} = \frac{e^{i\theta_m}}{\left(g^2 + \frac{d^2}{d_m^2}\right)^{1/2}} \tag{2.66}$$

where

$$d_m = \frac{k w_{m0}^2}{2} \tag{2.67}$$

and

$$\theta_m = \tan^{-1}\left[\frac{d/d_m}{g}\right] \tag{2.68}$$

Now the exponential function in the Eq. (2.64) can be rewritten in a new form in terms of new defined parameters as:

$$\exp\left[\left(-i\frac{k}{2d} - \frac{k^2\left(\frac{1}{w_{m0}^2} - i\frac{kg}{2d}\right)}{4d^2\left(\frac{1}{w_{m0}^4} + \frac{k^2 g^2}{4d^2}\right)}\right)\left(x^2 + y^2\right)\right] = \exp\left[\left(-i\frac{k}{2d} - \frac{\left(\frac{1}{w_{m0}^2} - i\frac{kg}{2d}\right)}{\left(g^2 + \frac{d^2}{d_m^2}\right)}\right)\left(x^2 + y^2\right)\right] =$$

$$\exp\left[\left(-i\frac{k}{2d}\left(1 - \frac{g}{\left(g^2 + \frac{d^2}{d_m^2}\right)}\right) - \frac{1}{w_{m0}^2\left(g^2 + \frac{d^2}{d_m^2}\right)}\right)\left(x^2 + y^2\right)\right] = \exp\left[\left(-ik\frac{\left(x^2 + y^2\right)}{2R_m}\right) - \frac{\left(x^2 + y^2\right)}{w_m^2}\right] \tag{2.69}$$

where the two new parameters are defined as follows:

$$R^{m} = d\left(1 - \frac{g}{g^{2} + \frac{d^{2}}{d_{m}^{2}}}\right)^{-1} \tag{2.70}$$

and

$$w_{m}^{2} = w_{m0}^{2}\left(g^{2} + \frac{d^{2}}{d_{m}^{2}}\right) \tag{2.71}$$

Hence, the electric field distribution on the aperture plane is obtained as:

$$E_{a}(z,r,t) = E(r=0,z,t)e^{-ikd}e^{-\frac{1}{2}\alpha L}\sum_{m=0}^{\infty}\left[\frac{\left(-i\Delta\Phi_{0}(z,t)\right)^{m}}{m!}\left(\frac{w_{m0}}{w_{m}}\right)\times e^{-ik\frac{r^{2}}{2R_{m}}}\times e^{-\frac{r^{2}}{w_{m}^{2}}}\times e^{i\theta_{m}}\right] \tag{2.72}$$

where (x^2+y^2) in previous equations has been replaced with r^2.

In the Z-scan experiment the sample (a transparent solid or a cuvette filled with a liquid) is moved along the beam propagation direction (considered as z axis) from a pre-focus position to a post-focus position. The energy transmitted through an aperture located in the far field is measured by a photo-diode as a function of sample position z and then, the transmittance T is plotted versus z.

The normalized transmittance is defined as the entire transmittance divided by its maximum occurring at the positions far enough from the focal point where the intensity is not high enough for the nonlinear refraction to occur so that the phase distortion is negligible and the transmittance remains constant.

$$T(z) = \frac{\int_{-\infty}^{+\infty} \mathrm{P}(\Delta\Phi)\,dt}{\int_{-\infty}^{+\infty} \mathrm{P}(\Delta\Phi = 0)\,dt} \tag{2.73}$$

where P is the power transmitted through an aperture of radius a given by:

$$\mathrm{P(t)} = \int_0^a I(r,t)\, 2\pi\, r\, dr \tag{2.74}$$

Where $I(t)$ denotes the intensity of the electric field which is related to the electric field amplitude through $I(r,t) = \frac{1}{2} c\, n_0\, \varepsilon_0 \left|E(r,t)\right|^2$. Hence, the power transmitted through an aperture of radius *a* is obtained from:

$$\mathrm{P(t)} = \pi\, \varepsilon_0\, c\, n_0 \int_0^a \left|E(r,t)\right|^2 r\, dr \tag{2.75}$$

The normalized transmittance is now given by the following in terms of electric field amplitude on the aperture plane.

$$T(z) = \frac{\int_{-\infty}^{+\infty} \int_0^a \left|E_a(r,t,\Delta\Phi)\right|^2 r\, dr\, dt}{\int_{-\infty}^{+\infty} \int_0^a \left|E_a(r,t,\Delta\Phi = 0)\right|^2 r\, dr\, dt} \tag{2.76}$$

By replacing the electric field from Eq. (2.72) into (2.76), the normalized transmittance can be calculated although this is not an easy task. For the (very) small aperture limit, the on-axis electric field on the aperture plane can be calculated by setting *r*=0 in Eq. (2.72). Therefore, the on-axis transmittance defined as the transmitted energy through a very small aperture centered on the optical axis can be easily calculated.

It should be mentioned that the electric field in Eq. (2.76) contains spatial as well as temporal parts. The temporal profile of the electric field should also be identified. For the sake of simplicity, the on-axis normalized transmittance for temporally square pulses, which behave like CW laser light, is first calculated. For these limitations the electric field is no longer a function of *r* and *t*. Thus, the electric field in Eq. (2.76) can be brought out of integral and then both integrals in the numerator and denominator of Eq. (2.76) are vanished. So

$$T(z,\Delta\Phi_0) = \frac{\left|E_a(z,r=0,t=0,\Delta\Phi_0)\right|^2}{\left|E_a(z,r=0,t=0,\Delta\Phi_0=0)\right|^2} \tag{2.77}$$

In the limit of small nonlinear phase change, $\Delta\Phi_0 << 1$, only the first two terms in Eq. (2.72) is adequate to retain. The far field approximation in which $\frac{d}{z_0} >> 1$ is also assumed. Therefore

$$T(z,\Delta\Phi_0)=\frac{\left|\left(\frac{1}{g-i\frac{d}{d_0}}\right)-i\Delta\Phi_0(z)\left(\frac{1}{g-i\frac{d}{d_1}}\right)\right|^2}{\left|\frac{1}{g-i\frac{d}{d_0}}\right|^2} \tag{2.78}$$

where $d_1=d_0/3$. The numerator of the above equation is calculated as:

$$\begin{aligned}
&\left|\left(\frac{1}{g-i\frac{d}{d_0}}\right)-i\Delta\Phi_0(z)\left(\frac{1}{g-i\frac{d}{d_1}}\right)\right|^2=\left|\left(\frac{g}{g^2+\frac{d^2}{d_0^2}}+\Delta\Phi_0(z)\frac{3\frac{d}{d_0}}{g^2+9\frac{d^2}{d_0^2}}\right)+i\left(\frac{\frac{d}{d_0}}{g^2+\frac{d^2}{d_0^2}}-\frac{\Delta\Phi_0(z)g}{g^2+9\frac{d^2}{d_0^2}}\right)\right|^2\\
&=\left(\frac{g}{g^2+\frac{d^2}{d_0^2}}+\Delta\Phi_0(z)\frac{3\frac{d}{d_0}}{g^2+9\frac{d^2}{d_0^2}}\right)^2+\left(\frac{\frac{d}{d_0}}{g^2+\frac{d^2}{d_0^2}}-\frac{\Delta\Phi_0(z)g}{g^2+9\frac{d^2}{d_0^2}}\right)^2\\
&=\frac{g^2}{\left(g^2+\frac{d^2}{d_0^2}\right)^2}+\Delta\Phi_0(z)^2\frac{9\frac{d^2}{d_0^2}}{\left(g^2+9\frac{d^2}{d_0^2}\right)^2}+\frac{6g\Delta\Phi_0(z)\frac{d}{d_0}}{\left(g^2+\frac{d^2}{d_0^2}\right)\left(g^2+9\frac{d^2}{d_0^2}\right)}+\\
&\frac{\frac{d^2}{d_0^2}}{\left(g^2+\frac{d^2}{d_0^2}\right)^2}+\frac{\Delta\Phi_0(z)^2g^2}{\left(g^2+9\frac{d^2}{d_0^2}\right)^2}-\frac{2\Delta\Phi_0(z)g\frac{d}{d_0}}{\left(g^2+\frac{d^2}{d_0^2}\right)\left(g^2+9\frac{d^2}{d_0^2}\right)}
\end{aligned} \tag{2.79}$$

In the limit of a small nonlinear phase shift the phase distortion square is much smaller than the phase distortion itself. Therefore, those terms in the above equation containing $\Delta\Phi_0^2$ are negligible compared to the other terms and ignored. Hence, the numerator of the Eq. (2.78) is calculated as:

$$\left|\left(\frac{1}{g-i\frac{d}{d_0}}\right)-i\Delta\Phi_0(z)\left(\frac{1}{g-i\frac{d}{d_1}}\right)\right|^2=\frac{\left(g^2+\frac{d^2}{d_0^2}\right)}{\left(g^2+\frac{d^2}{d_0^2}\right)^2}+\frac{4\Delta\Phi_0(z)\,g\,\frac{d}{d_0}}{\left(g^2+\frac{d^2}{d_0^2}\right)\left(g^2+9\frac{d^2}{d_0^2}\right)} \tag{2.80}$$

The denominator of Eq. (2.78) is calculated as:

$$\left|\frac{1}{g-i\frac{d}{d_0}}\right|^2=\frac{1}{g^2+\frac{d^2}{d_0^2}} \tag{2.81}$$

After dividing Eq. (2.80) by Eq. (2.81) the normalized transmittance is obtained in the following form:

$$T(z,\Delta\Phi_0)=1+\frac{4\Delta\Phi_0(z)\,g\,\frac{d}{d_0}}{g^2+9\frac{d^2}{d_0^2}} \tag{2.82}$$

It should be reminded that g was previously defined as $1+d/R(z)$. For the far field approximation, in which the aperture plane is far enough away from the focal plane, it can be shown that $g\cong d/R(z)$ is a reasonable approximation.

$$g\cong\frac{d}{R(z)}=\frac{d}{z\left(1+\frac{z_0^{\,2}}{z^2}\right)}=\frac{x\,d}{z_0\left(1+x^2\right)}\Rightarrow g^2=\frac{x^2\,d^2}{z_0^{\,2}\left(1+x^2\right)^2} \tag{2.83}$$

$$d_0=k\frac{\omega(z)^2}{2}=z_0\left(1+x^2\right)\Rightarrow\frac{d^2}{d_0^2}=\frac{d^2}{z_0^{\,2}\left(1+x^2\right)^2} \tag{2.84}$$

$$g^2+9\frac{d^2}{d_0^2}=\frac{x^2\,d^2}{z_0^{\,2}\left(1+x^2\right)^2}+9\frac{d^2}{z_0^{\,2}\left(1+x^2\right)^2}=\frac{d^2}{z_0^{\,2}\left(1+x^2\right)^2}\left(x^2+9\right) \tag{2.85}$$

$$g\,\frac{d}{d_0}=\frac{x\,d}{z_0\left(1+x^2\right)}\times\frac{d}{z_0\left(1+x^2\right)}=\frac{x\,d^2}{{z_0}^2\left(1+x^2\right)^2} \tag{2.86}$$

After substitution of Eq. (2.85) and (2.86) into Eq. (2.82), the normalized transmittance is obtained to

$$T(z,\Delta\Phi_0)=1+\frac{4x\Delta\Phi_0(z)}{(x^2+9)} \tag{2.87}$$

where $\Delta\Phi_0(z)=\dfrac{\Delta\Phi_0}{1+x^2}$. Therefore, the normalized transmittance as a function of the sample position is given as:

$$T(z,\Delta\Phi_0)=1+\frac{4x\Delta\Phi_0}{(x^2+1)(x^2+9)} \tag{2.88}$$

where $\Delta\Phi_0 = kn_2L_{eff}I_0$, k is the wave number, L_{eff} is the effective length of the sample, I_0 is the on-axis intensity at the focus and n_2 is the nonlinear refractive index which is supposed to be measured.

So far, temporally square pulses with pulse duration longer than the nonlinear response time have been assumed. These kinds of pulses are treated similar to CW laser radiation for which the nonlinearity reaches the steady state. Now, the steady state results are extended to include transient effect induced by pulsed radiation. For this purpose the pulse temporal behavior must be specified. The most frequently produced laser pulse known as Gaussian pulse is now examined. It is also assumed that the nonlinear medium has an instantaneous response and decay time relative to the pulse width of the laser pulses. Thus, the on-axis normalized transmittance is derived from Eq. (2.76) as

$$T(z)=\frac{\int_{-\infty}^{+\infty}\left|E_a(r=0,z,t,\Delta\Phi)\right|^2\,dt}{\int_{-\infty}^{+\infty}\left|E_a(r=0,z,t,\Delta\Phi=0)\right|^2\,dt} \tag{2.89}$$

In the limit of small nonlinear phase distortion, only the first two terms in the summation (2.72) is adequate to be retained. Under this assumption the on-axis normalized transmittance can be written as

$$T(z)=\frac{\int_{-\infty}^{+\infty}\left|E(z,r=0)e^{-2\ln 2\frac{t^2}{\tau^2}}e^{-i\theta(z,t)}\left\{\left(\frac{1}{g-i\frac{d}{d_0}}\right)-i\Delta\Phi_0(z,0)e^{-4\ln 2\frac{t^2}{\tau^2}}\left(\frac{1}{g-i\frac{d}{d_1}}\right)\right\}\right|^2 dt}{\int_{-\infty}^{+\infty}\left|\frac{E(z,r=0)e^{-2\ln 2\frac{t^2}{\tau^2}}e^{-i\theta(z,t)}}{g-i\frac{d}{d_0}}\right|^2 dt} \tag{2.90}$$

After performing some lengthy calculation, similar to that completed for the CW radiation case, the following equation is obtained.

$$T(z,\Delta\Phi_0)=\frac{\int_{-\infty}^{+\infty}e^{-4\ln 2\frac{t^2}{\tau^2}}dt+\frac{4x\,\Delta\Phi_0(0)}{\left(x^2+1\right)\left(x^2+9\right)}\int_{-\infty}^{+\infty}e^{-8\ln 2\frac{t^2}{\tau^2}}dt}{\int_{-\infty}^{+\infty}e^{-4\ln 2\frac{t^2}{\tau^2}}dt} \tag{2.91}$$

So the on-axis normalized transmittance assuming a temporally Gaussian pulse is given as:

$$T(z,\Delta\Phi_0)=1+\frac{2\sqrt{2}\,x\,\Delta\Phi_0(0)}{\left(x^2+1\right)\left(x^2+9\right)} \tag{2.92}$$

where $\Delta\Phi_0(0)=k\,n_2\,L_{eff}\,I_0(0)$ and $I_0(0)$ is the peak on-axis intensity at the focus.

The only difference between Equations (2.88) and (2.92) is that $\Delta\Phi_0$ has been replaced with $\Delta\Phi_0(0)/\sqrt{2}$. That is not astonishing because Eq. (2.88) has been derived for CW irradiation whereas in the pulse radiation case, phase change $\Delta\Phi_0$ must be replaced by the time averaged phase change $\langle\Delta\Phi_0(t)\rangle$ over the pulse duration. The time averaged phase change is defined as follows:

$$\left\langle\,\Delta\Phi_0(t)\,\right\rangle=\frac{\int_{-\infty}^{+\infty}\Delta\Phi_0(t)\,I(t)\,dt}{\int_{-\infty}^{+\infty}I(t)\,dt} \tag{2.93}$$

Assuming a temporally Gaussian pulse, where $I(t)=I_0 e^{-4\ln 2\frac{t^2}{\tau^2}}$, the time averaged amount of phase change is obtained as

$$\left\langle \Delta\Phi_0(t) \right\rangle = \frac{\Delta\Phi_0(0)\int_{-\infty}^{+\infty} e^{-4\ln 2\frac{t^2}{\tau^2}} I_0\, e^{-4\ln 2\frac{t^2}{\tau^2}}\, dt}{\int_{-\infty}^{+\infty} I_0\, e^{-4\ln 2\frac{t^2}{\tau^2}}\, dt} = \frac{\Delta\Phi_0(0)}{\sqrt{2}} \tag{2.94}$$

Therefore, the coefficient $1/\sqrt{2}$ in Eq. (2.92) is a consequence of time averaging for Gaussian pulses.

It was previously mentioned that the closed aperture Z-scan transmittance has two extrema (one peak and one valley). The positions of these extrema can be found by solving the following equation:

$$\begin{gathered} \frac{dT(x)}{dx} = 0 \Rightarrow \\ (x^2+9)(x^2+1) - \left(2x(x^2+1) + 2x(x^2+9)\right)x = 0 \Rightarrow \\ 3x^4 + 10x^2 - 9 = 0 \end{gathered} \tag{2.95}$$

With the substitution $y=x^2$ the above equation results in a quadratic equation.

$$\begin{gathered} 3y^2 + 10y - 9 = 0 \Rightarrow \\ y = \frac{-5 \pm \sqrt{52}}{3} \Rightarrow \\ x = \pm\sqrt{y} = \pm\sqrt{\frac{\sqrt{52}-5}{3}} = \pm 0.858 \end{gathered} \tag{2.96}$$

Therefore, the position of extrema will be:

$$x_m = \frac{z}{z_0} = \pm 0.858 \Rightarrow z = \pm 0.858 z_0 \Rightarrow \Delta z_{(p\to v)} = 1.717 z_0 \tag{2.97}$$

It should be noticed that the position of the extrema does not depend on the temporal behavior of radiation such that these extrema occur at the same position for both CW and Gaussian pulse radiation.

Knowing the extremes positions enables one to calculate the maximum and minimum transmittance and then the difference between them. That is:

$$\Delta T_{(\mathrm{p}\to\mathrm{v})} = T_{\max} - T_{\min} = 4\,\Delta\Phi_0 \left[\frac{x_{\max}}{(x_{\max}^2+1)(x_{\max}^2+9)} - \frac{x_{\min}}{(x_{\min}^2+1)(x_{\min}^2+9)} \right] \Rightarrow$$

$$\Delta T_{(\mathrm{p}\to\mathrm{v})} = 0.406\,\Delta\Phi_0 \tag{2.98}$$

As seen in Eq. (2.98), the transmittance has a linear relationship with the phase distortion. Utilizing this relation simply yields the nonlinear refractive index without any need to fit the Z-scan data to the theoretical formula. One should notice that the coefficient in Eq. (2.98) was obtained assuming a small aperture size and also a small phase change. In chapter 3, it will be shown that this coefficient depends on the aperture size and decreases as the size of aperture increases.

2.2.2. Closed aperture Z-scan for fifth order nonlinearity

In this section, the fifth order nonlinearity is examined where the change in the index of refraction is proportional to the intensity square whereas, the refractive index change was proportional to the intensity itself in case of third order nonlinearity. Fifth order nonlinearity can be observed in semiconductors where the index of refraction is altered through charge carriers generated by 2PA [43].

Under the assumption that the nonlinear absorption of the sample is negligible and its thickness is small enough, such that the electric field amplitude changes only due to the linear absorption, the following pair of equations leads to determine the electric field amplitude $\sqrt{I}$ and phase change $\Delta\psi$ within the sample.

$$\frac{dI}{dz'} = -\alpha_0 I \tag{2.99}$$

and

$$\frac{d(\Delta\Psi)}{dz'} = k\, n_4\, I^2 \tag{2.100}$$

The intensity attenuation within the sample due to linear absorption is described by the following equation

$$I(z') = I\, e^{-\alpha_0 z'} \tag{2.101}$$

Therefore the entire phase distortion for the laser beam traveling through the sample of length L can be obtained by calculating the following integral.

$$\Delta\Psi = k\, n_4 \int_0^L I(z')^2\, dz' = k\, n_4\, I^2(z,r,t) \int_0^L e^{-2\alpha_0 z'}\, dz' \tag{2.102}$$

$$\Delta\Psi = k\, n_4\, L'_{eff}\, I^2(z,r,t) \tag{2.103}$$

where L'_{eff} is known as the effective length of the sample given by

$$L'_{eff} = \frac{1 - e^{-2\alpha_0 L}}{2\alpha_0} \tag{2.104}$$

where L is the physical length of the sample and α is the linear absorption coefficient.

By substituting $I^2(z,r,t)$ in Eq. (2.103) the phase change is obtained as

$$\Delta\Psi(z,r,t) = \Delta\Psi(z,r=0,t)\, e^{-4\frac{r^2}{w(z)^2}} \tag{2.105}$$

where

$$\Delta\Psi(z,r=0,t) = \frac{\Delta\Psi_0(t)}{\left(1+x^2\right)^2} \tag{2.106}$$

and

$$\Delta\Psi_0(t) = k\, n_4\, L'_{eff}\, I_0(t)^2 \tag{2.107}$$

The complex electric field exiting the sample now can be written as

$$E_e(z,r,t) = \left| E_e(z,r,t) \right| e^{-i\Delta\Psi(z,r,t)} = E(z,r,t)\, e^{-\frac{1}{2}\alpha_0 L} \exp\left(-i\,\Delta\Psi_0(z,t)\, e^{-4\frac{r^2}{w(z)^2}} \right) \tag{2.108}$$

where $E(z,r,t)$ is the electric field amplitude at the entering surface of the sample, the second terms is an attenuation factor due to the linear absorption within the sample and the third term contains nonlinear phase change.

Exponential term in Eq. (2.108) can be expanded employing a Taylor series expansion with respect to a certain coordinates where the argument is zer. That is

$$E_e(z,r,t) = E(z,r,t)\, e^{-\frac{1}{2}\alpha_0 L} \sum_{m=0}^{\infty} \frac{\left[-i\,\Delta\Psi_0(z,t)\right]^m}{m!} e^{-4m\frac{r^2}{w(z)^2}} \tag{2.109}$$

Separating the longitudinal and lateral distribution of the incident electric field in the equation above gives the exiting electric field as

$$E_e(z,r,t) = \sum_{m=0}^{\infty} E(z,r=0,t)\, e^{-\frac{1}{2}\alpha_0 L} e^{-ik\frac{r^2}{2R(z)}} \frac{\left[-i\,\Delta\Psi_0(z,t)\right]^m}{m!} \exp\left(- \frac{r^2}{w(z)^2 \big/ (4m+1)} \right) \tag{2.110}$$

which is similar to the exiting electric field in Eq. (2.52). The exiting electric field in the above equation has been expressed as a sum of an infinite number of Gaussian beams propagating in z direction with the same wavefront curvature radius but with different electric field amplitudes and also different beam radii. The radius of the m^{th} beam is given by $w(z)\big/\sqrt{(4m+1)}$. All these Gaussian beams propagate through the free space to reach the aperture plane and then superpose to reconstruct the Gaussian beam distribution on the aperture plane.

To obtain the electric field distribution on the aperture plane, a calculation similar to what was done previously in section 2.2.1 (Equations (2.54) to (2.72)) can be performed:

$$E_a(z,r,t) = E(z,r=0,t)\, e^{-ikd}\, e^{-\frac{1}{2}\alpha_0 L} \sum_{m=0}^{\infty} \frac{\left[-i\,\Delta\Psi_0(z,t)\right]^m}{m!} \left(\frac{w_{m0}}{w_m}\right) e^{-ik\frac{r^2}{2R_m}}\, e^{-\frac{r^2}{w_m^2}}\, e^{i\theta_m} \tag{2.111}$$

where

$$w_{m0}^2 = \frac{w(z)^2}{4m+1} \tag{2.112}$$

In Eq. (2.111) g, d_m, θ_m, R_m and w_m have the same meaning as given in Eqs. (2.65), (2.67), (2.68), (2.70) and (2.71). One should note that all the mentioned parameters contain w_{m0} which is defined in Eq. (2.112). It should also be noticed that z is the sample position whereas r is transverse component on the aperture plane measured with respect to the optical axis.

The on-axis normalized Z-scan transmittance for fifth order nonlinearity assuming small phase distortion and also CW radiation can be written similar to Eq. (2.78) as follows

$$T(z)=\frac{\left|\frac{1}{g-i\frac{d}{d_0}}-i\Delta\Psi_0(z)\frac{1}{g-i\frac{5d}{d_0}}\right|^2}{\left|\frac{1}{g-i\frac{d}{d_0}}\right|^2} \tag{2.113}$$

After lengthy calculation like the one performed in section 2.2.1 assuming far field approximation $d > z_0$, the normalized transmittance is obtained as follows

$$T(z)=1+\frac{8x\Delta\Psi_0}{(x^2+1)^2(x^2+25)} \tag{2.114}$$

where

$$\Delta\Psi_0=k\,n_4\,L'_{eff}\,I_0{}^2 \tag{2.115}$$

And for the temporally Gaussian pulsed radiation, $\frac{\Delta\Psi_0}{\sqrt{3}}$ will replace $\Delta\Psi_0$ so that the transmittance is given as

$$T(z)=1+\frac{8x\frac{\Delta\Psi_0(0)}{\sqrt{3}}}{(x^2+1)^2(x^2+25)} \tag{2.116}$$

where $\Delta\Psi_0(0)=k\,n_4\,L'_{eff}\,I_0(0)^2$ and $I_0(0)$ is the peak on-axis intensity at the focus.

When Eq. (2.116) is fitted to the experimental data, the nonlinear refractive index is extracted. The plot of transmittance versus the sample position has two extrema. If there is a peak followed by a valley, it indicates self defocusing that means $n_4 < 0$ and if there is a valley followed by a peak, it indicates self focusing that means $n_4 > 0$.

It should be noted that the plot is symmetric implying that the maximum and minimum transmittance occur at the same distance from the focal plane. The position of extrema can be found by solving the following differential equation.

$$\frac{dT(x)}{dx}=0\Rightarrow(x^2+1)^2(x^2+25)-\left[4x(x^2+1)(x^2+25)+2x(x^2+1)^2\right]x=0$$
$$5x^6+81x^4+51x^2-25=0\Rightarrow x=\pm\,0.568 \tag{2.117}$$

The distance between the position of maximum and minimum transmittance is obtained as follows

$$\Delta z_{p\to v}=1.135\,z_0 \tag{2.118}$$

The above distance does not depend on the temporal behavior of the light radiation.

By substituting the position of extrema in the Eq. (2.86) the maximum and minimum transmittance and thus the difference between them is obtained as follows

$$\Delta T_{p\to v}=0.205\Delta\Psi_0 \tag{2.119}$$

By using the above linear equation the nonlinear index of refraction can be simply obtained without need for further calculation such as performing fitting process.

2.2.3. Closed aperture Z-scan for simultaneous third and fifth order nonlinearity

In this section, the simultaneous presence of third and fifth order nonlinearity will be examined. If the sample length is small and the nonlinear absorption is also negligible then the following pair of equations gives the amplitude and phase of electric field within the sample.

$$\frac{dI}{dz'}=-\alpha_0 I \tag{2.120}$$

$$\frac{d(\Delta\Phi_{tot})}{dz'}=k\,n_2\,I+k\,n_4\,I^2 \tag{2.121}$$

The phase distortion arose from third order nonlinearity and fifth order nonlinearity has been separately calculated in sections 2.2.1 and 2.2.2. Therefore, the entire phase change is the superposition of both individual cases as follows:

$$\Delta\Phi_{tot}(z,r,t)=k\,n_2\,L_{eff}\,I(z,r,,t)+k\,n_4\,L'_{eff}\,I^2(z,r,t) \tag{2.122}$$

After substitution of the intensity in Eq. (2.122), the phase change is given as:

$$\Delta\Phi_{tot}(z,r,t)=\Delta\Phi_0(z,t)e^{-2\frac{r^2}{w(z)^2}}+\Delta\Psi_0(z,t)e^{-4\frac{r^2}{w(z)^2}} \tag{2.123}$$

Where $\Delta\Phi_0(z,t)$ and $\Delta\Psi_0(z,t)$ have been defined in Equations (2.50) and (2.106).

Hence, the complex electric field exiting the sample is given as:

$$E_e(z,r,t)=E(z,r,t)e^{-\frac{1}{2}\alpha_0 L}\exp\left(-i\Delta\Phi_0(z,t)e^{-2\frac{r^2}{w(z)^2}}\right)\exp\left(-i\Delta\Psi_0(z,t)e^{-4\frac{r^2}{w(z)^2}}\right) \tag{2.124}$$

By expanding the two exponential in above equation using the Taylor series expansion the existing electric field is written as

$$E_e(z,r,t)=E(z,r,t)e^{-\frac{1}{2}\alpha_0 L}\sum_{m=0}^{\infty}\frac{\left[-i\Delta\Phi_0(z,t)\right]^m}{m!}e^{-2m\frac{r^2}{w(z)^2}}\times \sum_{n=0}^{\infty}\frac{\left[-i\Delta\Psi_0(z,t)\right]^n}{n!}e^{-4n\frac{r^2}{w(z)^2}} \tag{2.125}$$

Now, separating the axial and radial part of electric field will lead to

$$E_e(z,r,t)=E(z,r=0,t)e^{-\frac{1}{2}\alpha_0 L}e^{-ik\frac{r^2}{2R(z)}}\times \sum_{m=0}^{\infty}\sum_{n=0}^{\infty}\frac{\left[-i\Delta\Phi_0(z,t)\right]^m}{m!}\frac{\left[-i\Delta\Psi_0(z,t)\right]^n}{n!}e^{-\frac{r^2}{w_{mn0}{}^2}} \tag{2.126}$$

where

$$w_{mn0}^2=\frac{w(z)^2}{2m+4n+1} \tag{2.127}$$

By using Gaussian decomposition and Huygens integrals the electric field distribution on the aperture plane placed at distance *d* from the sample is obtained as follows:

$$E_a(z,r,t) = E(z,r=0,t)\,e^{-\frac{1}{2}\alpha_0 L}\sum_{m=0}^{\infty}\sum_{n=0}^{\infty}\frac{\left[-i\,\Delta\Phi_0(z,t)\right]^m}{m!}\times$$
$$\frac{\left[-i\,\Delta\Psi_0(z,t)\right]^n}{n!}\left(\frac{w_{mn0}}{w_{mn}}\right)e^{-\frac{r^2}{{w_{mn}}^2}}\;e^{-ik\frac{r^2}{2R_{mn}}}\;e^{i\theta_{mn}} \tag{2.128}$$

where

$$\left(\frac{w_{mn0}}{w_{mn}}\right)e^{i\theta_{mn}} = \frac{1}{g - i\dfrac{d}{d_{mn}}} \tag{2.129}$$

and

$$d_{mn} = \frac{k\,w_{mn0}^2}{2} = \frac{d_{00}}{2m+4n+1} \tag{2.130}$$

The on-axis normalized transmittance for CW radiation assuming a small phase distortion ($\Delta\Phi^2$, $\Delta\psi^2$ and $\Delta\Phi.\Delta\psi$ are negligible) can be written as

$$T(z) = \frac{\left|\dfrac{1}{g - i\dfrac{d}{d_{00}}} - i\,\Delta\Phi_0\dfrac{1}{g - i\dfrac{3d}{d_{00}}} - i\,\Delta\Psi_0\dfrac{1}{g - i\dfrac{5d}{d_{00}}}\right|^2}{\left|\dfrac{1}{g - i\dfrac{d}{d_{00}}}\right|^2} \tag{2.131}$$

After a lengthy calculation the Z-scan normalized transmittance of a medium, in which both third and fifth order nonlinearities occur, is obtained as

$$T(z) = 1 + \frac{4\Delta\Phi_0\,x}{(x^2+1)(x^2+9)} + \frac{8\Delta\Psi_0\,x}{(x^2+1)^2(x^2+25)} \tag{2.132}$$

As seen in Eq. (2.132) the transmittance for concurrent third and fifth order nonlinearities is the superposition of both individual nonlinearities given in Equations (2.92) and (2.116).

$$T(z)-1=\Delta T(z)_{total}=\Delta T(z)_{third}+\Delta T(z)_{fifth} \tag{2.133}$$

And the normalized transmittance for the temporally Gaussian pulsed radiation will be given as

$$T(z)=1+\frac{4\dfrac{\Delta\Phi_0(0)}{\sqrt{2}}x}{(x^2+1)(x^2+9)}+\frac{8\dfrac{\Delta\Psi_0(0)}{\sqrt{3}}x}{(x^2+1)^2(x^2+25)} \tag{2.134}$$

The trace of transmittance given by Eq. (2.134) is also symmetric having two extrema. The position of extrema is obtained by solving the following differential equation:

$$\frac{dT(x)}{dx}=0\Rightarrow 3x^{12}+171x^{10}+2860x^8+12606x^6+15795x^4-1769x^2-7650=0$$
$$x=\pm\,0.72\Rightarrow\Delta z_{p\to v}=1.44z_0 \tag{2.135}$$

The difference between maximum and minimum transmittance depending on both third order nonlinear phase shift and fifth order nonlinear phase shift is given by

$$\Delta T_{p\to v}=0.4\,\Delta\Phi_0(t)+0.2\,\Delta\Psi_0(t) \tag{2.136}$$

In practice, the above relation is only helpful when one of the nonlinear phase shifts is already known.

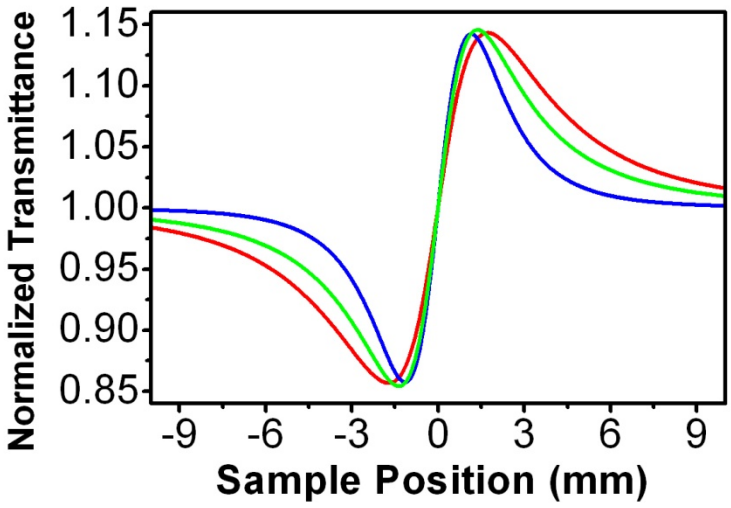

Fig. 2.5. Closed aperture Z-scan normalized transmittance curve. Red curve corresponds to ΔΦ=1 (Rad) for third order nonlinearity, blue curve corresponds to Δψ=1.4 (Rad) for fifth order nonlinearity and green curves corresponds to ΔΦ=0.5 and Δψ=0.7 for concurrent third and fifth order nonlinearity.

Fig. 2.5 shows the normalized Z-scan transmittance for third order nonlinearity (red curve), fifth order nonlinearity (blue curve) concurrent third and fifth order nonlinearity. The distance between maximum transmittance and minimum transmittance position is seen different as calculated previously (Δz_{third}=1.717 z_0, Δz_{fifth}=1.135 z_0, $\Delta z_{third\ and\ fifth}$=1.44 z_0). The normalized transmittance for third order nonlinearity is wider than that of fifth order nonlinearity. This is due to this fact that the nonlinear refractive index change is proportional to intensity for third order nonlinearity whereas it depends quadratically on the irradiance for fifth order nonlinearity. Fig. 2.6 illustrate intensity (red curve) and intensity square (blue curve) versus lateral position. This illustration helps one to better understand why the normalized transmittance for third order nonlinearity is wider than that for fifth order nonlinearity. The square of intensity decreases more rapidly than the intensity itself as the transverse component increases.

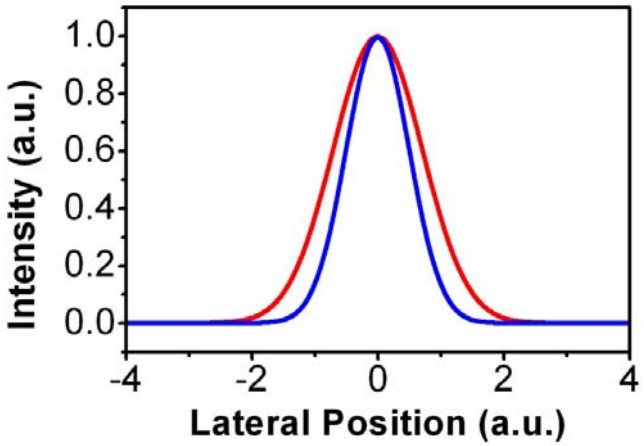

Fig. 2.6. Spatially Gaussian intensity distribution (red curve) and its square (blue curve) versus lateral position.

2.3. Open aperture Z-scan

2.3.1. Nonlinear absorption

Molecular systems can interact with optical fields in two ways, namely by: 1) dissipative or resonant processes and 2) parametric or non-resonant processes. If the energy and momentum from the light beam are exchanged between different longitudinal modes of the optical field but no energy is exchanged between the optical field and molecules in the system (e.g. second harmonic generation), this process is called parametric or non-resonant. However, in dissipative or resonant processes, the energy and momentum is exchanged between the optical field and molecules in the system through absorption and emission. Therefore, dissipative or resonant nonlinear processes are related to multi-photon absorption such as two-photon or three-photon absorption [44].

In the parametric processes, the frequency of the light is far from any internal resonant frequency of the molecular oscillating dipoles. The energy of the electric field of the light wave perturbs the electron cloud of the molecules, causing a change in the oscillations of the electron spring, which

immediately transfers the energy of the optical field to other modes. This instantaneous perturbation-excitation of the molecules is called a "virtual transition". In virtual transition, the energy of the photon is actually stored in the electronic springs of the molecules for a short time, whereby it can remain coherent with the light field and hence the light emitted in a new mode is coherent with the incident light in the previous mode. This is the main different between the parametric and dissipative processes.

In dissipative processes, the frequency of the incident light is close to an internal resonant frequency of the molecular oscillating dipoles so that the time for which the energy of the photon spends in the excited state of the molecules becomes longer and the stored energy is no longer coherent with the incident optical field, and the physics associated with the virtual transitions no longer apply and real transitions occur which result in energy absorption.

In the expression for the polarization in Eq. (1.1), the even-order susceptibility such as $\chi^{(2)}$, $\chi^{(4)}$ etc, do not contribute to the dissipative processes except in the case of a DC field. Therefore, the lowest-order nonlinear absorption is described by the imaginary part of the $\chi^{(3)}$ which corresponds to 2PA. The imaginary part of $\chi^{(5)}$ relates to 3PA.

Now, the attempt is made to derive the relation between the two- and three-photon absorption coefficient and the imaginary part of the third- and fifth-order susceptibility.

For a dissipative process at the presence of a monochromatic field the polarization is given by

$$p = \varepsilon_0 \left(\chi^{(1)} E \cos(\omega t) + \chi^{(3)} (E \cos(\omega t))^3 + \chi^{(5)} (E \cos(\omega t))^5 + \ \ldots \ \right) \qquad (2.137)$$

The polarization in Eq. (2.137) contains components oscillating at frequencies ω, 3ω, 5ω and higher harmonics whereas the applied electric field oscillates at frequency ω. The effective first order susceptibility, from which the index of refraction and absorption coefficient are calculated, is a proportionality coefficient between induced polarization and the driven electric field. Neglecting the higher order nonlinearity and also higher harmonic terms in Eq. (2.137) will lead to the following.

$$p_{\omega}^{(1)}(t) = \varepsilon_0 \left(\chi^{(1)} + \frac{3}{4} E^2 \chi^{(3)} + \frac{5}{8} E^4 \chi^{(5)} \right) E \cos(\omega t) \qquad (2.138)$$

The effective first order susceptibility is now modified such that it contains two additional terms arising from the third- and fifth-order nonlinearity. Therefore, the complex refractive index is now given by

$$n = \sqrt{1 + \chi_{eff}^{(1)}} = \sqrt{1 + \chi^{(1)} + \frac{3}{4} \chi^{(3)} E^2 + \frac{5}{8} \chi^{(5)} E^4} \qquad (2.139)$$

The real part of susceptibility relates to the index of refraction whereas the imaginary part relates to the absorption coefficient. Therefore, the complex refractive index can be written as

$$n = \sqrt{\left(1 + \chi_R^{(1)} + \frac{3}{4}\chi_R^{(3)} E^2 + \frac{5}{8}\chi_R^{(5)} E^4\right) + i\left(\chi_I^{(1)} + \frac{3}{4}\chi_I^{(3)} E^2 + \frac{5}{8}\chi_I^{(5)} E^4\right)} \qquad (2.140)$$

Exploiting this fact that the imaginary part of the complex refractive index is always smaller than its real part allows us to separate the real and imaginary parts of the complex refractive index using the following approximation.

$$n = n_R + i\,n_I = \sqrt{1 + \chi_R^{(1)} + \frac{3}{4}\chi_R^{(3)}E^2 + \frac{5}{8}\chi_R^{(5)}E^4} + i\frac{\chi_I^{(1)} + \frac{3}{4}\chi_I^{(3)}E^2 + \frac{5}{8}\chi_I^{(5)}E^4}{2\sqrt{1 + \chi_R^{(1)} + \frac{3}{4}\chi_R^{(3)}E^2 + \frac{5}{8}\chi_R^{(5)}E^4}} \qquad (2.141)$$

The real part of the complex refractive index can be expressed in terms of the linear and nonlinear refractive indices as follows:

$$n_R = \sqrt{1 + \chi_R^{(1)}} + \frac{3\chi_R^{(3)} E^2}{8\sqrt{1 + \chi_R^{(1)}}} + \frac{5\chi_R^{(5)} E^4}{16\sqrt{1 + \chi_R^{(1)}}} \qquad (2.142)$$

$$n_R = n_0 + \frac{3\chi_R^{(3)} I}{4 n_0^2 c \varepsilon_0} + \frac{5\chi_R^{(5)} I^2}{4 n_0^3 c^2 \varepsilon_0^2} = n_0 + n_2 I + n_4 I^2 \qquad (2.143)$$

where the nonlinear index for third and fifth order nonlinearities are defined as follows respectively

$$n_2 = \frac{3\chi_R^{(3)}}{4 n_0^2 c \varepsilon_0} \qquad (2.144)$$

and

$$n_4 = \frac{5\chi_R^{(5)}}{4 n_0^3 c^2 \varepsilon_0^2} \qquad (2.145)$$

With a good approximation, the imaginary part of the complex refractive index can be written as:

$$n_I = \frac{\chi_I^{(1)} + \frac{3}{4}\chi_I^{(3)} E^2 + \frac{5}{8}\chi_I^{(5)} E^4}{2\sqrt{1+\chi_R^{(1)}}} = \frac{\chi_I^{(1)}}{2n_0} + \frac{3\chi_I^{(3)} I}{4n_0^2 c\varepsilon_0} + \frac{5\chi_I^{(5)} I^2}{4n_0^3 c^2 \varepsilon_0^2} \tag{2.146}$$

The absorption coefficient is connected to the imaginary part of the complex refractive index through the following relation.

$$\alpha(I) = \frac{2\omega}{c} n_I = \alpha_0 + \alpha_2 I + \alpha_3 I^2 \tag{2.147}$$

where the linear absorption coefficient is defined as:

$$\alpha_0 = \frac{\omega \chi_I^{(1)}}{c n_0} \tag{2.148}$$

The 2PA coefficient is an intrinsic property of a medium at a particular frequency describing the efficiency of the ground state molecules to reach an excited state via simultaneous absorption of two photons. Comparison between Equations (2.146) and (2.147) allows one to determine the relation between nonlinear absorption coefficients and nonlinear susceptibilities as given in Equations (2.149) and (2.151).

$$\alpha_2 = \frac{3\omega \chi_I^{(3)}}{2n_0^2 c^2 \varepsilon_0} \tag{2.149}$$

2PA coefficient depends on the number of absorbing molecules within the irradiated region of a medium and thus it depends on the concentration of absorbing particles. Since a liquid compound can be prepared with different concentrations, thus a concentration independent variable called 2PA cross section is defined for liquids as follows:

$$\sigma_2 = \frac{\hbar\omega\,\alpha_2}{N} = \frac{\hbar\omega\,\alpha_2}{N_A \rho \times 10^{-3}} \tag{2.150}$$

where ω is the angular frequency of the incident beam, N_A is Avogadro number and ρ is the concentration of compound in mole per liter. The unit of σ in SI is $cm^4.sec$ but it is usually given in the units of Goeppert-Mayer (GM) where 1 GM=10^{-50} $cm^4.sec$.

The 3PA coefficient defined as the probability of simultaneous absorption of three photons at frequency ω is obtained as:

$$\alpha_3 = \frac{5\omega\ \chi_I^{(5)}}{2n^3c^3\varepsilon_0^2} \tag{2.151}$$

Since the 3PA coefficient is also a concentration dependent variable, a concentration independent variable for 3PA process is defined as 3PA cross section given by

$$\sigma_3 = \frac{(\hbar\omega)^2\,\alpha_3}{N} = \frac{(\hbar\omega)^2\,\alpha_3}{N_A\,\rho\times 10^{-3}} \tag{2.152}$$

The unit of 3PA cross section in SI is $cm^6.s^2$.

2.3.2. Open aperture Z-scan at the presence of two-photon absorption

Two-photon absorption is a third-order nonlinear resonance process where two photons are absorbed nearly simultaneously to excite the subject molecule to a real higher energy level. If a two-photon transition between two levels is allowed, one-photon transition between these two levels (by absorbing a photon at frequency twice larger) is forbidden due to the selection rules.

Since 2PA is a third-order process it is described by $\chi^{(3)}$ and thus, 2PA coefficient α_2 and 2PA cross section σ relate to the imaginary part of $\chi^{(3)}$. The 2PA cross section σ describes the efficiency of a particular molecule in the ground state to reach the excited state via a 2PA process and is related to α_2 by Eq. (2.150).

A cubic nonlinearity is a nonlinear response in which the the absorption coefficient and index of refraction are no longer constant but variy with the incident light intensity as follows.

$$\alpha(I) = \alpha_0 + \alpha_2 I \tag{2.153}$$

For a thin sample the intensity of the light beam within the sample is attenuated only due to absorption including linear and nonlinear absorption. Hence, the intensity of light beam as a function of z' within the sample is governed by the following simple equation.

$$\frac{dI}{dz'} = -\alpha(I)\,I = -\left(\alpha_0 + \alpha_2 I\right)I \tag{2.154}$$

In order to obtain the light intensity within the sample, both side of above equation should be integrated. That is:

$$\int_{I(z)}^{I(z')} \frac{dI}{I\left(\alpha_2 I + \alpha_0\right)} = -\int_0^{z'} dz' \tag{2.155}$$

The light intensity reduction along the light propagation direction is described by the following relation

$$I(z') = \frac{\alpha_0 I(z) e^{-\alpha_0 z'}}{\alpha_0 + \alpha_2 I(z) - \alpha_2 I(z) e^{-\alpha_0 z'}} \tag{2.156}$$

where $I(z)$ is the intensity of incident light on the entrance surface of the sample (z'=0) when the sample is placed at the position z.

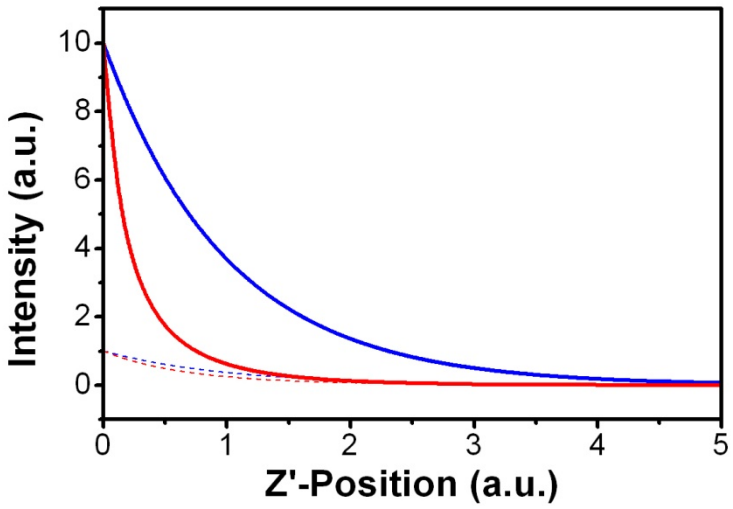

Fig. 2.7. The intensity versus propagation length within the sample at the presence of 2PA (red curve) and at the absence of 2PA (blue curve) for lower incident intensity (dashed curves) and higher incident intensity (solid curves) for comparison

In Fig. 2.7 the intensity is plotted versus propagation length in a typical nonlinear medium. Blue curves indicate intensity attenuating due to only linear absorption whereas the red curves illustrate a more rapidly attenuation in intensity since 2PA also contributes to the whole absorption. As can be seen from Fig. 2.7, 2PA does not contribute too much to the absorption at low intensities. As the incident intensity increases the contribution of 2PA becomes more significant and the rate of intensity attenuation at the presence of 2PA highly differs from that at the absence of 2PA.

The sample is assumed thin. In a thin sample the changes in the beam diameter due to either diffraction or nonlinear refraction is negligible and thus, the change in intensity is only due to

linear and nonlinear absorption. When the sample is moved along the propagation direction of a focused laser beam from pre-focus to post-focus positions the intensity of the laser beam changes that leads to a change in absorption coefficient and consequently in transmittance. The Z-scan transmittance as a function of sample position is expected to be a symmetric V-shape trace indicating a maximum absorption occurring at the focal point where the sample experiences the highest intensity in a Z-scan.

According to Eq. (2.156), the intensity on the exit surface of a thin sample of length L is obtained as

$$I_e(z,r,t) = \frac{I(z,r,t)e^{-\alpha_0 L}}{1+q(z,r,t)} \tag{2.157}$$

where

$$q(z,r,t) = \alpha_2 I(z,r,t) L_{eff} \tag{2.158}$$

and

$$L_{eff} = \frac{1-e^{-\alpha_0 L}}{\alpha_0} \tag{2.159}$$

$I(z,r,t)$ is the incident intensity at the entrance surface of the sample when the sample is placed at the position z.

In order to calculate the normalized transmittance, the transmitted power through the nonlinear medium must be first obtained by calculating the following integral.

$$\mathrm{P}_{Trans} = \int_0^{\infty} \frac{I(z,r,t)e^{-\alpha_0 L}}{1+\alpha_2 I(z,r,t) L_{eff}} 2\pi r\, dr \tag{2.160}$$

where the incident intensity $I(z,r,t)$ of a Gassian beam is given by

$$I(z,r,t) = I_0(z,t) e^{-2\frac{r^2}{w(z)^2}} \tag{2.161}$$

Thus, the intensity differential dI can be obtained as

$$dI = -\frac{4r}{\omega(z)^2} I\, dr \tag{2.162}$$

Changing the differential element from *dr* to *dI* will makes the calculation of Eq. (2.160) much more convenient.

$$\mathrm{P}_{Trans}(z,t) = 2\pi \int_0^{\infty} \frac{I(z,r,t)\, e^{-\alpha_0 L}}{1+\alpha_2\, I(z,r,t)\, L_{eff}} \left(-\frac{w(z)^2}{4\, I(z,r,t)} \right) dI \tag{2.163}$$

$$\mathrm{P}_{Trans}(z,t) = -\frac{\pi\, w(z)^2\, e^{-\alpha_0 L}}{2\,\alpha_2\, L_{eff}} \int_0^{\infty} \frac{\alpha_2\, L_{eff}\, dI}{1+\left(\alpha_2\, L_{eff}\, I(z,r,t)\right)} \tag{2.164}$$

$$\mathrm{P}_{Trans}(z,t) = -\frac{\pi\, w(z)^2\, e^{-\alpha_0 L}}{2\,\alpha_2\, L_{eff}} \ln\left(1+\alpha_2\, L_{eff}\, I(z,r,t)\right)\Big|_{r=0}^{r=\infty} \tag{2.165}$$

$$\mathrm{P}_{Trans}(z,t) = -\frac{\pi\, w(z)^2\, e^{-\alpha_0 L}}{2\,\alpha_2\, L_{eff}} \ln\left(1+\alpha_2\, L_{eff}\, I(z,r,t)\right)\Big|_{r=0}^{r=\infty} \tag{2.166}$$

$$\mathrm{P}_{Trans}(z,t) = \frac{\pi\, w(z)^2}{2} I_0(z,t)\, \frac{\ln\left(1+q_0(z,t)\right)}{q_0(z,t)} \tag{2.167}$$

Assuming a temporally Gaussian pulse, the time dependent and position dependent parts of $q(z,t)$ can be separated as follows

$$q(z,t) = q(z,0)\, e^{-4\ln 2\, \frac{t^2}{\tau^2}} \tag{2.168}$$

Eq. (2.167) is now rewritten by substitution q from (2.168).

$$\mathrm{P}_{Trans}(z,t) = \frac{\pi\, w_0^2}{2} I_0(0)\, e^{-4\ln 2\, \frac{t^2}{\tau^2}}\, \frac{\ln\left(1+q_0(z,0)\, e^{-4\ln 2\, \frac{t^2}{\tau^2}}\right)}{q_0(z,0)\, e^{-4\ln 2\, \frac{t^2}{\tau^2}}} \tag{2.169}$$

The normalized transmittance as the quotient of the transmitted energy to the incident energy is now obtained as:

$$T(z)=\frac{\frac{\pi w_0^2}{2}I_0(0)\frac{1}{q_0(z,0)}\int_{-\infty}^{+\infty}\ln\left(1+q_0(z,0)e^{-4\ln 2\frac{t^2}{\tau^2}}\right)dt}{\frac{\pi w_0^2}{2}I_0(0)\int_{-\infty}^{+\infty}e^{-4\ln 2\frac{t^2}{\tau^2}}dt} \tag{2.170}$$

where

$$\int_{-\infty}^{+\infty}e^{-4\ln 2\frac{t^2}{\tau^2}}dt=\tau\sqrt{\frac{\pi}{4\ln 2}} \tag{2.171}$$

In the limit of $q_0<1$ (which can be controlled by adjusting the light intensity) the term $\ln\left(1+q_0(z,0)e^{-4\ln 2\frac{t^2}{\tau^2}}\right)$ in Eq. (2.170) can be expanded using the Taylor series expansion as follows:

$$\ln\left(1+q_0(z,0)e^{-4\ln 2\frac{t^2}{\tau^2}}\right)=\sum_{n=0}^{\infty}(-1)^n\frac{\left(q_0(z,0)e^{-4\ln 2\frac{t^2}{\tau^2}}\right)^{n+1}}{n+1} \tag{2.172}$$

Fig. 2.8 shows the logarithm in the left hand side of Eq. (2.172) (green curve) and its Taylor series expansion (red and blue curves) as a function of q_0. The red and blue curves show the sum of the first 16 and 17 terms in the Taylor series summation respectively. Note that, for $q_0 > 1$, as q_0 grows the difference between the values of the Taylor polynomials and the original function increases rapidly. However, the Taylor polynomials for $q_0<1$ represents an acceptable approximation.

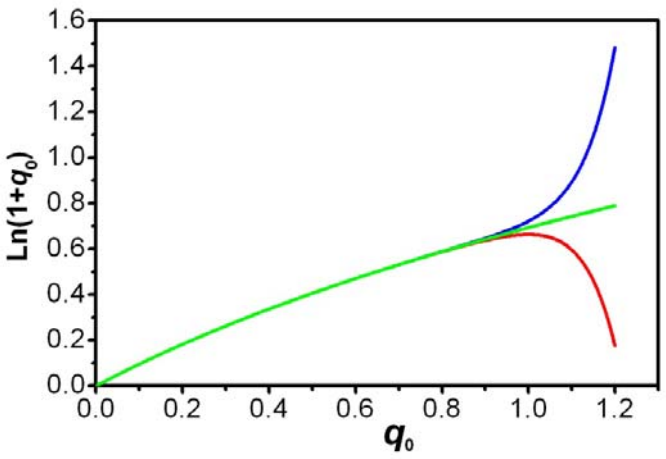

Fig. 2.8. Green curve shows the plot of ln(1+ q_0) versus q_0 and the red and blue curves show the sum of the first 16 and 17 terms of its Taylor series

After substitution Eq. (2.172) in Eq. (2.170) the transmittance is obtained as:

$$T(z)=\frac{1}{\tau\sqrt{\frac{\pi}{4\ln 2}}\,q(z,0)}\sum_{n=0}^{\infty}\frac{(-1)^n\,q(z,0)^{n+1}}{n+1}\int_{-\infty}^{+\infty}e^{-4\ln 2\,(n+1)\frac{t^2}{\tau^2}}\,dt \tag{2.173}$$

$$T(z)=\frac{1}{\tau\sqrt{\frac{\pi}{4\ln 2}}}\sum_{n=0}^{\infty}\frac{(-1)^n\,q(z,0)^{n}}{n+1}\frac{\tau\sqrt{\frac{\pi}{4\ln 2}}}{\sqrt{n+1}} \tag{2.174}$$

$$T(z)=\sum_{n=0}^{\infty}\frac{\left(-q(z,0)\right)^n}{(n+1)^{3/2}} \tag{2.175}$$

where

$$q(z,0)=\frac{q_0}{1+\frac{z^2}{z_0^2}} \tag{2.176}$$

and

$$q_0=\alpha_2\,L_{eff}\,I_0 \tag{2.177}$$

where $I_0 = I(t=0, r=0, z=0)$ is the maximum on-axis intensity at the focus. Therefore, the normalized transmittance as a function of sample position is given by

$$T(z) = \sum_{n=0}^{\infty} \frac{(-q_0)^n}{(n+1)^{3/2}(1+x^2)^n} \tag{2.178}$$

where x is the dimensionless parameter z/z_0.

As mentioned above I_0 is the peak intensity at the focus which is not a measurable parameter. In order to calculate I_0 some measurable laser parameters such as laser output power, pulse duration and beam waist radius must be given. It is worth to mention that the pulse duration and beam waist radius depends on the spatial and temporal energy distribution of the pulsed laser beam.

In order to find the relation between I_0 and its respective measurable laser parameter, it can be started from

$$\mathrm{P(t)} = \mathrm{P}_0 e^{-4\ln 2 \frac{t^2}{\tau^2}} \tag{2.179}$$

where P(t) denots the power of a temporally Gaussian pulse and τ is the pulse width (duration) defined as full width at half maximum (FWHM).

The average power over pulse duration is defined as the quotient of pulse energy to the pulse width as follows:

$$\mathrm{P}_{aver} = \frac{\int_{-\infty}^{+\infty} \mathrm{P(t)}\, dt}{\tau} = \frac{\mathrm{P}_0 \int_{-\infty}^{+\infty} e^{-4\ln 2 \frac{t^2}{\tau^2}}\, dt}{\tau} = \mathrm{P}_0 \sqrt{\frac{\pi}{4\ln 2}} \tag{2.180}$$

On the other hand and from the empirical point of view, the average power over pulse duration or so-called peak power is given by:

$$\mathrm{P}_{aver} = \frac{E_{pulse}}{\tau} = \frac{\mathrm{P}_{out}}{R\tau} \tag{2.181}$$

where P_{out} is the laser output power and R is the repetition rate.

Therefore, the relation between the maximum peak power and the laser output power is given by

$$\mathrm{P}_0 = 2\sqrt{\frac{\ln 2}{\pi}}\,\frac{\mathrm{P}_{out}}{R\,\tau} \tag{2.182}$$

The peak intensity, referred to as the maximum intensity at the middle of a temporally Gaussian pulse, is the desired variable to be found. For a spatially Gaussian laser beam, the relation between power and intensity is given by

$$\mathrm{P}(t) = \frac{\pi w_0^2}{2} I_0(t) \tag{2.183}$$

$$I_0 = \frac{2\,\mathrm{P}_0}{\pi {w_0}^2} = 4\sqrt{\frac{\ln 2}{\pi}}\,\frac{\mathrm{P}_{\mathrm{out}}}{\pi\,{w_0}^2\,R\,\tau} = 4\sqrt{\frac{\ln 2}{\pi}}\,\frac{\mathrm{P}_{\mathrm{out}}}{M^2\,\lambda\,z_0\,R\,\tau} = 4\sqrt{\frac{\ln 2}{\pi}}\,\frac{\mathrm{E}}{M^2\,\lambda\,z_0\,\tau} \tag{2.184}$$

I_0 is called peak on-axis intensity at the focus that means the intensity at $t=0$, $r=0$ and $z=0$, E is the pulse energy, z_0 is the Rayleigh range that depends on the focal length of the focusing lens and M^2 is the beam quality factor that is equal to unity for an ideal Gaussian beam and bigger than one for a real Gaussian beam.

With a good approximation, one can retain the first two terms in Eq. (2.178) and ignore the higher order exponents. Following this approximation the transmittance is simply given by the below equation indicating that the maximum absorption, occurring at the focus, scales linearly with the peak on-axis intensity as shown in Fig. 2.9.

$$T(z) = 1 - \frac{\beta\,L_{eff}\,I_0}{\sqrt{2^3}\,\left(1+x^2\right)} \Rightarrow A_{\max} = 1 - T_{\min} = \left(\frac{\beta\,L_{eff}}{\sqrt{2^3}}\right) I_0 = \frac{q_0}{\sqrt{2^3}} \tag{2.185}$$

where $A_{\max}$ and $T_{\min}$ are the maximum absorption and minimum transmittance occurring at the focal point of the focused laser beam.

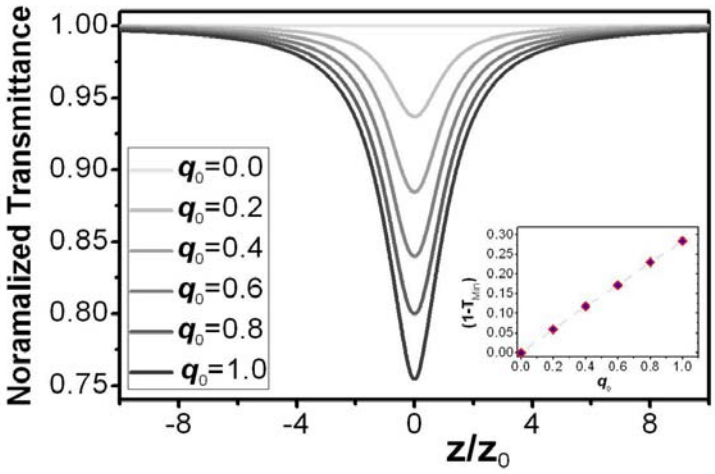

Fig. 2.9. Normalized open aperture Z-scan Transmittance versus the sample position plotted for different q_0

It must be mentioned that the expansion in Eq. (2.172) was achieved under criterion of $q_0<1$ and consequently the final Eq. (2.178) can only be employed in this limitation. The minimum transmittance in Eq. (2.178) assuming $q_0=1$ is 0.765. This means that it is only allowed to employ this equation to extract the 2PA coefficient if the transmittance is higher than 0.765 or, on the other words, the absorption is lower than 0.235.

2.3.3. Open aperture Z-scan at the presence of three-photon absorption

3PA is a fifth-order nonlinear resonance process where three photons are absorbed simultaneously to excite the irradiated molecule to a real exited state. Since 3PA is a fifth-order process, it is described by $\chi^{(5)}$.

At the presence of 3PA and absence of 2PA, the variation of the intensity of a laser beam propagating through a thin sample is simply governed by

$$\frac{dI}{dz'} = -\left(\alpha_0 + \alpha_3 I^2\right) I \tag{2.186}$$

where α_3 is called 3PA coefficient.

$$\frac{dI}{I(\alpha_3 I^2 + \alpha_0)} = -dz' \tag{2.187}$$

$$\frac{1}{\alpha_3}\int_{I(z'=0)}^{I(z')}\frac{dI}{I(I^2+\frac{\alpha_0}{\alpha_3})}=-\int_0^{z'}dz' \tag{2.188}$$

The light intensity within the sample is then obtained as follows.

$$I(z')=\frac{\sqrt{\alpha_0}\,I(z)e^{-\alpha_0 z'}}{\sqrt{\alpha_0+\alpha_3 I(z)^2-\alpha_3 I(z)^2 e^{-2\alpha_0 z'}}} \tag{2.189}$$

where *I(z)* is the incident intensity at the entrance surface of the sample.

The light intensity exiting the sample of length *L* is now given as [45].

$$I_e(z,r,t)=\frac{I(z,r,t)\,e^{-\alpha_0 L}}{\sqrt{1+p^2(z,r,t)}} \tag{2.190}$$

where

$$p(z,r,t)=\sqrt{2\alpha_3 L'_{eff}}\;I(z,r,t) \tag{2.191}$$

and L'_{eff} is referred to as the effective length of the sample given by

$$L'_{eff}=\frac{1-e^{-2\alpha_0 L}}{2\alpha_0} \tag{2.192}$$

If the frequency of applied radiation is far from the absorption band of irradiated material the linear absorption is negligible and thus the linear absorption coefficient α_0 is almost zero. In this limit the effective length of the sample is identical to its physical length and thus the Eq. (2.190) can be written as

$$I(z')=\frac{I_0}{\sqrt{1+2\alpha_3 z' I_0^2}} \tag{2.193}$$

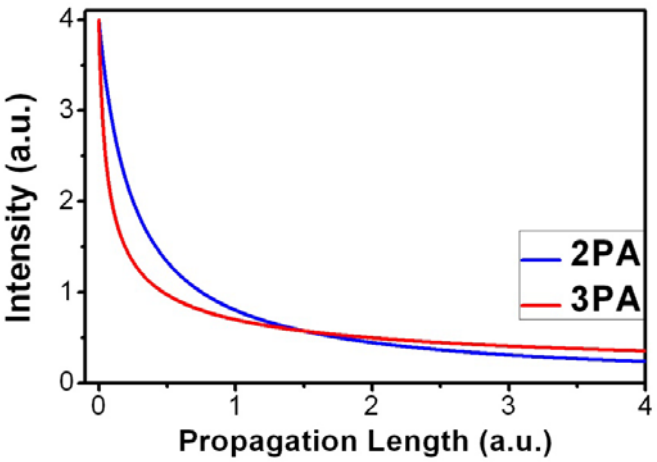

Fig. 2.10. Intensity versus propagation length at the presence of only 2PA (blue curve) and only 3PA (red curve) by letting linear absorption coefficient equal to zero for both cases

Fig. 2.10 shows the intensity within a nonlinear medium as a function of propagation length. The 3PA coefficient is considered high enough such that the 3PA exceeds the 2PA assuming a certain high enough intensity. As can be seen in the above figure for a higher intensity the rate of 3PA is larger than the rate of 2PA. On the other word, the intensity is reduced more rapidly in case of 3PA than in case of 2PA as the light propagates though the nonlinear medium. Therefore, after traveling some distance through the medium, when the intensity is much lower than the incident intensity, the rate of 3PA becomes smaller than the rate of 2PA. This behavior is due to the fact that 3PA depends on the intensity in a cubic way, rather than quadratic as for 2PA.

In order to better illustrate the different intensity dependent of 3PA and 2PA the intensity exiting a nonlinear medium is shown as a function of incident intensity in Fig. 2.11 for both cases of 2PA and 3PA. At low intensities the rate of 3PA is lower than that of 2PA. But this rate increases with incident intensity, such that the saturated exiting intensity for the case of 3PA is lower than that for the case of 2PA. This suggests that three-photon absorbing materials are more reliable and efficient than two-photon absorbers for optical limiting if they possess a high enough 3PA probability.

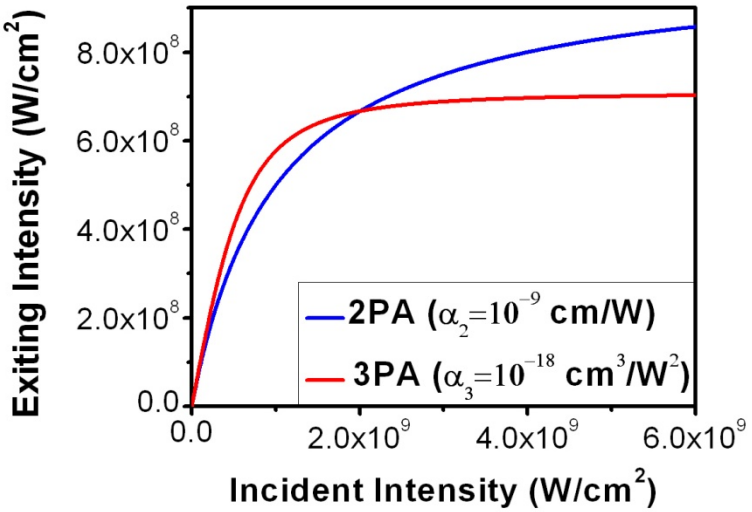

Fig. 2.11. Exiting intensity from a nonlinear medium of 1 cm length versus incident intensity. Blue curve shows the exiting intensity at the presence of 2PA and red curve at the presence of 3PA

The power exiting the sample can be calculated by integrating the exiting intensity over the exiting surface of the sample.

$$\mathrm{P}_e(z,t) = \int_0^\infty I_e(z,r,t)\, 2\pi\, r\, dr \tag{2.194}$$

$$\mathrm{P}_e(z,t) = \int_0^\infty \frac{I(z,r,t)\, e^{-\alpha_0 L}}{\sqrt{1+2\alpha_3 I^2(z,r,t) L'_{eff}}}\, 2\pi\, r\, dr \tag{2.195}$$

Since intensity is a function of *r* (distance from the optical axis) hence the redial element *dr* can be calculated as a function of intensity differential *dI*.

$$dI(z,r,t) = -\frac{4r}{w(z)^2} I(z,r,t)\, dr \tag{2.196}$$

Therefore

$$2r\, dr = -\frac{w(z)^2}{2}\left(\frac{dI(z,r,t)}{I(z,r,t)}\right) \tag{2.197}$$

After substitution from Eq. (2.197) into Eq. (2.194) the exiting power is obtained as:

$$\mathrm{P_e}(z,t) = -\frac{\pi\, w(z)^2}{2} e^{-\alpha_0 L} \int_0^{\infty} \frac{dI}{\sqrt{1+2\alpha_3 L'_{eff}\, I^2(z,r,t)}} \tag{2.198}$$

$$\mathrm{P_e}(z,t) = -\frac{\pi\, w(z)^2}{2\sqrt{2\alpha_3 L'_{eff}}} e^{-\alpha_0 L} \ln\left(I + \sqrt{I^2 + \frac{1}{2\alpha_3 L'_{eff}}} \right)\Big|_{r=0}^{\infty} \tag{2.199}$$

$$\mathrm{P_e}(z,t) = \frac{\pi\, w_0^2}{2} I_0(t)\, e^{-\alpha_0 L} \frac{\ln\left(p(z,t) + \sqrt{1+p^2(z,t)} \right)}{p(z,t)} \tag{2.200}$$

Where $p(z,t)$ was defined in Eq. (2.191). It should also be mentioned that the energy conservation given by the following has been utilized.

$$\frac{\pi\, w(z)^2}{2} I(z,t) = \frac{\pi\, w_0^2}{2} I_0(t) = \mathrm{P_i}(t) \tag{2.201}$$

where $\mathrm{P_i}(t)$ is the incident power.

The normalized transmittance is defined as the quotient of the exiting energy to the incident energy as follows:

$$T(z) = \frac{\int_{-\infty}^{+\infty} \mathrm{P_e}(z,t)\, dt}{\int_{-\infty}^{+\infty} \mathrm{P_i}(z,t)\, dt} \tag{2.202}$$

$$T(z) = \frac{\int_{-\infty}^{+\infty} \frac{\pi\, w_0^2}{2} I_0(0) e^{-t^2}\, e^{-\alpha_0 L} \frac{\ln\left(p(z,0) e^{-t^2} + \sqrt{1+p^2(z,0) e^{-t^2}} \right)}{p(z,0) e^{-t^2}} dt}{\int_{-\infty}^{+\infty} \frac{\pi\, w_0^2}{2} I_0(0) e^{-t^2}\, dt} \tag{2.203}$$

a temporally Gaussian pulse as $I(z,t) = I(z,0) e^{-t^2}$ has been assumed.

So:

$$T(z) = \frac{e^{-\alpha_0 L}}{\sqrt{\pi}\, p(z,0)} \int_{-\infty}^{+\infty} \ln\left(p(z,0) e^{-t^2} + \sqrt{1+p^2(z,0) e^{-2t^2}} \right) dt \tag{2.204}$$

where

$$p(z,0)=\sqrt{2\alpha_3 L'_{eff}}\;\frac{I_0(0)}{(1+\frac{z^2}{z_0^2})} \tag{2.205}$$

and I_0 is the maximum on-axis intensity at the focus.

Eq. (2.204) gives the normalized transmittance as a function of sample position. When this equation is fitted to the experimental Z-scan data the desired parameter as 3PA coefficient is obtained.

Eq. (2.204) can be simplified in the limit of P_0<1. Under this assumption, the logarithm in Eq. (2.204) can be expanded using Taylor series expansion using the following formula:

$$\ln\left(x+\sqrt{1+x^2}\right)=\sum_{m=0}^{\infty}(-1)^m\frac{x^{2m+1}}{(2m+1)!} \tag{2.206}$$

Fig. 2.12 (red curve) shows the logarithm on the left hand side of above equation (blue curve) and its Taylor series expansion as a function of x. It demonstrates that the difference between the amount of these two functions increases with x. For instance employing the above Taylor series as an approximated function instead of the logarithm as the original function leads to 10% error when x=1.2 and even 20% when x=1.5.

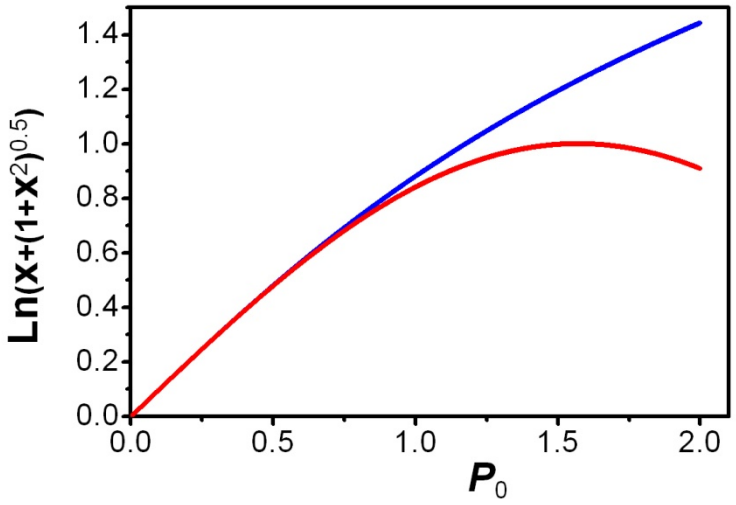

Fig. 2.12. Blue curve shows the logarithm on the left hand side of Eq. (2.206) and the red curve shows it Taylor series expansion

Substituting the Taylor series expansion instead of logarithm in Eq. (2.204) facilitates calculation of the integral in this equation. That is

$$T(z) = \frac{e^{-\alpha_0 L}}{\sqrt{\pi}\ p(z,0)} \sum_{m=0}^{\infty} \frac{(-1)^m}{(2m+1)!} \int_{-\infty}^{+\infty} p(z,0)^{2m+1} e^{-(2m+1)t^2}\, dt \tag{2.207}$$

Ultimately, the normalized transmittance in the open aperture Z-scan experiment at the presence of 3PA is given by

$$T(z) = \sum_{m=0}^{\infty} \frac{(-1)^m p_0^{2m}}{(2m+1)!(2m+1)^{1/2}(x^2+1)^{2m}} \tag{2.208}$$

where $p_0 = \sqrt{2\alpha_3 L'_{eff}}\ I_0$, I_0 is the peak on-axis intensity at the focus, α_3 is the 3PA coefficient (desired to be measured), $x=z/z_0$, z is the sample position and z_0 is the Rayleigh range.

With a good approximation one can retain the first two terms in Eq. (2.208) and ignore the higher order exponents. Following this approximation the transmittance is simply given by the below equation indicating that the maximum absorption, occurring at the focus, scales quadrically with the peak on-axis intensity as shown in Fig. 2.13.

$$T(z) = 1 - \frac{\alpha_3 L'_{eff}\ {I_0}^2}{3\sqrt{3}\ (x^2+1)^2} \Rightarrow 1 - T_{\min} = A_{\max} = \left(\frac{\alpha_3 L'_{eff}}{3\sqrt{3}}\right) {I_0}^2 = \left(\frac{\sqrt{3}}{18}\right) p_0^2 \tag{2.209}$$

where $T_{\min}$ and $A_{\max}$ are the normalized transmittance and absorbance at the focus respectively.

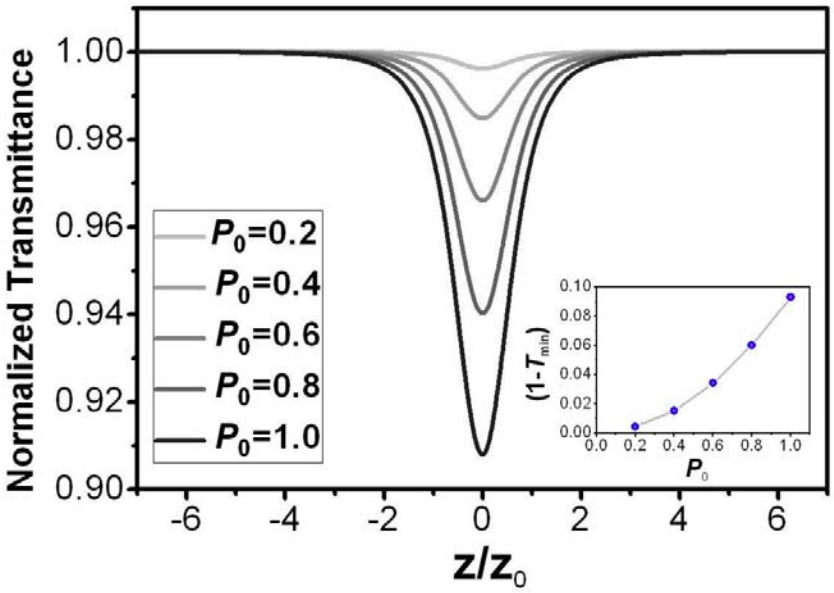

Fig. 2.13. Z-scan normalized transmittance at the presence of 3PA for different amount of P_0

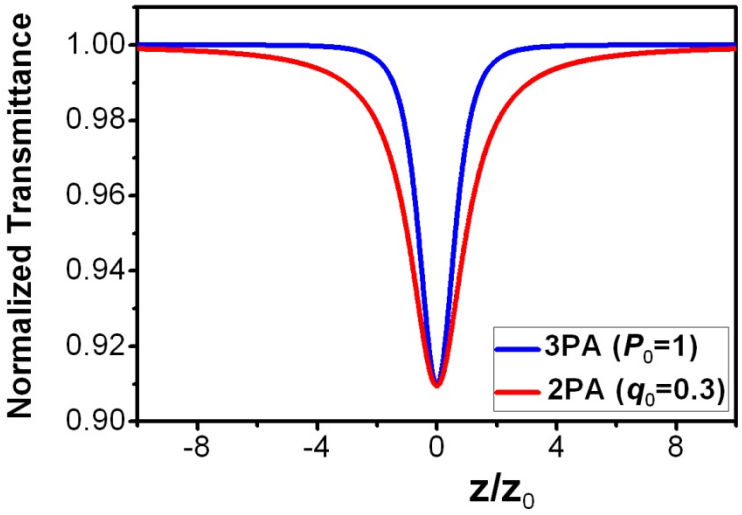

Fig. 2.14. Z-scan normalized transmittance at the presence of 2PA (red curve) and 3PA (blue curve). The 3PA respective signal is narrower than that of 2PA showing this fact that 3PA occurs at shorter vicinity of the focal point where the sample experiences higher intensity

Fig. 2.14 shows open aperture Z-scan trace at the presence of 3PA calculated with p_0=1 (blue curve) and at the presence of 2PA calculated with q_0=0.3. It reveals that higher intensity requires for 3PA process to occur in comparison with 2PA process. It also manifests that a scanning range of about $10z_0$ is sufficient for Z-scan experiment at the presence of 3PA since 3PA is almost zero at the distance of about $5z_0$ away from the focal plane. However, a scanning range larger than 20z0 is recommended for Z-scan at the presence of 2PA to find a reliable base line in order to normalize the Z-scan signal.

2.4. Closed aperture Z-scan at the presence of nonlinear absorption

2.4.1. Closed aperture Z-scan for third order nonlinearity at the presence of two-photon absorption

Previously, the nonlinear phase shift for a Gaussian beam was derived assuming Kerr effect and a negligible nonlinear absorption. Now, the similar procedure can be pursued for calculating the phase distortion at the presence of 2PA. The phase and intensity changes within the sample are given as

$$\frac{dI}{dz'} = -(\alpha_0 + \alpha_2 I) I \tag{2.210}$$

$$\frac{d(\Delta\Phi)}{dz'} = k n_2 I \tag{2.211}$$

The first equation yields the intensity within the medium as a function of propagation length.

$$I(z') = \frac{\alpha_0 I(z) e^{-\alpha_0 z'}}{\alpha_0 + \alpha_2 I(z) - \alpha_2 I(z) e^{-\alpha_0 z'}} \tag{2.212}$$

Therefore, the entire phase shift due to self-lensing after exiting the medium of length L can be obtained through

$$\Delta\Phi(z) = k n_2 \int_0^L \frac{\alpha_0 I(z) e^{-\alpha_0 z'}}{\alpha_0 + \alpha_2 I(z) - \alpha_2 I(z) e^{-\alpha_0 z'}} dz' \tag{2.213}$$

where $I(z)$ is the incident intensity on the iterance surface of the sample when it is placed at the position z. The phase shift is now given by

$$\Delta\Phi(z,r,t) = \frac{k n_2}{\alpha_2} \ln\left[1 + q(z,r,t)\right] \tag{2.214}$$

Where $q(z,r,t)$ was defined in Eq. (2.158) so that $q(z,r,t) = \alpha_2 I(z,r,t) L_{eff}$.

The complex electric field exiting the sample can be written as:

$$E_e(z,r,t) = \left| E_e(z,r,t) \right| e^{-i\Delta\Phi(z,r,t)} \tag{2.215}$$

where $|E_e(z,r,t)|$ is the amplitude of exiting electric field that is proportional to the square root of the intensity on the exiting surface of the sample given by the following relation:

$$|E_e(z,r,t)| = \sqrt{\frac{2I_e(z,r,t)}{cn\varepsilon_0}} \tag{2.216}$$

After substitution from Eq. (2.156) into Eq. (2.216) and then form Eq. (2.216) and (2.214) into the Eq. (2.215), the complex electric field exiting the sample is given by

$$E_e(z,,r,t) = \frac{\sqrt{\frac{2I(z,r,t)}{cn\varepsilon_0}}}{\sqrt{1+q(z,r,t)}} e^{-\frac{1}{2}\alpha_0 L} e^{-i\frac{kn_2}{\alpha_2}\ln(1+q(z,r,t))} \tag{2.217}$$

$$E_e(z,,r,t) = E(z,,r,t) e^{-\frac{1}{2}\alpha_0 L} \left(1+q(z,r,t)\right)^{-i\frac{k\gamma}{\beta}-\frac{1}{2}} \tag{2.218}$$

The term $\left(1+q(z,r,t)\right)^{-i\frac{k\gamma}{\beta}-\frac{1}{2}}$ in Eq. (2.218) can be expanded using the binomial series. Thus, the exiting electric field is obtained as

$$E_e(z,,r,t) = E(z,,r,t) e^{-\frac{1}{2}\alpha_0 L} \sum_{m=0}^{\infty} \left[\frac{q(z,r,t)^m}{m!} \prod_{n=0}^{m} \left(-i\frac{k n_2}{\alpha_2} - \frac{1}{2} - n + 1 \right) \right] \tag{2.219}$$

$$E_e(z,r,t) = E(z,r,t) e^{-\frac{1}{2}\alpha_0 L} \sum_{m=0}^{\infty} \left[\frac{\left[-i\Delta\Phi(z,t)\right]^m}{m!} \prod_{n=0}^{m} \left(1 - i(2n-1)\frac{\alpha_2}{2k n_2} \right) \right] e^{-2m\frac{r^2}{w(z)^2}} \tag{2.220}$$

Eq. (2.220) is basically identical with Eq. (2.54) derived at the absence of 2PA. The main difference is that the term $\left[-i\Delta\Phi(z,t)\right]^m / m!$ in Eq. (2.54) has been replaced with the new term $\left[\left(\left[-i\Delta\Phi(z,t)\right]^m / m! \right) \prod_{n=0}^{m} \left(1 - i(2n-1)\left(\alpha_2 / 2k n_2\right) \right) \right]$. This represents the fact that the absorptive and refractive contributions to the Z-scan transmittance are coupled with the coupling factor of $\alpha_2 / 2k n_2$. This means that in each position within the sample only the residual light intensity after the 2PA is the cause of the phase change.

Therefore, the electric field distribution on the aperture plane can be written similar to Eq. (2.72) by performing the above replacement. That is

$$E_a(z,r,t) = E(z,r=0,t)e^{-ikd}\, e^{-\frac{1}{2}\alpha_0 L} \sum_{m=0}^{\infty} \left[\frac{\left(-i\Delta\Phi_0(z,t)\right)^m}{m!} \times \prod_{n=1}^{m} \left(1 - i(2n-1)\frac{\alpha_2}{2kn_2} \right) \left(\frac{w_{m0}}{w_m} \right) \times e^{-ik\frac{r^2}{2R_m}}\, e^{-\frac{r^2}{w_m^2}}\, e^{i\theta_m} \right] \tag{2.221}$$

Now, the normalized transmittance through a finite aperture, in terms of electric field amplitude, is written as

$$T(z) = \frac{\int_{-\infty}^{+\infty} \int_0^a \left| E_a(r,t,\Delta\Phi) \right|^2 2\pi r\, dr\, dt}{\int_{-\infty}^{+\infty} \int_0^a \left| E_a(r,t,\Delta\Phi = 0) \right|^2 2\pi r\, dr\, dt} \tag{2.222}$$

In order to calculate the on-axis ($r = 0$) normalized transmittance for small phase change ($\Delta\Phi < 1$) retaining only the first two terms in Eq. (2.221) and neglecting the other terms gives a reasonable approximation. Hence, the normalized transmittance assuming CW radiation can be given as:

$$T(z,\Delta\Phi_0) = \frac{\left| \left(\frac{1}{g - i\frac{d}{d_0}} \right) - i\Delta\Phi_0(z) \left(1 - i\frac{\alpha_2}{2kn_2} \right) \left(\frac{1}{g - i\frac{3d}{d_0}} \right) \right|^2}{\left| \frac{1}{g - i\frac{d}{d_0}} \right|^2} \tag{2.223}$$

After a lengthy calculation, the normalized transmittance is obtained as follows:

$$T(z,\Delta\Phi_0) = 1 + \frac{4\Delta\Phi_0(z)\, g\, \frac{d}{d_0} - \Delta\Phi_0(z) \left(\frac{\alpha_2}{kn_2} \right) \left(g^2 + 3\frac{d^2}{d_0^2} \right)}{g^2 + 9\frac{d^2}{d_0^2}} \tag{2.224}$$

By using approximation assumed in Eq. (2.83) and also substituting from equations (2.84), (2.85) and (2.86) the normalized transmittance for closed aperture Z-scan at the presence of two-photon absorption is obtained as follows:

$$T(z) = 1 + \frac{4x\Delta\Phi_0 - q_0(x^2+3)}{(x^2+1)(x^2+9)} \tag{2.225}$$

The on-axis transmittance assuming a temporally Gaussian pulsed laser beam is given as

$$T(z) = 1 + \frac{4x\Delta\Phi_0(0) - q_0(0)(x^2+3)}{\sqrt{2}\,(x^2+1)(x^2+9)} \tag{2.226}$$

Fitting Eq. (2.226) to the experimental closed aperture Z-scan data allows one to extract both the nonlinear refractive index and the 2PA coefficient simultaneously.

It is seen that Eq. (2.226) is converted into Eq. (2.92) by letting q_0=0 as it is expected. It is also allowed and practicable to extract 2PA coefficient by fitting Eq. (2.226) to open aperture Z-scan data measured at the presence of 2PA by setting $\Delta\Phi_0$=0.

Fig. 2.15 shows a Z-scan transmittance of a 0.2 mm thick cell of Rhodamine B using 25 fs pulses at 798 nm. Fitting Eq. (2.226) (derived for closed aperture Z-scan at the presence of 2PA) with $\Delta\Phi_0(0) = 0$ as well as Eq. (2.178) (derived for open aperture Z-scan at the presence of 2PA) to the measured data for Rhodamine B yielded the same q_0 of 0.9. This proves that Eq.(2.226) is enough accurate in order to extract the absorptive properties from both closed and open aperture Z-scan trace.

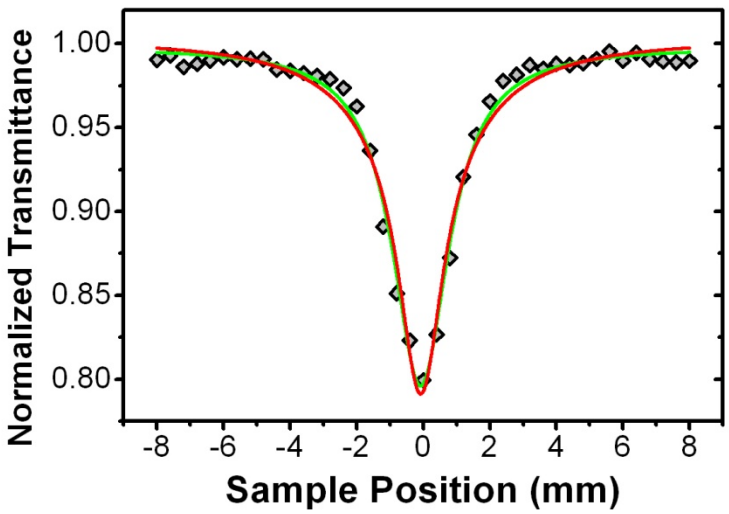

Fig. 2.15. Open aperture Z-scan of Rhodamine B. diamond data points show measured data, solid green curve shows fit curve using Eq. (2.178) and solid red curve shows fit curve using Eq. (2.226) with $\Delta\Phi_0(0) = 0$. A q_0=0.9 was extracted from both fitting curves.

Fig. 2.16 shows closed aperture Z-scan normalized transmittance at the presence of absorptive nonlinearities. Figure (a) shows how 2PA influences the transmittance and figure (b) indicate the effect of SA on the closed aperture trace that is no longer symmetric. 2PA suppresses the peak and enhances the valley while SA produces the opposite effect.

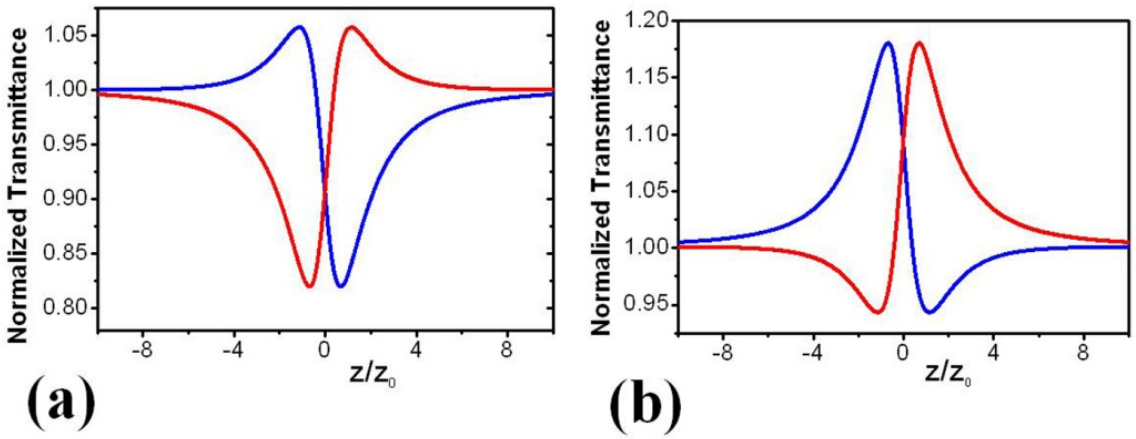

Fig. 2.16. Close aperture Z-scan normalized transmittance at the presence of 2PA (a) and at the presence of SA (b). Red curves indicate positive refraction and blue curves indicate negative refraction in both figures (a) and (b).

2.4.2. Closed aperture Z-scan for fifth order nonlinearity at the presence of 3PA

Fifth order refraction and absorption were described separately in sections 2.2.2 and 2.3.3. In order to obtain the phase distortion induced by fifth order nonlinearity, in which the change in the refractive index and also the absorption coefficient are both proportional to intensity square, the following pair of differential equation must be solved.

$$\frac{d(\Delta\Phi)}{dz'} = k n_4 I^2 \tag{2.227}$$

$$\frac{dI}{dz'} = -(\alpha_0 + \alpha_3 I^2) I \tag{2.228}$$

The differential equation in (2.228) has previously been solved gave the position dependent intensity within the sample as follows

$$I(z') = \frac{\sqrt{\alpha_0}\, I(z) e^{-\alpha_0 z'}}{\sqrt{\alpha_0 + \alpha_3 I(z)^2 - \alpha_3 I(z)^2 e^{-2\alpha_0 z'}}} \tag{2.229}$$

The entire phase change due to self-lensing produced by an intense light beam, whose intensity is governed by Eq. (2.229), after propagation through a medium of length L is written as

$$\Delta\Phi(z,r,t) = k\, n_4 \int_0^L \frac{\alpha\, I(z)^2\, e^{-2\alpha_0 z'}}{\alpha_0 + \alpha_3 I(z)^2 - \alpha_3 I(z)^2\, e^{-2\alpha_0 z'}}\, dz' \tag{2.230}$$

$$\Delta\Phi(z,r,t) = \frac{k\, n_4}{2\alpha_3} \ln\left[1 + 2\alpha_3 I^2(z,r,t) \frac{\left(1 - e^{-2\alpha_0 L}\right)}{2\alpha_0}\right] \tag{2.231}$$

$$\Delta\Phi(z,r,t) = \frac{k\, n_4}{2\alpha_3} \ln\left[1 + p^2(z,r,t)\right] \tag{2.232}$$

where P has already given in Eq. (2.191)

The complex electric field exiting the sample E_e now contains the nonlinear phase distortion:

$$E_e(z,r,t) = \left| E(z,r,t) \right| e^{-i\Delta\Phi(z,r,t)} = \sqrt{\frac{2I_e(z,r,t)}{c\, n\, \varepsilon_0}}\; e^{-i\Delta\Phi(z,r,t)} \tag{2.233}$$

After substitution $I(z,r,t)$ and $\Delta\Phi(z,r,t)$ from Eq. (2.190) and (2.51) into Eq. (2.233) the exiting electric field is obtained as:

$$E_e(z,r,t) = \frac{\sqrt{\frac{2I(z,r,t)}{c\, n\, \varepsilon_0}}\; e^{-\frac{1}{2}\alpha_0 L}}{\left(1 + p^2(z,r,t)\right)^{1/4}}\; e^{-i\frac{k n_4}{2\alpha_3}\ln\left[1 + p^2(z,r,t)\right]} \tag{2.234}$$

$$E_e(z,r,t) = E(z,r,t) e^{-\frac{1}{2}\alpha_0 L} \left[1 + p^2(z,r,t)\right]^{\left(-i\frac{k n_4}{2\alpha_3} - \frac{1}{4}\right)} \tag{2.235}$$

The term $\left(1 + p^2(z,r,t)\right)^{\left(-i\frac{k n_4}{2\alpha_3} - \frac{1}{4}\right)}$ in Eq. (2.235) can be expanded using a binomial series.

$$E_e(z,r,t) = E(z,r,t)\, e^{-\frac{1}{2}\alpha_0 L} \sum_{m=0}^{\infty}\left[\frac{p^{2m}(z,r,t)}{m!}\prod_{n=0}^{m}\left(-i\frac{k\,n_4}{2\,\alpha_3}-\frac{1}{4}-n+1\right)\right] \tag{2.236}$$

$$E_e(z,r,t) = E(z,r,t)\, e^{-\frac{1}{2}\alpha_0 L} \sum_{m=0}^{\infty}\left[\frac{\left(-i\,\Delta\Psi(z,t)\right)^m}{m!}\prod_{n=0}^{m}\left(1-i\frac{(4n-3)\,\alpha_3}{2\,k\,n_4}\right)\right] e^{-4m\frac{r^2}{w(z)^2}} \tag{2.237}$$

$$\Delta\Psi(z,t) = k\,n_4\,L'_{eff}\,I(x,t)^2 \tag{2.238}$$

Eq. (2.238) would be basically identical to Eq. (2.55) if the term $\left(-i\,\Delta\Phi(z,r,t)\right)^m/m!$ is replaced by the term $\left(-i\,\Delta\Psi(z,r,t)\right)^m/m!\prod_{n=0}^{m}\left(1-i\,(4n-3)\,\alpha_3/(2\,k\,n_4)\right)$ thus, the same calculation procedure can be applied in order to obtain the electric field distribution on the aperture plane. The result in this case will be analogous to Eq. (2.72) given by

$$E_a(z,r,t) = E(z,r=0,t)\, e^{-ikd}\, e^{-\frac{1}{2}\alpha_0 L} \sum_{m=0}^{\infty}\left\{\frac{\left(-i\,\Delta\Psi(z,t)\right)^m}{m!}\times \prod_{n=0}^{m}\left(1-i\frac{(4n-3)\,\alpha_3}{2\,k\,n_4}\right)\left(\frac{w_{m0}}{w_m}\right) e^{-ik\frac{r^2}{2R_m}}\, e^{-\frac{r^2}{w_m^2}}\, e^{i\theta_m}\right\} \tag{2.239}$$

w_{m0} in Eq. (2.239) defined as follows which differs from what was defined in Eq. (2.70).

$$w_{m0}^2 = \frac{w(z)^2}{4m+1} \tag{2.240}$$

All other parameters such as d_m, θ_m, R_m and w_m (defined in Eqs. (2.67), (2.68), (2.70) and (2.71)) are rewritten with the above definition for w_{m0}.

The on-axis electric field at the aperture plane can be obtained by letting r=0 in Eq. (2.239). Furthermore, in the limit of small nonlinear phase change, only the first two terms in (2.239) need to be retained. Following such simplification and assuming CW radiation, the on-axis normalized transmittance can be written as:

$$T(z) = \frac{\left|\,E_a(z,r=0,\Delta\Psi)\right|^2}{\left|\,E_a(z,r=0,\Delta\Psi=0)\right|^2} \tag{2.241}$$

$$T(z)=\frac{\left|\dfrac{1}{g-i\dfrac{d}{d_0}}-i\Delta\Psi(z)\left(1-i\dfrac{\alpha_3}{2kn_4}\right)\dfrac{1}{g-i\dfrac{5d}{d_0}}\right|^2}{\left|\dfrac{1}{g-i\dfrac{d}{d_0}}\right|^2} \tag{2.242}$$

$$T(z)=\left(g^2+\frac{d^2}{d_0^2}\right)\left|\frac{g+i\dfrac{d}{d_0}}{g^2+\dfrac{d^2}{d_0^2}}-\frac{i\Delta\Psi(z)\left(g+i\dfrac{5d}{d_0}\right)+\Delta\Psi(z)\dfrac{\alpha_3}{2kn_4}\left(g+i\dfrac{5d}{d_0}\right)}{g^2+\dfrac{25d^2}{d_0^2}}\right|^2 \tag{2.243}$$

After lengthy calculation and neglecting the terms having $\Delta\Psi^2$, the on-axis normalized transmittance is obtained as:

$$T(z)=1+\frac{8x\Delta\Psi_0-\dfrac{1}{2}{p_0}^2(x^2+5)}{(x^2+1)^2(x^2+25)} \tag{2.244}$$

In order to extend the steady-state results to include transient effects induced by pulsed radiation the time-averaged $\langle\Delta\Psi_0(t)\rangle$ and $\langle P_0^2(t)\rangle$ must replace $\Delta\Psi_0$ and P_0^2 in Eq. (2.244). Assuming a Gaussian profile for temporal behavior of the laser pulses, the time averaged of aforementioned quantities are obtained $\langle\Delta\Psi_0(t)\rangle=\Delta\Psi_0(0)/\sqrt{3}$ and $\langle P_0^2(t)\rangle=P_0^2(0)/\sqrt{3}$.

Therefore, the on-axis normalized transmittance using temporary Gaussian pulses in the closed aperture Z-scan is given by

$$T(z)=1+\frac{8x\dfrac{\Delta\Psi_0(0)}{\sqrt{3}}-\dfrac{1}{2}\dfrac{{p_0(0)}^2}{\sqrt{3}}(x^2+5)}{(x^2+1)^2(x^2+25)} \tag{2.245}$$

where $\Delta\Psi_0(0) = k\, n_4\, L'_{eff}\, I_0(0)^2$, $p_0(0)^2 = 2\alpha_3\, L'_{eff}\, I_0(0)^2$ and $I_0(0)$ is the peak on-axis intensity at the focus.

Fitting Eq. (2.245) to the measured Z-scan data allows obtaining both parameters of the nonlinear refractive index n_4 and the 3PA coefficient α_3.

2.4.3. Closed aperture Z-scan for concurrent third and fifth order nonlinearity at the presence of two-photon absorption

The concurrent third and fifth order nonlinearity for a negligible nonlinear absorption was examined in section 2.2.3. Now, the previous results are extended to include the phase changes induced at the presence of 2PA. The phase distortion induced by concurrent third and fifth order nonlinearities changes with respect to the propagation length. It is given by

$$\frac{d\left(\Delta\Phi\right)}{dz'} = k\, n_2\, I(z') + k\, n_4\, I^2(z') \tag{2.246}$$

$$\Delta\Phi = k\, n_2 \int_0^L I(z')\, dz' + k\, n_4 \int_0^L I^2(z')\, dz' \tag{2.247}$$

where $I(z')$ is the intensity within the sample given by

$$I(z') = \frac{\alpha_0\, I(z)\, e^{-\alpha_0 z'}}{\alpha_0 + \alpha_2\, I(z) - \alpha_2\, I(z)\, e^{-\alpha_0 z'}} \tag{2.248}$$

The first term in Eq. (2.247) has already been calculated in section 2.4.1. It is given by

$$\Delta\Phi_{(n_2)} = \frac{k\, n_2}{\alpha_2} \ln\left[1 + q(z,r,t)\right] \tag{2.249}$$

The second term in Eq. (2.247) representing the contribution of the fifth order nonlinearity to the entire induced phase shift is now calculated as follows

$$\Delta\Phi_{(n_4)} = k\, n_4 \int_0^L \frac{{\alpha_0}^2\, I^2\, e^{-2\alpha_0 z'}\, dz'}{\left(\alpha_0 + \alpha_2\, I - \alpha_2\, I\, e^{-\alpha_0 z'}\right)^2} \tag{2.250}$$

$$\Delta\Phi_{(n_4)} = \frac{k\, n_4\, I}{\alpha_2}\left(1 - \frac{e^{-\alpha_0 L}}{\left(1+q(z,r,t)\right)}\right) - \frac{k\, n_4\, \alpha_0}{{\alpha_2}^2}\ln\left(1+q(z,r,t)\right) \tag{2.251}$$

Under the assumption of thin sample and applying low intensity, so that the amount inside the bracket in Eq. (2.251) tends towards zero, the first term in Eq. (2.251) can be neglected with regard to the second term. In this limit the calculation will be greatly simplified. The entire distortion arises from the third and fifth order nonlinearity is now written as

$$\Delta\Phi = \frac{k\, n_2}{\alpha_2}\ln\left(1+q(z,r,t)\right) - \frac{k\, n_4\, \alpha_0}{{\alpha_2}^2}\ln\left(1+q(z,r,t)\right) \tag{2.252}$$

$$\Delta\Phi = \ln\left(1+q(z,r,t)\right)\left(\frac{k\, n_2}{\alpha_2} - \frac{k\, n_4\, \alpha_0}{{\alpha_2}^2}\right) \tag{2.253}$$

At the presence of two-photon absorption, the complex electric field on the exiting surface of a sample of length L is given by

$$E_e(z,r,t) = \frac{E(z,r,t)\, e^{-\frac{\alpha_0 L}{2}}}{\left(1+q(z,r,t)\right)^{1/2}} e^{-i\Delta\Phi} \tag{2.254}$$

$$E_e(z,r,t) = E(z,r,t)\, e^{-\frac{\alpha_0 L}{2}} \left(1+q(z,r,t)\right)^{-i\left(\frac{k\, n_2}{\alpha_2} - \frac{k\, n_4\, \alpha_0}{{\alpha_2}^2}\right) - \frac{1}{2}} \tag{2.255}$$

$$E_e(z,r,t) = E(z,r,t)\, e^{-\frac{\alpha_0 L}{2}} \sum_{m=0}^{\infty} \frac{q^m}{m!} \prod_{n=0}^{\infty} \left\{ i\left(\frac{k\, n_4\, \alpha_0}{{\alpha_2}^2} - \frac{k\, n_2}{\alpha_2} \right) - \frac{1}{2} - n + 1 \right\} \tag{2.256}$$

$$E_e(z,r,t) = E(z,r,t)\, e^{-\frac{\alpha_0 L}{2}} \sum_{m=0}^{\infty} \frac{\left(-i\,\Delta\Phi(z,r,t)\right)^m}{m!} \prod_{n=0}^{\infty} \left\{ 1 - \frac{n_4\, \alpha_0}{n_2\, \alpha_2} - i\frac{(2n-1)\,\alpha_2}{2\, k\, n_2} \right\} \tag{2.257}$$

The above equation indicates that the third and fifth order refractive and third order absorptive contributions to the Z-scan transmittance are coupled with the coupling factors of $\alpha_2 / 2\, k\, n_2$ and $n_4\, \alpha_0 / n_2\, \alpha_2$. Since Eq. (2.257) is basically similar to Eq. (2.55), the electric field distribution on the aperture plan placed in the far field can be written analogous to Eq. (2.72) as follows

$$E_a(z,r,t)=E(x=0,y=0,z,t)\,e^{-ikd}\,e^{-\frac{1}{2}\alpha_0 L}\sum_{m=0}^{\infty}\left\{\frac{\left(-i\,\Delta\Phi_0(z,t)\right)^m}{m!}\times\right.$$
$$\left.\prod_{n=0}^{\infty}\left\{1-i\frac{(2n-1)\,\alpha_2}{2k\,n_2}-\frac{n_4\,\alpha_0}{n_2\,\alpha_2}\right\}\left(\frac{w_{m0}}{w_m}\right)e^{-ik\frac{\left(x^2+y^2\right)}{2R_m}}\;e^{-\frac{\left(x^2+y^2\right)}{w_m^2}}\;e^{i\theta_m}\right\} \tag{2.258}$$

The on-axis normalized transmittance now can be calculated as follows

$$T(z)=\frac{\left|\dfrac{1}{g-i\dfrac{d}{d_0}}-i\dfrac{\Delta\Phi(z)\left(1-\dfrac{n_4\,\alpha_0}{n_2\alpha_2}-i\dfrac{\alpha_2}{2k\,n_2}\right)}{g-i\dfrac{3d}{d_0}}\right|^2}{\left|\dfrac{1}{g-i\dfrac{d}{d_0}}\right|^2} \tag{2.259}$$

After a very lengthy calculation, on-axis the normalized transmittance on-axis is obtained as

$$T(z)=1+\frac{4\,\Delta\Phi_0\,x-4\,\alpha\,L\dfrac{\Delta\Psi_0}{q_0}\,x-q_0\,(x^2+3)}{(x^2+1)(x^2+9)} \tag{2.260}$$

2.5. Z-scan with astigmatic and elliptical beams

2.5.1. Closed aperture Z-scan for cubic nonlinearity using astigmatic and elliptical beams

So far the calculations were restricted to circular Gaussian beams with identical beam waist radius in both orthogonal directions *x* and *y* in the plane normal to the propagation direction. Such a circular Gaussian beam has only one beam waist position. An astigmatic Gaussian beam has two separated waist positions with two distinct spot sizes. Therefore, in each waist position the beam radius is minimized only in one direction [35]. Several lasers, such as mode locked lasers, frequency doubled lasers, semiconductor lasers and also lasers having astigmatic cavity (a cavity whose mirrors possess different curvature radius in *x*-*z* and *y*-*z* planes) emit astigmatic

beams. Also focusing a circular Gaussian beam by a cylindrical lens results in an astigmatic beam [36]. Fig. 2.17 shows the beam radius in both x and y directions of a 5 mm radius circular beam focused by a lens with 100 mm and 100.6 mm focal length in x and y directions. This non-spherical lens makes the focused beam astigmatic, which leads to a beam waist separation of 0.6 mm and also a strong ellipticity of about 6 at the both focal points (w_{0x}=5.1 μm and w_{0y}=30.4 μm at the position z=100 mm away from the lens, w_{0x}=30.4 μm and w_{0y}=5.1 μm at a distance of 100.6 mm away from the lens) assuming a 800 nm wavelength for the laser radiation. As can be seen from Fig. 2.17, the beam cross section becomes circular between the two beam waist positions with a beam radius of 15.8 mm. This corresponds, however, not to the smallest spot size.

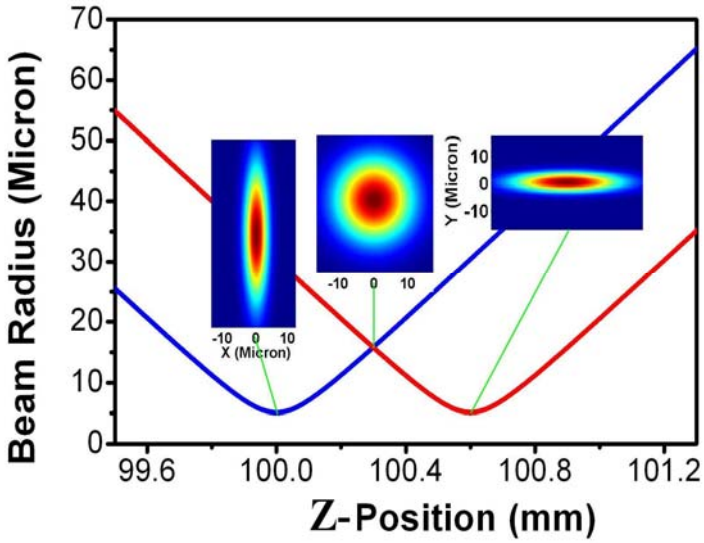

Fig. 2.17. Beam radius versus z position measured with respect to the lens. Blue curve shows the beam radius in x direction and red curve shows the beam radius in y direction.

An elliptical beam is a beam whose radius in directions x and y are not equal. If such a beam is focused by a spherical lens the beam radius in both x and y directions are simultaneously minimized such that only one waist is observed. The beam cross section at the waist is also elliptical but with a 90 degree rotation with suspect to the beam cross section on the focusing lens; the bigger beam radius on the lens, the smallest beam waist radius is created. Fig. 2.18 shows how the cross section of an elliptical beam changes first to a circular beam and then to an elliptical beam at the waist. The ellipticity of the beam at the waist position is the same as that on the focusing lens.

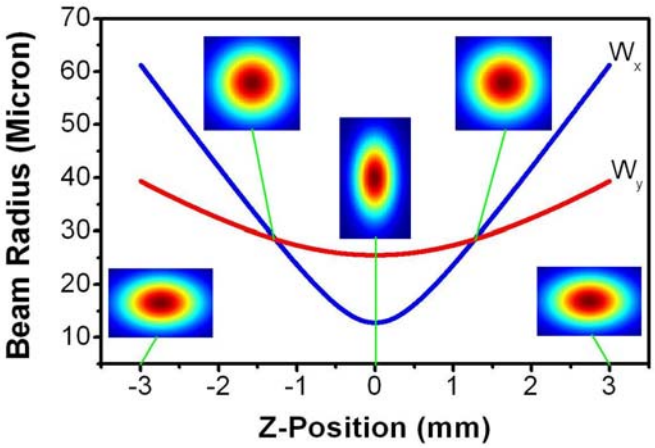

Fig. 2.18. Beam radius in both x and y direction of an elliptical beam with w_x=4mm and w_y=2 mm focused with a 200 mm focal length spherical lens.

As derived in previous sections, the following is a possible solution of the Helmholts equation for the paraxial approximation.

$$E(r) = \frac{A}{z}\exp\left(-i\,k\,z - \frac{i\,k}{2\,z}(x^2 + y^2)\right) \tag{2.261}$$

If the parameter z is replaced by $\sqrt{((z-z_x)+iz_{0x})((z-z_y)+iz_{0y})}$, Eq. (2.261) is still a solution for Helmholtz equation but with entirely different characteristic. z_x and z_y are the beam-waist positions in the x-z and y-z planes [46].

$$E(r,z,t) = E_0(t)\sqrt{\frac{w_{0x}}{w_x(z)}\frac{w_{0y}}{w_y(z)}}\; e^{i\phi}\, e^{-ikz}\, e^{-ik\frac{x^2}{2R_x(z)}}\, e^{-\frac{x^2}{w_x(z)^2}}\, e^{-ik\frac{y^2}{2R_y(z)}}\, e^{-\frac{y^2}{w_y(z)^2}} \tag{2.262}$$

where

$$w_{x,y}(z)^2 = w_{0x,0y}^2\left(1 + \frac{(z-z_{x,y})^2}{z_{0x,0y}^2}\right) \tag{2.263}$$

$$R_{x,y}(z) = (z-z_{x,y}) + \frac{z_{0x,0y}^2}{(z-z_{x,y})} \tag{2.264}$$

$$\phi = \frac{1}{2} tag^{-1}\left(\frac{z - z_x}{z_{0x}}\right) + \frac{1}{2} tag^{-1}\left(\frac{z - z_y}{z_{0y}}\right) \tag{2.265}$$

$$z_{0x,0y} = \frac{k\, w_{0x,0y}^2}{2} \tag{2.266}$$

Here $w_{x,y}(z)$ and $R_{x,y}$ (z) are the beam radius and the wavefront curvature radius in x and y directions that are orthogonal to each other and also normal to the beam propagation direction z and $\varphi(z)$ is the phase of the elliptical beam. The beam waist radiuses are denoted by $w_{0x,0y}$. The Rayleigh ranges in x and y directions are denoted by $z_{0x,0y}$ and related to the beam waist radius through Eq. (2.266). E_0(t) contains all temporal behavior of the electric field. The z axis and its increasing direction are assumed parallel with the beam propagation direction with an origin located on the focusing lens position [34].

If the thickness of the medium, through which the Gaussian beam is propagating, is small enough so that changes in the beam diameter within the medium due to diffraction or nonlinear refraction can be neglected the medium is regarded as thin sample. Under this criterion the dielectric field amplitude changes only due to absorption and its phase changes due to nonlinear refraction. In this case the amplitude and the phase of the electric field as a function of z' (coordinate within the sample) are governed by the following pair of equations:

$$\frac{d(\Delta\Phi)}{dz'} = k\,\Delta n(I) \tag{2.267}$$

$$\frac{dI}{dz'} = -\alpha(I)\, I \tag{2.268}$$

In the case of cubic nonlinearity and negligible nonlinear absorption $\Delta n(I)$ changes linearly with intensity and $\alpha(I)$ remains as a constant referred to as the linear absorption coefficient α_0. Now, the differential equations (2.267) and (2.268) can be solved to find the nonlinear phase shift at the exit surface of sample. For the case of negligible nonlinear absorption the Eq. (2.268) is rewritten as:

$$\frac{dI}{dz'} = -\alpha_0\, I \tag{2.269}$$

$$I(z') = I(z)\, e^{-\alpha_0 z'} \tag{2.270}$$

where z is the sample position.

By knowing the intensity within the sample now the phase change can be obtained from the following

$$\frac{d(\Delta\Phi)}{dz'} = k\, n_2\, I(z') = k\, n_2\, I(z)\, e^{-\alpha_0 z'} \tag{2.271}$$

After integration over z' for the whole length of the sample the entire phase change is obtained as:

$$\Delta\Phi = k\, n_2\, I(z) \int_0^L e^{-\alpha_0 z'}\, dz' \tag{2.272}$$

$$\Delta\Phi(x, y, z, t) = k\, n_2\, L_{eff}\, I(x, y, z, t) \tag{2.273}$$

where the effective length of the sample L_{eff} is defined as follows:

$$L_{eff} = \left(\frac{1 - e^{-\alpha_0 L}}{\alpha_0} \right) \tag{2.274}$$

where α_0 is the linear absorption coefficient and L is the physical length of the sample.

The spatial intensity distribution can be separated in two terms as function of radial (x and y) and longitudinal (z) components.

$$\Delta\Phi(x, y, z, t) = k\, n_2\, L_{eff}\, I(z, t)\, e^{-2\frac{x^2}{w_x(z)^2}}\, e^{-2\frac{y^2}{w_y(z)^2}} \tag{2.275}$$

The relationship between power and intensity for an elliptical Gaussian beam can be written analogous to that for a circular Gaussian beam.

$$I(z, t) = \frac{2\,\mathrm{P}(t)}{\pi\, w_x(z)\, w_y(z)} \tag{2.276}$$

$$\Delta\Phi(x,y,z,t) = k\, n_2\, L_{eff} \left(\frac{2\,\mathrm{P}(t)}{\pi\, w_{0x}\, w_{0y}} \right) e^{-2\frac{x^2}{w_x(z)^2}}\, e^{-2\frac{y^2}{w_y(z)^2}} \times \left(\frac{1}{\sqrt{\left(1+\frac{(z-z_x)^2}{z_{0x}^2}\right)\left(1+\frac{(z-z_y)^2}{z_{0y}^2}\right)}} \right) \tag{2.277}$$

Therefore, the phase shift of the electric field at the exiting plane of the sample is:

$$\Delta\Phi(x,y,z,t) = \Delta\Phi_0(z,t)\, e^{-2\frac{x^2}{w_x(z)^2}}\, e^{-2\frac{y^2}{w_y(z)^2}} \tag{2.278}$$

where

$$\Delta\Phi_0(z,t) = \Delta\Phi_0(t) \left(\frac{1}{\sqrt{\left(1+\frac{(z-z_x)^2}{z_{0x}^2}\right)\left(1+\frac{(z-z_y)^2}{z_{0y}^2}\right)}} \right) \tag{2.279}$$

$$\Delta\Phi_0(t) = k\, n_2\, L_{eff} \left(\frac{2\,\mathrm{P}(t)}{\pi\, w_{0x}\, w_{0y}} \right) \tag{2.280}$$

one must note that $2\,\mathrm{P}(t)/(\pi w_{0x}\, w_{0y})$ is not the on-axis intensity at the focus hence, $\Delta\Phi_0(t)$ cannot be considered as the on-axis phase shift at the focus because there are two beam waists at two different *z* position.

The complex electric field exiting the sample of length L containing two terms representing linear absorption and nonlinear refraction can be written as

$$E_{exit}(x,y,z,t) = E(x,y,z,t)\, e^{-\frac{1}{2}\alpha_0 L}\, e^{-i\,\Delta\Phi(x,y,z,t)} \tag{2.281}$$

The nonlinear phase-change of the electric field can be expanded by means of the Taylor series expansion given by

$$e^{-i\Delta\Phi(x,y,z,t)} = \sum_{m=0}^{\infty} \frac{\left[-i\Delta\Phi(x,y,z,t)\right]^m}{m!} \tag{2.282}$$

$$e^{-i\Delta\Phi(x,y,z,t)} = \sum_{m=0}^{\infty} \frac{\left[-i\Delta\Phi_0(z,t)\right]^m}{m!} e^{-2m\frac{x^2}{w_x(z)^2}} e^{-2m\frac{y^2}{w_y(z)^2}} \tag{2.283}$$

After substitution of $e^{-i\Delta\Phi(x,y,z,t)}$ from Eq. (2.283) into Eq. (2.281) the electric field exiting the sample is obtained as:

$$E_{exit}(x,y,z,t) = \sum_{m=0}^{\infty} \left\{ E_0(t) \sqrt{\frac{w_{0x}}{w_x(z)} \frac{w_{0y}}{w_y(z)}}\, e^{-ikz} e^{i\phi} e^{-\frac{1}{2}\alpha_0 L} \times \right.$$
$$\left. e^{-ik\frac{x^2}{2R_x(z)}} e^{-ik\frac{y^2}{2R_y(z)}} \frac{\left[-i\Delta\Phi_0(z,t)\right]^m}{m!} e^{-\frac{x^2}{\left(w_x(z)^2/2m+1\right)}} e^{-\frac{y^2}{\left(w_y(z)^2/2m+1\right)}} \right\} \tag{2.284}$$

Eq. (2.284) represent a summation of infinite number of Gaussian beams where the beam radius of the m^{th} beam is $w(z)/\sqrt{2m+1}$.

The propagation of each individual Gaussian beam through free space between the sample and the aperture plane is governed by the Huygens integral where the input plane is the exit surface of sample and the output plane is the aperture plane at the distance of d away from the sample.

All those Gaussian beams in summation (2.284) are composed and superposed on the aperture plane to reconstruct the beam. Therefore, like in Eq. (2.72) the complex electric field on the aperture plane is given by

$$E_a(z,r,t) = E(x=0,y=0,z,t) e^{-ikd} e^{-\frac{1}{2}\alpha_0 L} \sum_{m=0}^{\infty} \left\{ \frac{\left(-i\Delta\Phi_0(z,t)\right)^m}{m!} \times \right.$$
$$\left. \sqrt{\frac{w_{m0x}}{w_{mx}} \frac{w_{m0y}}{w_{my}}}\, e^{-ik\frac{x^2}{2R_{mx}}} e^{-ik\frac{y^2}{2R_{my}}} e^{-\frac{x^2}{w_{mx}^2}} e^{-\frac{y^2}{w_{my}^2}} e^{i\theta_m} \right\} \tag{2.285}$$

The normalized transmittance is defined as

$$T(z)=\frac{\int_{-\infty}^{+\infty}\int_{0}^{a}\left|E_a(r,t,\Delta\Phi)\right|^2 r\,dr\,dt}{\int_{-\infty}^{+\infty}\int_{0}^{a}\left|E_a(r,t,\Delta\Phi=0)\right|^2 r\,dr\,dt} \tag{2.286}$$

The on axis electric field can be obtained by setting r=0 in Eq.(2.285) therefore, the on-axis normalized transmittance for closed aperture Z-scan using CW astigmatic laser beams is give by

$$T(z,\Delta\Phi_0)=\frac{\left|E_a(z,r=0,\Delta\Phi_0)\right|^2}{\left|E_a(z,r=0,\Delta\Phi_0=0)\right|^2} \tag{2.287}$$

In the limit of small nonlinear phase change ($\Delta\Phi_0<1$) and also far field approximation ($d >> z_0$) only the first two terms in the sum in Eq.(2.285) is adequate to be retained

$$T(z,\Delta\Phi_0)=\frac{\left|\left(\left(g_x-i\frac{d}{d_{0x}}\right)\left(g_y-i\frac{d}{d_{0y}}\right)\right)^{-\frac{1}{2}}-i\Delta\Phi_0(z)\left(\left(g_x-i\frac{3d}{d_{0x}}\right)\left(g_y-i\frac{3d}{d_{0y}}\right)\right)^{-\frac{1}{2}}\right|^2}{\left|\left(\left(g_x-i\frac{d}{d_{0x}}\right)\left(g_y-i\frac{d}{d_{0y}}\right)\right)^{-\frac{1}{2}}\right|^2} \tag{2.288}$$

$$T(z,\Delta\Phi_0)=\left|1-i\Delta\Phi_0(z)\sqrt{\frac{\left(g_x-i\frac{d}{d_{0x}}\right)\left(g_y-i\frac{d}{d_{0y}}\right)}{\left(g_x-i\frac{3d}{d_{0x}}\right)\left(g_y-i\frac{3d}{d_{0y}}\right)}}\right|^2 \tag{2.289}$$

$$T(z,\Delta\Phi_0)=\left|1-i\Delta\Phi_0(z)\sqrt{\frac{\left(g_xg_y-\frac{d^2}{d_{0x}d_{0y}}\right)\left(g_xg_y-\frac{9d^2}{d_{0x}d_{0y}}\right)+3\left(g_y\frac{d}{d_{0x}}+g_x\frac{d}{d_{0y}}\right)^2+2i\left(g_xg_y+\frac{3d^2}{d_{0x}d_{0y}}\right)\left(g_y\frac{d}{d_{0x}}+g_x\frac{d}{d_{0y}}\right)}{\left(g_xg_y-\frac{9d^2}{d_{0x}d_{0y}}\right)^2+9\left(g_y\frac{d}{d_{0x}}+g_x\frac{d}{d_{0y}}\right)^2}}\right|^2 \tag{2.290}$$

In terms of new defined parameters of $x = \frac{z - z_x}{z_{0x}}$ and $y = \frac{z - z_y}{z_{0y}}$ the normalized transmittance is written as

$$T(z,\Delta\Phi_0) = \left| 1 - i\,\Delta\Phi_0(z) \sqrt{\frac{(xy-1)(xy-9) + 3(x+y)^2 + 2i(xy+3)(x+y)}{(xy-9)^2 + 9(x+y)^2}} \right|^2 \tag{2.291}$$

$$T(z,\Delta\Phi_0) = \left| 1 - i\,\Delta\Phi_0(z) \frac{\sqrt{a+ib}}{h} \right|^2 \tag{2.292}$$

where

$$a = (xy-1)(xy-9) + 3(x+y)^2 \tag{2.293}$$

$$b = 2(xy+3)(x+y) \tag{2.294}$$

$$h = \sqrt{(xy-9)^2 + 9(x+y)^2} \tag{2.295}$$

Eq. (2.292) can be recast in the following form in order to eliminate the square root

$$T(z,\Delta\Phi_0) = \left| 1 - i\,\Delta\Phi_0(z) \frac{A+iB}{h} \right|^2 \tag{2.296}$$

$$T(z,\Delta\Phi_0) = 1 + 2\frac{\Delta\Phi_0(z)B}{h} + \left(\frac{\Delta\Phi_0(z)B}{h}\right)^2 + \left(\frac{\Delta\Phi_0(z)A}{h}\right)^2 \cong 1 + 2\frac{\Delta\Phi_0(z)B}{h} \tag{2.297}$$

The terms possessing $\Delta\Phi_0(z,t)^2$ was ignored in the above expression in the limit of $\Delta\Phi_0(z,t)$ <1.

B can be found in terms of *a* and *b.* that is

$$\sqrt{a+ib} = A + iB \Rightarrow A^2 - B^2 + 2iAB = a + ib \tag{2.298}$$

$$\begin{cases} A^2 - B^2 = a \\ 2AB = b \end{cases} \tag{2.299}$$

$$4B^4 + 4aB^2 - b^2 = 0 \tag{2.300}$$

$$B = \pm\sqrt{\frac{\sqrt{a^2+b^2}-a}{2}} \tag{2.301}$$

$$T(z) = 1 \pm 2\Delta\Phi_0(z)\sqrt{\frac{\sqrt{a^2+b^2}-a}{2h^2}} \tag{2.302}$$

$$T(z) = 1 \pm 2\Delta\Phi_0\sqrt{\frac{\sqrt{(x^2+9)(x^2+1)(y^2+9)(y^2+1)}-(x^2+3)(y^2+3)+4xy}{2(x^2+9)(x^2+1)(y^2+9)(y^2+1)}} \tag{2.303}$$

By setting $x=y$ it was verified that the above equation is converted to Eq. (2.88) which was derived for the case of a circular Gaussian beam:

$$T(z,\Delta\Phi_0) = 1 + \frac{4x\Delta\Phi_0}{\left(x^2+1\right)\left(x^2+9\right)} \tag{2.304}$$

In Fig. 2.19 red curve shows the normalized transmittance for the closed aperture Z-scan. The results are calculated assuming an elliptical beam with ellipticity of 5 (w_x=0.4 mm and w_y=2 mm) focused by a 200 mm focal length lens leading to an astigmatic beam having two separated waist position of z=181.6 mm (measured with respect to the focusing lens) with beam radius of w_{0x}=121 μm and w_y=186 μm and Rayleigh range of 57.8 mm and also z=199.96 mm with beam radius of w_x=127 μm and w_{0y}=25.4 μm and Rayleigh range of 2.55 mm. As seen from Fig. 2.19, the intensity at position z=199.96 mm (almost equal to focal length of the focusing lens) is high enough to induce self-focusing whereas on other waist position (z=181.6 mm) no beam broadening or narrowing occur since the beam spot size is quite large and thus the intensity is not high enough to induce refractive index change. A simple calculation indicates that the beam diameter at the position z=181.6 mm is 7 time larger than that on the position z=199.96 mm and thus the intensity on the position z=181.6 almost equals to 2% of that on the position z=199.96 mm.

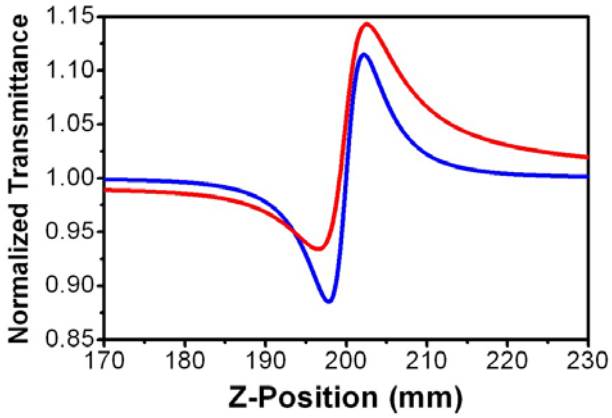

Fig. 2.19. Closed aperture Z-scan normalized transmittance. Red curve is the calculated result for closed aperture Z-scan employing an elliptical beam with beam radius on the lens of w_x=0.4 mm and w_y=2 mm focused by a 200 mm focal length lens. Blue curve is plotted for comparison using a circular beam of 2 mm beam radius focused by the same lens

The transmittance trace for a circular beam is symmetric whereas it becomes asymmetric when using an elliptical beam and becomes more asymmetric with increasing ellipticity of the laser beam [47].

Fig. 2.20 shows the normalized on-axis transmittance for closed aperture considering cubic nonlinearity using an astigmatic laser beam. A circular beam with radius of 5 mm has been focused using a non-spherical lens with focal length of f_x=200 mm and f_y=205 mm. It results in appearing two separated beam waists located at z=200 mm (measure with respect to the focusing lens) with beam radius of w_{0x}=10.2 μm and w_y=125 μm and also z=205 mm with beam radius of w_x=125 μm and w_{0y}=10.2 μm. The laser beam spot size at both waist positions are the same hence, the same refractive index change is expected to occur at both waists. As seen from Fig. 2.20, the same transmittance change occurs while passing both beam waist positions. The laser beam spot is circular at the position z=202.5 (middle of two beam waists) with a radius of 63 μm. The transmittance traces are not symmetric when scanning the sample though the either waist positions. The reason is that the beam radius does not increase identically when scanning away from the beam waist position in positive or negative z direction.

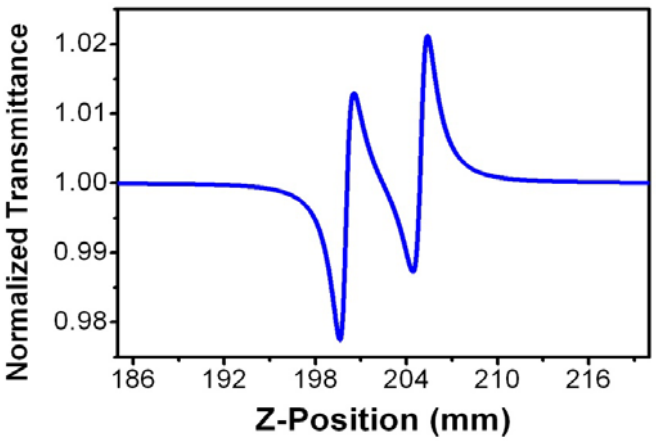

Fig. 2.20. Normalized transmittance for closed aperture Z-scan using an astigmatic beam resulting from focusing of a circular beam of radius 5 mm by a non-spherical lens with 200 mm and 205 mm focal length in orthogonal direction of x and y normal to the optical axis. It is calculated assuming $\Delta\Phi_0$=1.

While scanning a sample with a positive nonlinearity in the beam propagation direction through the beam waist, beam broadening and narrowing resulted from refractive index change leads to first decreasing and then increasing the transmittance (negative nonlinearity gives rise to an opposite configuration). This suggests that there is a zero-crossing as the sample passes the beam waist position. It means that the beam size on the aperture plane and thus the transmittance is the same as in the linear regime. This occurs due to cancelling of beam broadening by beam narrowing because the beam waist located in the middle of the sample. Using a circular laser beam in the closed aperture Z-scan experiment leads to appearing only one null whereas two or three nulls occur in case of employing astigmatic beam. The reason is that a circular beam has only one waist whereas an astigmatic beam has two waists.

The position of nulls can be found by letting T(z)=1 in Eq. (2.303).

$$T(z)=1 \Rightarrow \sqrt{\frac{\sqrt{(x^2+9)(x^2+1)(y^2+9)(y^2+1)}-(x^2+3)(y^2+3)+4xy}{2(x^2+9)(x^2+1)(y^2+9)(y^2+1)}}=0$$
$$\Rightarrow \; y=-x \quad \text{or} \quad y=\frac{-3}{x} \tag{2.305}$$

For the case of $y = -x$ the null occurs at:

$$y=-x \Rightarrow \frac{z-z_x}{z_{0x}}=-\frac{z-z_y}{z_{0y}}$$
$$z_{null}=\frac{z_x z_{0y}+z_y z_{0x}}{z_{0y}+z_{0x}} \tag{2.306}$$

Note that for the case of a circular Gaussian beam where z_x=z_y and z_{0x}=z_{0y} the null position is obtained as z_{null}= z_x=z_y indicating that the null occurs at the focal point as expected for a circular beam. The second case in Eq. (2.305) (y=-3/x) implies that one or even two more nulls can happen.

$$y = -\frac{3}{x} \Rightarrow \left(\frac{z - z_x}{z_{0x}} \right)\left(\frac{z - z_y}{z_{0y}} \right) = -3$$
$$z_{null} = \frac{1}{2}\left((z_x + z_y) \pm \sqrt{(z_x - z_y)^2 - 12\, z_{0x}\, z_{0y}} \right) \tag{2.307}$$

Eq. (2.307) gives two null positions occurring for an astigmatic beam only provided that the term under radical is greater than zero (or at least equal to zero that implies occurring only one null). Two nulls obtained from Eq. (2.307) are equidistant from the midpoint of two beam waists. For instance, three nulls are seen in Fig. 2.20 that are calculated from Eq. (2.306) as z_{null} = 202.44 mm and from Eq. (2.307) as z_{null} = 200.11 mm and z_{null} = 204.89 mm. It can be concluded that the Z-scan signature for an astigmatic beam may contain an additional peak and valley as shown in Fig. 2.20. It can also be verified that the null positions obtain from the above equation for a circular beam are coincident with the focal point of the focused laser beam.

2.5.2. Open aperture Z-scan for cubic nonlinearity using astigmatic and elliptical beams

In this section, the open aperture Z scan transmittance at the presence of 2PA is derived assuming an astigmatic laser beam. Here the intensity on the exit surface of the sample as a function of incident intensity is still governed by Eq. (2.156) although the distribution is no longer circularly symmetric.

$$I_e(x,y,z,t) = \frac{I(x,y,z,t)\, e^{-\alpha_0 L}}{1 + q(x,y,z,t)} \tag{2.308}$$

The radial intensity distribution on the x-y plane for an astigmatic beam is given by

$$I(x,y,z,t) = I_0(z,t)\, e^{-2\frac{x^2}{w_x(z)^2}}\, e^{-2\frac{y^2}{w_y(z)^2}} \tag{2.309}$$

In order to simplify the calculation, the coordinate system can be changed from Cartesian coordinate to polar coordinate. In the new coordinate

$$I(z,r,\theta,t) = I_0(z,t)\, e^{-2r^2 f(z,\theta)} \tag{2.310}$$

And

$$q(z,r,\theta,t)=q_0(z,t)e^{-2r^2 f(z,\theta)} \tag{2.311}$$

where

$$f(z,\theta)=\frac{\cos(\theta)^2}{w_x(z)^2}+\frac{\sin(\theta)^2}{w_y(z)^2} \tag{2.312}$$

The laser power exiting the sample is obtained by the surface integration of intensity as follows:

$$\mathrm{P}_{\mathrm{exit}}(z,t)=\int_0^{2\pi}\int_0^{r} I_e(z,r,\theta,t)\,r\,dr\,d\theta=\frac{e^{-\alpha_0 L}}{\alpha_2 L_{eff}}\int_0^{2\pi}\int_0^{r}\frac{q(z,r,\theta,t)}{1+q(z,r,\theta,t)}\,r\,dr\,d\theta \tag{2.313}$$

In order to facilitate the calculation of above double integral the differential elements can be changed as follows

$$d[q(z,r,\theta,t)]=-2f(z,\theta)q(z,r,\theta,t)r\,dr \tag{2.314}$$

Therefore, the radial integral is calculated as

$$\int_0^{r}\frac{q(z,r,\theta,t)}{1+q(z,r,\theta,t)}r\,dr=\frac{1}{2f(z,\theta)}\ln\left(1+q_0(z,t)\right) \tag{2.315}$$

The laser power transmitted through the sample is obtained as:

$$\mathrm{P}_{\mathrm{exit}}(z,t)=\frac{\pi\,w_x(z)\,w_y(z)\,e^{-\alpha L}\ln\left(1+q_0(z,t)\right)}{2\alpha_2 L_{eff}} \tag{2.316}$$

The power in Eq. (2.316) will be exactly the same as Eq. (2.166) if $w_x(z)w_y(z)$ is replaced by $w(z)^2$ hence, a calculation analogous to that performed from Eq. (2.167) to Eq. (2.175) can be done to obtain the normalized transmittance for open aperture Z-scan at the presence of 2PA using an astigmatic laser beam. That is

$$T(z)=\sum_{n=0}^{\infty}\frac{\left(-q(z,0)\right)^n}{(n+1)^{3/2}} \tag{2.317}$$

where

$$q(z,0) = \frac{q_0}{\sqrt{\left(1+\frac{(z-z_x)^2}{z_{0x}^2}\right)\left(1+\frac{(z-z_y)^2}{z_{0y}^2}\right)}} \tag{2.318}$$

and

$$q_0 = \frac{2\alpha_2 L_{eff} \mathrm{P_{in}}}{\pi w_{0x} w_{0y}} \tag{2.319}$$

It should be reminded that the lens position is taken to be z=0 and z_x and z_y are the beam waist positions where the beam radius in x and y direction is minimized.

The beam waist radius of an elliptical beam focused by a non-spherical lens is given by the following [48].

$$w_{0x,y} = \frac{\lambda f_{x,y}}{\pi w_{x,y}} \frac{1}{\sqrt{1+\frac{f_{x,y}^2}{z_{0x,y}^2}}} \tag{2.320}$$

where $f_{x,y}$ is the focal length of the focusing lens, $w_{x,y}$ is the beam radius on the lens and $z_{0x,y}$ is the Rayleigh rang attributed to the pre-lens beam in x and y directions.

The beam waist position measured with respect to the position of the focusing lens is given by the following

$$z_{x,y} = \frac{f_{x,y}}{1+\frac{f_{x,y}^2}{z_{0x,y}^2}} \tag{2.321}$$

From Eq. (2.321) it can be seen that focusing an elliptical beam by any lens or even focusing a circular beam by a non-spherical lens leads to astigmatism in the focused beam. Z-scan transmittance of an astigmatic beam is no longer symmetric as it is for a circular beam. For comparison, in Fig. 2.21 the normalized Z-scan transmittance for an elliptical beam with radius of w_x = 0.2 mm and w_y = 0.6 mm (red curve) and a circular beam with radius of w = 0.6 mm (blue curve) are plotted assuming q_0 = 1 for both cases. Both beams are focused by a 200 mm focal length lens. The waist position of the focused circular beam is z = 196 mm and the waist positions of the focused elliptical beam are z = 196 mm and z = 76 mm.

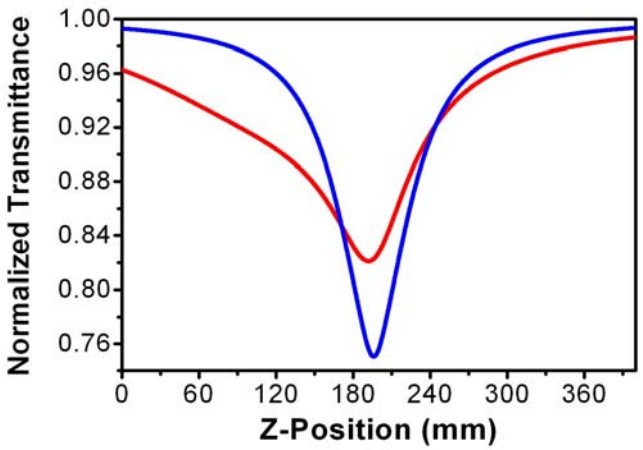

Fig. 2.21. Blue curve shows the Z-scan transmittance of a circular beam of radius 0.6 mm focused by a 200 mm focal length lens. Red curve shows the Z-scan transmittance of an elliptical beam with radiuses of w_x= 0.2 mm and w_y=0.6 mm. Both transmittance are calculated assuming q_0=1. (z_x=76 mm, z_y=196 mm, z_{0x}=97 mm and z_{0y}=28)

Chapter 3

3. Numerical integration

Numerical integration is a type of numerical computing that provides a very useful means by which, one can evaluate a numerical approximation for the value of an integral which is difficult to solve it analytically and sometimes it is even impossible to be solved analytically. For instance, Eq. (2.76) contains a two dimensional integral for calculating the normalized transmittance in a CA Z-scan measurement which is impossible to be solved unless one tends to calculate only the on-axis (r=0) transmittance under assumption of small induced phase shift ($\Delta\Phi_0$<1). Another example is Eq. (2.170) that contains an integral over infinity. only under the assumption of q_0<1 the integrant in that integral can be expanded as a power series using Taylor series expansion and then, the integral can be calculated analytically. For values of q_0 larger than one, the unique way to evaluate the value of that integral is employing numerical integration.

3.1. Intensity distribution on the far field

The phase of an intense laser beam is modulated during the propagation through a nonlinear medium due to the change in the refractive index. By recalling Eq. (2.52), the complex electric field exiting a thin sample at the absence of nonlinear absorption is given by

$$E_e(x,y,z,t) = E(x,y,z,t)e^{-\frac{1}{2}\alpha_0 L} e^{-i\Delta\Phi(x,y,z,t)} \tag{3.1}$$

where E is the electric field on the entrance plane of the medium.

$\Delta\Phi$ is the entire induced phase change during the propagation through a nonlinear medium with a length of L which can be written as

$$\Delta\Phi(r,z,t) = k\,L\,\Delta n(r,z,t) \tag{3.2}$$

The complex electric field distribution on the far field can be calculated using the Fresnel–Kirchhoff diffraction theory via the following integral.

$$E(x,y,t) = \frac{i}{\lambda d} e^{-ikd} \int_{-\infty}^{+\infty}\int_{-\infty}^{+\infty} E_e(x',y',z,t) e^{-i\frac{k}{2d}\left((x-x')^2+(y-y')^2\right)} dx'dy' \tag{3.3}$$

Then, the intensity distribution on the far field can be calculated through the following relation

$$I(x,y,t) = \frac{1}{2} c\, n_0\, \varepsilon_0 \left| E(x,y,t) \right|^2 \tag{3.4}$$

$$I(x,y,t) = I'(t) \left| \int_{-\infty}^{+\infty} \int_{-\infty}^{+\infty} e^{-ik\frac{\left(x'^2+y'^2\right)}{2R(z)}}\, e^{-i\Delta\Phi(x,y,z,t)}\, e^{-\frac{\left(x'^2+y'^2\right)}{w(z)^2}}\, e^{-i\frac{k}{2d}\left((x-x')^2+(y-y')^2\right)}\, dx'dy' \right|^2 \tag{3.5}$$

Far field condition allows one to apply Fraunhofer diffraction criteria under which the intensity distribution can be written in the polar coordinate using Bessel function as

$$I(\rho,t) = I'(z,t) \left| \int_0^{+\infty} \exp\left[-i\left(k\frac{r^2}{2d} + k\frac{r^2}{2R(z)} + \Delta\Phi(r,z,t) \right) - \frac{r^2}{w(z)^2} \right] J_0\left(\frac{k\rho r}{d} \right) r\, dr \right|^2 \tag{3.6}$$

where r is the radial coordinate on the exit plane of the medium, ρ is the radial coordinate on the observational plane, J_0 is the first kind zero-order Bessel function and $I'(z,t)$ is defined as

$$I'(z,t) = \frac{16\sqrt{\pi \ln 2}\; E_p\, e^{-\alpha_0 L}}{w_0^2\, \lambda^2\, d^2\, \tau \left(1+\frac{z^2}{z_0^2}\right)}\, e^{-4\ln 2 \frac{t^2}{\tau^2}} \tag{3.7}$$

Where E_p is the pulse energy, τ is the pulse width, w_0 is the beam waist radius, λ is the wavelength, d is the distance from the exit plane of the medium to the observational plane and z_0 is the Rayleigh range.

3.1.1. Far field intensity distribution of a Gaussian laser beam transmitted through a medium at the presence of third order nonlinearity

For the case of third order nonlinearity, the change in the refractive index is proportional to the light intensity thus the entire induced phase change in a Gaussian beam during the propagation through a nonlinear medium positioned on the coordinate of z is given by

$$\Delta\Phi(r,z,t) = k\,L\,n_2\,I(r,z,t) = \frac{k\,L\,n_2\,I_0}{1+\frac{z^2}{z_0^2}} e^{-\frac{2r^2}{w(z)^2}} e^{-4\ln 2\frac{t^2}{\tau^2}} \tag{3.8}$$

If the induced phase change is small ($\Delta\Phi_0$<1) the laser beam maintains its Gaussian profile during the propagation therefore, the far field intensity will be distributed spatially Gaussian on the observational screen. As the induced phase change increases the intensity profile on the far files screen will deviate from a Gaussian profile so that a number of concentric rings will appear.

The number of rings, the thickness of rings and also the brightness of the center of rings, that determines whether the center is dark or bright, depends on two conditions first, the sign of nonlinearity and second, the sign of the radius of the wavefront curvature. When the sign of the nonlinear refractive index in a medium is positive it is referred to as a self-focusing media in which a positive phase change is induced in the propagating laser beam. In contrast to a self-focusing media, the sign of the nonlinear refractive index in a self-defocusing media and thus the induced phase change in the propagating laser beam is negative. The sign of the radius of the wavefront curvature is defined positive for a divergent beam (a post-focal beam) and negative for a convergent beam (a pre-focal beam).

In Eq. (3.6) the phase consists of three terms. The first one is a constant, depends neither on the laser pulse energy nor the medium position. The second term is not constant as its magnitude changes while the medium is moved and its sign will be reversed as the medium passes through the focal plane. The third term depends on the medium position as well as the laser pulse energy. It is worth to be mentioned that the second and the third terms have the same sign thus it is the sum of these two phases that determines the diffraction pattern on the observation plane. Therefore, as long as the sign of the radius of wavefront curvature and the induced phase change are the same, the result of the sum of these two phases will be additive resulting in the same diffraction pattern for the following two cases [49-54].

a) A self-focusing medium (n_2>0) is exposed to a divergent beam (R>0).

b) A self-defocusing medium (n_2<0) is exposed to a convergent beam (R<0).

If the sign of the radius of wavefront curvature and induced phase change are different the result of the sum of these two phases will be subtractive but the net phase will be identical for the following two cases resulting in the same diffraction pattern.

a) A self-focusing medium (n_2>0) is exposed to a convergent beam (R<0).

b) A self-defocusing medium (n_2<0) is exposed to a divergent beam (R>0).

Our calculation reveals that when the divergent beam propagates through the self-focusing medium or the convergent beam propagates through the self-defocusing medium the far-field intensity distribution pattern is a series of thin diffraction rings with a central bright spot [51]. The calculation also indicates that when the divergent beam propagates through the self-defocusing medium or the convergent beam propagates through the self-focusing medium the

far-field intensity distribution pattern is a series of thick diffraction rings with a central brightness depending on the value of the induced phase change. If the magnitude of the induced phase change is an odd integer multiple of π the center of rings is dark whereas when the magnitude of the induced phase change is an even integer multiple of π the center of rings is bright [49].

Numerical integrations using MATLAB have been carried out in order to calculate the laser intensity distribution and the diffraction pattern on the far field. All calculation was performed under the following condition. It was assumed that a 15 mm diameter laser beam emerges from a femtolaser amplifier that produces 25 fs pulses with a central wavelength of 800 nm. This laser beam is focused using a 300 mm focal length convergent lens. Considering a beam quality factor of 2 the laser beam radius on the focal plane will be 20.4 Micron implying a Rayleigh length of 0.815 mm. The nonlinear medium was assumed 1 mm thick with a nonlinear refractive index n_2 of $5*10^{-15}$ (cm^2/W). It is positioned at the coordinate of z=±0.54 mm implying a radius of wavefront curvature of ±1.77 mm. Negative positions implies a negative radius of wavefront curvature which is the signature of a convergent beam whereas positive positions implies a positive radius of wavefront curvature which is the signature of a divergent beam. The observation plane was located at a distance of 20 cm from the focal plane fulfilling the far field criterion ($d>>z_0$).

The induced phase change can be controlled changing the laser pulse energy. The maximum (t=0) on-axis (r=0) induced phase change can be obtained through the following equation

$$\Delta\Phi(r=0,z,t=0)=k\,L\,n_2\,I((r=0,z,t=0)=8\sqrt{\frac{\ln 2}{\pi}}\;L\,n_2\,\frac{E_p}{w_0^2\,\lambda\,\tau\,(1+\frac{z^2}{z_0^2})} \qquad (3.9)$$

Calculation shows that 20 nJ pulses are capable to induce a phase change of 1π at the middle of pulse (t=0) and on the center of the beam cross section (r=0). Since the induced phase change is proportional to the laser pulse energy thus, a 2π phase change corresponds to 40 nJ pulses and so on.

Fig. 3.1 indicates the intensity distribution and the diffraction pattern on the observation plane when the nonlinear medium was located at the position of z=+0.54 mm. Figures (a) and (b) shows the intensity distribution and diffraction pattern for 20 nJ laser pulses. Figures (c) and (d) corresponds to 40 nJ pulses, (e) and (f) corresponds to 60 nJ pulses and (g) and (h) corresponds to 80 nJ pulses.

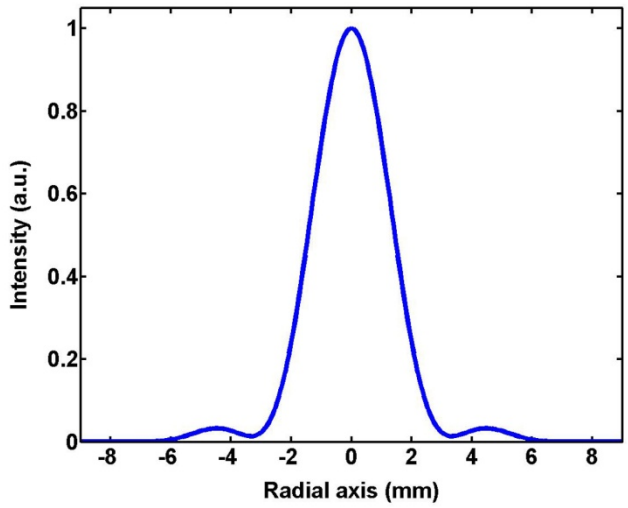

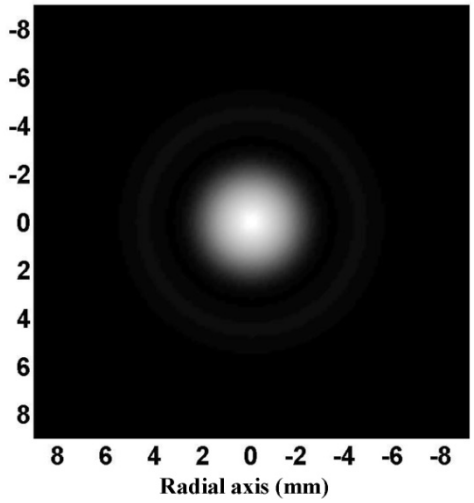

(a) $\Delta\Phi_0(z=+0.54\text{ mm}, E_p=20\text{ nJ})=1\pi$ **(b)**

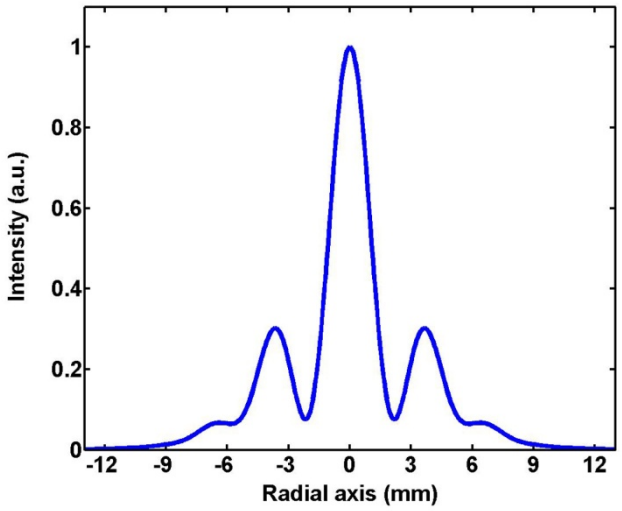

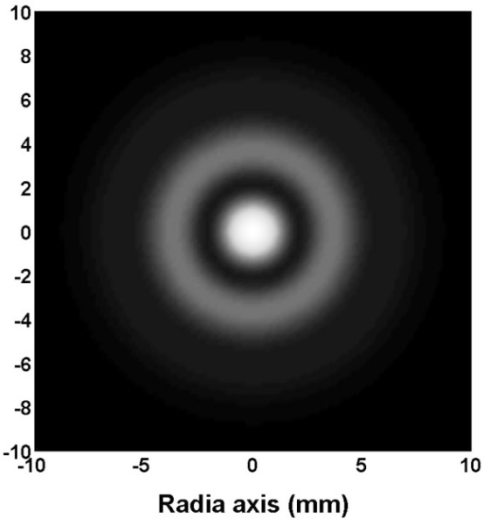

(c) $\Delta\Phi_0(z=+0.54\text{ mm}, E_p=40\text{ nJ})=2\pi$ **(d)**

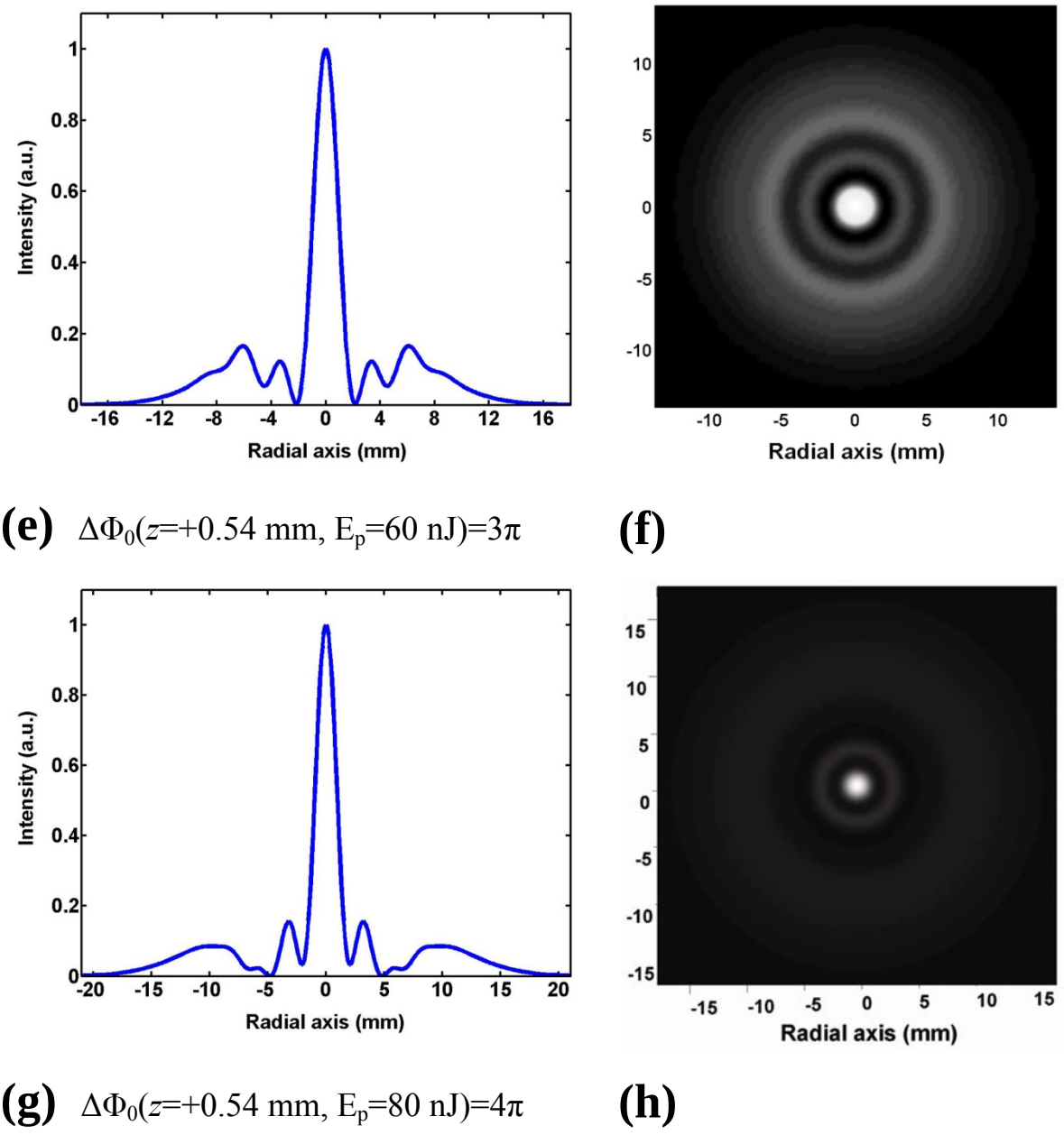

Fig. 3.1 Far field intensity distribution and diffraction pattern of a divergent beam transmitted through a self-focusing medium for different laser pulse energies corresponding to different induced phase change.

Fig. 3.1 shows that when a divergent Gaussian beam passes through a self-focusing medium the diffraction pattern has a central bright spot surrounded by less brighter concentric rings for any value of induced phase change.

Fig. 3.2 indicates the intensity distribution and the diffraction pattern on the observation plane when the nonlinear medium was located at the position of z=-0.54 mm. Figures (a) and (b) shows the intensity distribution and diffraction pattern for 20 nJ laser pulses. Figures (c) and (d)

corresponds to 40 nJ pulses, (e) and (f) corresponds to 60 nJ pulses and (g) and (h) corresponds to 80 nJ pulses.

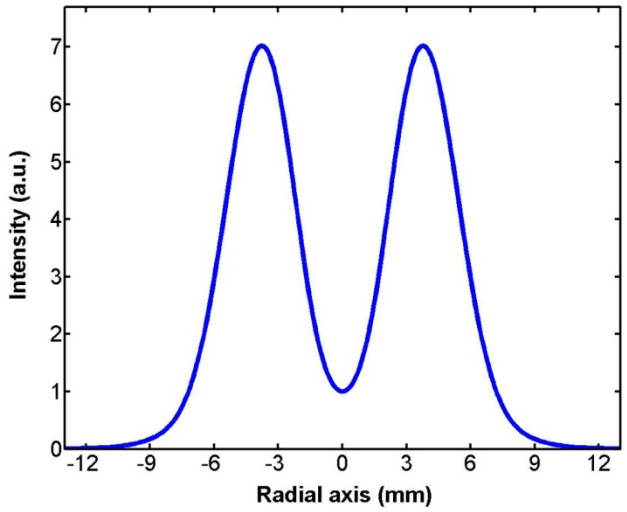

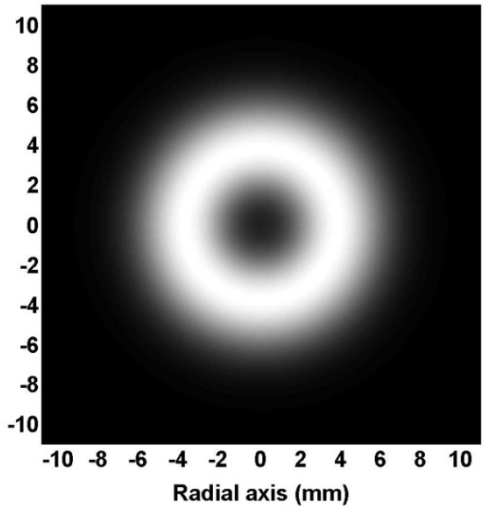

(a) $\Delta\Phi_0(z\text{=-0.54 mm}, E_p\text{=20 nJ})=1\pi$ **(b)**

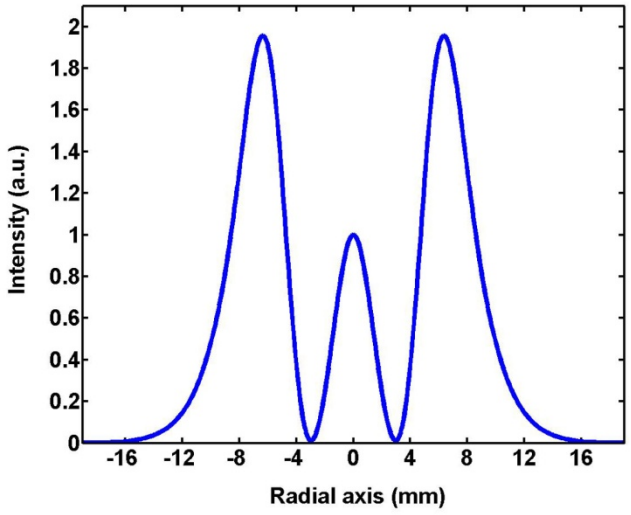

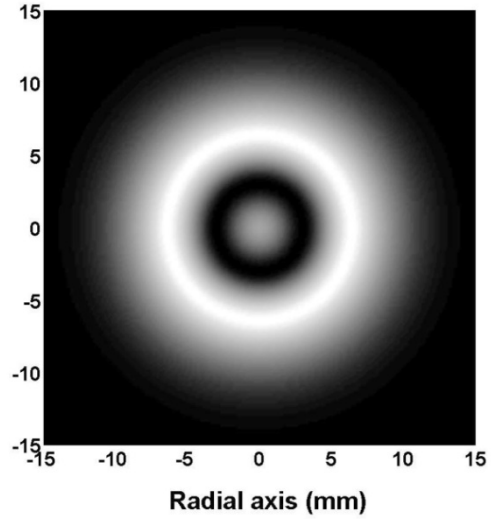

(c) $\Delta\Phi_0(z\text{=-0.54 mm}, E_p\text{=40 nJ})=2\pi$ **(d)**

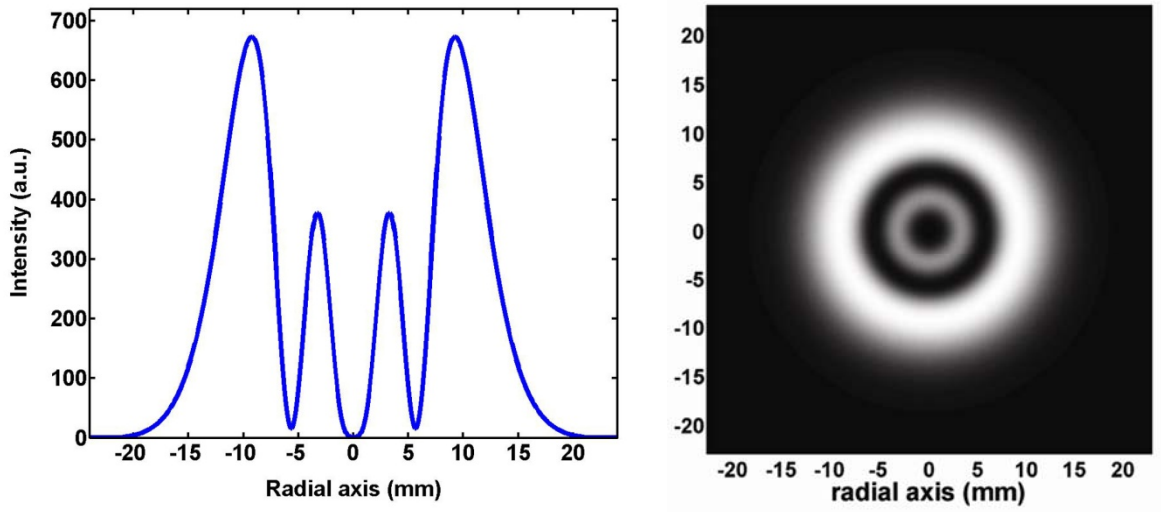

(e) $\Delta\Phi_0(z\text{=-0.54 mm}, E_p\text{=60 nJ})=3\pi$ **(f)**

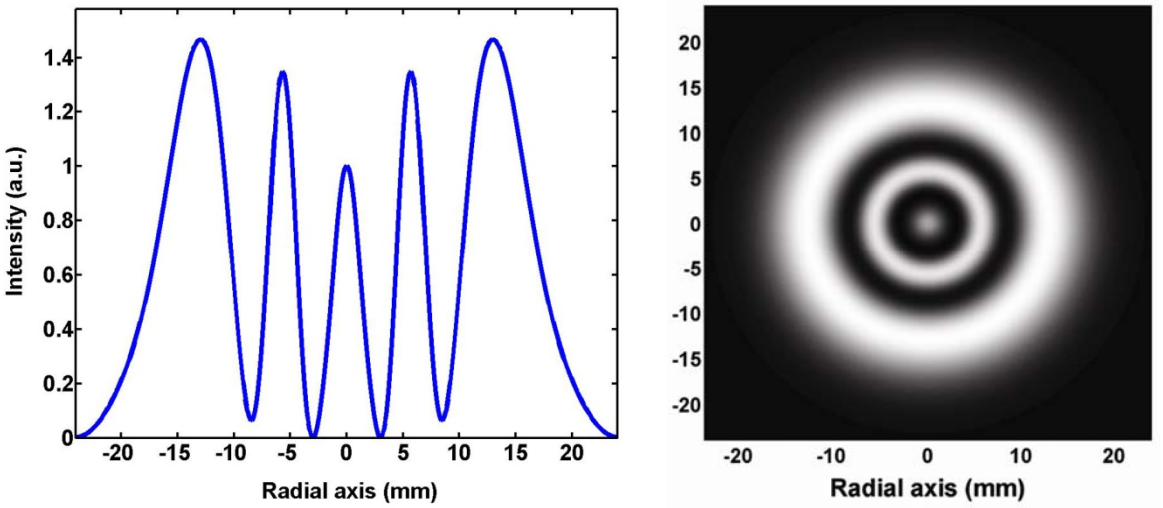

(g) $\Delta\Phi_0(z\text{=-0.54 mm}, E_p\text{=80 nJ})=4\pi$ **(h)**

Fig. 3.2 Far field intensity distribution and diffraction pattern of a convergent beam transmitted through a self-focusing medium for different laser pulse energies corresponding to different induced phase change.

Fig. 3.2 shows that when a convergent Gaussian beam passes through a self-focusing media the diffraction pattern consists of concentric rings such that the outer rings are thicker and brighter. The center of diffraction rings is dark or a less bright spot depending on the magnitude of the induced phase change.

3.1.2. Far field intensity distribution of a Gaussian laser beam transmitted through a medium at the presence of fifth order nonlinearity

Numerical computings have also performed to obtain the laser intensity distribution and diffraction pattern on the far field when a Gaussian convergent or divergent beam passes through a nonlinear medium in which the 5th order nonlinearity is the origin of refractive index change.

One should notes that at the presence of 5th order nonlinearity the change in the refractive index is proportional to intensity square thus the induced phase change is given as

$$\Delta\Phi(r,z,t) = k\,L\,n_4\,I^2(r,z,t) = \frac{k\,L\,n_4\,I_0^2}{(1+\frac{z^2}{z_0^2})^2}\,e^{-\frac{4r^2}{w(z)^2}}\,e^{-8\ln 2\frac{t^2}{\tau^2}} \tag{3.10}$$

Therefore, when the nonlinear medium is located on the position coordinate of z the maximum on-axis induced phase change in terms of pulse energy can be written as

$$\Delta\Phi(r=0,z,t=0) = \frac{32\ln 2\,L\,n_4}{\pi^2\,w_0^4\,\lambda\,\tau^2}\,\frac{E_p^2}{(1+\frac{z^2}{z_0^2})^2} \tag{3.11}$$

A nonlinear refractive index n_4 of $5*10^{-26}$ (cm^4/W^2) was assumed. The sample was located on the position coordinates of z=±1.03 mm. The radius of wavefront curvature on the z position of 1.03 mm was calculated to be 1.66 mm. All other parameters were assumed to be the same as those in previous calculation mentioned earlier. Under these conditions, the induced phase change obtained through Eq. (3.11) will be 1π for 40 nJ laser pulses, 2π for 40√2 nJ laser pulses, 3π for 40√3 nJ laser pulses and 4π for 80 nJ laser pulses.

Fig. 3.3 shows the far field diffraction pattern of a divergent Gaussian beam when passes through a self-focusing medium for different laser pulse energies. Figures (a), (b), (c) and (d) indicates the diffraction patterns when the laser pulse energies were adjusted to 40, 40√2, 40√3 and 80 nJ respectively. All diffraction patterns have a central bright spot surrounded by a number of thin and less bright rings. The number of rings increases with increasing the induced phase change.

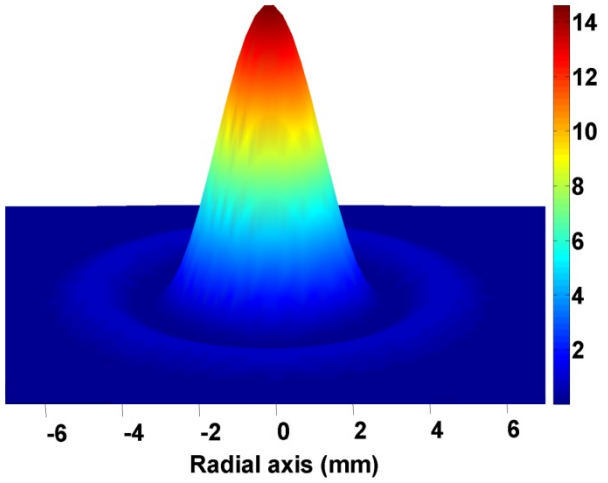

(a) $\Delta\Phi_0(z=+1.03 \text{ mm}, E_p=40 \text{ nJ})=1\pi$

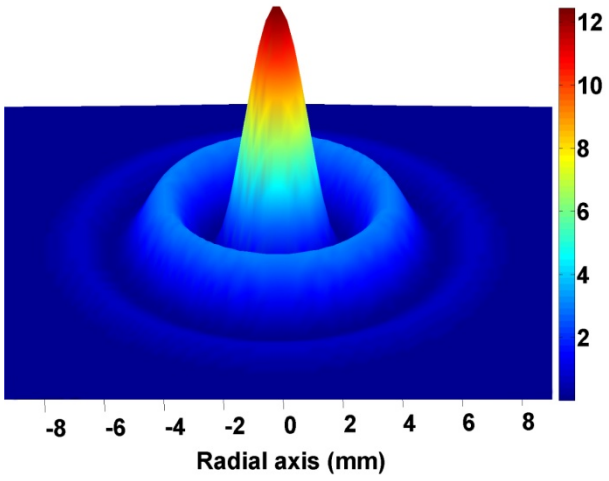

(b) $\Delta\Phi_0(z=+1.03 \text{ mm}, E_p=40\sqrt{2} \text{ nJ})=2\pi$

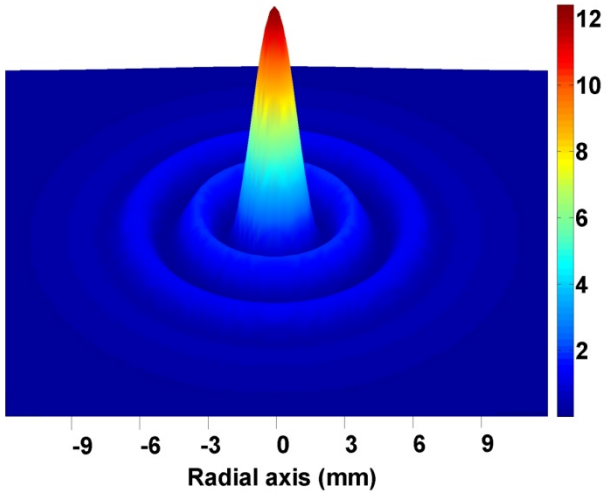

(c) $\Delta\Phi_0(z=+1.03 \text{ mm}, E_p=40\sqrt{3} \text{ nJ})=3\pi$

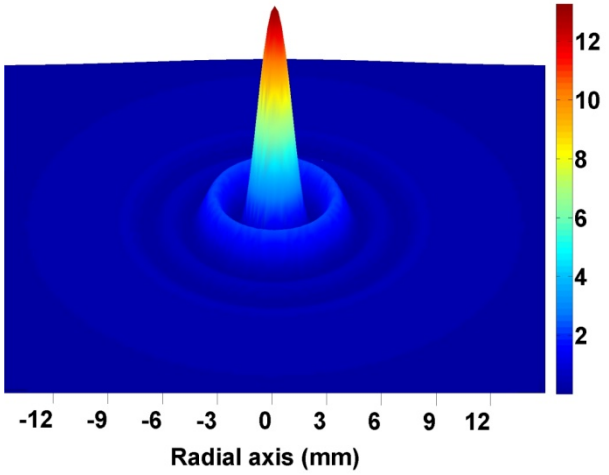

(d) $\Delta\Phi_0(z=+1.03 \text{ mm}, E_p=80 \text{ nJ})=4\pi$

Fig. 3.3 Far field diffraction pattern of a divergent Gaussian beam transmitted through a self-focusing medium at the presence of 5^{th} order nonlinearity for different pulse energies.

Fig. 3.4 shows the far field diffraction pattern of a convergent Gaussian beam when passes through a self-focusing medium for different laser pulse energies. Figures (a), (b), (c) and (d) indicates the diffraction patterns when the laser pulse energies were adjusted to 40, 40√2, 40√3 and 80 nJ respectively. As seen in Fig. 3.4 all diffraction patterns consist of a number of concentric rings. As the induced phase change increases the number of rings increases such that the outer rings are thicker.

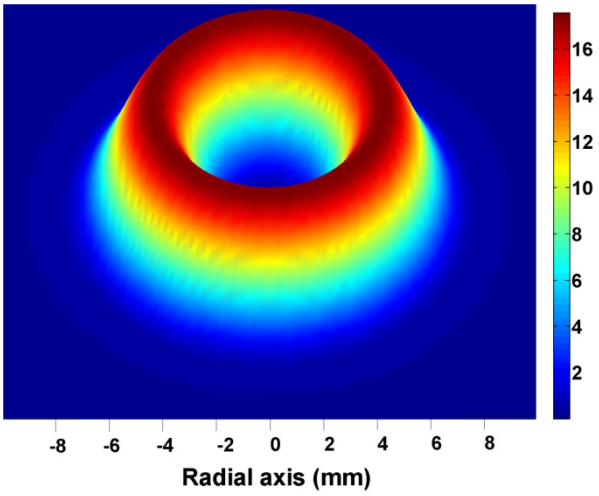

(a) $\Delta\Phi_0(z\text{=-}1.03\text{ mm}, E_p\text{=}40\text{ nJ})\text{=}1\pi$

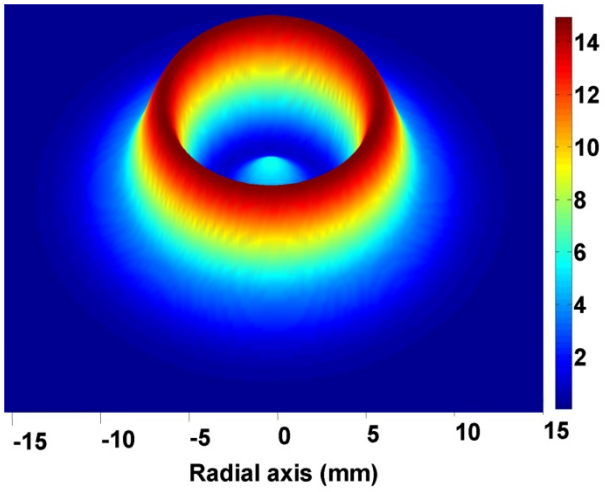

(b) $\Delta\Phi_0(z\text{=-}1.03\text{ mm}, E_p\text{=}40\sqrt{2}\text{ nJ})\text{=}2\pi$

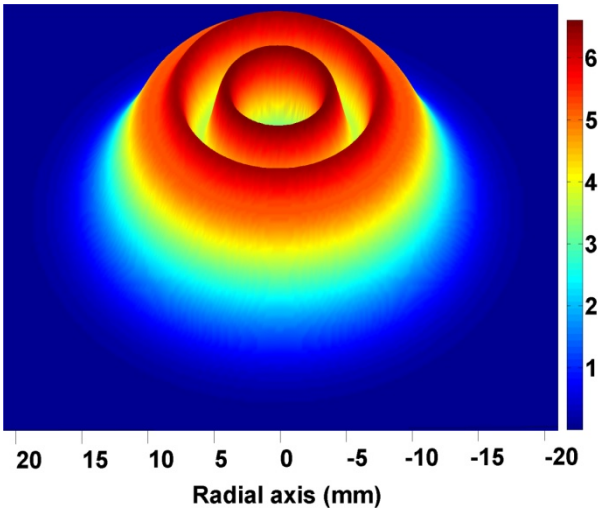

(a) $\Delta\Phi_0(z\text{=-}1.03\text{ mm}, E_p\text{=}40\sqrt{3}\text{ nJ})\text{=}3\pi$

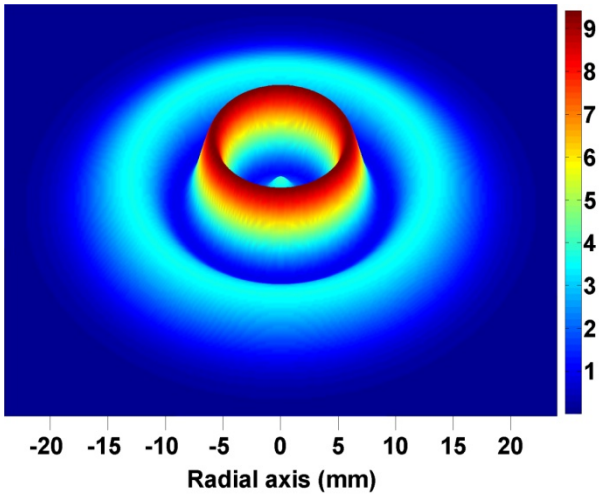

(a) $\Delta\Phi_0(z\text{=-}1.03\text{ mm}, E_p\text{=}80\text{ nJ})\text{=}4\pi$

Fig. 3.4 far field diffraction pattern of a convergent Gaussian beam transmitted through a self-focusing medium at the presence of 5th order nonlinearity for different pulse energies

3.2. Normalized transmittance in CA Z-scan set up

Normalized transmittance is defined as the quotient of the transmitted energy through the aperture at the presence of nonlinear self-lensing to the transmitted energy through the aperture at the linear regime, when the medium is far enough away from the focal plane so that the intensity is not high enough to induce phase change.

$$T_{norm}(z) = \frac{\int_{-\infty}^{+\infty} \mathrm{P}(\Delta\Phi)\, dt}{\int_{-\infty}^{+\infty} \mathrm{P}(\Delta\Phi = 0)\, dt} \tag{3.12}$$

where

$$\mathrm{P}(\Delta\Phi) = \int_0^a I(\rho, \Delta\Phi)\, 2\pi\, \rho\, d\rho \tag{3.13}$$

where a is the aperture radius and ρ is the radial coordinate on the aperture plane and $I(\rho)$ was given in Eq. (3.6).

3.2.1. Normalized transmittance at the presence of 3rd order nonlinearity

The normalized transmittance has been calculated for different aperture sizes keeping the pulse energy constant and also for different laser pulse energies keeping the aperture size constant.

The results of calculation show that the normalized transmittance highly dependents on the size of the aperture. As the size of the aperture increases the difference between the maximum transmittance and minimum transmittance will decrease. It is clear that for a large enough aperture size (comparable with the beam spot size on the aperture plane) the transmitted energy through the medium entirely passes through the aperture therefore, the transmittance will no longer be sensitive beam focusing or defocusing so that there will be no difference between transmittance in the linear and nonlinear regime. Thus, the transmittance will no longer be a function of medium position but it will remain constant as a straight line.

Fig. 3.5 shows CA normalized transmittance and transmittance peak to valley difference for different aperture size when $\Delta\Phi_0$=0.9 and Z_0=0.815 mm. The laser beam radius on the aperture plane was considered to be 5 mm thus, the transmittance of a 5mm radius aperture is 86.5%.

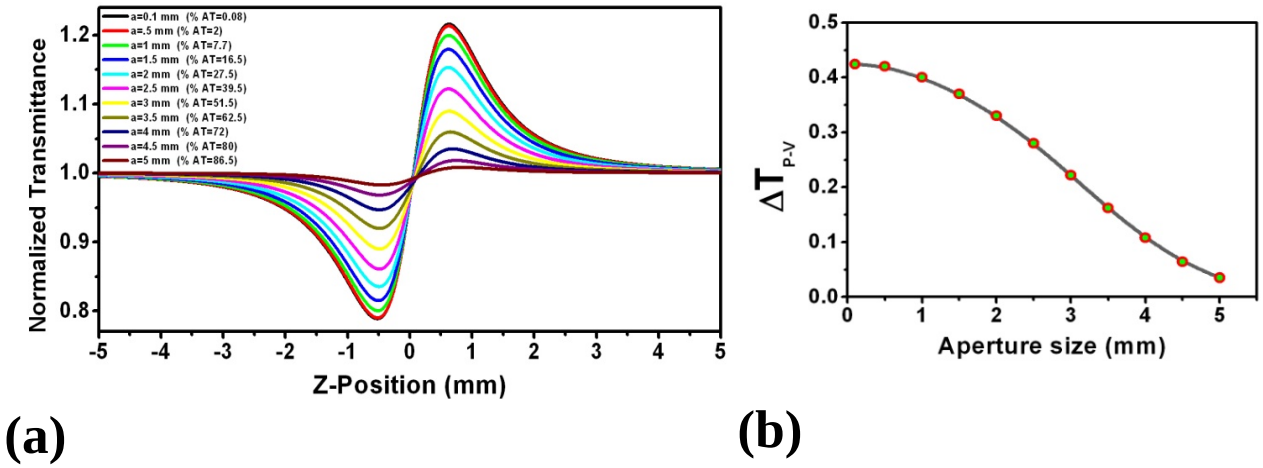

Fig. 3.5. Normalized transmittance for different size of the aperture while the laser pulse energy was kept constant

As seen in Fig. 3.5 for aperture transmittance of less than 2% the normalized transmittance has not a sharp dependence on the aperture size. Therefore, Eq. (2.88) derived for on-axis transmittance can be used for aperture transmittance of up to 2% with a considerable accuracy.

Fig. 3.6 shows CA normalized aperture measured with an aperture transmittance of 2% for different pulse energies that lead to different induced phase changes. As the pulse energy increases the effect of self-focusing grows stronger and thus leading to transmittance saturation for pre-focus positions.

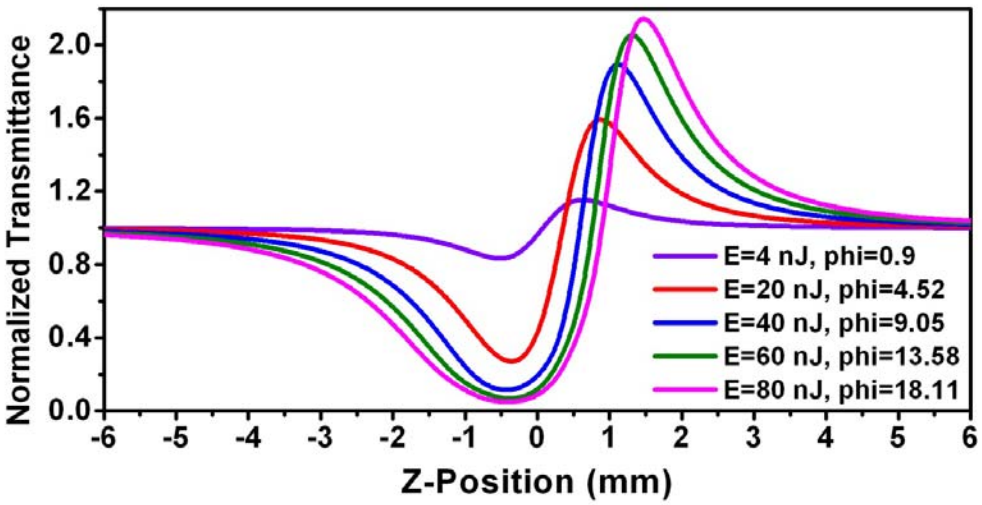

Fig. 3.6. Normalized transmittance with an aperture transmittance of 2% for different pulse energy

3.2.2. Normalized transmittance at the presence of 5rd order nonlinearity

The normalized transmittance for CA Z-scan has also been calculated assuming 5th order nonlinearity as the predominant process responsible for the self-lensing effect. The calculation revealed the same results as obtained in the case of 3rd order nonlinearity in previous section.

Fig. 3.7 shows normalized transmittance for different aperture size (keeping the pulse energy constant) and for different pulse energy (same aperture size). In Fig. 3.7 (a) the induced phase change was considered to be 1 and in Fig. 3.7 (b) the aperture transmittance was decided to be 2%. In both calculation the beam waist radius and Rayleigh range was assumed to be 20.4 μm and 0.815 mm respectively.

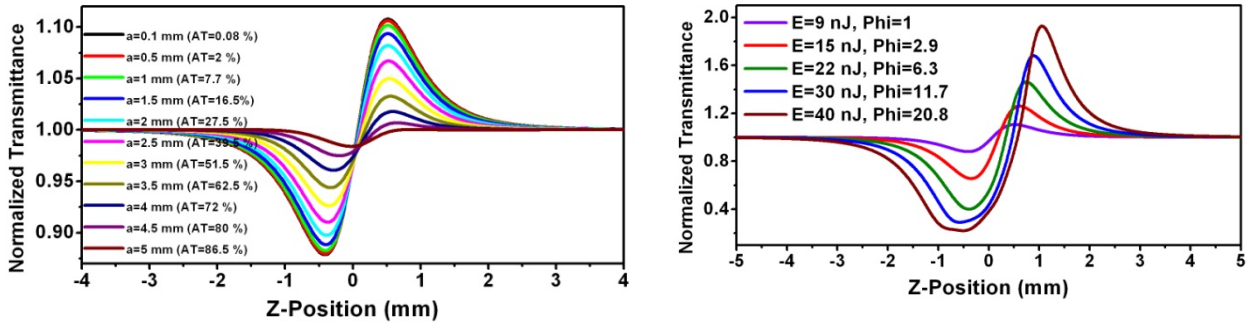

Fig. 3.7. Normalized transmittance for different aperture size ($\Delta\Phi_0$=1) (a) and for different pulse energy (AT=2%) (b)

3.3. Normalized transmittance in OA Z-scan set up

In the OA Z-scan experiment the entire transmitted energy through the nonlinear medium is collected then it is not sensitive to beam narrowing or broadening due to self-lensing effect. Eq. (3.13) and then Eq. (3.12) can be used to calculate the OA normalized transmittance considering this point that the aperture size in Eq. (3.13) should be theoretically chosen infinite. However, the results will be satisfactory when the aperture radius is decided to be √5 times of the beam radius on the aperture plane as long as the intensity profile remains Gaussian.

3.3.1 Normalized transmittance at the presence of 2PA

It is first reminded that Eq. (2.178) was derived as an approximation solution with criterion of q_0<1. Using numerical integration allows us to predict the Z-scan curves for higher absorption and even make possible to find a correction coefficient for Eq. (2.178) for q_0s higher than 1.

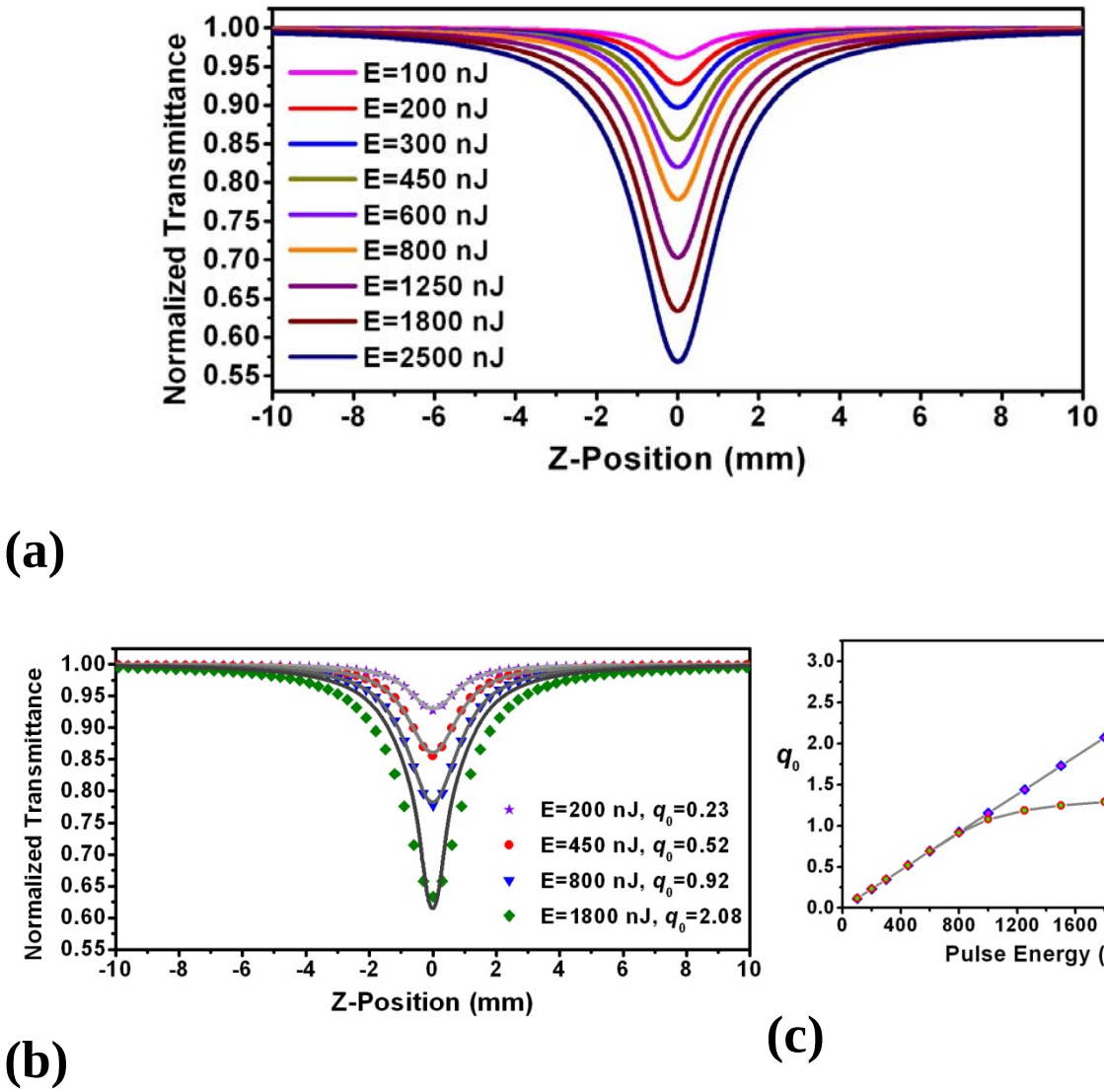

Fig. 3.8. OA Z-scans for different pulse energy (a), calculated Z-scan data along with the fit curves (b) and extracted q_0 from fit curves using Eq. (2.178) versus pulse energy (c)

In Fig. 3.8, part (a) shows the normalized transmittance in an OA Z-scan experiment at the presence of 2PA. It indicates that the transmittance decreases with increasing the pulse energy. Part (b) of Fig. 3.8 represents Z-scan data calculated via numerical integration along with the fit curves using Eq. (2.178). This figure indicates that Eq. (2.178) suitably fits with the calculated data while q_0 is less than one. However, the fit curve deviates from the calculated data as q_0 grows to values higher than one. Part (c) of Fig. 3.8 signifies that Eq. (2.178) only can be used to extract q_0s less than one since for q_0s larger than one, the difference between the extracted values from fit curves and the expected values grows as the pulse energy increases. It is also comprehended from part (c) that q_0 approaches saturation with a value of 1.5 which is the maximum extracted q_0 when the transmittance is zero.

3.3.2 Normalized transmittance at the presence of 3PA

Eq. (2.208) was derived for OA Z-scan at the presence of 3PA with criterion of p_0<1. By performing numerical integration it is feasible to calculate the normalized transmittance for any value of p_0. Fig. 3.9 (a) shows Z-scans of a 1mm thick 5th nonlinear medium using different pulse energies with pulse duration of 25 fs. The 15 mm diameter laser beam was focused using a 300 mm focal length convergent lens leading to a 20.4 μm beam waist radius and a Rayleigh length of 0.815 mm.

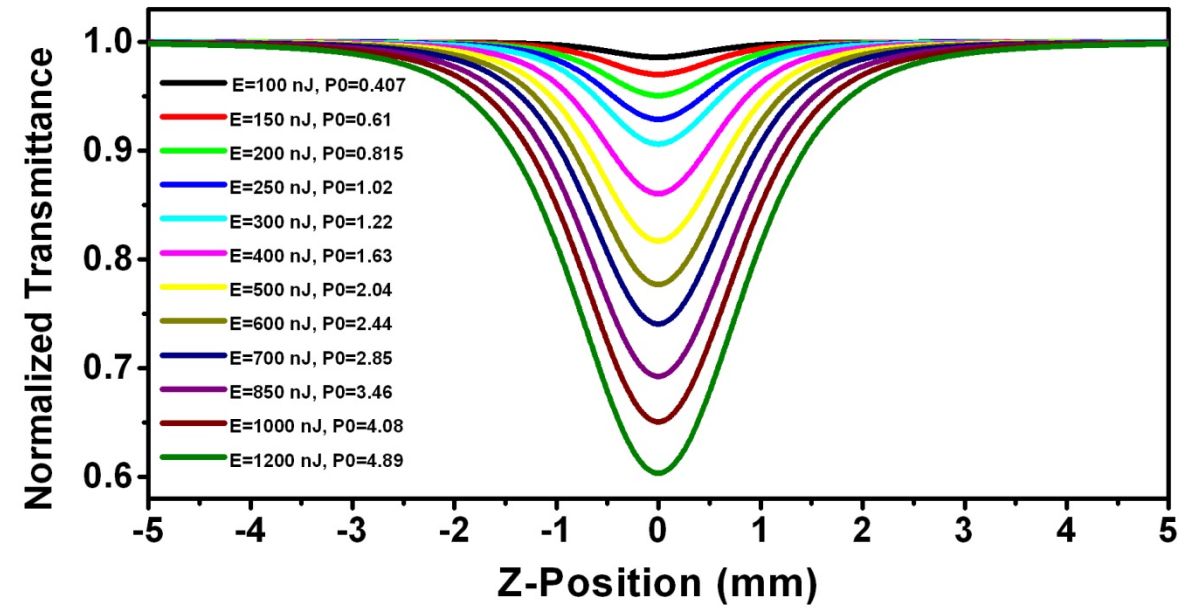

(a)

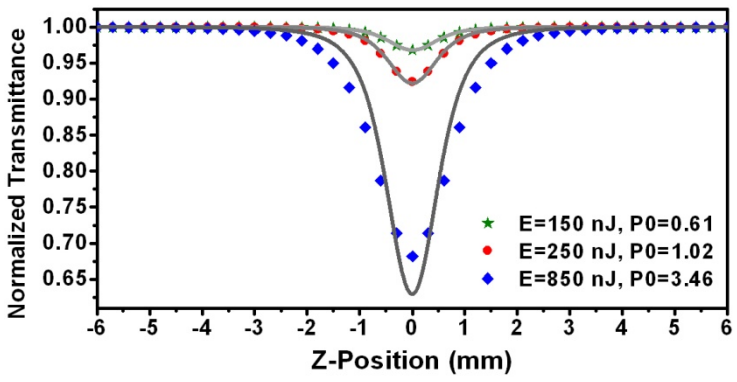

(b)

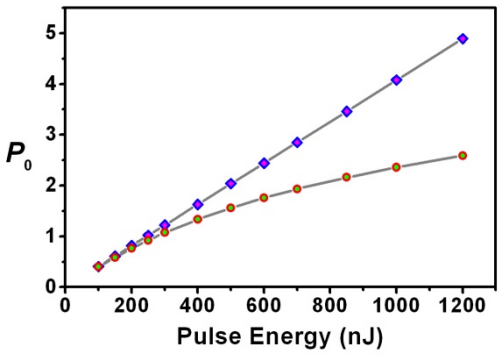

(c)

Fig. 3.9. OA Z-scans for different pulse energy (a), calculated Z-scan data along with the fit curves (b) and extracted p_0 from fit curves using Eq. (2.208) versus pulse energy (c)

In Fig. 3.9 (b) fit curves to the calculated data using Eq. (2.208) are shows for different pulse energy and correspondingly for different p_0. It is clearly seen that for p_0s less than one the fit

curves are suitably fitted to the calculated data whereas for p_0s larger than one a nice fitness cannot occur. Fig. 3.9 (c) demonstrates p_0 versus E for both expected values (square blue points) and extracted values (circle red points) from fit curves using Eq. (2.208).

It is reminded from section 4.2.2 that the analytically calculated slop of log (1-T) versus log (E) in the case of 3PA is two times larger than that in the case of 2PA. Fig. 3.10 exhibits the numerically calculated results for log (1-T) in both cases of 2PA (square blue points) and 3PA (circle red points) confirming the same conclusion as obtained from analytical calculations.

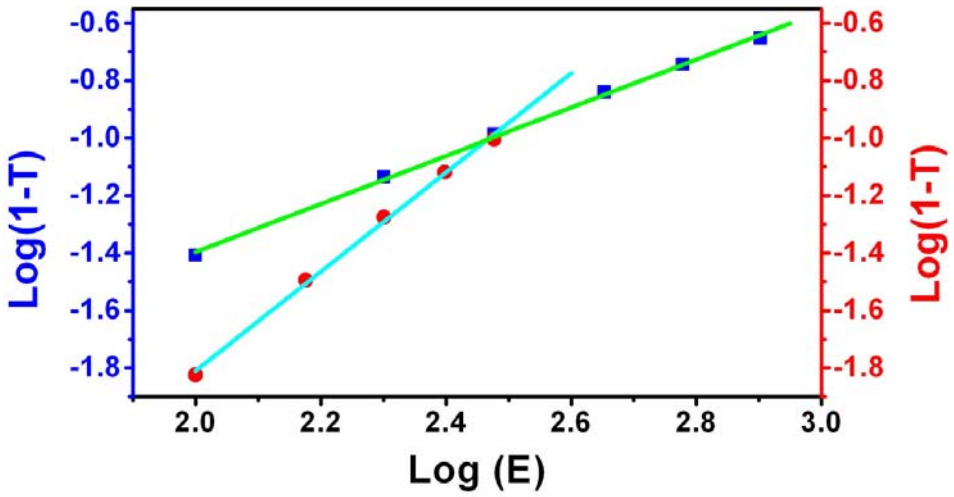

Fig. 3.10. Log (1-T) versus log (E) shows a slope of 0.85 in the case of 2PA (square blue points) and a slope of 1.72 in the case of 3PA (circle red points)

3.3.3 Normalized transmittance for different order of nonlinearity

Using integral calculations allows one to calculate the transmittance for any order of nonlinear absorption. As a demonstrating example OA Z-scan normalized transmittance for 2PA, 3PA, 4PA and 5PA have been calculated assuming the same setup and laser parameters. The absorption cross sections were chosen so that the transmittance in all cases is the same allowing us to compare the width of the Z-scan signals for different order or nonlinearity. From Fig. 3.11 it is clearly seen that the width of the signals decreases with increasing the order of nonlinearity. This is due to the higher dependence on pulse energy in higher order nonlinearity.

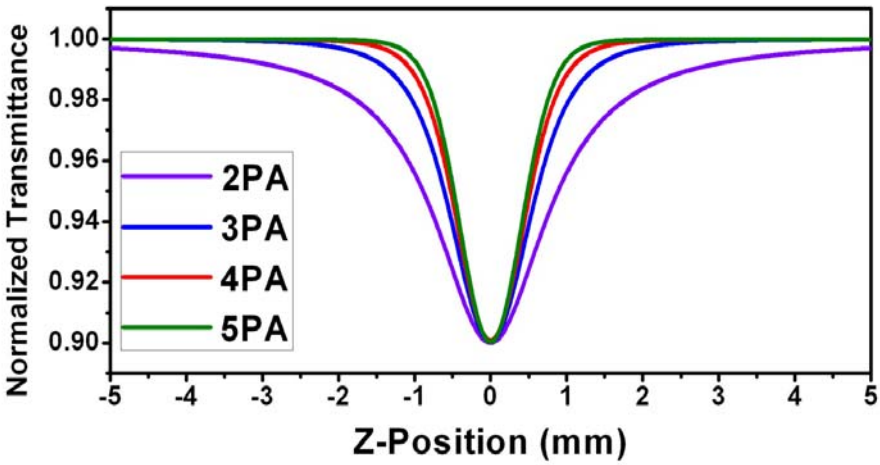

Fig. 3.11. Calculated normalized transmittance for different order of nonlinear absorption

Chapter 4

4. Experimental set up and preparation

4.1. Femtosecond laser system

The ultrashort laser system used for the nonlinear absorption measurements is a Ti: sapphire femtosecond multipass amplifier system (FEMTOPOWER ^{TM} COMPACT^{TM} PRO Femtolasers Productions GmbH Austria). This system delivers ultra short laser pulses with a maximum average power of approximately 1W at a repetition rate of 1 kHz. The pulse duration, estimated as the FWHM of a Gaussian temporal profile, is typically 25 fs and the spectrum is centered at 798 nm. The femtolaser system consists of three parts; Oscillator, Amplifier and Compressor as shown in Fig. 4.1.

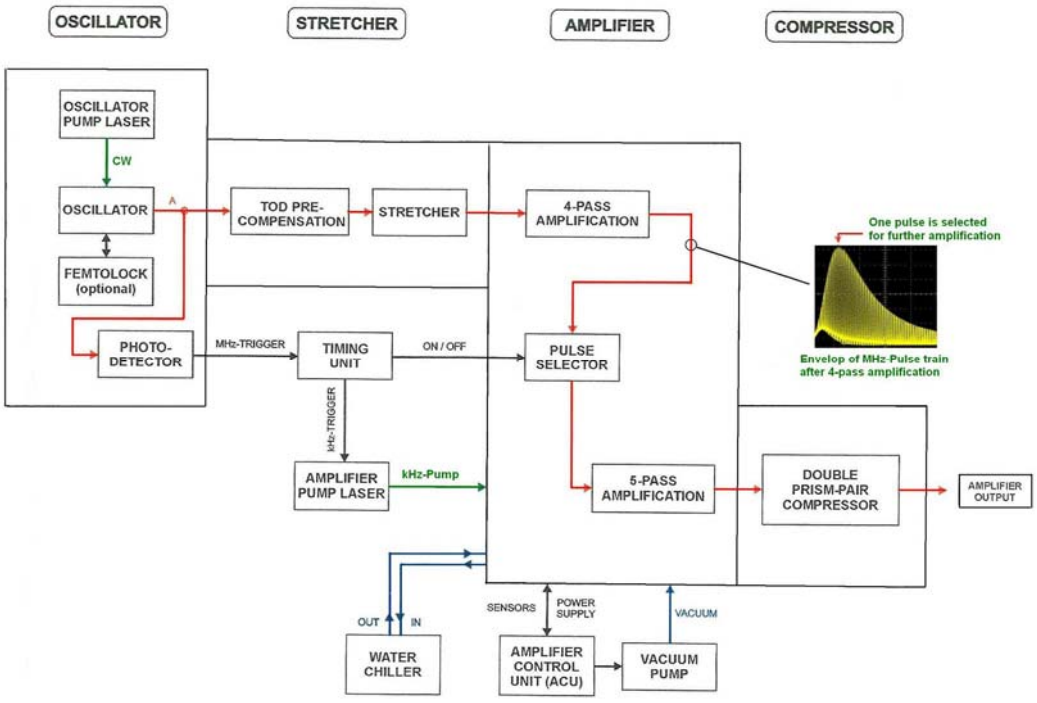

Fig. 4.1. A schematic showing different parts of a femtolaser system

4.1.1. Pump lasers

The pump laser for amplifier is an intra-cavity frequency doubled and Q-switched Nd: YLF (Model DM 10-527) laser. It produces 220 ns pulses having an energy of 10 mJ at a repetition rate of 1 kHz. Nd: YLF emits at 1054 nm wavelength but the output wavelength after the frequency doubling crystal is 527 nm. This laser fulfils the requirements as a pump laser for amplifier since pulses with energies > 8mJ and duration between 100 ns and 500 ns are required. The beam must be horizontally polarized.

The pump laser for oscillator is a compact solid-state diode-pumped, intra-cavity frequency doubled Neodymium-doped yttrium orthovanadate (Nd:YVO_4) laser (Coherent, Inc. Santa Clara, CA) that provides single frequency green (532 nm) output at power level greater than 5W. It is pumped by a Diode laser at a wavelength of 808 nm.

4.1.2. Oscillator

A mirror dispersion-controlled Ti:sapphire oscillator (FemtoSource Pro; FemtoLasers GmbH) delivers 12 fs pulses of few nJ energy at a repetition rate of 76MHz with an output power of more than 600 mW. The spectrum is centered at 788 nm with a bandwidth of about 122 nm. It is a Kerr-lens mode locked laser with TEM_{00} mode. Fig. 4.2 shows the beam trace in the oscillator.

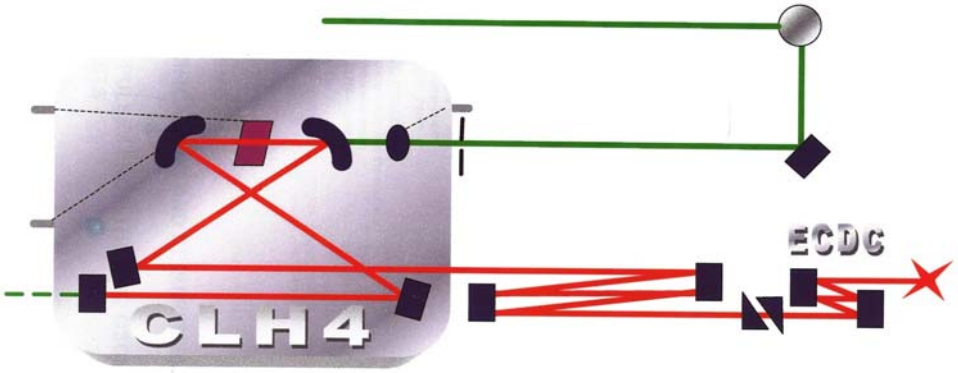

Fig. 4.2. A schematic showing oscillator beam trace

4.1.3. Amplifier

The broadband ($\Delta\lambda$~122 nm, 76 MMz)) pulse train from the Ti:sapphire oscillator is seeded to a 9-pass amplifier arrangement. It consists of two curved mirrors, two retro reflectors and a 2.5-mm thick Brewster-cut Ti: sapphire crystal. The highly doped Ti: sapphire crystal is placed in a vacuum chamber and is thermo electrically cooled down to (- 15 °c) to reduce the effect of thermal lensing. One of the retroreflectors is made up of two chirped mirrors specially designed for providing third- and fourth-order dispersion control to compensate for the higher-order-dispersion of the prism compressor and all the material in the amplifier.

Pulse stretching before amplification is accomplished by a comparatively small amount of dispersion introduced by a 10-cm-long block of heavy flint-glass (SF57) and other system components (e.g. Faraday isolators, Pockels cell and polarizers) to a duration of ps.

The pulse propagates nine times along slightly different paths through the gain region of amplifier medium. After first four passes through the crystal, a single pulse is selected out of the pulse train with a Pockels cell. The selected single pulse is reinjected and amplified in another five passes.

The amplifier delivers 25 fs pulses with an energy of 1mJ at the repetition rate of 1 kHz. The spectrum is centered at 798 nm with a bandwidth of about 44 nm measured as FWHM. The output beam diameter is 15 mm

4.1.4. Compressor

The laser pulses were stretched from femtosecond regime to picosecond regime before amplifier to prevent damaging the optical components inside amplifier. A linear pulse compression technique is used to obtain the ultrashort amplified pulses. Two pairs of prism were used for dispersion compensation. The angle of prism pair as well as the distance between the first and second prism pair is responsible for introducing positive or negative dispersion. In Fig. 4.3 CPR1A and CPR1B are the first prism pair. The second prism pair comprising CPR2A and CPR2B is mounted on a micro-stage which enables us to change the distance between prism pairs. By moving the second prism pair more in, more positive dispersion is introduced and vice versa.

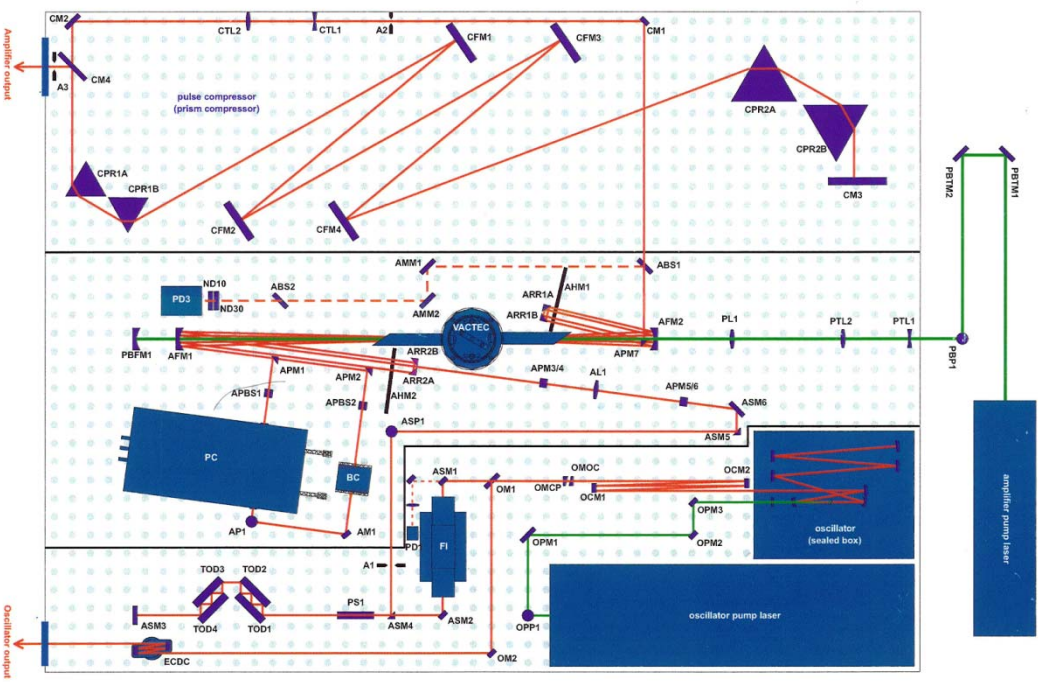

Fig. 4.3. A sketch of femtolaser system showing three different parts as well as the trace of pump beam, seed beam and amplifier beam

4.2. Laser radiation characterization

In order to extract an accurate multi-photon absorption coefficient or cross section from a Z-scan trace many parameters concerning the laser radiation must first be precisely determined. Some characteristic parameter such as radiation wavelength, repetition rate, pulse energy and laser beam diameter can be determined easily using a spectrometer and power meter. However, determining some other parameters such as pulse duration, laser beam quality factor, laser beam waist radius and Raleigh range are not straightforward and require using more complex equipment such as an autocorrelator and a beam viewer camera.

4.2.1. Pulse phase controlling employing a DAZZLER system

The DAZZLER system is an acousto-optic programmable dispersive filter. It enables to control separately both spectral amplitude and spectral phase. The DAZZLER system composed of an acousto-optic crystal and a radio frequency (RF) generator that is controlled by a computer program. By using a DAZZLER system one can shape the spectral amplitude properly to avoid gain narrowing. It can also be used to flatten the phase over the whole spectral to make the pulse free of chirp and also to split a single pulse into two pulses with a separation of a few tens of femtosecond. This system was used to stretch the pulse duration up to few hundreds of fs via increasing the group delay dispersion (GDD) of the pulses propagating through the crystal that is drived by an appropriate RF signal.

The pulse duration increases by introducing chirp to the laser pulse according to the following equation.

$$\tau = \tau_0 \sqrt{1 + \left(4 \ln 2 \frac{\mathrm{GDD}}{{\tau_0}^2} \right)^2} \qquad (4.1)$$

where τ is the pulse duration of a chirped pulse, τ_0 is the pulse duration of a Fourier-transform-limited pulse and GDD is the magnitude of group delay dispersion. For instance, introducing a GDD of 870 fs^2 to a chirped-free pulse will lead to increasing the pulse duration from 25 fs to 100 fs.

4.2.2. Exact determination of Pulse duration

A FEMTOMETER autocorrelator (model:ENV40CSG from Femtolasers company) which is specially designed for high-fidelity characterization of ultrashort pulses in the <10 fs – 100 fs range was used to measure the pulse duration. This autocorrelator can be used in two modes; background free (non-collinear) autocorrelation or interferometric (collinear) autocorrelation.

In Fig. 4.4, (a) shows a schematic of intensity autocorrelor and (b) exhibits intensity autocorrelation of four temporally Gaussian pulses possessing a GDD of 0, 340, 660 and 870 fs^2 corresponding to pulse duration of 25, 46, 77 and 100 fs respectively.

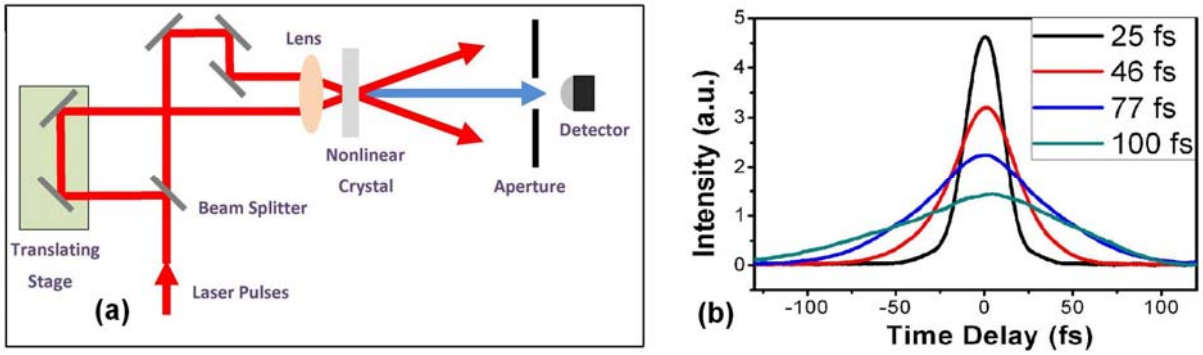

Fig. 4.4. Intensity autocorrelor (a) and Intensity autocorrelation measurements (b). Pulse durations have been measured as the full width at half maximum (FWHM).

4.2.3. Laser beam diameter measurement

A beam profiler was used to specify the laser beam spatial intensity distribution as well as to measure the beam diameter. An orthogonal scanning method was also carried out to measure the beam diameter. In this method a 1 mm aperture scanned orthogonal to the beam propagation direction and the transmittance was measured as a function the aperture position.

Figure Fig. 4.5 (a) shows a pseudo colored spatial intensity profile taken by a laser beam profiler [LaserCam –HR (Coherent)]. Intensity distribution in both *x* and *y* directions indicates a spatially Gaussian beam of 15 mm diameter measured as full width at $1/e^2$ of maximum. The colors represent the variation in the intensity from the central maxima to the edges of the profile with minimum intensity. Fig. 4.5 (b) shows the orthogonal scanning results and the Gaussian fit curve to the data from which the beam diameter was measured to be 15 mm; the same value as measured by the beam profiler.

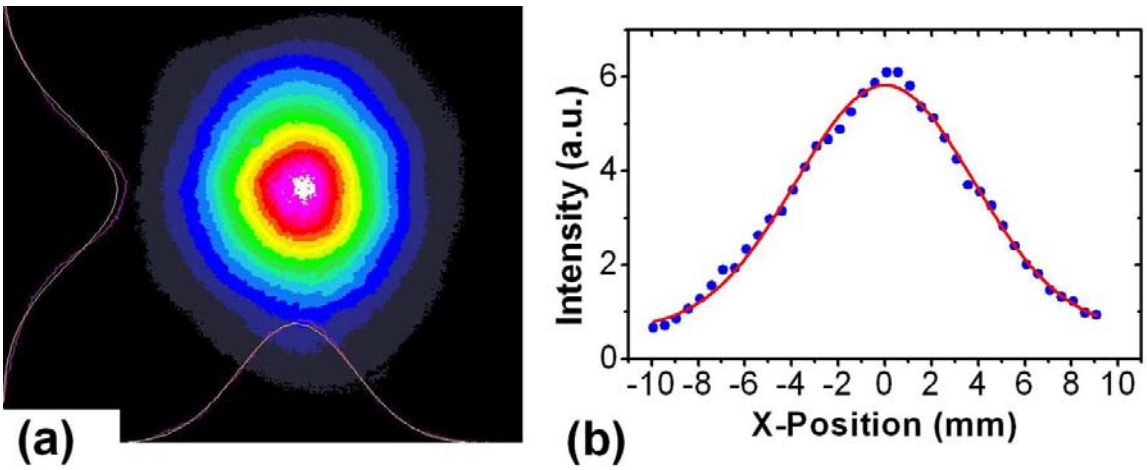

Fig. 4.5. 2D intensity profile taken by a beam profiler (a) and orthogonal scanning data with a Gaussian fit (b)

4.2.4. Raleigh range measurement

The Rayleigh range is defined as the distance from the waist of a laser beam where the beam radius increases by a factor of √2. A beam profiler was mounted on the translation stage in the Z-scan apparatus in order to measure the Rayleigh range of the laser beam focused by a 300 mm focal length lens. The beam profiler was moved along the beam propagation direction in small steps of 0.1 mm so that in each position the radius of the focused laser beam was recorded. The ISO 11146 standard demands that about half of the measurement points must be more than two effective Rayleigh lengths away from the beam focus whereas the other half of the points are close to the focus, i.e., within one Rayleigh range [55]. Fig. 4.6 shows the measured beam radius and the fit curve to the measured data using Eq. (4.2). A Rayleigh range of 0.86 mm was extracted from the fitting process. As will be shown later, this value for the Rayleigh range resulted in the best fits of the Z-scan data using Eq. (2.178) for 2PA measurements and Eq. (2.208) for 3PA measurements. This can be taken as a strong argument for the reliability of the Rayleigh range measurement.

$$w(z)^2 = w_0^2\left(1+\frac{z^2}{z_R^2}\right) \tag{4.2}$$

where w_0 is the beam waist radius and z_R is the Rayleigh range.

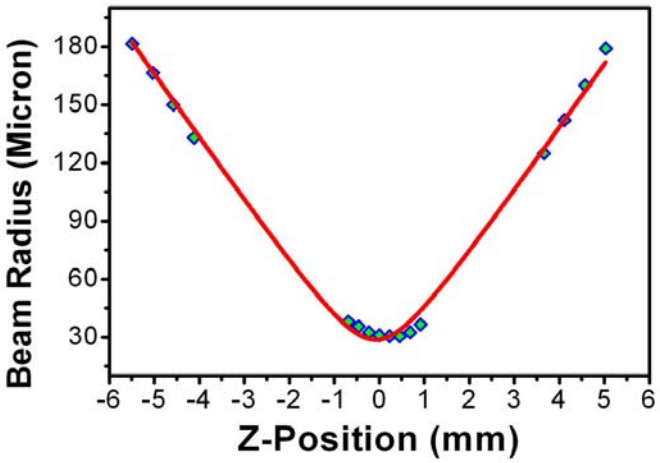

Fig. 4.6. Measured beam radius around the waist. Red solid curve is the fit curve to the data using Eq. (4.2).

4.2.5. Laser beam waist radius measurement

A beam profiler was used to measure the beam radius around the waist of the focused laser but it should be noted that the beam is focused too tightly so that the beam waist is too small. That makes a precise beam radius measurement very difficult. The measured beam waist radius, typically a few tens of μm as shown in Fig. 4.6, is not precise enough because of the limited resolution of about 6 μm due to the pixel size of the beam profiler. Hence, the beam profiler

cannot be used for precise measurements since the beam waisr radius corresponds only to a few pixels.

In order to obtain the beam waist radius precisely, a pinhole scanning method was used. A 50 μm radius pinhole was mounted on the translation stage in the Z-scan apparatus. The pinhole was moved 10 mm along the beam propagation direction through the waist of the laser beam focused by a 300 mm focal length lens in very small steps of 0.2 mm. The energy transmitted through the pinhole was collected by a 60 mm focal length lens and detected on a diode. The obtained z-dependent transmittance was fitted using Eq. (4.3) as shown in Fig. 4.6. From the fitting process the precise beam waist radius of 22 μm was obtained.

$$T_{Norm}(z) = \frac{1 - e^{-\frac{2a^2}{w(z)^2}}}{1 - e^{-\frac{2a^2}{w_0^2}}} \tag{4.3}$$

where a is the radius of the pinhole, w_0 is the beam waist radius and $w(z)$ is the beam radius at the position z that is given by Eq. (4.2).

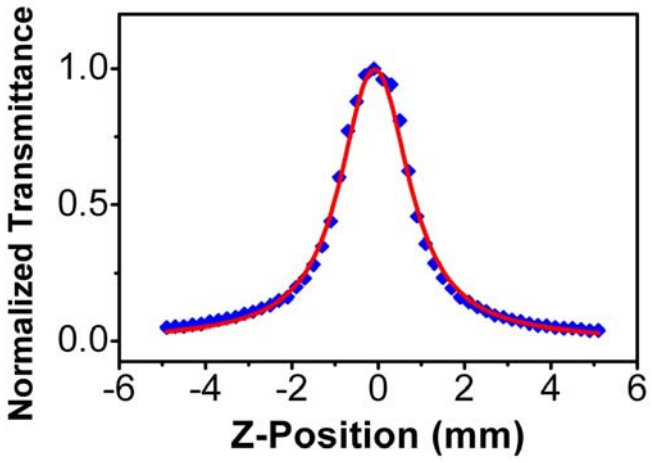

Fig. 4.7. Measured transmittance of a 50 μm pinhole along the propagation direction of a laser beam focused by a 300 mm focal length lens. Red solid curve is the fit curve using Eq. (4.3)

4.2.6. Laser beam quality factor measurement

A diffraction-limited beam known as Gaussian beam has a beam quality factor M^2 of 1. The beam waist radius of a Gaussian beam is calculated from $w_0 = \sqrt{\lambda \cdot z_R / \pi}$ where λ is the wavelength and z_R is the Rayleigh range. For our setup (λ=798 nm and z_R=0.86 mm) the beam waist radius for a Gaussian beam was calculated 14.8 μm. The quality factor of a laser beam is defined as $M^2 = W_0^2 / w_0^2$ [56] where W_0 is the measured beam waist radius and w_0 is the calculated beam waist radius of the specified Gaussian laser beam. A quality factor of M^2=2.2

was obtained for the laser beam used in our experiments as W_0 was measured 22 μm and w_0 was calculated 14.8 μm. The request for determining the beam quality factor M^2 is that the wavelength λ must be replaced by $M^2\lambda$ in all equations. For instance $w_0 = \lambda f / \pi w$ gives the beam waist radius of a diffraction-limited laser beam focused by a convex lens where f is the focal length of the focusing lens, λ is the wavelength of the laser radiation and w is the laser beam radius on the focusing lens. Replacing λ by $M^2\lambda$ in the above equation allows calculating the waist radius of an M^2 times diffraction-limited. By considering M^2=2.2, λ=798 nm, f=300 mm and w=7.5 mm the beam waist radius is obtained 22.3 μm which is in good agreement with the obtained value (22 μm).

4.2.7. Bandwidth measurement

The central wavelength and spectral width of both oscillator and amplifier radiation were measured using a fiber optic spectrometer (S2000 from Ocean Optic Inc.). The spectrum of the oscillator radiation is centered at 788 nm with 122 nm bandwidth and the spectrum of the amplifier is centered at 798 nm with 44 nm bandwidth. In Fig 3.3 the spectrum of oscillator and amplifier radiations are compared.

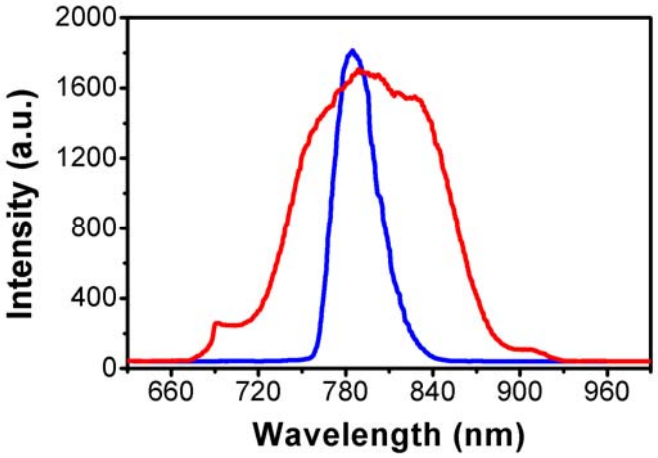

Fig. 4.8. Spectrum of oscillator radiation (red) and amplifier radiation (blue)

4.2.8. Counter

An NI USB-6211 Data acquisition device controlled by a Lab View program was used as a shutter to block the laser beam and also as a counter to allow a certain number of pulses to pass. It helps to prevent sample irradiatingt while it is translated from one position to the next position and thus causes less damage to the examind sample.

4.3. Sample preparation

Three different kinds of samples were examined in order to verify and test the theoretically obtained formula for determining 2PA and 3PA coefficients applying Z-scan technique. They

include solids and liquids, 2P absorbers and 3P absorbers and also synthesized and commercially available substances.

4.3.1. Photo-initiators

A photoinitiator (PI) is any chemical compound that decomposes into radicals (often referred to as free radicals) when exposed to light. By this definition, a two-photon initiator is a chemical compound that is capable to generate radicals via dissociation by simultaneous absorbing of two photons at a wavelength situated within the transparent region for the photoinitiator. Radicals are atoms, molecules, or ions with unpaired electrons on an open shell configuration. The unpaired electrons cause radicals to be very unstable and react quickly with other compounds, trying to capture the needed electron to gain stability. Generally, radicals attack the nearest stable molecule, stealing its electron. When the attacked molecule loses its electron, it becomes a radical itself, beginning a chain reaction. Hence, radicals play an important role in polymerization notably in the production of polyethylene plastic. In two-photon induced polymerization (2PIP) the chain process of polymerization is triggered by linking a radical, derived from a 2PI, to an unsaturated monomer molecule such as an acrylate leading to produce a new radical that links immediately to another molecule. In this way a chain process continues to generate a long molecule consisting of many numbers (thousands) of monomer that conducts phase transfer from monomer to polymer. Fig. 4.9 and Fig. 4.10 show typical radical generation via 1PA and 2PA respectively.

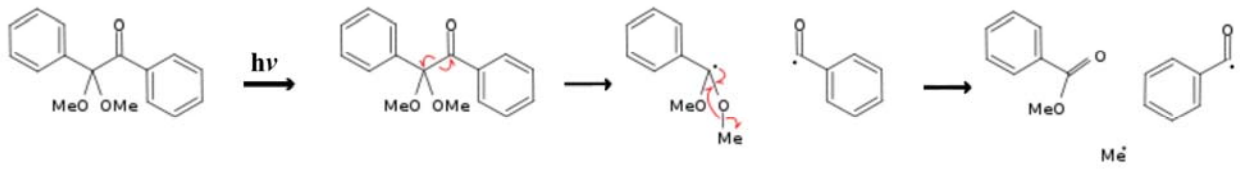

Fig. 4.9. A typical radical generation process via 1PA

Commercially available one-photon initiators (Fig. 4.9) were used at the early stage of 2PIP research. These initiators exhibit high quantum yield of reactive radicals after excitation. However, due to their rather low 2PA cross section (σ_{2PA}) long exposure time and high excitation intensities are required in order to generate radicals via 2PA processes that generally cause the damage to the structures and thus greatly limit their widespread use. Therefore, intensive studies have focused on improving the 2PA sensitivity. In the last decades plenty of chromophores with large σ_{2PA} were synthesized. The structure of those compounds generally contains electron donor groups (D) and electron acceptor groups (A) bridged by a π-conjugated system (e.g. double bonds or triple bonds), such as D-π-D or D-π-A-π-D [44, 57-60]. However, most of the reported chromophores exhibit high fluorescence yields as desirable for fluorescence imaging applications. To be effective as a 2PI, low fluorescence quantum yields are preferred as this leads

to a higher population of the triplet state, which is usually the active state of the initiators producing radicals or ions for inducing the polymerization.

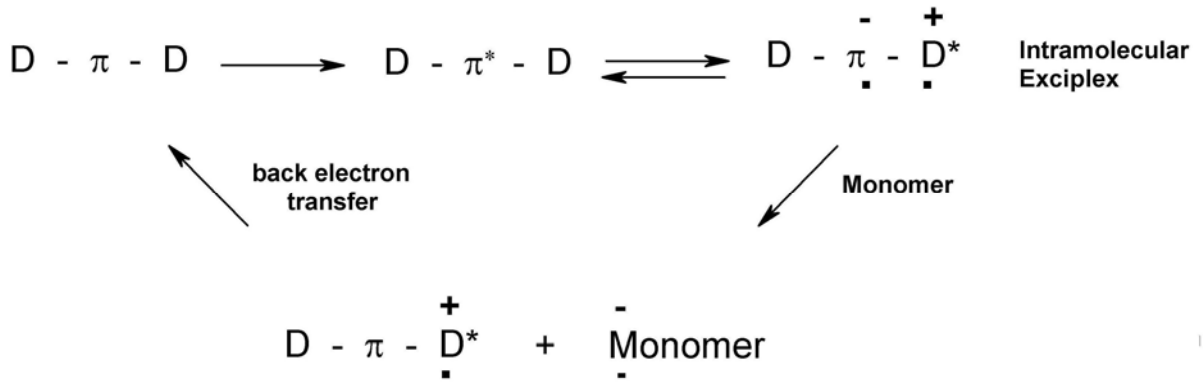

Fig. 4.10. Excitation and radical generation process for a typical 2PI

It has been found that structural elements which can increase the effective conjugation length and polarizability of the molecule would enhance the molecular 2PA cross-section [44]. In order to obtain efficient 2PIs, the strategy of molecules design demands: 1) chromophoric systems which exhibit large σ_{2PA}; 2) functionalities that can produce active initiating species in high quantum yield such as those in one-photon radical initiators; 3) mechanisms through which the excitation of chromophoric systems result in the activation of the functionalities. It is not easy and rational to compare the efficiency of two-photon absorbing molecules since the peak of 2PA occurs at different position for different molecules. If one wishes to find out the absolute relationship between molecular structure and two-photon absorption cross-section of the studied molecules, the entire two-photon absorption spectra should be determined. However, at this stage we are not capable to carry out these measurements due to the lack of a high-power laser system providing a broad tunable range.

Additionally, good biocompatibility, low toxicity, high solubility and photostabitity are required for biological applications and practical purposes.

Based on the above strategy to design high efficient 2PIs, a series of newly synthesized compounds were measured. 1,5-Bis(4-(N,N-dibutylamino)phenyl) penta-1,4-diyn-3-one **(B3K)** which contains triple bonds and cross-conjugated D-π-A-π-D structure. Bis(4-((4(dibutylamino)phenyl)ethynyl)phenyl)methanone **(B3BP)** which exhibits a longer conjugation length and thus a higher σ_{2PA} can be expected. 2,7-Bis((4-(dibutylamino)phenyl)ethynyl)-9H-fluoren-9-one (**B3FL**), 3,6-Bis((4-(dibutylamino)phenyl)ethynyl)-9H-fluoren-9-one (**3,6-B3FL**) and 2,6-Bis((4-(dibutylamino)phenyl)ethynyl)anthracene-9,10-dione (**B3AN**) that ensure good coplanarity resulting to facilitate the intermolecular charge transfer process which is critical in enhancing σ_{2PA}. **B3FL** also exhibits high thermal and photochemical stability. 2,7-Bis((4-(butyl(2-ethylhexyl)amino)phenyl)ethynyl)-9Hfluoren-9-one (**BB3FL**) and 2,6-Bis((4-(butyl(2ethylhexyl)amino)phenyl)ethynyl)anthracene-9,10-dione (**BB3AN**) that exhibit high solubility in the monomers that is an important issue for the efficiency of 2PIs [61, 62]. The

detailed information for synthesis method and chemical properties of these compounds can be found in [63].

All evaluated 2PIs do not exhibit any linear absorption beyond 600 nm, which could thus interfere at the wavelength used in the Z-scan experiments and the two-photon polymerization microfabrication (800 nm). Determining the MPA cross section of these PIs requires some particular considerations without them an accurate measurement cannot be expected.

a) Each PI is dissolved in a solvent. The amount of the absorbed energy by the medium depends on the number of the absorbing particles within the exposed volume of the medium. Thus, in order to determine an accurate 2PA cross section, the concentration of these compounds must be measured very precisely.

b) To make a logic comparison between the 2PA cross section of PIs, all compounds must be dissolved in the same solvent since, a different polarity of the solvent causes a change in activity of the molecules. Furthermore, all compounds must show a sufficient solubility in the used solvent.

c) After absorbing energy by the molecules any structural change such as dissociation might happen to a number of molecules that causes a reduction in the number of 2P absorbers which leads to obtain a nonrealistic 2PA cross section. In order to avoid such a problem the exposed volume of the compound must be continuously refreshed.

d) After excitation, each molecule might undergo radiative relaxation emitting fluorescence. These radiations must be somehow eliminated from the original beam transmitted through the medium.

e) One should notice that only the 2PA cross section of the PIs can be determined by applying the Z-scan technique but not initiating activity. A high 2PA absorber compound may not be a high active initiator and might show a high fluorescence yield instead. 2P polymerization using different PIs can reveals the initiating activity of each PI.

f) In order to determine the nonlinear absorption cross section of each compound one should first determine the order of nonlinearity. Using different formula calculated in chapter 2 helps one to determine whether 2PA or 3PA occurs in the compound under investigation.

g) In order to extract the 2PA cross section of a compound from the Z-scan data the on-axis intensity at the focus within the sample must be measured. The laser power is usually measured before the sample thus, the reflection from the wall of the cell containing the chemical compound must be taken into account.

h) The solvent itself might contribute to the effective nonlinear absorption. Thus, in order to extract the pure MPA cross section of the PIs, the contribution of the solvent must be somehow subtracted.

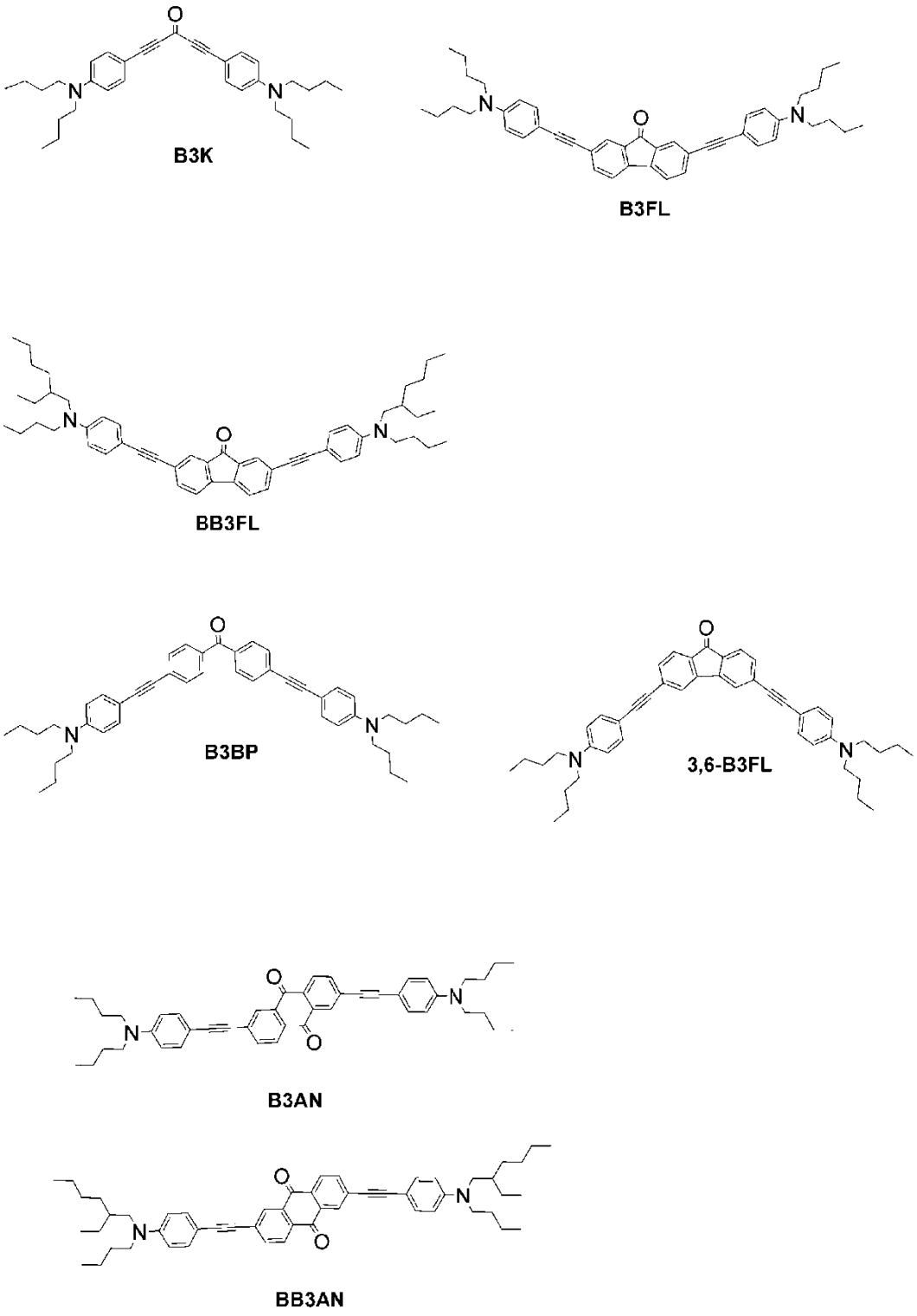

Fig. 4.11. Structure of synthesized compounds

4.3.2. Metal nanoparticle doped glasses

Glass substrates have recently attracted growing interest due to the fact that they can serve as substrates for nano-structured systems with remarkable optical nonlinear properties [64]. Glass

substrates possess overall advantages as compared to many crystals or polymers. In particular, the composition of the glass can be well designed and tuned according to the needs of the encompassed photonic components and also their fabrication is usually feasible and inexpensive [65]. Silicate glasses (i.e., glasses based on silica SiO_2) are both chemically and thermally stable, and it is rather simple to fabricate waveguides compatible with currently used optical fibers.

The metal nano-cluster composite glasses synthesized by ion implantation have been shown as particularly promising nonlinear photonic materials [1, 64, 66-68]. Nanometric metal particles can exhibit a nonlinear optical response several orders of magnitude larger than bulk metals due to a phenomenon referred to as surface Plasmon resonance. When the particle size ranges from nanometer to a few tens of nanometers, confinement results in the possibility of resonantly exciting the electron gas collectively by coupling with an appropriate oscillating electromagnetic field. As the local electric field in the particles is enhanced due to the oscillation of the electron gas, the metal nonlinear optical response can be amplified as compared to the bulk solid one [69].

Metal nano-cluster composite materials could offer the possibility to realize all-optical switching devices which would operate in a time range faster than the electronic ones without the need of converting optical signals to electrical ones. These devices are essentially based on nonlinear optical properties of materials, i.e. changes of the refractive index or absorption coefficient of materials caused by an intense optical beam or by a strong electric field.

Recent experiments have shown that standard glass substrates containing nanoparticles of Au can be regarded as one of the most promising nonlinear optical materials [70-78]. The experiments have shown that such materials exhibit very strong nonlinear third order susceptibility $\chi^{(3)}$.

Metal nanoparticle doped glasses have promising properties for potential application in optical devices such as all optical switching devices [67]. These properties sensitively depend on their size, shape, density and spatial distribution.

Metal nanoparticles are synthesized in glass matrix by various methods [79], such as direct ion implantation [80, 81], sol-gel method [82] and ion exchange [83, 84]. Conventionally, ion exchange is used to introduce silver ions in glass by immersing the samples into a molten salt such as AgNO3, and additional processing such as light irradiation or thermal annealing then follows to generate particles.

Metal glass composite samples, prepared by employing ion implantation method, have been measured. Au+ ions were implanted into the silicate glasses using an accelerator at the Nuclear Physics Institute in Prague, Czech Republic. The energy of the implanted Au+ ions was 1701 keV. The fluence of the Au+ ions into Glasses was kept 10^{16} cm^{-2}. The as-implanted glasses were annealed at temperatures of 600 °C for 5 h [85]. Fig. 4.8 shows the depth distribution of nanoparticles in a 402 nm thick layer 500 nm under the surface.

The following considerations should be taken into account in order to determine an accurate MPA coefficient of a metal glass composite.

a) in a metal glass composite, many factors such as the type of the host medium, the kind of the implanted ions, the amount of the ion fluence, the energy of the implanted ions, the annealing temperature and the annealing time influence the size, shape and depth distribution of nanoparticles formed in the glass. Thus, in order to verity the affect of any factor (mentioned above) on the MPA coefficient the other factors must be kept identical.

b) The thickness of the nanoparticles layer is very narrow, in the range of a few hundreds of nanometers, whereas the thickness of the substrates is, at least, few hundreds of micron. Therefore, a thousand times thicker host medium might have a contribution to the nonlinear absorption comparable to that of the nanoparticle layer itself. Thus the main challenge and difficulty in the determination of MPA coefficient of these metal glass composite samples is the subtraction of the substrate contribution from the entire nonlinear absorption.

c) The essential points and guidances mentioned in parts d, f, g and h in section 4.3.1 should also be considered and followed.

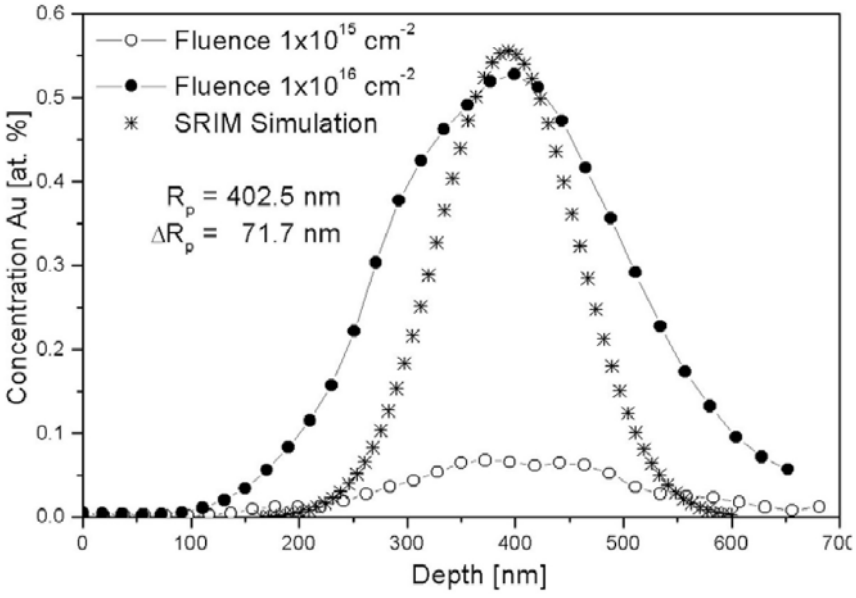

Fig. 4.12. Depth distribution of gold nanoparticles introduced in glass employing ion implantation method for two different fluences

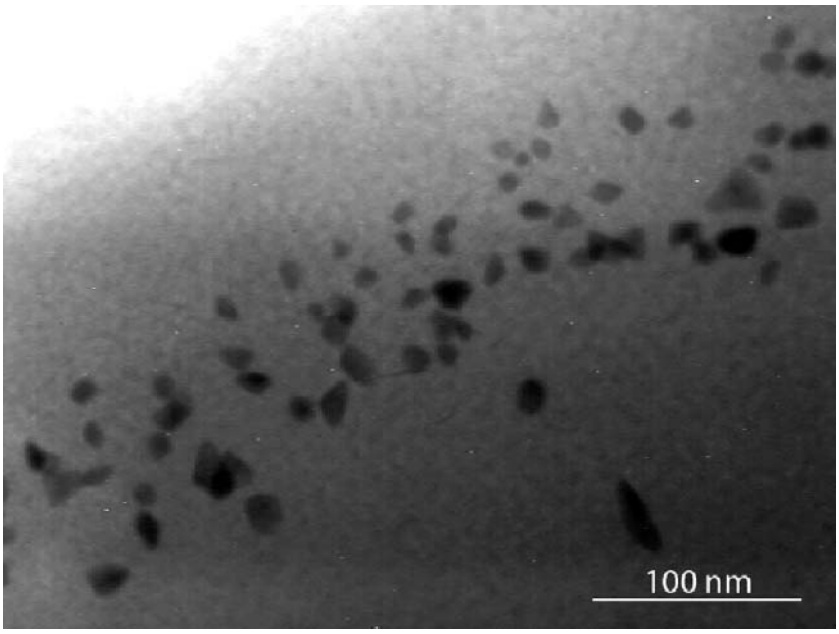

Fig. 4.13. TEM image of gold nanoparticled implanted in glass

4.4. Z-scan setup for nonlinear absorption measurement

Our setup for the open aperture Z-scan measurement to determine MPA consists of the following parts:

A - Laser source: a Ti:sapphire laser as described in section 3.1 was used. The Laser beam diameter is 15 mm, the shortest pulse width is 25, the central wavelength is 798 nm, the bandwidth is 44 nm and the beam quality factor is 2.2.

B - Attenuator: A continuous variable attenuator (Model C-VARM from COHERENT Company) with a maximum attenuation by a factor of 10^{-7} and a fine pitch adjustment control to precisely set the attenuation is employed to attenuate the pulse energy from several hundred μJ down to a few nJ. Using this attenuator enables us to change the laser intensity for different Z-scan measurements.

C - Beam splitter: a large 5 cm diameter beam splitter splits the laser beam into two parts with fraction of 1/3 and 2/3. The less intense part is directed towards the reference diode and the more intense part propagates straightly through the focusing lens.

D - Focusing lens: 25 mm diameter plano-convex lenses with different focal lengths were employed. The focal length of employed lenses ranged from 175 to 400 mm depending on the sample thickness in order to fulfill the thin sample criterian. It should be noticed that the Rayleigh range, which is proportional to the focal length square of the focusing lens, must be larger than the thickness of the sample.

E - Translation stage: using a stepper motor (DC-Motor model MFA-CC from Newport Company) enabled us to move the sample up to 25 mm along the beam propagation direction through the beam focus in minimum steps of 50 nm. This motor was handled and controlled by computer exploiting a Lab VIEW program.

F – Cuvette: for liquid samples like dyes or photoinitiator solutions, a 0.2 mm thick one-time flow cell (170.700 QS from HELLMA Company) connected to a syringe pump (NE-300 from SYRINGPUMP) providing a wide range of flow rates was used.

G - Collecting lens: A large diameter short focal length lens (50 mm diameter and 60 mm focal length) was used. This ensures that the entire energy transmitted through the sample is collected and directed toward the detecting diode to be measured.

H - Detectors: Two Si diodes with 1 cm^2 detecting area were used as reference and detecting diode. Both diodes were connected to a picoscope. The signal measured by the detecting diode is divided by the signal receiving from the reference diode to eliminate the influence of the laser pulse energy fluctuation.

I - Neutral density filter: For adjusting the absolute intensity at the diodes, but to stay within their dynamic range, neutral density filters were used. A low-pass filter also was mounted before the detecting diode to block unwanted emissions such as up-converted fluorescence from the excited sample.

J - Picoscope: The signals at the diodes were recorded with a two-channel personal computer oscilloscope (Picoscope3204 from Picotech Company).

K - Computer: The computer software (Lab View) analyzed the intensity of individual laser pulses (including averaging over several laser shots) and also handled the movement of the translation stage as well as the entire data acquisition process.

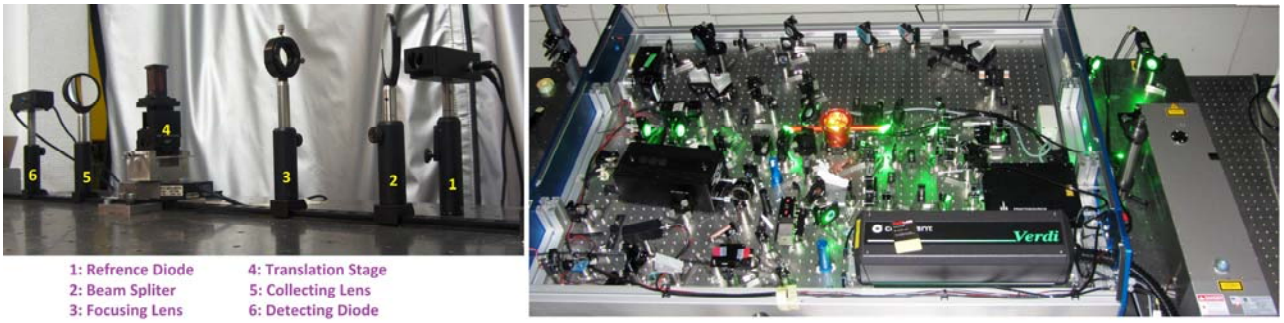

Fig. 4.14. Open aperture Z-scan setup

4.5. 3D structuring unit

This unit was used to make 3D microstructures using two or three photon absorption. It consists of the following parts:

A – Laser source: a Ti:sapphier laser producing 150 fs pulses at a repetition rate of 80 MHz was used. The average output power is about 300 mw corresponding to a few nJ pulse energy.

B – Acousto-optic modulator: it is used as a shutter with nanosecond response time. It can block the laser beam or allow a certain number of pulses to pass through it by receiving an appropriate order from computer.

C – Polarizer: it is mounted on a rotation stage controlled by computer. The laser beam intensity can be controlled by rotating this polarizer.

D – Telescope: in order to increase the beam size on the focusing objective that leads to produce a tighter focused laser beam within the resin. It helps to create structurs with finer resolution.

E – 3D translation stage: three piezoelectric translation stages were installed on a heavy granite stone enabling us to scan the sample in three orthogonal directions.

F: Camera: it is utilized to visualize the polimerzation process. It is needed to find the focal point and also to specify whether the laser power is enough to trigger the polymerization or not.

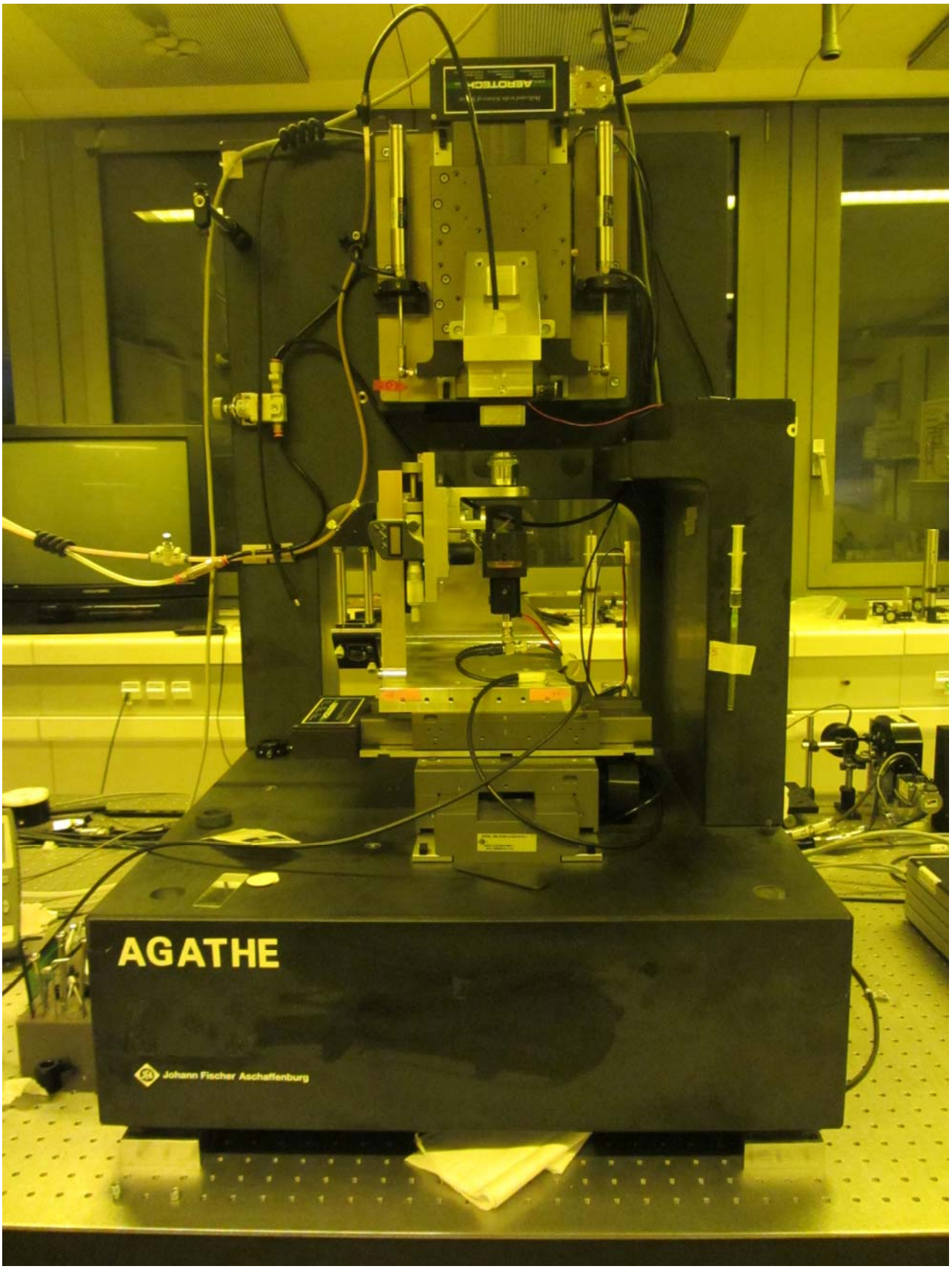

Fig. 4.15. 3D structuring unit

Chapter 5

5. Measurements, results and discussion

Variety of samples such as chemical compounds (including a series of PIs and photo-grafting molecules) and metal-glass composites (including different types of glasses in which gold nanoparticles are implanted) were investigated. These samples were prepared and characterized somewhere else [62, 81, 86]. Their absorption spectra show that none of them exhibits absorption at the wavelength used in the Z-scan measurements. An OA Z-scan setup was installed in order to determine first the order of nonlinear absorption and then the MPA cross section. Rhodamine B as a reference dye was used to check the accuracy of the theory as well as the setup. In this chapter, it is discussed which experimental conditions and criteria are required to extract a meaningful MPA cross section from a Z-scan trace. Then, the methods for determining the order of nonlinear absorption are presented. Next, the Z-scan data and results for all samples are illustrated and ultimately the correlation between sample characters and the OA Z-scan results will be discussed

5.1. Conditions and criteria in OA Z-scan measurements

In order to extract an accurate MPA coefficient or cross section from measured Z-scan data using equations derived in chapter 2, several criteria must be met in performing the Z-scan.

5.1.1. Optimum range of pulse energy

To measure an appropriate Z-scan signal, from which the MPA cross section can be extracted using equations obtained in chapter 2, the pulse energy should be adjusted lower than a threshold value at which the solvent (in case of PIs) or glass substrate (in case of metal glass composite) shows nonlinear absorption. It also be noticed that the pulse energy must be kept below the value corresponding to a normalized transmittance of 0.765. The minimum pulse energy is determined as the value at which the nonlinear medium starts to nonlinear absorption.

5.1.2. Thin sample criterion

The analytical calculations to obtain the normalized transmittance in the Z-scan experiment were carried out under the thin sample approximation. In this approximation the sample thickness is assumed smaller than the Rayleigh range of the focused laser beam within the sample. This assumption facilitates the calculation since, the laser beam divergence and then the intensity reduction due to linear diffraction or nonlinear refraction is negligible and can be ignored. In case of chemical compound measurements, a 300 mm focal length plano-convex lens was employed. It focuses the 15 mm diameter laser beam into a 22 μm radius spot resulting in a

Rayleigh range of 0.86 mm. The Rayleigh range is four times larger than the thickness of the sample (A 0.2 mm cell containing a chemical compound) that fully fulfills the thin sample criterian. In case of metal-glass composite measurements, a 175 mm focal length plano-convex lens was employed. It focuses the 15 mm diameter laser beam into a 13 μm radius spot resulting in a Rayleigh range of 0.3 mm which is very much longer than the thickness of the nanoparticles layers within the glass substrates (few hundreds of nanometers).

5.1.3. Compound preparation conditions

For the OA Z-scan measurements an equimolar concentration of the compounds (1×10^{-2} M) was prepared using spectroscopic grade solvents. For the two Rhodamine compounds, methanol (MeOH) was chosen as solvent as often described in the literature in order to achieve a reliable reference and to test the Z-scan device. The other initiators were all dissolved in tetrahydrofuran (THF) as all compounds showed a sufficient solubility in this solvent. For comparison, it is important that the same solvent is used for all compounds, because a different polarity of the solvent causes a change in activity of the molecules.

5.1.4. Base line fluctuation

The measured Z-scan trace is the quotient of the transmitted signal (measured by the detecting diode) by the reference signal (measured by the reference diode). If one scans along the beam axis without a sample mounted on the stage, the measured Z-scan is expected to be an exact straight line. Practically, this is not the case due to several reasons such as the limited precision of the Picoscope. In order to reduce these errors, the Labview software was designed so that it can calculate the average pulse energy when the sample is irradiated by a large number of laser pulses. It turned out that 300 pulses was a sufficient number of pulses. Additional increase in the number of pulses per each step could not result in further reduction of the fluctuation in the so-called straight base line.

5.1.5. Determining the scanning length and normalizing the Z-scan signal

The sample mounted on the translation stage should be located at a place so that the middle of the scanning range coincides with the focusing point of the focused laser beam. Using a DC motor as a translation stage allows to scan the sample for a maximum length of 25 mm. it is not always necessary to scan the sample for 25 mm but a shorter length might be enough depending on the thickness of the sample and also the Rayleigh range. The important issue is that the Z-scan signal should have straight horizontal wings on both sides showing the regions where no nonlinear absorption occurs due to the low intensity. It means that the scanning should start far enough away from the focus where the intensity is not sufficient to induce nonlinear absorption. The straight part of the Z-scan signal is of great importance for determining the base line in order to normalize the transmittance.

5.1.6. Determining the sufficient flow rate of the compounds

The formation of active species during the MPA cross section measurement for PIs leads to a decrease in the concentration of initiators. This decrease would reduce the reliability of the MPA

measurements as it is based on several individual measurements extended over a certain period of time during which the reduction in the number of initiators occurs. Therefore, during the entire MPA measurement for the same compound the same concentration should always be present. This can be achieved by a continuous material flow using a one-time flow-cell connected to a syringe pump. As shown in Fig. 5.1 experimental tests exhibited that the absorption in case the material is kept flowing through the laser beam intersection is almost twice the absorption without flow. The reason for this is photo-degradation. This can be easily ascribed to the photochemical processes which form the active species for polymerization and which display a significantly different absorptive behavior. These tests also revealed that 5 ml/h is the optimum flow rate to refresh the irradiated sample in the focal volume in a reasonable time without losing too much compound; therefore all measurements for determining the MPA cross section of PIs have been carried out with a 5 ml/h flow rate.

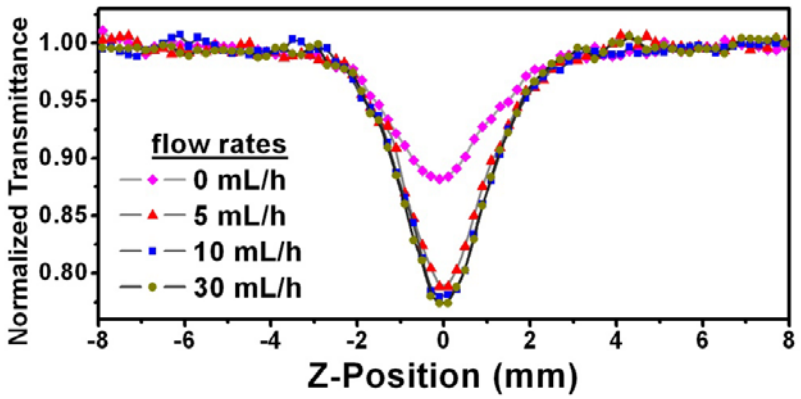

Fig. 5.1. Measured Z-scan of B3FL with the same pulse energy of 150 nJ but different flow rates

5.2. Determining the order of nonlinear absorption

Appearance of the closed aperture Z-scan signal is a signature of positive or negative nonlinearity corresponding to self-focusing and self-defocusing. In open aperture Z-scan measurements, the appearance of the signal reveals that whether the saturation of absorption (SA) has occurred or MPA has occurred. In Fig. 5.2, part (a) demonstrates a typical signal in the case of MPA whereas (b) display a typical signal in the case of SA.

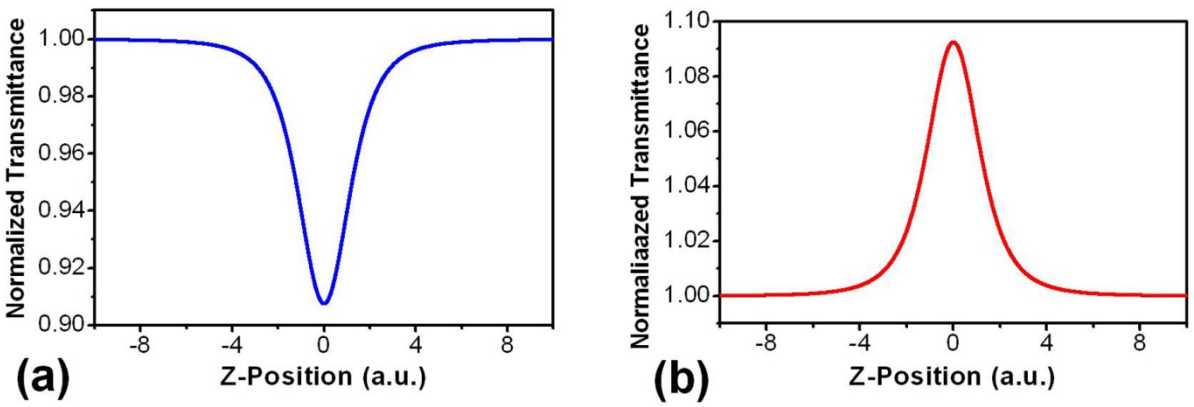

Fig. 5.2. A typical open aperture Z-scan signal, (a) shows MPA and (b) shows SA

The main task now is the determination of the order of the nonlinear absorption. Although Fig. 5.2 (a) demonstrates that MPA has occurred in the medium under investigation but it does not reveal any information about the order of MPA; It does not answer to this question that whether 2PA has occurred or 3PA or even higher order of MPA. The following methods can be applied to determine the order of MPA.

5.2.1. Comparing the extracted Rayleigh range from fitting curves with the experimentally measured Rayleigh range

By fitting Eq. (2.178) and (2.208) to the measured Z-scan data, 2PA and 3PA coefficients can be extracted respectively. In addition to this, the Rayleigh range can also be extracted from the fitting curves. This gives us the possibility for determining the order of MPA. This method can be illustrated by presenting the following example. In Fig. 5.3 the data points are measured Z-scan data for Rhodamine B. In figure (a) the solid line is the fit curve using Eq.(2.178) from which a Rayleigh range of 0.87 mm was extracted. In figure (b) the solid line is the fit curve using Eq. (2.208) from which a Rayleigh range of 1.64 mm was extracted and in figure (c) the solid line is the fit curve using Eq. (2.208) while the Rayleigh range has been fixed equal to 0.86 mm, the same value as experimentally measured . Fitting Eq. (2.178) to the measured Z-scan data as shown in Fig. 5.3 (a) leads to firstly a well-fitted curve to the data and secondly an extracted Rayleigh range that is in good agreement with its measured value. Comparison between figure (a) and (b) or between figure (a) and (c) results in this conclusion that 2PA has occurred in Rhodamine B because, in figure (b) the extracted Rayleigh range is very different from its measured value and in figure (c), the fit curve is not well-fitted to the data in comparison with the fit curve in figure (a).

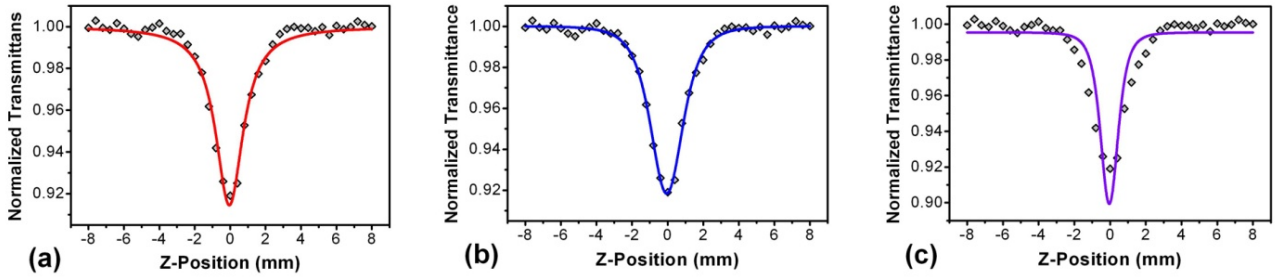

Fig. 5.3. Measured Z-scans for a 0.2 mm thick cell of Rhodamine B. (a) shows the fit cure assuming 2PA from which the Rayleigh range was extracted 0.87 mm. (b) shows the fit cure assuming 3PA from which the Rayleigh range was extracted 1.64 mm. (c) shows the fit cure assuming 3PA with a Rayleigh range fixed to 0.87 mm in the fitting process

5.2.2. Slope of log (1-*T*) versus log (*I*) as a signature for determining the order of nonlinear absorption

From Eq. (2.185) (derived for 2PA) the following equation can easily be obtained.

$$\log(1-T_{\min}) = \log(I) + \log\left(\frac{\alpha_2 L_{eff}}{\sqrt{2^3}}\right) \tag{5.1}$$

The above equation indicates that the slope of log (1-T_{min}) versus log (I) is one.

From Eq. (2.209) (derived for 3PA) the following equation can be obtained.

$$\log(1-T_{\min}) = 2\log(I) + \log\left(\frac{\alpha_3 L_{eff}}{3\sqrt{3}}\right) \tag{5.2}$$

Eq. (5.2) indicates that the slope of log (1- T_{min}) versus log (I) is two assuming 3PA. Therefore, one can determine the order of MPA via examining the slope of log (1- T_{min}) versus log (I). Fig. 5.4 (a) shows the log (1- T_{min}) versus log (I) for B3FL. The slope of the trace was measured to be 1.05 that is an indicative of 2PA process. Fig. 5.4 (b) shows the log (1- T_{min}) versus log (I) for BAC-M. The slope of this trace was measured to be 1.94 that is an indicative of 3PA process. It should be mentioned that 2PA process in B3FL and 3PA in BAC-M were proved using the method presented in section 4.2.1.

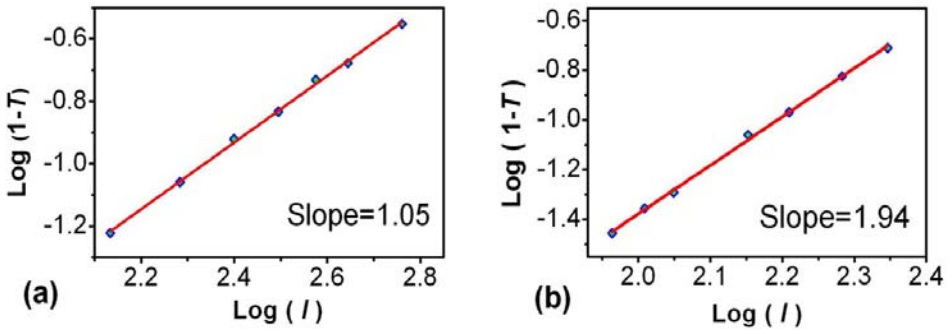

Fig. 5.4. Log (1-*T*) versus log (*I*) for B3FL (a) and BAC-M (b).

5.2.3. Deducing from linear absorption spectra

To some extent, linear and nonlinear absorptions are linked. The 2PA generally occurs at shorter wavelengths than twice the linear absorption peak [87] ($\lambda_{1pA} < \lambda_{2pA} < 2\lambda_{1pA}$). Based on this link one can predict the order of MPA by measuring the linear absorption spectra. Fig. 5.5 shows the linear absorption spectra of B3FL and BAC-M as an example. The wavelength of the laser beam used in our experiments was 798 nm that corresponds to a photon energy of 1.56 eV. The peak absorption for B3FL is 430 nm corresponding to a photon energy of 2.9 eV. Therefore, simultaneous absorption of two photons of 798 nm provides enough energy (3.12 eV) to complete this transition in B3FL. The peak absorption for BAC-M occurs at 355 nm that corresponds to a photon energy of 3.5 eV. Therefore two photons of 798 nm cannot provide the required energy to complete this transition in BAC-M and hence, three photons must be simultaneously absorbed to excite this molecule from the ground to the excited state. In this way the linear absorption spectra can be utilized to give a reasonable proof to predict the order of MPA.

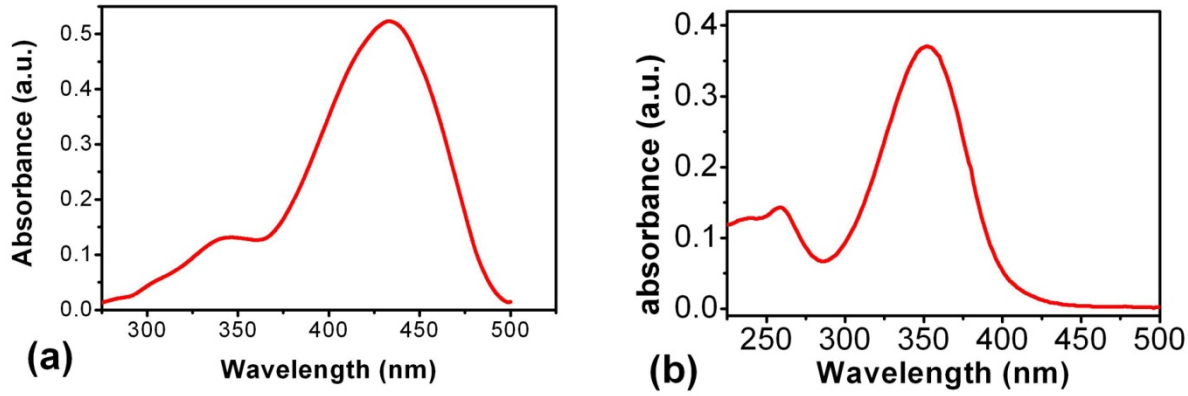

Fig. 5.5. Linear (1P) absorption spectra for B3FL (a) and BAC-M (b)

For all samples, the three methods presented in above sections have been applied to ensure the deduced order of MPA.

5.3. Evaluating the 2PA properties of synthesized 2PIs

In this section the Z-scan results obtaineded for 2PIs are presented from which the 2PA cross section of examined compounds will be extracted. The synthesized 2PIs in terms of their 2PA behavior will be compared. The initiating activities of these compounds, that display their ability to be exploited in 2PIP based microstructuring, are discussed.

5.3.1. Determining the 2PA cross section of 2PIs

The first step in measuring the MPA cross section of a new PI is to establish a reference. For this purpose a Rhodamine B sample with otherwise identical experimental parameters is a good choice, because it is an accessible and inexpensive compound with its linear and nonlinear optical properties well determined and reported in literature. For the Rhodamine B compound, methanol (MeOH) was chosen as the solvent. When the laser starts working it is required to wait for about half an hour for the pulse energy approaches its maximum value and becomes stable. Before starting the Z-scan both signals from the reference and the collecting diodes should be checked and the height of the signal should be adjusted so that it should be neither saturated nor too weak. The cuvette filled with Rhodamine B was mounted on the translation stage and the beam waist was adjusted at the middle of the scanning range. The scanning range was chosen 16 mm and the scanning points were chosen to be 41 points in order to translate the sample within an experimentally acceptable distance but for which a reasonable difference in transmittance is observed. In each step the sample was irradiated with 300 pulses. The power of each individual pulse is measured by the picoscope. The individual pulse energy and then the average pulse energy over 300 pulses is calculated by the program. In order to fit Eq. (2.178) or (2.208) to the Z-scan data the transmittance must be normalized. For this purpose the entire transmittance measured during a complete scanning must be divided by the transmittance measured in the linear regime (referred to as the base line); where, the sample is far enough away from the beam waist so that the intensity is not high enough to induce nonlinear absorption. In Fig. 5.6 (a) the base line corresponds to a transmittance of 3.65. In Fig. 5.6 (b) the normalized transmittance as the result of dividing the transmittance by the base line is shown. The solid pink line indicates the fit curve assuming 2PA whereas the solid orange line represents the fit curve assuming 3PA while the Rayleigh range was fixed equal to 0.86 mm in both fitting process. By comparing the quality of being well-fitted for these two fit curves and also examining the methods presented in section 4.2, it was concluded that 2PA is the predominant nonlinear absorption process occurring in Rhodamine B.

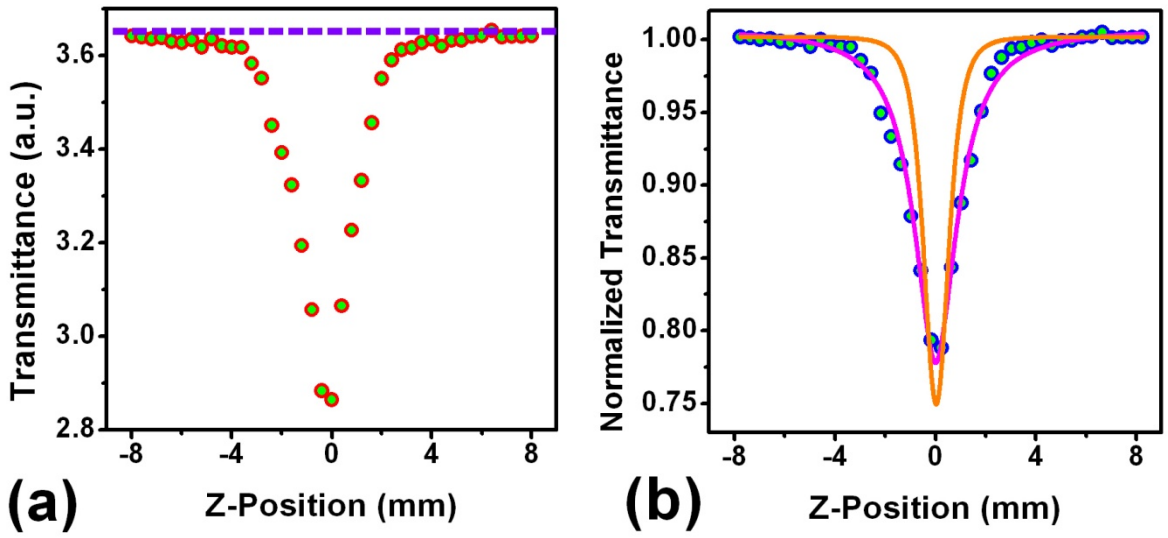

Fig. 5.6. Measured Z-scan of a 0.2 mm cuvette filled with Rhodamine B (a). the blue dashed line shows the base line. (b) shows the normalized transmittance along with the fit curves assuming 2PA (pink line) and 3PA (orange line)

From fitting Eq. (2.178) to the measured normalized transmittance the parameter $q_0=\alpha_2 L_{eff} I$ is extracted from which 2PA coefficient is calculated. However, in order to calculate the average value of 2PA coefficient firstly and to verify the contribution of exited state absorption (ESA) secondly, several Z-scans at different pulse energies for each sample have been carried out. Unlike the conventional local fitting which separately treats data at each pulse energy the global fitting for processing Z-scan data was used. This allows processing a set of experimental data measured with different pulse energies together [88]. In Fig. 5.7 (a) the measured Z-scans of a 0.2 mm thick cuvette of Rhodamine B for different pulse energies are depicted. Solid gray lines show the fit curves using Eq. (2.178) from which q_0 corresponding to different energies was extracted. In Fig. 5.7 (b) the results for q_0 versus pulse energy is depicted. The plot shows a linear behavior that is a clear indication for pure 2PA and nonexistence of ESA or any higher order nonlinear absorption. By fitting Eq. (5.3) to the extracted q_0 versus pulse energy, the 2PA coefficient was extracted and then the 2PA cross sections of 118 GM was obtained using Eq. (2.150) ($\sigma_2 = \hbar\omega\alpha_2 / N_A \rho \times 10^{-3}$).

$$q_0 = \alpha_2 L_{eff} \, 4\sqrt{\frac{\ln 2}{\pi}} \, \frac{E}{\pi w_0^{\,2} \tau} \tag{5.3}$$

where L_{eff}=0.2 mm, w_0=22 μm, τ=100 fs, α_2 is the 2PA coefficient and E is the pulse energy that is obtained by the dividing the laser output power by the repetition rate (1 kHz).

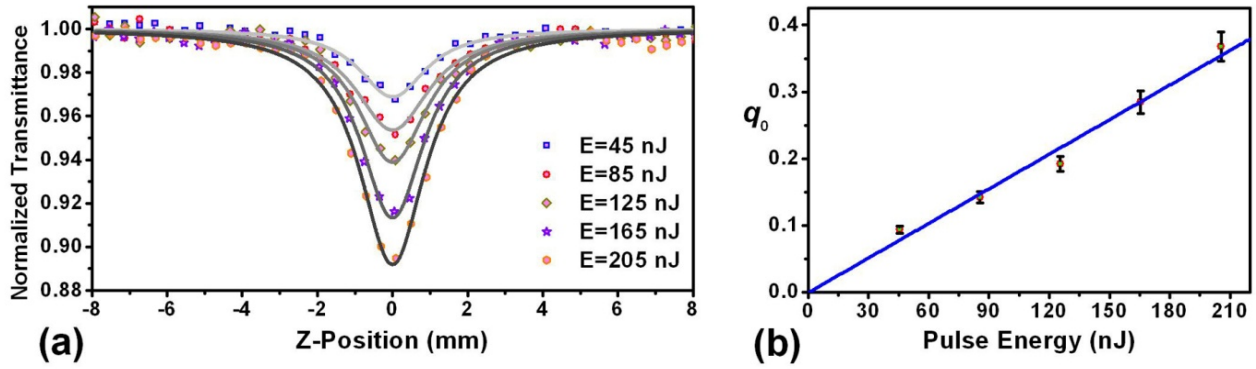

Fig. 5.7. Measured Z-scans of 0.2 mm thick cuvette of Rhodamine B at different pulse energies (a) and q_0 versus pulse energy (b)

In the next step, the Z-scan measurements for all initiators were carried out as performed for Rhodamine B. For the OA Z-scan measurements an equimolar concentration of the compounds

(1×10^{-2} M) was prepared using spectroscopic grade solvents. The initiators were all dissolved in tetrahydrofuran (THF) as all compounds showed a sufficient solubility in this solvent. For comparison, it is important that the same solvent is used for all compounds, because a different polarity of the solvent causes a change in activity of the molecules. For all synthesized PIs the methods suggested in section 4.2 were employed to determine the order of nonlinear absorption. The results revealed that 2PA is the predominant nonlinear absorption process occurring in all these compounds.

In Fig. 5.8 (a) measured Z-scan of a 0.2 mm cuvette of **B3K** for different pulse energies range from 35 nJ to 215 nJ are shown. Solid lines represent fit curve using Eq. (2.178) under assumption of 2PA. In part (b) the q_0s extracted from figure (a) are depicted versus pulse energy. The solid straight line demonstrates the fit curve using Eq. (5.3) from which a 2PA cross section of 260 GM was obtained for **B3K**.

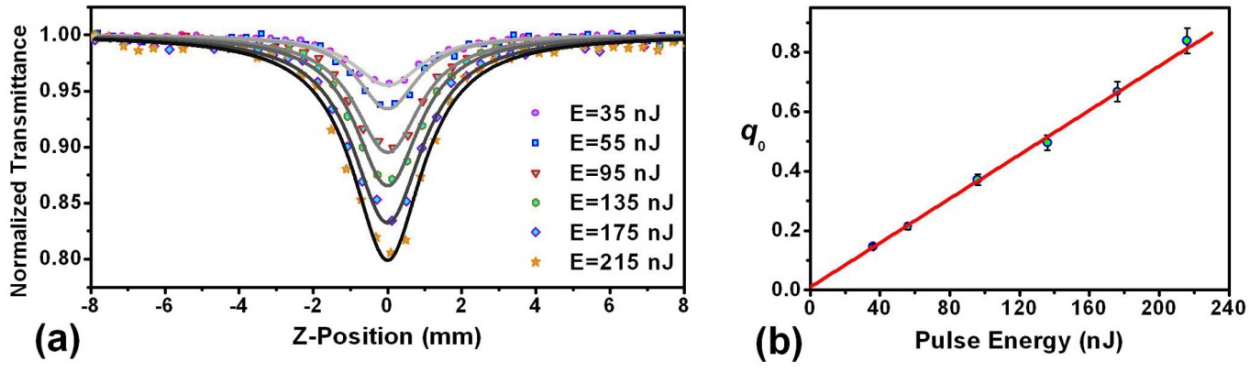

Fig. 5.8. Measured Z-scans of B3K for different pulse energy (a). q_0 versus pulse energy (b).

Fig. 5.9 (a) shows the measured Z-scans of **B3BP** for different pulse energy ranges from 25 nJ to 165 nJ. Fitting Eq. (2.178) to the experimental Z-scan data gives q_0 for different energies that are shown in part (b). Solid straight line demonstrates the fit curve using Eq. (5.3) that proves the predominance of 2PA and also confirms that no ESA has occurred in this compound. 2PA cross section was found to be 317 GM for B3BP compound.

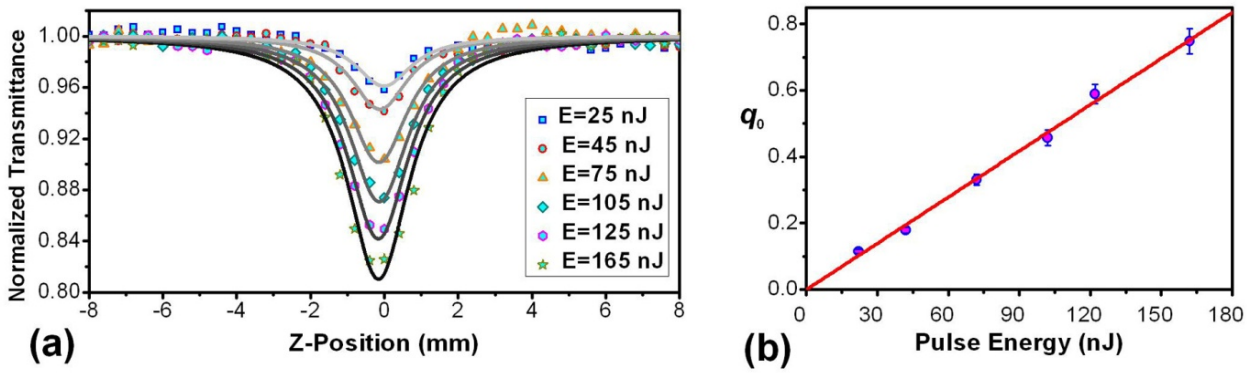

Fig. 5.9. Measured Z-scans of B3BP for different pulse energy (a) and q_0 versus pulse energy (b)

Fig. 5.10 shows measured Z-scans of **B3FL** for different pulse energies ranges from 20 nJ to 140 nJ. The highest 2PA cross section in 2PIs was measured for this compound that is 443 GM.

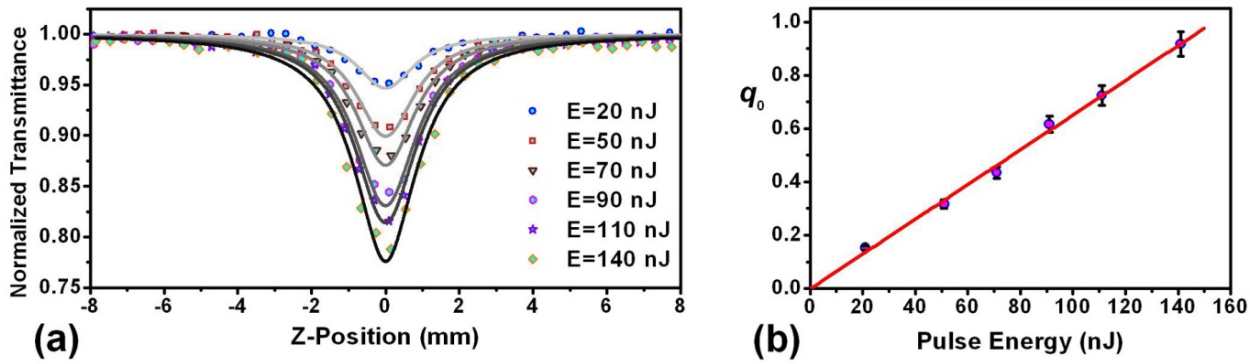

Fig. 5.10. Measured Z-scans of B3FL for different pulse energy (a) and extracted q_0 versus pulse energy

In Fig. 5.11 measured Z-scans for **3,6,B3FL** are depicted. Normalized transmittance was measured for different pulse energies range from 30 nJ to 210 nJ. Extracted q_0s scales linearly with pulse energy that is a signature of 2PA process. By fitting Eq. (5.3) to extracted q_0s for different pulse energy, the 2PA cross section of 296 GM was found for **3,6,B3FL.**

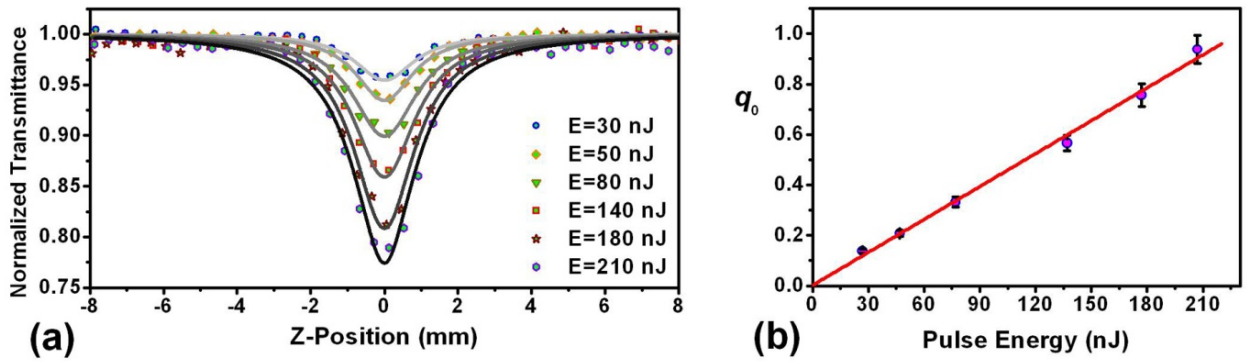

Fig. 5.11. Measured Z-scans of 3,6,B3FL for different pulse energy (a) and q_0 versus pulse energy

Fig. 5.12 shows measured Z-scans (a) and extracted q_0s (b) for **BB3FL**. Fit curves in part (a) as well as (b) demonstrate the predominance of 2PA process. 2PA cross section of 370 GM was measure for **BB3FL.**

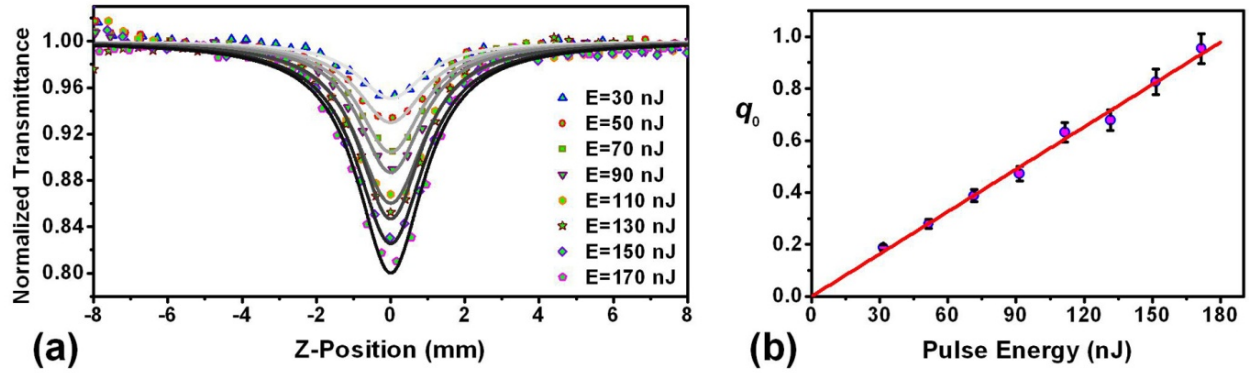

Fig. 5.12. Measured Z-scans of BB3FL for different pulse energy (a) and q_0 versus pulse energy

In Fig. 5.13 Z-scans data for **B3AN** and fit curve assuming 2PA are shown in part (a) and extracted q_0s for different pulse energy are depicted in part (b). 2PA cross section for this compound was measured 234 GM.

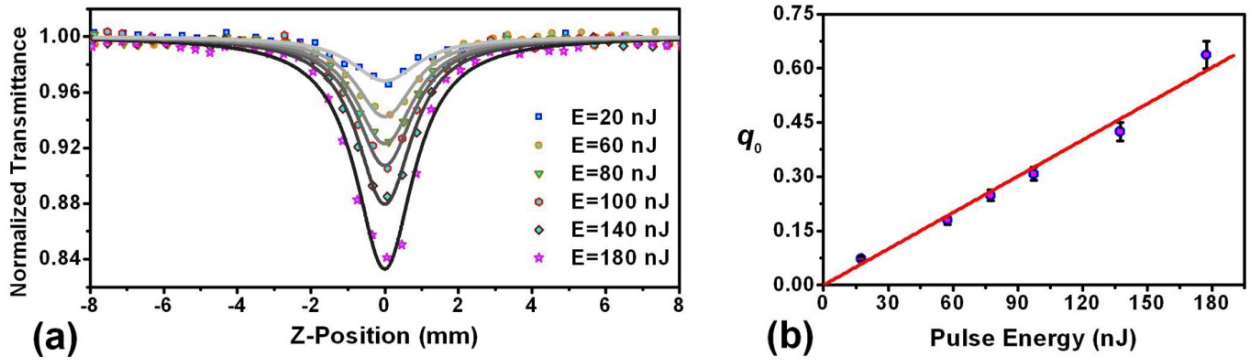

Fig. 5.13. Measured Z-scans of B3AN for different pulse energy (a) and q_0 versus pulse energy

In Fig. 5.14 Z-scans data for **BB3AN** and fit curve assuming 2PA are shown in part (a) and extracted q_0s for different pulse energy are depicted in part (b). 2PA cross section for this compound was measured 255 GM.

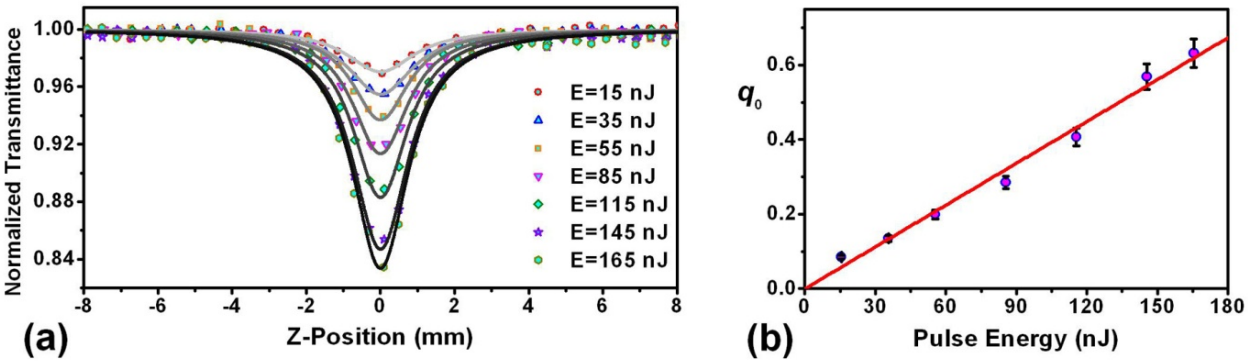

Fig. 5.14. Measured Z-scans of BB3AN for different pulse energy (a) and q_0 versus pulse energy

5.3.2. Comparison of the 2PA probability of 2PIs and Discussion

In Table 1 2PA cross section for all initiators is summarized.

Table 1

Compound	Rhod B[1]	B3AN	BB3AN	B3K	3,6,B3FL	B3BP	BB3FL	B3FL
2PA cross section (GM)	118	234	255	260	296	317	370	443

[1] Rhodamine B is a dye and was examined as a reference.

In Fig. 5.15 (a) q_0 versus pulse energy for all samples is depicted. Fig. 5.15 (b) also provides a comparison between 2PA cross section of all compounds.

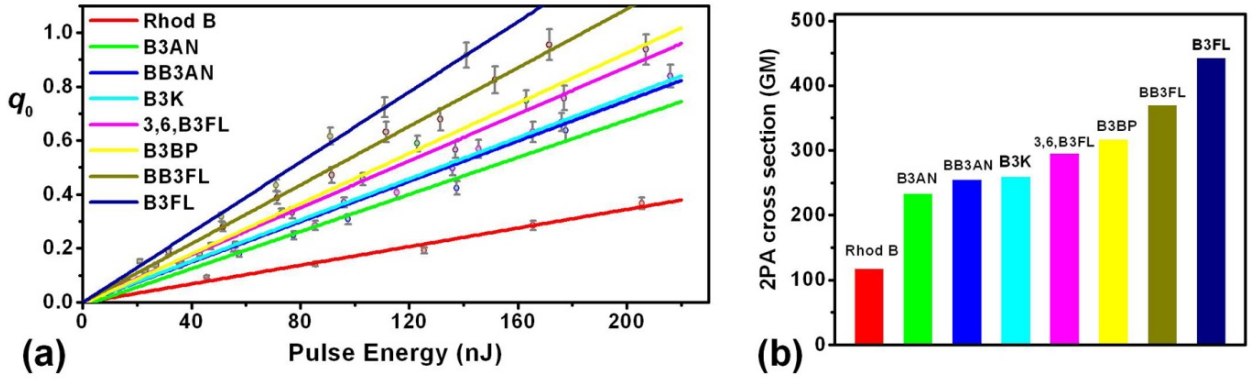

Fig. 5.15. q_0 versus pulse energy for all synthesized compounds (a) and a graphical representation for comparing the 2PA cross section in all samples (b)

It is theoretically predicated and experimentally found that the 2PA cross section can be enhanced by increasing the conjugation length and the donor and acceptor strengths [89, 90]. Our experimental results obtained from Z-scan measurements for 2PA evaluation also manifested that the **B3BP** initiator with longer conjugation length reveals a larger cross section value (317 GM) than **B3K** of 260 GM. The lower 2PA cross section of **B3AN** compared to that of **B3BP** may be due to the relatively lower absorption in one-photon spectra at about 400 nm, which indicates that the 2PA peaks in 2PA spectra are shifted in wavelength away from 800 nm. Interestingly, **3,6,B3FL**, which theoretically should facilitate an intermolecular electron transfer process, exhibits a lower cross section value compared to **B3FL**. An explanation can be given by the red-shift-induced low 2PA at the given wavelength. Among the synthesized compounds, **B3FL** had the highest 2PA cross section value of 443 GM. One reason is the suitably strong absorption around 400 nm, which ensured the considerable 2PA at 800 nm. However, determination of the 2PA cross section gives only information about the absorption behavior (similar to the extinction coefficient of one-photon absorption in Lambert-Beer's law). Thus, 2PIP structuring tests were performed to further characterize the new PIs.

5.3.3. Comparing the initiating activities of the PIs via determining the 2PIP structuring performance and structural quality

To estimate the activity of the PIs, defined test structures (lateral dimension: 50 ×50 µm, 10 µm hatch-distance, 0.7 µm layer-distance, 20 layers) were written into the monomer formulation by means of 2PIP. A 1:1 mixture of Trimethylolpropane triacrylate (TTA) and ethoxylated (20/3) trimethylolpropane triacrylate (ETA) as an acrylate-based test resin with the same molar PI concentration of 6.3 $\times 10^{-6}$ mol PI/g resin was used. For the direct laser writing of 3D structures, a Ti-sapphire laser providing NIR pulses at 780 nm wavelength with a pulse duration of 100 fs was used. The system operates at a repetition rate of 80 MHz. The laser intensity was screened in a range of 1–32 mW (measured after passing objective). The laser is focused by a 100× oil immersion microscope objective (NA = 1.4) and the sample is mounted on a high-precision piezoelectric XYZ scanning stage with a 200 nm positioning accuracy. For all samples the same fabrication process was implemented: The optical material was drop-cast onto a glass substrate.

Subsequently, the samples were exposed to the laser beam, and the focus was scanned across the photosensitive material, which leads to an embedded 3D structure inside the material volume. After laser writing, the unexposed material was removed by development of the structure in ethanol. The resulting structures, particularly their structural dimensions, integrity and surface quality, were studied by means of SEM.

5.3.4. Comparison between the structuring activity of the PIs and discussion

Fig. 5.16 (a) shows the structuring process windows for various newly synthesized PIs and some commercially available PIs and Fig. 5.16 (b) shows four quality-classified structures indicated by 1, 2, 3 and 4. The different color of the bars and their corresponding numbers in Figure (a) indicate the quality of the structures. At the lower end of each ideal processing window in the diagram, only not well-connected structures could be obtained after the standard post processing procedure, as the threshold of initiation is not reached. Above that, class 1 defines excellent structures with fine hatch-lines and class 2 good structures with thick hatch-lines (compared to class 1). Generally, broader "perfect" processing windows (class 1 and 2) and lower laser intensities are desired in terms of high throughput in mass production because this allows a splitting of the initial laser beam for parallel processing with multiple laser heads at high feed rates, while thermally induced decomposition of the material can be avoided. Samples rated as class 3 have shapes that can be identified but with small mistakes (e.g. holes, exploded regions caused by overexposure). Parts structured with laser intensities rated as class 4 no longer showed acceptable results. The shapes are no longer identifiable with completely missing walls and/or vast holes.

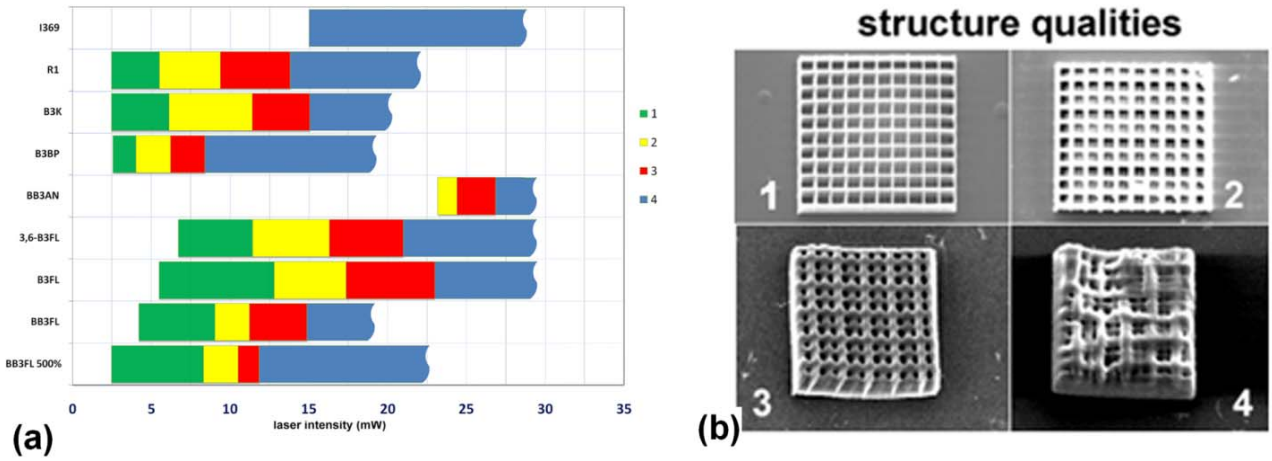

Fig. 5.16. TPIP screening tests for different PIs (a) and Classification of the structures by the typical quality of their shapes (b). 1: excellent structures with fine hatch-lines, 2: good structures with thick hatch-lines, 3: having identified shapes but with small mistakes and 4: non-acceptable results.

In our measurements, the well-known initiator from the literature R1 can be used to build nicely shaped structures at low laser intensities. The commercially available PI Irgacure 369 did not show good results at 800 nm at the given PI concentration (6.3×10^{-6} mol PI/g resin), which is

in good agreement with the low 2TA cross section [91]. The benzophone-based initiator B3BP is able to build up nice structures at similarly low laser intensities as R1, but its ideal processing window is significantly smaller. In the structuring tests, it was not feasiable to obtain any good results with B3AN due to its poor solubility (data not shown). Although BB3AN, to some extent, showed higher solubility in the resin but high laser intensities are required to obtain good structures. This might be explained by the relatively small 2TA cross section and also the low solubility in the resin.

The initiators 3,6-B3FL, B3FL and BB3FL showed very good results in these tests. The ideal processing windows are broader than that of the references, but the required laser intensities are slightly higher. Despite the lower cross section compared to that of B3BP, the ideal window of 3,6-B3FL is much broader. B3FL exhibited much broader ideal processing windows than those of 3,6-B3FL, which is in good agreement with the Z-scan values. The lower laser intensity required for BB3FL might be attributed to the increased solubility. Laser intensity as low as 2.47 mW was required to obtain nice structures at higher concentrations (3.2×10^{-5} mol PI/g resin which is 5 times higher than that of previous structuring test) of BB3FL. B3FL turned out to be the best performing initiator in our tests having the broadest ideal structuring process window at low concentration (6.4×10^{-6} mol PI/g resin) and good solubility in the resin.

The tests were repeated also with lower molar PI concentrations in order to determine the lowest possible PI concentration under these conditions. For the lower concentration (1.6×10^{-6} mol PI/g resin, 0.1%wt of B3FL) the results for all initiators are very similar to those at higher concentration, with the only difference having a slight shift of the ideal processing window towards higher laser intensities.

Additionally, more complex 3D structures were inscribed into the material volume using B3FL (6.4×10^{-6} mol PI/g resin) as initiator as shown in Fig. 5.17. These shapes are showing perfectly the advantages of 2PIP compared to other rapid prototyping techniques. High spatial resolution, which is otherwise inaccessible, and complex 3D structures with massive overhangs such as the Stephen's Cathedral of Vienna (Fig. 5.17a) can be easily obtained [86].

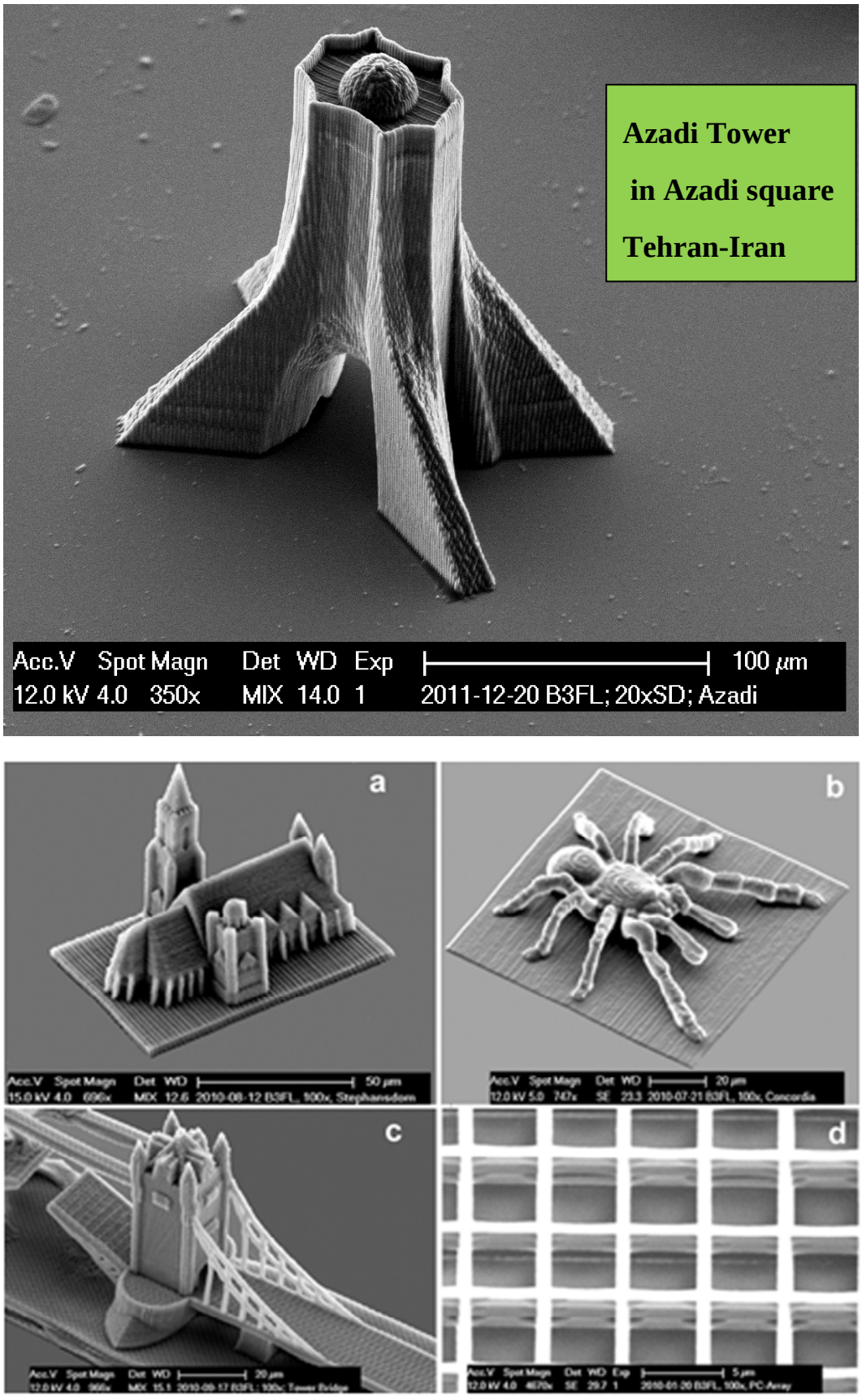

Fig. 5.17. 3D structures (resin ETA/TTA 1:1, B3FL as initiator): (a) St. Stephen's Cathedral; (b) Tarantula Spider; (c) detail of the London Tower Bridge; (d) detailed view of the woodpile structure

5.4. Multi-photon induced photo-grafting

Molecular grafting is a versatile tool providing means for tailoring physio-chemical properties of surfaces. True 3D grafting has been recently achieved by multi-photon excited process. MPA requires more intense laser beam and also high MP absorptive materials. The higher the MPA cross section the lower light intensity is required. For this reason, much effort has been put on designing molecular structures with higher MPA. Determining the MPA cross section is the main task after producing a new compound. The Z-scan theory was extended in order to determine the order of any nonlinear absorption and then to determine the nonlinear absorption cross section.

In this section the measurements for the exact determining of the order of nonlinear absorption and then 3PA cross section of a reagent, with the marketing name of BAC-M, as a grafting molecule are presented. At the end, the efficient exploitation of this compound in 3D microstructuring via photo-grafting process will be exhibited.

5.4.1. Determining the 3PA cross section of 2,6-Bis(4-azidobenzylidene)-4-methylcyclohexanone (BAC-M); a reagent as a grafting molecule

Z-scan measurements for the exact determining of the nonlinear absorption cross section of BAC-M were performed using the same setup as used for PIs. It is of primary importance that the order of nonlinear absorption must be first determined. To determine the order of nonlinearity, 2PA and 3PA respective equations were fitted to the experimentally measured Z-scan data as shown in Fig. 5.18 (a). The blue line, which is well fitted to the data points, represents the fit curve assuming 3PA whereas the pink line is the fit curve under assumption of 2PA in BAC-M. By looking at both fit curves, it can visually be estimated that the 3PA process is the most predominate nonlinear absorption occurs in BAC-M. Fig. 5.19 (a) shows the Z-scans performed for BAC-M with different pulse energies ranging from 90 nJ (corresponds to a peak intensity of 1.4×10^{11} W.cm^{-2}) up to 220 nJ. No nonlinear absorption was observed for Pulse energies lower than 90 nJ. Pulse energies higher than 220 nJ was not used because the solvent itself started to exhibit nonlinear absorption using pulse energies higher than 230 nJ that makes so difficult to subtract the pure 3PA for BAC-M from the effective 3PA. From Fig. 5.19 (a) the maximum normalized transmittance corresponding to each pulse energy can be measured. To be certainly convinced that our prediction of 3PA in BAC-M is correct, the log (1-*T*) versus the log (*I*) was also plotted to measure the slope of the curve, by which one can determine the order of nonlinear absorption. By fitting a linear equation to the data in Fig. 5.18 (b) a slope of 1.94 was measured, which is an indication of a 3PA process. It is also mentioned that the linear peak absorption of this compound occurs at about 355 nm, which corresponds to a photon energy of 3.5 eV. This is greater than the energy of a pair of photons of 798 nm (used in the Z-scan experiment). Thus, three photons of 798 nm are needed to excite this molecule. Therefore, employing all three different methods presented in 4.2 for determining the order of nonlinear absorption in BAC-M revealed for certain that 3PA is the predominant nonlinear absorption occurs in this compound.

It is worthwhile to mention this important fact that, exploiting higher order nonlinear absorption in photo-grafting or photo-polymerization leads to a finer structural resolution. It is due to this

fact that the n[th] order nonlinear absorption probability increases with the same order of intensity. For instance, a focal volume in which 3PA happens is smaller than that in 2PA case.

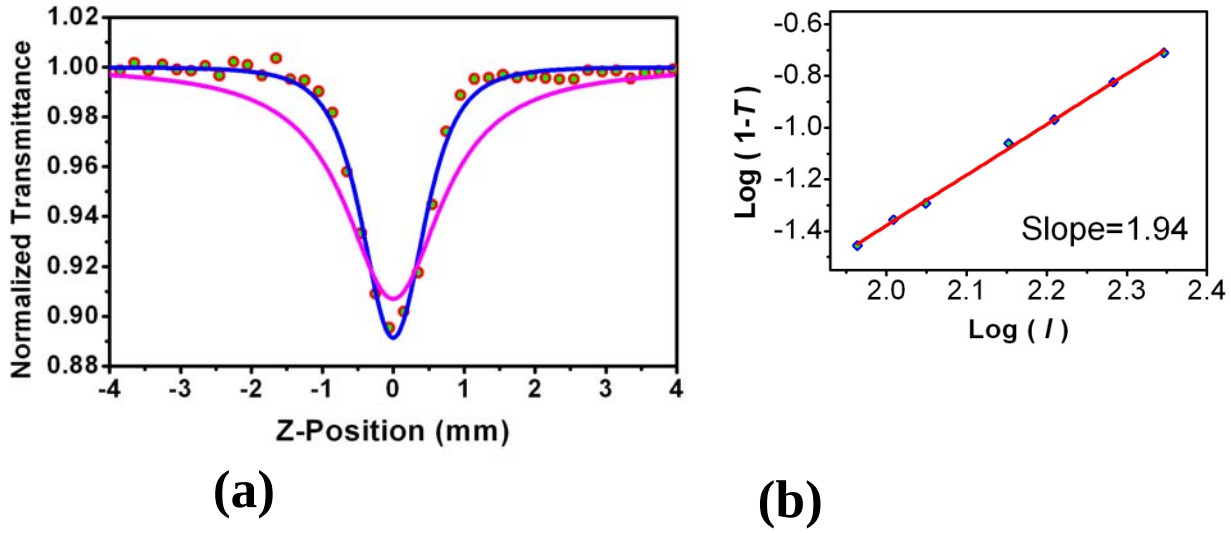

Fig. 5.18. (a) depicts a Z-scan of BAC-M along with the fit curves assuming 2PA (pink) and 3PA (blue). (b) shows the log (1-*T*) versus the log (*I*) for BAC-M

In Fig. 5.19 (b) the results for P_0, extracted from fitting Eq. (2.208) to the experimental Z-scan data, is plotted versus pulse energy. The plot shows a linearity dependence that provides an additional evidence proving the predominance of 3PA process and absence of excited state absorption or any other order of nonlinear absorption in BAC-M. By fitting the linear equation $p_0 = \sqrt{2\alpha_3 L'_{eff}}\ I_0$ to the extracted data for P_0, shown in Fig. 5.19 (b), the 3PA coefficient α_3 for BAC-M was obtained 1.15×10^{-4} ($cm^3.GW^{-2}$) and then, the 3PA cross section σ_3 for BAC-M was calculated 1.19×10^{-78} ($cm^6.S^2$) from Eq. (2.152).

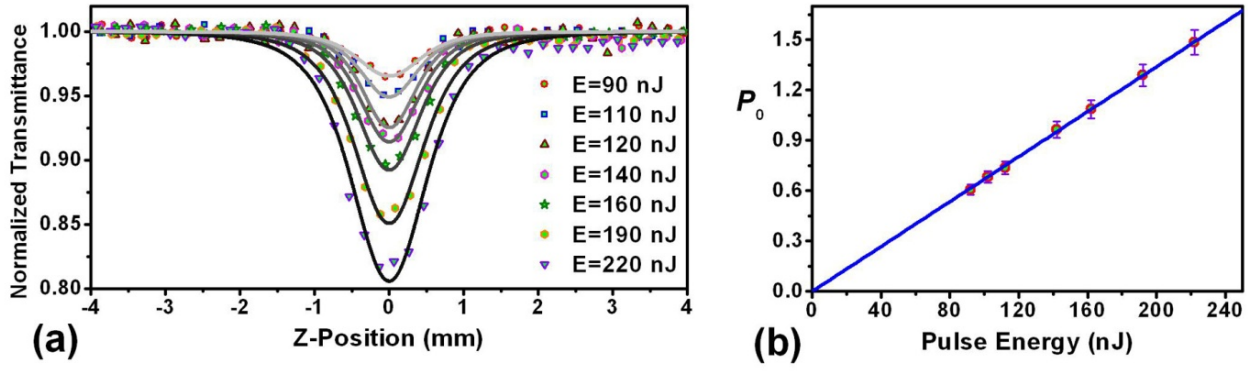

Fig. 5.19. Measured Z-scans of BAC-M for different pulse energy (a) and p_0 versus pulse energy

What can be learned from the above measurement is that 1). Analytical drived equations in chapter 2 for MPA are efficiently applicable to determine the order of nonlinear absorption and 2). The results obtained from Z-scan measurements showing a high nonlinear absorption cross section for BAC-M is consistent with the structuring test indicating a high grafting activity.

5.4.2. 3PA induced photo-grafting employing BAC-M as a grafting molecule

The samples are prepared from Polyethylene glycol (PEG) containing 1 wt. % of photoinitiator 4-(2-hydroxyethoxy)phenyl-(2-hydroxy-2-propyl)ketone (Irgacure 2959) by photopolymerization with UV light. Photopolymerized material pellets are soaked in 50 % Ethanol (EtOH) solution in order to remove residual monomer and photoinitiator. Next the EtOH is replaced with Dimethylformamide (DMF) and the samples are stored until used. Before laser photo-grafting the samples were immersed into the 10 wt% solution of BAC-M (grafting molecule) in DMF.

Ti:sapphire femtosecond laser (High Q, femtotrain) emitting pulses with duration of 80 fs at a 73MHz repetition rate around 793nm is used for 3PA laser grafting. The laser beam was focused with a 20x microscope objective (Zeiss, NA=0.4) into the samples. The focused laser beam into the volume of the sample interacts with the material (BAC-M) via 3PA. Since the 3PA process is highly localized, the process of BAC-M immobilization on the PEG matrix is restricted to a limited volume. By moving the laser focus within the sample 3D patterns of immobilized molecules can be "recorded". Immediately after the grafting procedure the samples are placed in DMF in order to remove residual BAC-M. Grafted BAC-M molecules were found to be fluorescent, thus the patterns produced by three-photon grafting was analyzed by a laser scanning microscope at the excitation wavelength of 488nm.

Fig. 5.20 (a) shows an image of a TU logo pattern produced starting from a 3D CAD file in an "stl" format. To produce a set of coordinates, which is later transferred to the sample positioning system, the 3D model is sliced along the vertical direction. Each slice is then produced by a series of parallel line scans, with scanning direction rotated by 90°C for each successive layer.

A 150μm large woodpile pattern shown in the Fig. 5.20 (b) is produced by a set of single scans at a distance of 25 μm within each layer. This pattern allows one to precisely evaluate the lateral size of the produced features. In this case the lateral resolution of around 4μm is obtained, by using a conventional 20 X microscope objective to focus the laser beam into the sample.

Achieved feature size is substantially smaller than dimensions of most mammalian cells, while the patterned volume is large enough for studies of single cell attachment and migration. Therefore, presented three-photon grafting is a good tool for fabrication of tailored surfaces for studies of cell adhesion and migration [92, 93].

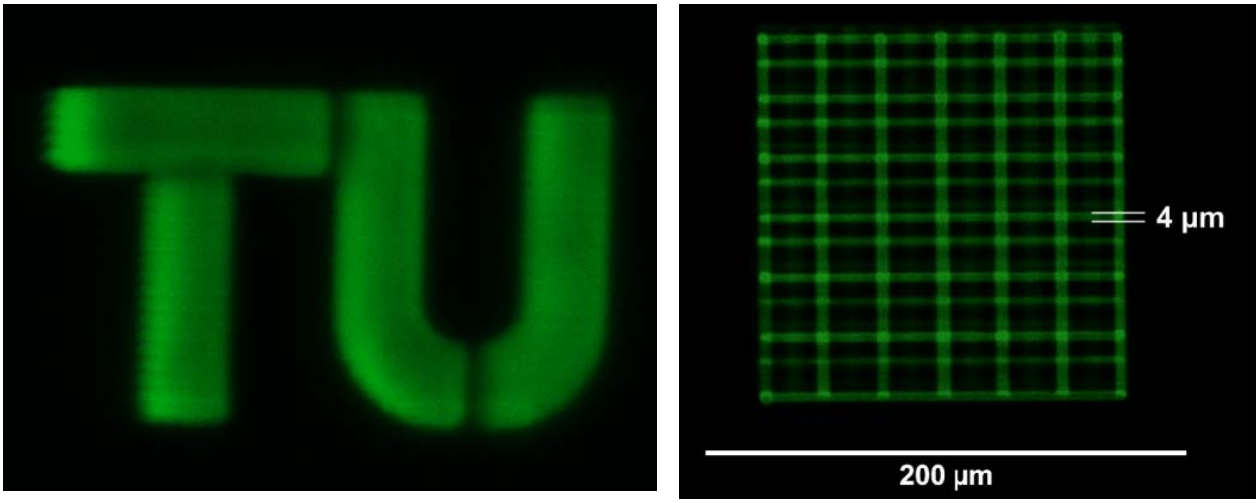

(a) **(b)**

Fig. 5.20. 3D patterns obtained by photo-grafting via multiphoton absorption: a) logo of the Technical University of Vienna; b) woodpile-like pattern with a lateral resolution of 4µm

5.5. Implanted Gold Nanoparticles in Various Types of Silicate Glasses

The metal nano-cluster composite glasses synthesized by ion implantation method have shown promising capability as photonic relevant materials. Nanometric metal particles implanted in glasses can exhibit a nonlinear optical response several orders of magnitude larger than that of bulk metals due to a phenomenon referred to as surface plasmon resonance. Metal nano-cluster composite glasses could offer the possibility to be employed for a variety of optical limiting applications (protective devices etc.) or to realize all-optical switching devices. The later would operate in a time range faster than the electronic ones without the need of converting optical signals to electrical ones. These devices are essentially based on nonlinear optical properties of materials, i.e. changes of the absorption coefficient (for optical limiting) or refractive index (for optical switching) of materials caused by an intense light beam or by a strong electric field. These properties sensitively depend on the size, shape, density and width distribution of the nanoparticles implanted in glass substrates.

The nonlinear absorption behaviors of the gold nanoparticles glass composites prepared by employing ion implantation method have been investigated. Four different types of optical silicate glasses, namely specially designed GIL49 and Glass B (made at the Glass Institute Hradec Kralove Ltd., Czech Republic) and commercially available silica glass and BK7 have been utilized as substrates in which the gold ions were implanted. The used glasses varied especially in the concentration of monovalent modifiers (Na_2O, K_2O) as well as their network formers (SiO_2, B_2O_3). The compositions of the glasses can be found in Table 2.

Table 2. The compositions of the silicate substrates (in wt. %)

Glass Substrate	SiO_2	Na_2O	Al_2O_3	CaO	MgO	K_2O	B_2O_3	BaO
GIL49	63.2	24.4	1.1	5.6	5.3	0.5	-	-
Glass B	88.0	8.7	3.3	-	-	-	-	-
BK7	68.3	8.8	-	0.1	-	8.1	12.1	2.5
Silica glass	100	-	-	-	-	-	-	-

Au+ ions were implanted into the silicate glasses under identical conditions using an accelerator at the Nuclear Physics Institute in Prague, Czech Republic. The energy of the implanted Au+ ions was 1701 keV. The fluence of the Au+ ions into Glasses was kept 10^{16} cm^{-2}. The nucleation of metal nanoparticles was initiated during the subsequent annealing of the as-implanted glasses. The as-implanted glasses were annealed at the temperatures of 600 °C for 5 h as identical conditions for all samples [85].

Annealed Glasses were characterized by TEM that confirmed the presence of metal nanoparticles in as-annealed glasses. The most relevant results of the characterization of the nano-structures obtained by TEM analysis for all samples are summarized in Table 3.

From Table 3, it is evident that the size and shape of the gold nanoparticles differ for the various types of glass although all the glasses were treated under identical conditions. Nanoparticles observed in glass B were small (1 - 7 nm) and were present in a relatively broad layer of 350 nm. In glass GIL49, nanoparticles with different sizes from 1 to 15 nm were found in a layer of 250 nm. Nanoparticles in BK7 glass were typically 6 - 25 nm and were concentrated in a narrow layer of 100 nm.

Table. 3. The TEM analysis of four different silicate glass substrates implanted and annealed under identical conditions.

Glass Substrate	Thickness of layer with nanoparticles	Size of nanoparticles	Shape of nanoparticles
Silica Glass	not measured	not measured	not measured
GIL49	250 nm	1 - 15 nm	spherical
Glass B	350 nm	1 - 7 nm	spherical
BK7	100 nm	6 - 25 nm	Non-spherical

5.5.1. Determining of the 2PA coefficient of the implanted Gold Nanoparticles

As seen from table 3, the gold nanoparticle layer in glass substrate has a thickness of about a few hundreds of nanometers. The thickness of glass substrates themselves are about one millimeter and indeed it is too difficult to polish them thiner than a few hundreds of microns. Thus, the thickness of the substratre is e few thousands times bigger than that of the embedded gold nanoparticle layer. In essence, the nonlinear absorption of a few hundres nanometers thick glassy host medum is much weaker than that of the gold nanoparticle layer but the nonlinear absorption of the entire substrate might be comparable with that of the embedded gold nanoparticle layer due the bigger thickness. In general, the order of nonlinear absorption in glass may differ from that in the the gold nanoparticle layer. Therefore, the main challenge and difficulty in the determination of the order and the magnitude of the nonlinear absorption of the metal nanocluster glass composite is the substraction of the host medium contribution to the entire nonlinear absorption.

It was focused on the measurement of nonlinear absorption and the study of the relationship between the nonlinear absorption and the size, depth distribution and shape of gold nanoparticles and also the structure of silicate glasses, which may be of crucial importance in designing e.g. nanoparticles based components for special applications.

In the first step, the laser parameters regime was determined such that MPA can be clearly attributed (from the measured Z-scans) to the existence of gold nano-clusters. By varying the pulse duration from 25 fs to 200 fs (possible range of our laser system) no dependence on the pulse duration was observed. All measurements were decided to be carried out with the shortest pulses possible (25 fs). Furthermore, it had to be verified that no nonlinear absorption is due to the glass substrates themselves. For this purpose, the intensity at which the standard glass (i.e. non implanted glass) starts exhibiting nonlinear absorption was first determined. The pulse

energy threshold for nonlinear absorption of the standard glasses was measure 50 nJ therefore; all the Z-scan measurements for the as-implanted and as-annealed samples were performed with pulse energies lower than 50 nJ. In this intensity regime the Z-scan results depend on the laser pulse energy, i.e. the nonlinear absorption of the sample increases with increasing pulse energy (see Fig. 5.22. (a)).

In the next step, the as-implanted glasses were measured. It was found that only as-implanted glass BK7 showed non-linear absorption. Applying recognition procedures for determining the order of nonlinear absorption led us to conclude that 2PA process is the most predominant nonlinear absorption occurring in as-implanted BK7 and all other as-annealed samples. By fitting Eq. (2.178) to the Z-scan of as-implanted BK7 shown in Fig. 5.21, a 2TA coefficient of 11.08 cm/GW was extracted.

In the next step, the influence of annealing on the 2TA of the resulting nano-composite material has been studied. Fig. 5.21 shows Z-scans of as-implanted and as-annealed BK7 performed with the same pulse energy of 30 nJ. It is evident from Fig. 5.21 that the 2TA property of BK7 showed a 40% increase after annealing.

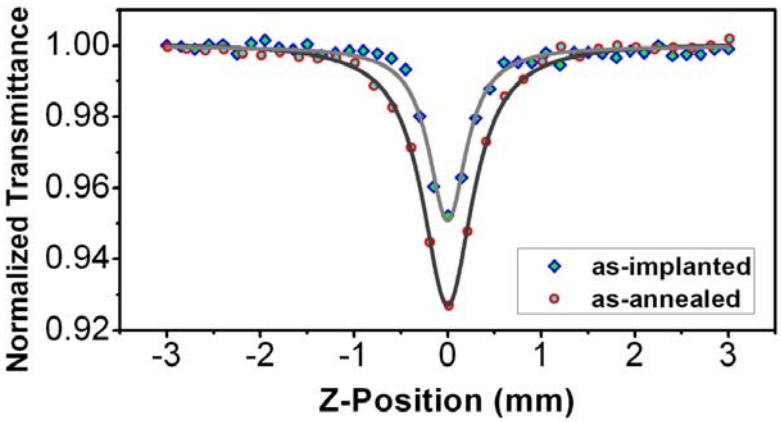

Fig. 5.21. Z-scan of gold nanoparticle as-implanted and as-annealed BK7 glass with the same pulse energy of 30 nJ

Fig. 5.22 (a) shows Z-scans of as-annealed glass BK7 measured with different pulse energies. As can be seen from Fig. 5.22 (a), the normalized absorbance increases linearly with laser pulse energy (laser intensity) which is an indication of 2TA due to the presence of gold nanoparticles in BK7. In Fig. 5.22 (b) q_0 is plotted versus pulse energy that shows a linear behavior providing an additional evidence to prove the predominance of 2PA in as-annealed BK7. By fitting $q_0 = \alpha_2 L_{eff} I_0$ to the extracted data for q_0 in Fig. 5.22 (b) a 2PA coefficient of 16.25 cm/GW was obtained for as-annealed BK7.

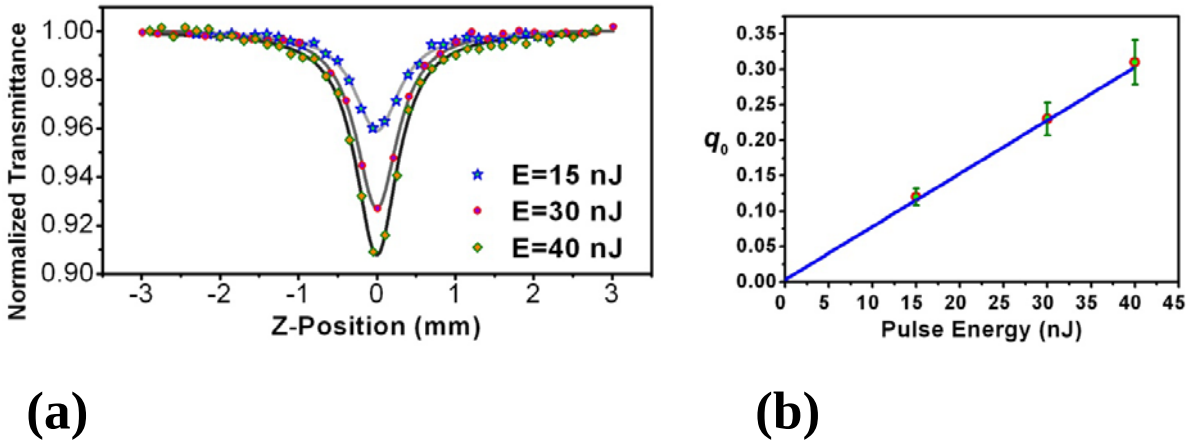

Fig. 5.22. Z-scans of as-annealed BK7 for different pulse energies (a) and q_0 versus pulse energy for this sample (b)

The same measurements were performed for all other as-annealed samples. The obtained 2TA coefficients for all samples are summarized in Table 4 and also are compared in Fig. 5.23. The highest 2TA coefficient of 16.3 cm/GW was obtained for as-annealed BK7 that had developed the largest non-spherical nanoparticles in the thinnest layer of 100 nm (see data presented in Table 3) whereas the smallest 2TA coefficient of 2.5 cm/GW was obtained for as-annealed silica glass that showed no absorption in the UV-VIS region (data is not shown) [94].

Table 4. 2PA coefficients

Glass substrate	***2PA coefficient (cm/GW)***
Silica glass	2.5
Glass B	5.2
GIL 49	7.8
BK 7	16.3

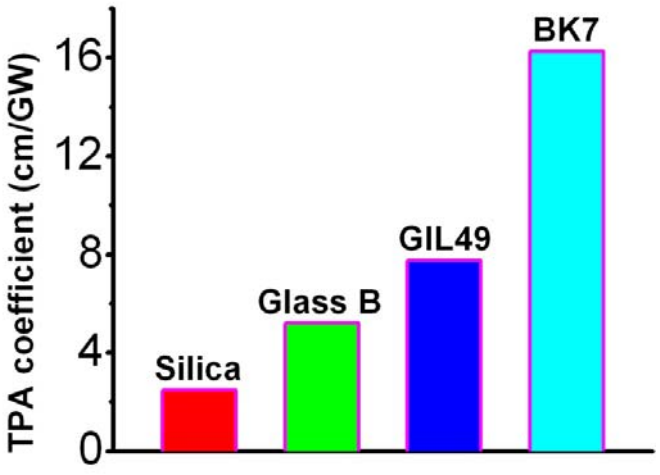

Fig. 5.23. A graphical comparison between 2PA coefficients

5.5.2. Discussion

The enhancement of the nonlinear response of the glass observed after implantation (in the case of BK7) and after annealing is caused due to the presence of gold nanoparticles in glass. This is because of the phenomenon referred to as surface plasmon resonance (SPR): The electron gas in the nanoscale particles is forced to resonate by oscillating electromagnetic field of the laser radiation. This results in an enhancement of the local electric field, and thus an increase in the optical nonlinear response of the metal nanoparticles implanted in the glasses. This causes an increase of several orders of magnitude in optical nonlinear response of metal nanoparticles compared to that of the bulk solid one.

From our data in Table 3 and 4, it becomes evident that the size of the nanoparticles is the most relevant factor for the 2PA coefficient. Measurements of the linear absorption spectra also show that the characteristic surface plasmon resonance feature is maximal for the largest clusters [95-99].

But also the shape and the layer thickness can have a substantial influence. Our results indicate that non-spherical nanoparticles in glass BK7 show higher 2PA coefficient than spherical ones in glass GIL49 and glass B. If the surface of a metal nanoparticle is rough, the surface plasmons (SP) are then strongly scattered leading to the accumulation of the electromagnetic field density [100]. This causes an enhancement of the local electric field and thus an increase in polarization. This is an indication of a susceptibility enhancement and a strong nonlinear response of the nano-composite material. Moreover, our results showed that the composition and structure of the used glass has significant impact on the resulting nonlinear optical properties.

One should notice that the metal nonlinear response is indeed further amplified by the SPR phenomenon which depends significantly on the difference of the dielectric constant of nanoparticles and the host medium. Therefore, the metal alone cannot explain by itself the high nonlinear response of nanocomposite media. Altogether it can be concluded that the substrate plays an important role in two different aspects: First, it affects the size, shape and distribution of the metal nanoparticles formed in the composite material (which are responsible for the strength of nonlinear response of metal nanoparticles) and secondly, as mentioned above, the dielectric contrast between the particles and the substrate is responsible for amplification of the local electric field, which thus determines the strength of the nonlinear optical response of the metal nanoparticles.

It is, as a conclusion, mentioned that the highest value of 2PA coefficient was found for glass BK7, in which the biggest non-spherical gold nanoparticles were developed, under the following conditions: Au^+ implantation, beam energy of 1701 keV, ion fluence of 1×10^{16} ion.cm^{-2}, post-implantation annealing in air at 600 °C for 5 hrs.

Chapter 6

6. Conclusion

2PA is a nonlinear process in which two-photons are nearly simultaneously absorbed to exit a molecule from the ground state to an excited state. The first photon excites the molecule to a non-existing virtual state having a life time depending on its difference energy with the nearest resonant state. If the second photon arrives in the time interval shorter than the virtual state life time, the absorption will complete; otherwise the virtual state will relax to the ground stats. Thus, the probability for a molecule to be excited via 2PA is proportional to the light intensity square.

Intensity dependence of 2PA has made this process as an efficient practical mean for bulk material modification. By focusing a pulsed laser beam within a transparent medium a small volume of materials around the focal point can be modified via 2PA whereas the rest of the medium remains unchanged. This capability allows 3D structuring by implementing two-photon induced polymerization (2PIP) technique. In 2PIP the focal point of a tightly focused pulsed laser beam is moved within a resin, consisting of a monomer and a two-photon initiator (2PI), using a 3D translation stage. Radicals produced by 2PIs via 2PA will trigger the polymerization process. After the completion of polymerization the uncured resin is washed away by a solvent and the 3D structures stands out.

Exploiting a 2PI with higher 2PA cross section allows irradiating the materials to the lower intensity laser radiation and thus leading to lower risk for damaging the materials. Thus, many researchers attempt to synthesize 2PI with higher 2PA cross section. To measure the 2PA cross section many techniques have been proposed within which the Z-scan method is the most popular one due to its easy-performing and high sensitivity. It also provides determining the asbolut measure of nonlinear absorption instead of relative values obtained by other techniques like four wave mixing. In the Z-scan technique a thin nonlinear medium is translated through the focal point of a focused pulsed laser beam. The energy transmitted through a small aperture on the far field is measured as a function of the sample position. The nonlinear refractive index as well as the sign of nonlinearity can be extracted from the CA Z-scan signal. To measure the MPA cross section the aperture is removed and the entire energy transmitted through the medium is collected for any sample position.

This work contains three parts: analytical calculation, numerical integration and experimental measurements. In analytical part, it was assumed that a thin nonlinear medium is moved along the propagation direction of a focused Gaussian beam through the focal plane. The propagation of the distorted laser beam through free space and then the intensity distribution on the far field aperture plane was calculated utilizing the Gaussian decomposition method. In this method the exiting complex electric field containing the nonlinear phase term is decomposed into a summation of Gaussian beam through a Taylor series expansion of the nonlinear phase term.

Propagation of each Gaussian beam and then the far field pattern of the beam on the aperture plane was calculated employing the Fresnel–Kirchhoff diffraction theory. The far field pattern and then the normalized transmittance was derived assuming different nonlinearity in the investigated medium as follows

1- Third order nonlinearity at the absence of 2PA

2- Third order nonlinearity at the presence of 2PA

3- Fifth order nonlinearity at the absence of 3PA

4- Fifth order nonlinearity at the presence of 3PA

5- Concurrent third and fifth order nonlinearity at the absence of 2PA and 3PA

6- Concurrent third and fifth order nonlinearity at the presence of 2PA

All the above calculations were performed assuming a circular Gaussian beam. For the case of irradiating a medium with an elliptical Gaussian beam, the far field patterns and then the normalized transmittance for the case of a cubic nonlinearity at the absence of 2PA have been derived.

As previously mentioned, if the aperture is removed and the entire energy transmitted through the nonlinear medium is collected, the Z-scan signal does not contain any information about the nonlinear refraction and only the nonlinear absorption coefficient can be extracted from such an OA Z-scan signal. The normalized transmittance assuming different orders of nonlinear absorption have been calculated as follows:

1- 2PA as a third order nonlinear absorption using a circular Gaussian beam

2- 2PA as a third order nonlinear absorption using an elliptical Gaussian beam

3- 3PA as a fifth order nonlinear absorption using a circular Gaussian beam

Calculations show that both the OA and the CA Z-scan signals will deviate out of symmetry when the irradiating light beam is assumed elliptical as shown in Fig. 2.19 and Fig. 2.21. In the case of an astigmatic light beam the CA Z-scan signal appears as a double peak signal as indicated in Fig. 2.20.

The numerical integrations have been carried out in order to numerically calculate the normalized transmittance. Employing MATLAB software made possible calculating the far field intensity pattern for any given induced phase change. As seen in Fig. 3.1 and Fig. 3.2, it was concluded that when a divergent beam passes through a positive nonlinear medium the far field diffraction pattern consists of a central bright spot surrounded by some narrow rings. It also concluded that when a convergent laser beam passes through a positive nonlinear medium the far field patterns contains some broad rings so that the outer rings are broader. The brightness of the center depends on the induced phase shift. If the phase change is an even integer multiple of π the center is dark but if the phase change is an odd integer multiple of π the center is bright but not as bright as the rings.

Our calculation for normalized transmittance showed that the transmittance highly depends on the aperture size as the difference between transmittance maxima and minima decreases if the aperture sized is increased as shown in Fig. 3.5. Calculation also indicates that the transmittance of a self-focusing media for phase distortions much higher than π turns away from the symmetry so that the transmittance minimum (valley) is saturated. That is a sigh of this fact that the transmitted energy, when a convergent beam passes through a positive nonlinear medium, is distributed more in the rings rather than the central spot. In conclusion, despite the analytical calculation that allowed to calculate the transmittance only for small aperture size and small phase change the numerical calculation provide the possibility to calculate the transmittance for any given aperture size and also for any given phase change. However, the numerical calculation results for aperture transmittances up to 2% and induced phase changes up to 1 (Radian) were consistent with the analytical calculation finding.

Numerical calculation was also performed to calculate the OA Z-scan signals for different order of nonlinear absorption such as 2PA, 3PA, 4PA and 5PA. Calculation results clearly manifest that the width of the OA signal reduces with increasing the order of nonlinearity. This reveals that higher order nonlinear absorptions depend on the light intensity with higher degree.

Our experimental works were devoted to measure the 2PA and 3PA coefficient or cross section of some prepared samples applying OA Z-scan technique. To do these measurements a well aligned set up and a well characterized laser beam with known respective parameters such as beam waist radius and Rayleigh rang are required. A method was proposed to measure the beam waist radius. In this method a small aperture is translated along the propagation direction of the laser beam. The aperture transmittance measured as a function of the aperture position contains information about the beam waist radius.

Our samples were comprised of three different categories.

1. Photo initiators (PI) synthesized in order to utilize in two-photon polymerization (2PP).

2. Metal glass composite in which gold nanoparticles were implanted.

3. Reagent photo grafting materials in order to exploit in multi-photon photo grafting

Among the synthesized PIs, **B3FL** showed the highest 2PA cross section value of 443 GM. One reason is the excellent coplanarity of the stereo rigid fluorenone carbon frame and the suitably strong absorption around 400 nm which ensures the considerable 2PA at 800 nm. 2PP structuring tests were also performed to further characterize the new PIs. B3FL exhibited much broader ideal processing windows than those of other PIs, which is in good agreement with the Z-scan results.

Among the metal glass composites the highest 2TA coefficient of 16.3 cm/GW was obtained for as-annealed BK7 that had developed the largest non-spherical nanoparticles in the thinnest layer of 100 nm under the following conditions: Au^+ implantation, beam energy of 1701 keV, ion fluence of 1×10^{16} ion.cm^{-2}, post-implantation annealing in air at 600 °C for 5 hrs. The smallest 2TA coefficient of 2.5 cm/GW was obtained for as-annealed silica glass that showed no absorption in the UV-VIS region.

A compound with commercial name of (BAC-M) was purchased to utilize as a reagent for photo grafting. Using Z-scan technique allowed us first determining the order of nonlinear absorption and then measuring the nonlinear absorption cross section. Applying fitting process and specifying the extracted Rayleigh length as well as verifying the quality of the fit curves resulted to this conclusion that 3PA is the predominant nonlinear absorption process in this compound. Then, a 3PA cross section of 4.8×10^{-78} ($cm^6.S^2$) was determined for BAC-M. Ultimately, 3D patterns of immobilized BAC-M molecules were successfully recorded in PEG matrices.

MATLAB code for calculating the intensity distribution on the far field plane

```
function I = Int ( rho, z, t, fdphi )
%   rho [mm] ... radial coordinate for calculation of I [W/m^2]
%   z [mm] ... z coordinate
%   t [fs] ... time
%   fdphi  ... 0 if dphi == 0, 1 else
%   D [cm] ... distance from the exit plane of the medium to the
%              far field observation plane
%   L0 [mm] ... physical length of the sample
%   Ep [nJ] ... laser pulse energy
%   alpha0 [1/mm] ... linear absorption coefficient
%   lambda [nm] ... wavelength
%   n0 ... 0th order refraction index
%   tau [fs] ... puls duration
%   gamma [cm^2/W] ... nonlinear refractive coefficient
%                      (for 3rd order nonlinearity)
%   M2 …. Beam quality factor
%   f ……. Focal length of the focusing lens
%   w …. Beam radius on the focusing lens



global D lam alpha0 L0 Ep tau gamma M2 f w;


%   k ... wave number
k = 2.*pi./lam;
%   w0 [micron] ... beam waist radius
w0=(1e-3.*M2.*lam.*f)./(pi.*w);
%   z0 ….. Rayleigh rang
z0 = (k.* w0.^ 2./(2.*M2));
Leff=1e-1.*((1-exp(-alpha0.*L0))./alpha0);
%   wz [micron] ... beam radius at z coordinate
```

```
wz = w0 .* sqrt(1 + z.^ 2./z0.^2);
% if z is 0, R(z) is infinite. Only calculate R(z) if z ~= 0
if z ~= 0
%   R(z) ... radius of curvature of the wave front
Rz = z .* (1 + z0.^2./z.^2);
end
%   r …. Radial coordinate on the
r = linspace(0,3.*wz,round(wz)./2);
dr = r(2)-r(1);

% I0 ... on axis intensity at the focus
I0 = 4 .* sqrt(log(2)/pi) .* Ep./pi./w0.^2./tau;

% delta phi ... phase shift
if fdphi == 0
    dphi = 0;
else
    dphi = k.*Leff.*gamma.*I0.*1e21;
    dphi= dphi.* exp(-2.*r.^2./ wz.^2);
    dphi = dphi./ (1 + z.^2/z0.^2);
    dphi = dphi.* exp(-4.*log(2.*t.^2./tau.^2);
   end

% Iint is the Integrand, which is independent of rho
Iint = -r.^2./ wz.^2;
% only add the Rz contribution if z~= 0 and this term is not equal to 0
if z ~= 0
    Iint = Iint - 1i.* k.* r.^2./(2.* Rz);
end
Iint = Iint - 1i.* dphi;
Iint = exp(Iint).*r;
```

```
for m = 1:length(rho)
    % Isec ... Iint multiplied by the bessel function and integrated
    Isec = k.*rho(m).*r./D;
    Isec = besselj(0,Isec).*Iint;
    Isec = trapz(Isec).*dr;
    Isec = abs(Isec);
    % Intensity without the constant factors
    I(m) = (Isec).^2;
end

% I prime ... Intensity factor
Iprim = (4.*pi.^2.*I0)./(lam.*D).^2;
Iprim = Iprim .* (w0./wz).^2.* exp(-alpha0.*L0);

if t ~= 0
    Iprim = Iprim.*exp(-4.*log(2).*t.^2./tau.^2);
end

% total Intensity
I = I.* Iprim*1e8;
plot(rho,I);
end
```

7. References

1. R. W. Boyd, *Nonlinear optics,* 2nd ed. (Academic, San Diego, 2003).

2. M. Sheik-Bahae and M. P. Hasselbeck, *Optical Properties of Materials, Nonlinear Optics, Quantum Optics,* third ed., HANDBOOK OF OPTICS (McGraw-Hill, New York, 2010), Vol. 4.

3. W. Koechner, *Solid-State Laser Engineering* (Springer Science, 2006).

4. D. L. Mills, *Nonlinear Optics* (Springer, Berlin, 1991).

5. B. A. Reinhardt, "Two-photon Technology: New materials and evolving applications," photonics Sci. News **4**, 21-33 (1999).

6. G. S. He, R. Gvishi, P. N. Prasad, and B. A. Reinhardt, "Two-photon absorption based optical limiting and stabilization in organic molecule-doped solid materials," Optics Communications **117**, 133-136 (1995).

7. G. S. He, J. D. Bhawalkar, C. F. Zhao, and P. N. Prasad, "Optical limiting effect in a two-photon absorption dye doped solid matrix," Applied Physics Letters **67**, 2433 (1995).

8. J. D. Bhawalkar, G. S. He, and P. N. Prasad, "Three-photon induced upconverted fluorescence from an organic compound: application to optical power limiting," Optics Communications **119**, 587-590 (1995).

9. Y. Pang, M. Samoc, and P. N. Prasad, "Third-order nonlinearity and two-photon-induced molecular dynamics: Femtosecond time-resolved transient absorption, Kerr gate, and degenerate four-wave mixing studies in poly (p-phenylene vinylene)/sol-gel silica film," The Journal of Chemical Physics **94**, 5282-5290 (1991).

10. X. Zhang, L. Wang, and Y. Song, "Spatial effects in two-photon excitation transient absorption spectroscopy," Journal of Modern Optics **55**, 3639-3649 (2008).

11. R. Philip, M. Ravikanth, and G. Ravindra Kumar, "Studies of third order optical nonlinearity in iron (III) phthalocyanine μ-oxo dimers using picosecond four-wave mixing," Optics Communications **165**, 91-97 (1999).

12. M. Hotzel, S. Urban, D. A. M. Egbe, T. Pautzsch, and E. Klemm, "Degenerate four-wave mixing measurements of the third-order nonlinearity of poly(aryleneethynylenes) and their model substances," Journal of the Optical Society of America B: Optical Physics **19**, 2645-2649 (2002).

13. K. Kasatani, "Large electronic third-order optical nonlinearities of cyanine dyes measured by resonant femtosecond degenerate four-wave mixing," Optical Materials **21**, 93-97 (2003).

14. M. Zhao, Y. Cui, M. Samoc, P. N. Prasad, M. R. Unroe, and B. A. Reinhardt, "Influence of two-photon absorption on third-order nonlinear optical processes as studied by degenerate four-wave mixing: The study of soluble didecyloxy substituted polyphenyls," The Journal of Chemical Physics **95**, 3991-4001 (1991).

15. M. Sheik-Bahae, A. A. Said, T.-H. Wei, D. J. Hagan, and E. W. Van Stryland, "Sensitive measurement of optical nonlinearities using a single beam," IEEE Journal of Quantum Electronics **26**, 760-769 (1990).

16. M. Sheik-Bahae, A. A. Said, T. H. Wei, D. J. Hagan, E. W. Van Stryland, and M. J. Soileau, "Sensitive n2 measurements using a single beam," NIST Special Publication 126-135 (1990).

17. M. Sheik-Bahae, D. J. Hagan, E. W. Van Stryland, T. H. Wei, A. A. Said, E. Canto, and A. Miller, "Relation between n2 and two-photon absorption," NIST Special Publication 591-597 (1990).

18. M. Sheik-Bahae, A. A. Said, Y. Y. Wu, T. H. Wei, D. J. Hagan, and E. W. Van Stryland, "Simple and sensitive technique for determining refractive nonlinearities," CONFERENCE ON LASERS AND ELECTRO-0PTICS 278-279 (1989).

19. K. V. Adarsh, K. S. Sangunni, C. S. S. Sandeep, R. Philip, S. Kokenyesi, and V. Takats, "Observation of three-photon absorption and saturation of two-photon absorption in amorphous nanolayered Se/As2S3 thin film structures," Journal of Applied Physics **102**, (2007).

20. J. He, J. Mi, H. Li, and W. Ji, "Observation of interband two-photon absorption saturation in CdS nanocrystals," Journal of Physical Chemistry B **109**, 19184-19187 (2005).

21. J. Wang, B. Gu, X. W. Ni, and H. T. Wang, "Z-scan theory with simultaneous two- and three-photon absorption saturation," Optics and Laser Technology (2011).

22. B. Gu, J. He, W. Ji, and H. T. Wang, "Three-photon absorption saturation in ZnO and ZnS crystals," Journal of Applied Physics **103**, (2008).

23. L. Luo, C. Li, S. Wang, W. Huang, C. Wu, H. Yang, H. Jiang, Q. Gong, Y. Yang, and S. Feng, "Optical microstructures fabricated by femtosecond laser two-photon polymerization," Journal of Optics A: Pure and Applied Optics **3**, 489-492 (2001).

24. A. Ostendorf and B. N. Chichkov, "Two-photon polymerization: A new approach to micromachining," Photonics Spectra **40**, 72-80 (2006).

25. G. Ashkenasy, D. Cahen, R. Cohen, A. Shanzer, and A. Vilan, "Molecular engineering of semiconductor surfaces and devices," Accounts of Chemical Research **35**, 121-128 (2002).

26. I. Bisson, M. Kosinski, S. Ruault, B. Gupta, J. Hilborn, F. Wurm, and P. Frey, "Acrylic acid grafting and collagen immobilization on poly(ethylene terephthalate) surfaces for adherence and growth of human bladder smooth muscle cells," Biomaterials **23**, 3149-3158 (2002).

27. C. B. Herbert, T. L. McLernon, C. L. Hypolite, D. N. Adams, L. Pikus, C. C. Huang, G. B. Fields, P. C. Letourneau, M. D. Distefano, and W. S. Hu, "Micropatterning gradients and controlling surface densities of photoactivatable biomolecules on self-assembled monolayers of oligo(ethylene glycol) alkanethiolates," Chemistry and Biology **4**, 731-737 (1997).

28. M. A. Holden and P. S. Cremer, "Light activated patterning of dye-labeled molecules on surfaces," Journal of the American Chemical Society **125**, 8074-8075 (2003).

29. M. S. Hahn, J. S. Miller, and J. L. West, "Three-dimensional biochemical and biomechanical patterning of hydrogels for guiding cell behavior," Advanced Materials **18**, 2679-2684 (2006).

30. D. A. Parthenopoulos and P. M. Rentzepis, "Three-dimensional optical storage memory," Science **245**, 843-845 (1989).

31. A. S. Dvornikov, E. P. Walker, and P. M. Rentzepis, "Two-photon three-dimensional optical storage memory," Journal of Physical Chemistry A **113**, 13633-13644 (2009).

32. H. E. Pudavar, M. P. Joshi, P. N. Prasad, and B. A. Reinhardt, "High-density three-dimensional optical data storage in a stacked compact disk format with two-photon writing and single photon readout," Applied Physics Letters **74**, 1338-1340 (1999).

33. G. Cheng, Y. Wang, J. D. White, Q. Liu, W. Zhao, and G. Chen, "Demonstration of high-density three-dimensional storage in fused silica by femtosecond laser pulses," Journal of Applied Physics **94**, 1304-1307 (2003).

34. M. Oheim, D. J. Michael, M. Geisbauer, D. Madsen, and R. H. Chow, "Principles of two-photon excitation fluorescence microscopy and other nonlinear imaging approaches," Advanced Drug Delivery Reviews **58**, 788-808 (2006).

35. C. Wang, Y. Ren, Z. Shao, X. Zhao, G. Zhou, D. Wang, Q. Fang, and M. Jiang, "Studies on two-photon pumped frequency up-converted lasing properties of a new material HMASPS," Journal of Modern Optics **48**, 1113-1122 (2001).

36. W. Rapp and B. Gronau, "Laser emission from two xanthene dyes via double-photon excitation," Chemical Physics Letters **8**, 529-532 (1971).

37. Y. F. Zhou, S. Y. Feng, and X. M. Wang, "Investigation of TPP up-conversion lasing of stilbene derivatives," Journal of Molecular Structure **613**, 91-94 (2002).

38. H. A. Collins, M. Khurana, E. H. Moriyama, A. Mariampillai, E. Dahlstedt, M. Balaz, M. K. Kuimova, M. Drobizhev, V. X. D. Yang, D. Phillips, A. Rebane, B. C. Wilson, and H. L. Anderson, "Blood-vessel closure using photosensitizers engineered for two-photon excitation," Nature Photonics **2**, 420-424 (2008).

39. D. Gao, R. R. Agayan, H. Xu, M. A. Philbert, and R. Kopelman, "Nanoparticles for two-photon photodynamic therapy in living cells," Nano Letters **6**, 2383-2386 (2006).

40. T. C. Lin, G. S. He, Q. Zheng, and P. N. Prasad, "Degenerate two-/three-photon absorption and optical power-limiting properties in femtosecond regime of a multi-branched chromophore," Journal of Materials Chemistry **16**, 2490-2498 (2006).

41. G. S. He, Q. Zheng, C. Lu, and P. N. Prasad, "Two- and three-photon absorption based optical limiting and stabilization using a liquid dye," IEEE Journal of Quantum Electronics **41**, 1037-1043 (2005).

42. D. Weaire, B. S. Wherrett, D. A. B. Miller, and S. D. Smith, "Effect of low-power nonlinear refraction on laser-beam propagation in InSb," Opt. Lett. **4**, 331-333 (1979).

43. A. A. Said, M. Sheik-Bahae, D. J. Hagan, T. H. Wei, J. Wang, J. Young, and E. W. V. Stryland, "Determination of bound-electronic and free-carrier nonlinearities in ZnSe, GaAs, CdTe, and ZnTe," J. Opt. Soc. Am. B **9**, 405-414 (1992).

44. T. C. Lin, S. J. Chung, K. S. Kim, X. Wang, G. S. He, J. Swiatkiewicz, H. E. Pudavar, and P. N. Prasad, "Organics and polymers with high two-photon activities and their applications," Advances in Polymer Science **161**, 157-193 (2003).

45. D. S. Corrêa, L. De Boni, L. Misoguti, I. Cohanoschi, F. E. Hernandez, and C. R. Mendonça, "Z-scan theoretical analysis for three-, four- and five-photon absorption," Optics Communications **277**, 440-445 (2007).

46. S. M. Mian, B. Taheri, and J. P. Wicksted, "Effects of beam ellipticity on Z-scan measurements," Journal of the Optical Society of America B: Optical Physics **13**, 856-863 (1996).

47. Y. L. Huang and C. K. Sun, "Z-scan measurement with an astigmatic Gaussian beam," Journal of the Optical Society of America B: Optical Physics **17**, 43-47 (2000).

48. P. W. MILONNI, *LASERS* (JOHN WILEY, New York, 1988), p. 747.

49. E. Koushki, A. Farzaneh, and S. H. Mousavi, "Closed aperture Z-scan technique using the Fresnel-Kirchhoff diffraction theory for materials with high nonlinear refractions," Applied Physics B: Lasers and Optics 1-6 (2010).

50. C. M. Nascimento, M. A. R. C. Alencar, S. Chvez-Cerda, M. G. A. Da Silva, M. R. Meneghetti, and J. M. Hickmann, "Experimental demonstration of novel effects on the far-field diffraction patterns of a Gaussian beam in a Kerr medium," Journal of Optics A: Pure and Applied Optics **8**, 947-951 (2006).

51. L. Deng, K. He, T. Zhou, and C. Li, "Formation and evolution of far-field diffraction patterns of divergent and convergent Gaussian beams passing through self-focusing and self-defocusing media," Journal of Optics A: Pure and Applied Optics **7**, 409-415 (2005).

52. D. Yu, W. Lu, R. G. Harrison, and N. N. Rosanov, "Analysis of dark spot formation in absorbing liquid media," Journal of Modern Optics **45**, 2597-2606 (1998).

53. H. Ono and Y. Harato, "Anisotropic diffraction pattern formation from guest host liquid crystals," Optics Communications **168**, 251-259 (1999).

54. S. Brugioni and R. Meucci, "Self-phase modulation in a nematic liquid crystal film induced by a low-power CO2 laser," Optics Communications **206**, 445-451 (2002).

55. D. R. Paschotta, in *Encyclopedia for Photonics and Laser Technology,* (2011).

56. T. F. Johnston Jr, "Beam propagation (M2) measurement made as easy as it gets: The four-cuts method," Applied Optics **37**, 4840-4850 (1998).

57. M. Rumi, S. Barlow, J. Wang, J. W. Perry, and S. R. Marder, "Two-photon absorbing materials and two-photon-induced chemistry," **213**, 1-95 (2008).

58. G. S. He, L. S. Tan, Q. Zheng, and P. N. Prasad, "Multiphoton absorbing materials: Molecular designs, characterizations, and applications," Chemical Reviews **108**, 1245-1330 (2008).

59. R. Kannan, G. S. He, L. Yuan, F. Xu, P. N. Prasad, A. G. Dombroskie, B. A. Reinhardt, J. W. Baur, R. A. Vaia, and L. S. Tan, "Diphenylaminofluorene-based two-photon-absorbing chromophores with various π-electron acceptors," Chemistry of Materials **13**, 1896-1904 (2001).

60. Y. Iwase, K. Kamada, K. Ohta, and K. Kondo, "Synthesis and photophysical properties of new two-photon absorption chromophores containing a diacetylene moiety as the central π-bridge," Journal of Materials Chemistry **13**, 1575-1581 (2003).

61. C. Heller, N. Pucher, B. Seidl, K. Kalinyaprak-Icten, G. Ullrich, L. Kuna, V. Satzinger, V. Schmidt, H. C. Lichtenegger, J. Stampfl, and R. Liska, "One- and two-photon activity of cross-conjugated photoinitiators with bathochromic shift," Journal of Polymer Science, Part A: Polymer Chemistry **45**, 3280-3291 (2007).

62. N. Pucher, A. Rosspeintner, V. Satzinger, V. Schmidt, G. Gescheidt, J. Stampfl, and R. Liska, "Structure-activity relationship in D-π-a-π-D-based photoinitiators for the two-photon-induced photopolymerization process," Macromolecules **42**, 6519-6528 (2009).

63. leo, "Synthesis and structure-activity relationship of several aromatic ketone-based two-photon initiators " ournal of Polymer Science Part A (2011).

64. P. C. S. Kasap, *Springer Handbook of Electronic and Photonic Materials,* 1st ed. (Springer, New York, 2006).

65. N. N. H. Bach, *The Properties of Optical Glass* (Springer-Verlag, Berlin, 1998).

66. R. L. Sutherland, *Handbook of Nonlinear Optics,* 2nd ed. (Marcel Dekker, New York, 2003).

67. P. Chakraborty, "Metal nanoclusters in glasses as non-linear photonic materials," Journal of Materials Science **33**, 2235-2249 (1998).

68. F. Gonella and P. Mazzoldi, *Handbook of Nanostructured Materials and Nanotechnology* (Academic, San Diego, 2000), Vol. 4.

69. B. Palpant, *Non-linear optical properties of matter*, CHALLENGES AND ADVANCES IN

COMPUTATIONAL CHEMISTRY AND PHYSICS (Springer, 2006), Vol. 1.

70. W. Rechberger, A. Hohenau, A. Leitner, J. R. Krenn, B. Lamprecht, and F. R. Aussenegg, "Optical properties of two interacting gold nanoparticles," Optics Communications **220**, 137-141 (2003).

71. A. I. Ryasnyanskiy, B. Palpant, S. Debrus, U. Pal, and A. L. Stepanov, "Optical nonlinearities of Au nanoparticles embedded in a zinc oxide matrix," Optics Communications **273**, 538-543 (2007).

72. A. Lesuffleur, P. Gogol, P. Beauvillain, B. Guizal, D. Van Labeke, and P. Georges, "Nonlinear optical properties of interconnected gold nanoparticles on silicon," Journal of Applied Physics **104 (12)**, (2008).

73. F. Z. Henari and A. A. Dakhel, "Linear and nonlinear optical properties of gold nanoparticle-Eu oxide composite thin films," Journal of Applied Physics **104 (3)**, (2008).

74. W. Wang, Y. Wang, Z. Dai, and Y. Sun, "Nonlinear optical properties of periodic gold nanoparticle arrays," Applied Surface Science **253**, 4673-4676 (2007).

75. A. I. Ryasnyanskiy, B. Palpant, S. Debrus, U. Pal, and A. Stepanov, "Third-order nonlinear-optical parameters of gold nanoparticles in different matrices," Journal of Luminescence **127**, 181-185 (2007).

76. N. Venkatram, R. Sai Santosh Kumar, D. Narayana Rao, S. K. Medda, S. De, and G. De, "Nonlinear optical absorption and switching properties of gold nanoparticle doped SiO2-TiO2 sol-gel films," Journal of Nanoscience and Nanotechnology **6**, 1990-1994 (2006).

77. J. T. Seo, S. M. Ma, Q. Yang, R. Battle, L. Creekmore, B. Tabibi, W. J. Kim, J. H. Heo, W. S. Yun, D. H. Ha, S. S. Jung, E. Bryant, C. Payne, W. Yu, and V. Colvin, "Cubic nonlinearity and hyperpolarizability of gold nanometals," presented at the IEEE 1258 (2006).

78. A. I. Ryasnyanskiy, B. Palpant, S. Debrus, U. Pal, and A. L. Stepanov, "Nonlinear optical properties of gold nanoparticles dispersed in different optically transparent matrices," Physics of the Solid State **51**, 55-60 (2009).

79. Y. Chen, L. Karvonen, A. Säynätjoki, C. Ye, A. Tervonen, and S. Honkanen, "Ag nanoparticles embedded in glass by two-step ion exchange and their SERS application," Opt. Mater. Express **1**, 164-172 (2011).

80. M. Dubiel, H. Hofmeister, and E. Wendler, "Formation of nanoparticles in soda-lime glasses by single and double ion implantation," Journal of Non-Crystalline Solids **354**, 607-611 (2008).

81. B. Svecova, P. Nekvindova, A. MacKova, P. Malinsky, A. Kolitsch, V. Machovic, S. Stara, M. Mika, and J. Spirkova, "Study of Cu+, Ag+ and Au+ ion implantation into silicate glasses," Journal of Non-Crystalline Solids **356**, 2468-2472 (2010).

82. B. Akkopru and C. Durucan, "Preparation and microstructure of sol-gel derived silver-doped silica," Journal of Sol-Gel Science and Technology **43**, 227-236 (2007).

83. J. Zhang, W. Dong, J. Sheng, J. Zheng, J. Li, L. Qiao, and L. Jiang, "Silver nanoclusters formation in ion-exchanged glasses by thermal annealing, UV-laser and X-ray irradiation," Journal of Crystal Growth **310**, 234-239 (2008).

84. B. Svecova, J. Spirkova, P. Nekvindova, M. Mika, and L. Svecova, "Ion exchange as a new tool to evaluate and quantify glass homogeneity," Journal of Non-Crystalline Solids **356**, 1509-1513 (2010).

85. P. Malinský, A. Macková, J. Bočan, B. Švecová, and P. Nekvindová, "Au implantation into various types of silicate glasses," Nuclear Instruments and Methods in Physics

Research, Section B: Beam Interactions with Materials and Atoms **267**, 1575-1578 (2009).

86. Z. Li, M. Siklos, N. Pucher, K. Cicha, A. Ajami, W. Husinsky, A. Rosspeintner, E. Vauthey, G. Gescheidt, J. Stampfl, and R. Liska, "Synthesis and structure-activity relationship of several aromatic ketone-based two-photon initiators," Journal of Polymer Science, Part A: Polymer Chemistry **49**, 3688-3699 (2011).

87. U. Gubler and C. Bosshard, "Molecular design for third-order nonlinear optics," Advances in Polymer Science **158**, 123-191 (2002).

88. L. Antonov, K. Kamada, and K. Ohta, "Estimation of two-photon absorption characteristics by a global fitting procedure," Applied Spectroscopy **56**, 1508-1511 (2002).

89. H. B. Sun and S. Kawata, "Two-photon photopolymerization and 3D lithographic microfabrication," Advances in Polymer Science **170**, 169-273 (2004).

90. B. H. Cumpston, S. P. Ananthavel, S. Barlow, D. L. Dyer, J. E. Ehrlich, L. L. Erskine, A. A. Heikal, S. M. Kuebler, I. Y. S. Lee, D. McCord-Maughon, J. Qin, H. Röckel, M. Rumi, X. L. Wu, S. R. Marder, and J. W. Perry, "Two-photon polymerization initiators for three-dimensional optical data storage and microfabrication," Nature **398**, 51-54 (1999).

91. K. J. Schafer, J. M. Hales, M. Balu, K. D. Belfield, E. W. Van Stryland, and D. J. Hagan, "Two-photon absorption cross-sections of common photoinitiators," Journal of Photochemistry and Photobiology A: Chemistry **162**, 497-502 (2004).

92. A. Ovsianikov, Z. Li, A. Ajami, J. Torgersen, W. Husinsky, J. Stampfl, and R. Liska, "3D grafting via three-photon induced photolysis of aromatic azides," Applied Physics A (2012).

93. A. Ajami, W. Husinsky, R. Liska, Z. Li, J. Stampfl, and A. Ovsianikov, "Three-photon Absorption Measurement of BAC-M, an Efficient Reagent for Three-photon Induced Photografting," in *Ultrafast Phenomena 2012,* (2012).

94. W. Husinsky, A. Ajami, P. Nekvindova, B. Svecova, J. Pesicka, and M. Janecek, "Z-scan study of nonlinear absorption of gold nanoparticles prepared by ion implantation in various types of silicate glasses," Optics Communications **285**, 2729-2733 (2012).

95. Y. H. Wang, Y. M. Wang, J. D. Lu, L. L. Ji, R. G. Zang, and R. W. Wang, "Nonlinear optical properties of Cu nanoclusters by ion implantation in silicate glass," Optics Communications **283**, 486-489 (2010).

96. S. Nah, L. Li, and J. T. Fourkas, "Field-enhanced phenomena of gold nanoparticles," Journal of Physical Chemistry A **113**, 4416-4422 (2009).

97. R. Sreeja, R. Reshmi, M. George, and M. K. Jayaraj, "Determination of third-order optical absorptive nonlinearity of ZnO nanoparticles by Z-scan technique," presented at the SPIE, 7155 Art. No.: 715521 (2008).

98. X. Liu, Y. Tomita, K. Yasui, K. Kojima, and K. Chikama, "Z-scan characterization of nonlinear optical effects in polymer films incorporating hyperbranched polymer-metallic nanoparticle complex," presented at the SPIE, 7722 Art. No.: 77222A (2010).

99. J. Shin, K. Jang, K. S. Lim, I. B. Sohn, Y. C. Noh, and J. Lee, "Formation and control of Au and Ag nanoparticles inside borate glasses using femtosecond laser and heat treatment," Applied Physics A: Materials Science and Processing **93**, 923-927 (2008).

100. P. Wang, Y. Lu, L. Tang, J. Zhang, H. Ming, J. Xie, F. H. Ho, H. H. Chang, H. Y. Lin, and D. P. Tsai, "Surface-enhanced optical nonlinearity of a gold film," Optics Communications **229**, 425-429 (2004).